EFFECTS OF TEMPERATURE AND ENVIRONMENT ON CREEP BEHAVIOR OF AN OXIDE-OXIDE CERAMIC MATRIX COMPOSITE

THESIS

Jason C. Braun, Captain, USAF

AFIT/GAE/ENY/07-M04

DEPARTMENT OF THE AIR FORCE
AIR UNIVERSITY

AIR FORCE INSTITUTE OF TECHNOLOGY

Wright-Patterson Air Force Base, Ohio

The views expressed in this thesis are those of the author and do not reflect the official policy or position of the United States Air Force, Department of Defense, or the U.S. Government.

AFIT/GAE/ENY/07-M04

EFFECTS OF TEMPERATURE AND ENVIRONMENT ON CREEP BEHAVIOR OF AN OXIDE-OXIDE CERAMIC MATRIX COMPOSITE

THESIS

Presented to the Faculty

Department of Aeronautical and Astronautical Engineering

Graduate School of Engineering and Management

Air Force Institute of Technology

Air University

Air Education and Training Command

In Partial Fulfillment of the Requirements for the

Degree of Master of Science in Aeronautical Engineering

Jason C. Braun, B.S.M.E.

Captain, USAF

March 2007

AFIT/GAE/ENY/07-M04

EFFECTS OF TEMPERATURE AND ENVIRONMENT ON CREEP BEHAVIOR OF AN OXIDE-OXIDE CERAMIC MATRIX COMPOSITE

Jason C. Braun, B.S.M.E.

Captain, USAF

Approved:

Marina Ruggles-Wrenn	3/12/07
Dr. Marina B. Ruggles-Wrenn (Chairman)	Date
S Soni	3/13/07
Dr. Som Soni (Member)	Date
R A Canfield	3/12/07
Dr. Robert Canfield(Member)	Date

Abstract

This research investigated the creep behavior of an N720/Al_20_3 composite. The composite consists of a porous alumina matrix reinforced with laminated, woven mullite/alumina fibers (Nextel™ 720). This ceramic matrix composite (CMC) has no fiber coating and relies on the porous matrix for flaw tolerance.

The tensile stress-strain behavior was investigated and the tensile properties measured in the 800-1100 °C temperature range. Tensile creep behavior was examined at 1000 and 1100 °C in laboratory air and in steam environment. In air creep stress was 150 MPa. In steam creep stresses ranged from 100 to 160 MPa.

Primary and secondary creep, but no tertiary creep, were observed in all tests. Minimum creep rate was reached in all tests. Creep rates accelerated with increasing temperature and creep stress. The presence of steam further increased creep rates. At 1000 °C creep run-out, defined as 100 hours at creep stress, was achieved in all tests. At 1100 °C run-out was achieved at 150 MPa in laboratory air, but only at 100 MPa in steam. The residual strength and modulus of all specimens that achieved run-out were characterized. At 1100 °C in the presence of steam, creep performance deteriorated rapidly with increasing creep stress. Composite microstructure, as well as damage and failure mechanisms, were explored.

Acknowledgments

I would like to express my heartfelt, sincere appreciation to those individuals whose help and time made this thesis possible: Dr. Marina Ruggles-Wrenn, my advisor, whose expertise and mentoring guided me and provided invaluable advice; Mr. Sean Miller and Mr. Barry Page, whose technical skills and hard effort ensured I had the best possible equipment for testing; Mr. Jan LeValley and his staff at the AFIT model fabrication shop, whose time and abilities allowed my testing specimens to be manufactured; Dr. Joseph Zelina, Dr. Ruth Sikorski, and Dr. Ron Kerans, whose sponsorship made my research possible; Dr. Robert Canfield and Dr. Som Soni, for their membership on my thesis committee and discerning comments; Lt Joseph Broeckert, Lt Christina Falcone, Capt Christine Ladrido, and LT Robert Salvia, whose companionship, friendship, and brainstorming sessions provided a welcome atmosphere of camaraderie; and most of all, the inspiration and constant support behind everything, my lovely fiancée. Thank you one and all.

Jason C. Braun

Table of Contents

Page

Page

Page

List of Figures

Page

Page

Page

Page

Page

Page

Page

Page

Page

Page

Page

Page

Page

Page

Page

Page

Page

Page

Page

Page

Page

Page

Page

Page

List of Tables

Page

EFFECTS OF TEMPERATURE AND ENVIRONMENT ON CREEP BEHAVIOR OF AN OXIDE-OXIDE CERAMIC MATRIX COMPOSITE AT 1000 & 1100 °C

I. Introduction

As the U.S. Air Force and aerospace industry continue to strive for improvements in aircraft weight reduction, performance, and reliability, composite materials are receiving more attention. A composite is "… a material system consisting of two or more phases on a macroscopic scale, whose mechanical performance and properties are designed to be superior to those of the constituent materials acting independently" [14:1].

Ceramic-matrix composites (CMCs) capable of maintaining excellent strength and fracture toughness at high temperatures continue to be attractive candidate materials, particularly for aerospace turbine engine applications.

In these applications, CMCs will be subjected to mechanical loading in complex environments. Before ceramic matrix composites can be widely used in high-temperature aerospace engine applications, their structural integrity and long-term environmental durability must be assured. Characterization of the mechanical behavior of candidate CMCs in relevant engine environments is required for design and safety assurance of structural components.

The focus of this effort is to characterize the creep behavior of the N720/A oxide-oxide ceramic matrix composite over the 1000-1100 °C temperature range in laboratory air and in steam environment. Oxide-oxide ceramic matrix composites exhibit excellent fatigue and durability, but relatively poor creep resistance.

II. Background

This chapter provides a brief discussion of ceramic matrix composites (CMCs), particularly oxide/oxide CMCs and the various possible damage propagation methods available to CMC designers. It concludes by discussing creep in relation to CMCs and relevant previous research.

2.1 Ceramic Matrix Composites

Ceramic matrix composites are prime candidate materials for use in components that must operate at high temperatures in aggressive environments. Figure 1 illustrates the advantages offered by ceramic materials as regards their operating temperatures.

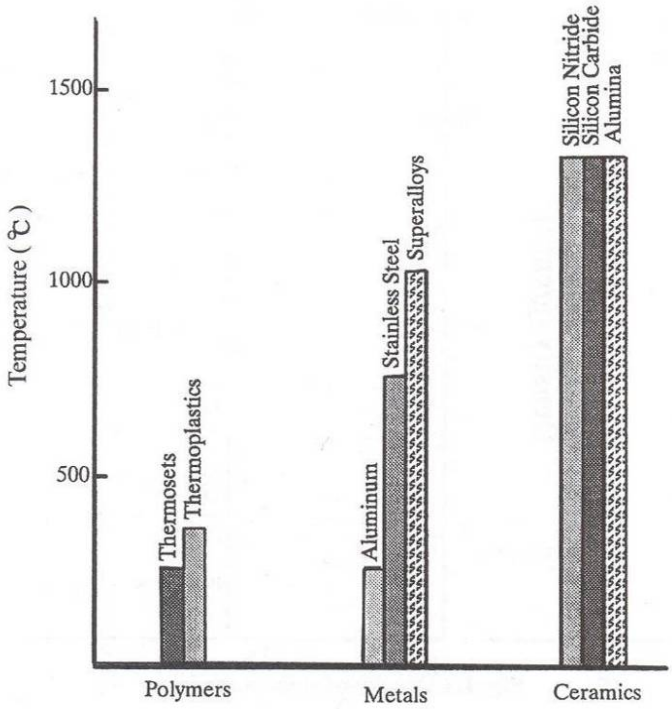

Figure 1. Maximum Material Service Temperatures [12:5].

Ceramics are inorganic, non-metallic materials, although their crystalline microstructures often contain compounds with metallic elements in their bonds [3]. Their positive qualities include high strength, elasticity, hardness, heat resistance, and their high uniform density [33:2077]. The density and thermal coefficients of expansion of ceramics are also lower than those of metals' [12:4]. However, ceramics also exhibit low shock tolerance and extreme brittleness, due to low fracture toughness [43]. This limits the use of monolithic ceramics in load-bearing applications.

Ceramic matrix composites (CMCs) combine the desirable high temperature performance of monolithic ceramics with damage tolerance. Ceramic matrix composites are also less sensitive to thermal shock [53].

2.2 "Ideal" Continuous Fiber Ceramic Composites

The "ideal" continuous fiber ceramic composite (CFCC) would possess many attributes, such as the ability to retain high strength, and exhibit high creep resistance and damage tolerance in high temperature, oxidizing environments for extended periods of time. Among the oxide-oxide ceramic matrix composites, N720/A shows potential for application in aggressive environments at elevated temperatures [21; 24; 30; 51].

2.2.1 Fibers

The fibers in a CFCC are the primary CMC reinforcement due to their high strength and stiffness [12:47]. They can be grouped into bundles or kept as larger monofilaments. The monofilaments range from 50 to 100 μm in diameter while the multifiber tows are bundled from 5 to 15 μm fibers. Monofilament fibers are more

prevalent in metal matrix composites, whereas bundles are preferred in CMCs because they lower the effects and severity of fiber defects [34:15].

Fibers are identified as oxide or non-oxide. Non-oxide fibers are made from silicon carbide (SiC) or boron nitride (BN). Nicalon, Tyranno, and Sylramic are examples of non-oxide fibers [59]. Oxide fibers include Nextel 610 (N610), an Al_2O_3 fiber, and Nextel 720 (N720), a two-phase mullite/alumina fiber. Nextel 610 fibers have small alumina grains, which provide high strength and a high stiffness of 400 GPa [67; 69]. However, the small, 0.1 μm grains of the N610 fibers lead to poor creep resistance as creep rate is inversely proportional to grain size [50]. Nextel 720 fibers contain mullite (SiO_2) in addition to alumina. The larger mullite grains serve to impede grain boundary sliding, thereby improving creep resistance [28:2333]. However, this improvement in creep resistance comes with the tradeoff of lowering strength and stiffness [41; 50:313]. Table 1 highlights desirable properties of fibers.

Table 1. Properties of Ceramic Fibers [15].

Fiber Property	CMC Benefit
• High Modulus	• Improves CMC stiffness and reduces matrix stresses
• High As-Produced Strength	• Improves CMC toughness and ultimate strength
• High Thermomechanical Stability	• Improves CMC as-fabricated strength, CMC strength retention and creep resistance during service
• High Oxidative Stability	• Improves CMC service life in oxidizing environments
• Small Diameter	• Improves matrix strength and facilitates fabrication of thin and complex-shaped CMCs
• Low Density	• Improves CMC specific properties for weight-sensitive applications and reduces stresses in CMC rotating components
• Low Cost	• Reduces CMC cost and improves CMC commercial viability

2.2.2 Matrix

The matrix is the "glue" holding a CMC together. Matrix in CMCs performs three main functions. The first is to relieve stress concentrations on and transfer loading between fibers. Second, matrix separates the fibers from each other so that if one fiber fails the failure doesn't cascade to other fibers. Finally, and perhaps most importantly for aggressive operating environments, matrix protects the fibers from degrading environmental effects [5:7]. This is accomplished by resisting oxidation and guarding against moisture infiltration. In addition, good creep and fatigue performance of the matrix are a benefit [12:41].

Matrix can be glassy (amorphous) or crystalline in structure. The alumina matrix in N720/A is crystalline, having a granular appearance. Its small grains contain a glassy

phase at grain boundaries [12:42]. As mentioned previously, the small grain size provides for higher strength but can lower the creep resistance of the matrix.

A good matrix will not react chemically with fibers during manufacturing. Good chemical compatibility between matrix and fibers is also important after infiltration. Post-infiltration sintering at elevated temperatures may incite a reaction, causing degradation of the fiber-matrix interface [44:10]. Even with good chemical compatibility, the mismatch between linear coefficients of thermal expansion of matrix and fiber can cause cracking when a CMC is cooled from the high processing temperatures to room temperature [21:607]. The difference in ductility and expansion coefficients also creates residual stresses in the composite [4:572]. Figure 2 and Figure 3 show as-processed matrix material. In Figure 2, 0° and 90° fibers are visible inter-mixed with the matrix. Matrix infiltration is evident in Figure 3.

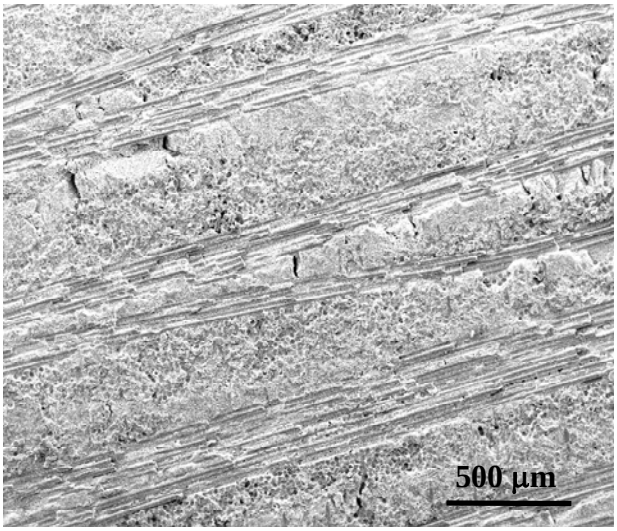

Figure 2. As-processed N720/A composite. Micro-cracking is apparent [37].

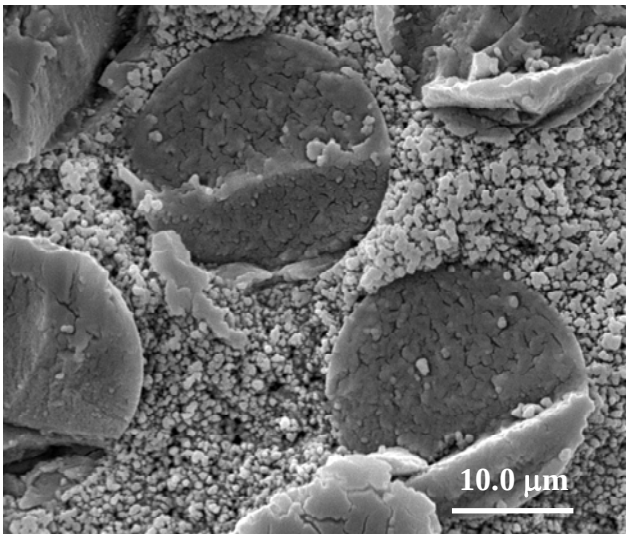

Figure 3. Micrograph of as-processed N720/A composite. Porous nature of the matrix is apparent [37].

2.3 Damage Tolerance Mechanisms

There are several ways to design a CMC so it will not fail in a brittle manner and will "tolerate" damage, thereby increasing its overall toughness. The overarching principle is to dissipate energy. This provides the opportunity for warning signs to appear before final failure, allowing periodic inspections to catch progressing damage early. Fiber-matrix de-bonding, crack deflection, crack bridging, and fiber pullout are all examples of energy dissipating behaviors that serve this purpose [12:148].

In CMCs, this energy dissipation largely centers on the interface between fiber and matrix [60]. As load is applied to a CFCC, the relatively weaker matrix cracks first. When there is a strong interfacial bond between the matrix and fibers, any cracks originating in the matrix will continue to propagate through any fibers encountered in their path [12:301]. A weak interface, however, will encourage crack fronts to move around fibers by providing a path of lesser resistance [50]. As the cracks form around the

fibers, they protect fibers from stress concentrations: debonding occurs, followed by crack deflection, and crack bridging [29]. Then fiber fracture and fiber pull-out occur [12:301]. Crack propagation paths for strong and weak interfaces are shown in Figure 4.

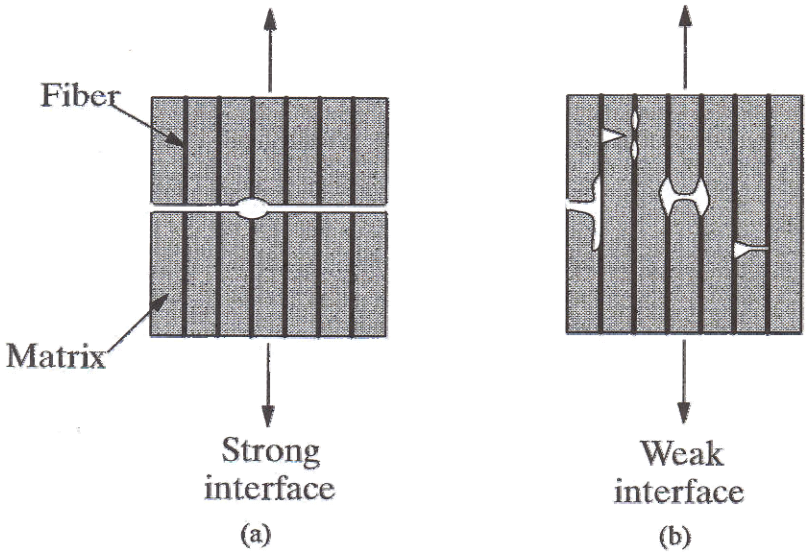

Figure 4. Crack propagation paths [12:148].

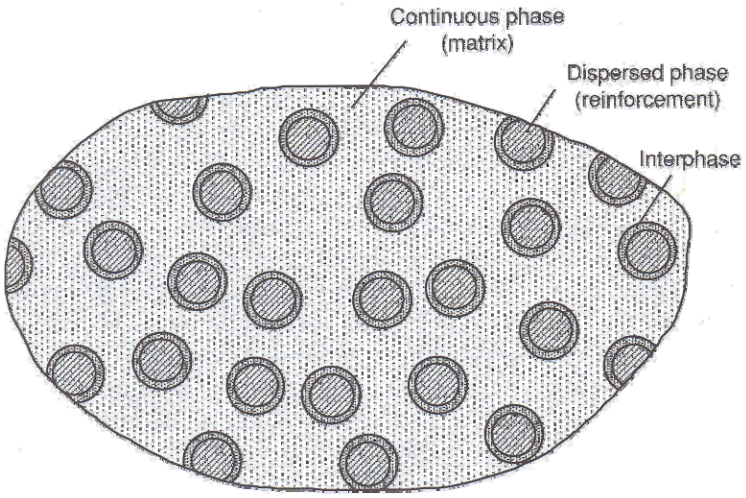

Figure 5. Composite phases [14:1].

Since most fiber-matrix bonds are not weak, an intermediary interphase layer is coated onto fibers to provide the needed weak interface, shown in Figure 5. The

interphase is usually a ~2 μm layer of boron nitride or carbon [29; 60]. The fiber coatings protect fibers, but also increase fabrication cost and are more difficult to produce [22; 26].

This interface imparts a stress-strain curve behavior with two distinct sections. A "knee" in the curve forms as the density of matrix micro-cracks increases and the load is transferred to the fibers (See Figure 6) [36:9].

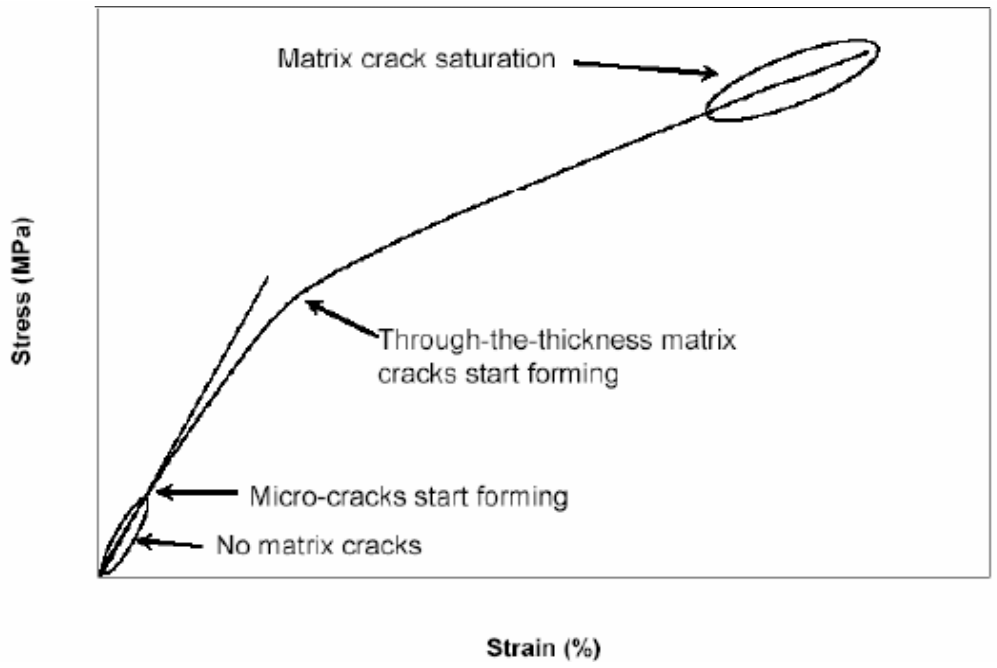

Figure 6. Two-portion stress-strain behavior caused by weak interface [31:10].

In an oxidizing environment the interphase breaks down, restoring the natural strong interfacial bond between fibers and matrix [50:212]. This increased bond strength causes composite "embrittlement" [21]. It lowers damage tolerance and thus decreases the chance of delayed failure. Since many CMCs are designed to operate in oxidizing environments, interphase material becomes a less desirable means of improving damage tolerance. Ceramic matrix composites based on environmentally stable oxide

constituents were developed that utilize a porous matrix for damage tolerance instead [32; 61]. The N720/A studied in this research is a porous matrix composite with oxide matrix and oxide fibers.

Figure 7a shows damage propagation in standard weak interface CFCCs with dense matrices and those with porous matrices and strong fiber-matrix interfaces. The path of least resistance for cracks is from pore to pore in the matrix. Grain pairs break at grain boundaries, and once a crack has propagated through the thickness of a composite part, fibers begin to randomly break. This is similar to how bundles of fibers would break if they were not embedded in matrix material [21]. Porous matrix CMCs do not exhibit the "knee" in the stress-strain curve, since load is carried primarily by fibers from the beginning [21].

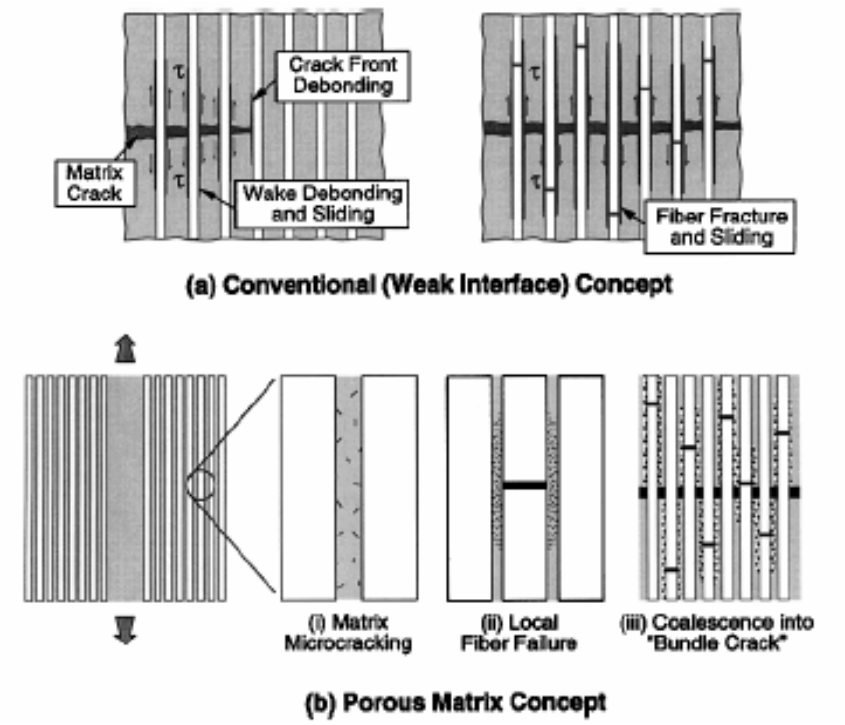

Figure 7. Damage propagation with (a) weak interface versus (b) porous matrix [71].

Careful attention must be paid to the level of porosity in a matrix [51]. Matrix porosity largely determines off-axis and interlaminar properties as well as toughness [33]. Lowering porosity increases off-axis strength but lowers overall strength and damage tolerance at the same time. As a benchmark, a matrix porosity of 35-40% allows considerable fiber pullout, an indication of the aforementioned random failure [71]. As porosity is lowered, more planar, flat fracture surfaces ensue.

2.4 Non-Oxide and Oxide/Oxide Ceramic Matrix Composites

Even though the porous matrix CMCs do not have interphases that break down in oxidizing environments, non-oxide CMCs can still oxidize and degrade – particularly through the fibers. A CMC is defined as a non-oxide if one or more of its phases are not oxidized. As micro-cracks develop, water vapor and/or oxygen oxidize fibers, damaging them. This leads to decreased strength and shortened component life. One way to prevent this is to limit using any non-oxide CMC, such as one containing silicon carbide, to below its matrix-cracking temperature [33:2077]. This severely limits the usefulness of these materials in structural applications, since that would prevent using most non-oxide CMCs in the high temperature regimes.

Oxide-oxide composites like N720/A, "designed to prevent high temperature oxidation damage to fibers or matrix", are inherently oxidation resistant [9:139]. Fibers and matrix are both already oxidized so that the degrading effects of high temperature and oxidizing environments are limited [25; 42; 48; 70]. The oxide-oxide CMCs were first conceived in the late 1980s and were meant to improve net composite properties and

performance [6:451]. Oxide-oxide CMCs are more chemically stable in already-oxidized forms and therefore resist further oxidation [45:379].

2.5 Oxide/Oxide Ceramic Matrix Composite Applications

As engineering design begins to push the physical limits of available traditional materials, especially in the aerospace industry, lightweight, high strength structural components capable of operating in aggressive, high temperature environments are increasingly in demand. Decreasing a component's weight without degrading its operating envelope allows cheaper aircraft with potentially greater range to be manufactured [54:87]. Currently, the U.S. Air Force's F-22 is made from ~25% composites; Boeing's 787 Dreamliner will be close to 50% composite by weight, largely in its fuselage and wings [2; 35:48].

As seen in Figure 8, ceramic matrix composites are less dense than high temperature superalloys yet still have comparable strength to weight ratios and much greater temperature operating ranges [57:410].

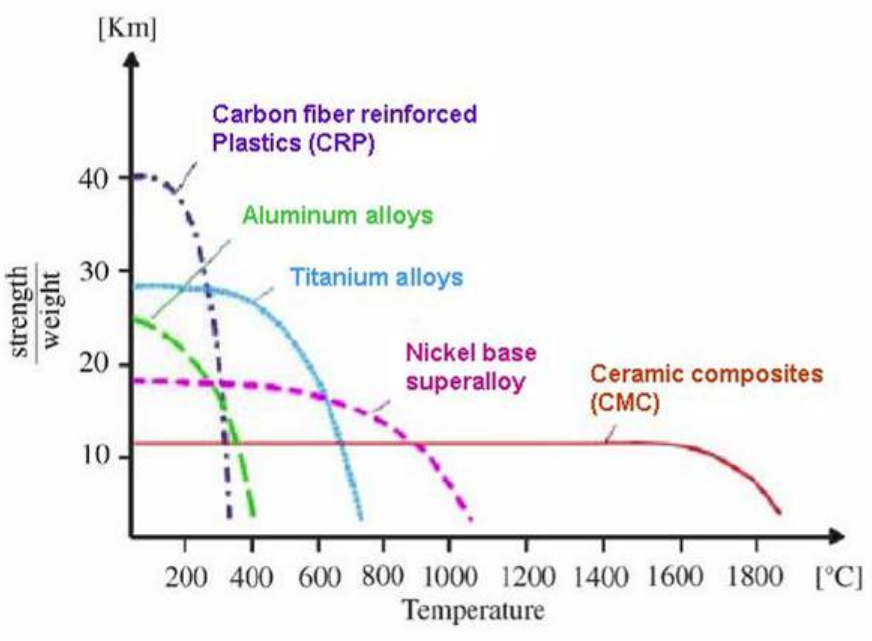

Figure 8. Strength to weight ratio versus operating temperature range [57:410].

As stated by General Electric (GE) Engines, "After waiting three decades for enabling technology to catch up with its design ideas, GE-Aviation is deeply embedding itself in composite materials as a next-generation answer to making engines quieter and cheaper to own and operate" [35:48]. General Electric's GEnx high bypass ratio turbofan engine, developed for the Boeing 787, has composites in its fan blades and housing. This contributes to its 15.4% specific fuel consumption reduction compared to GE's previous generation GECF6 engines on the Boeing 767-300ER jetliner [35].

Engine design is partially limited by the maximum operating temperatures of component materials [54:383]. If the ratio of turbine inlet temperature to freestream temperature can be increased, thrust and efficiency will increase (increased specific thrust) [46:143]. This leads to the design philosophy of high turbine inlet temperatures. Ceramic matrix composites can operate at these temperatures while lowering component

weight because they do not require active cooling to remain below their maximum operating temperatures.

Figure 9 highlights several other areas of air-breathing engines that could benefit from using CMCs. Combustor wall liners, exhaust nozzle flaps and other exhaust-washed structures, and blade outer air seals all stand to benefit [6:617; 50:211].

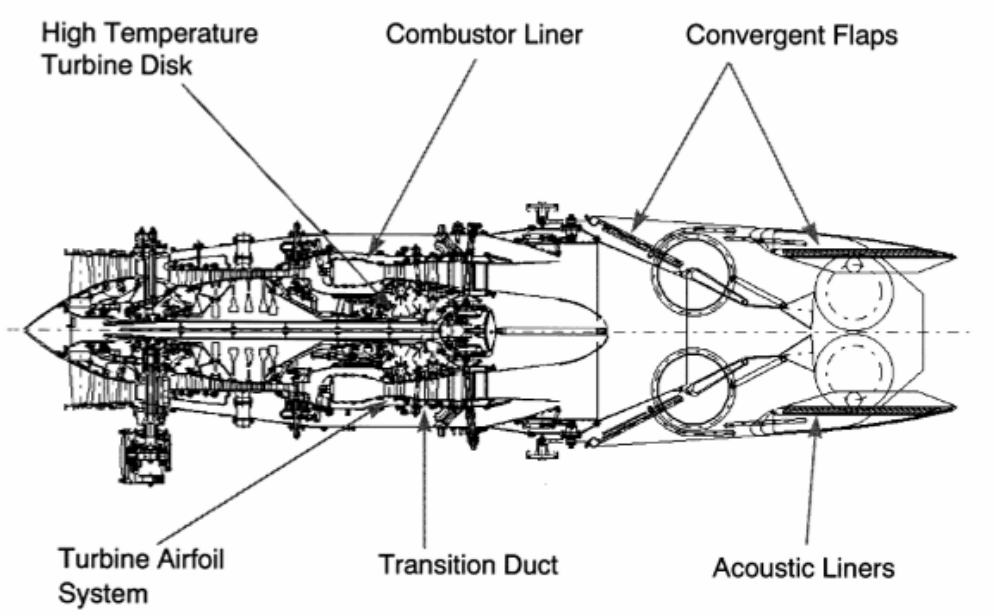

Figure 9. Potential engine CMC applications [47:492].

In addition to offering enhanced performance, CMCs also creep and oxidize less than superalloys at comparable conditions [49:122]. Using CMCs at higher operating temperatures also reduces noxious carbon monoxide and hydro-carbon emissions that are by-products of less-complete combustion at lower temperatures [57:410].

Rocket propulsion is also considering the use of CMC structural components: the European Aeronautic Defence and Space (EADS) Company is using CMCs in combustion chambers and rocket nozzle extensions [57].

2.6 Creep

Creep is deformation of a material over time, caused by a constant or very slightly varying applied load. In the case of ceramics, grain size, porosity, and impurities from processing also contribute to creep [50]. Creep strain is of particular import in crystalline ceramics at operating conditions above thirty to sixty percent of their melting temperature. Oxidation and environmental cracking will also promote creep as they can accelerate the chemical effects [16:706-707]. Steady-state creep strain rate, $\dot{\varepsilon}$, may be calculated using the general power law relationship:

$$\dot{\varepsilon} = \frac{ADGB}{kT}\left(\frac{B}{d_g}\right)\left(\frac{\sigma}{G}\right)^n \tag{1}$$

where A is a dimensionless constant, D is diffusivity, G is shear modulus, B is Burgers vector, k is Boltzmann's constant, T is temperature in degrees kelvin, d_g is grain size, σ is applied stress, and m and n are exponents [12:41].

Figure 10 shows the three stages of creep in a typical creep strain vs. time curve: primary (stage 1), secondary (stage 2), and tertiary (stage 3). Stage 2 creep is also called steady-state, since strain rate is nearly constant in this regime [12:42].

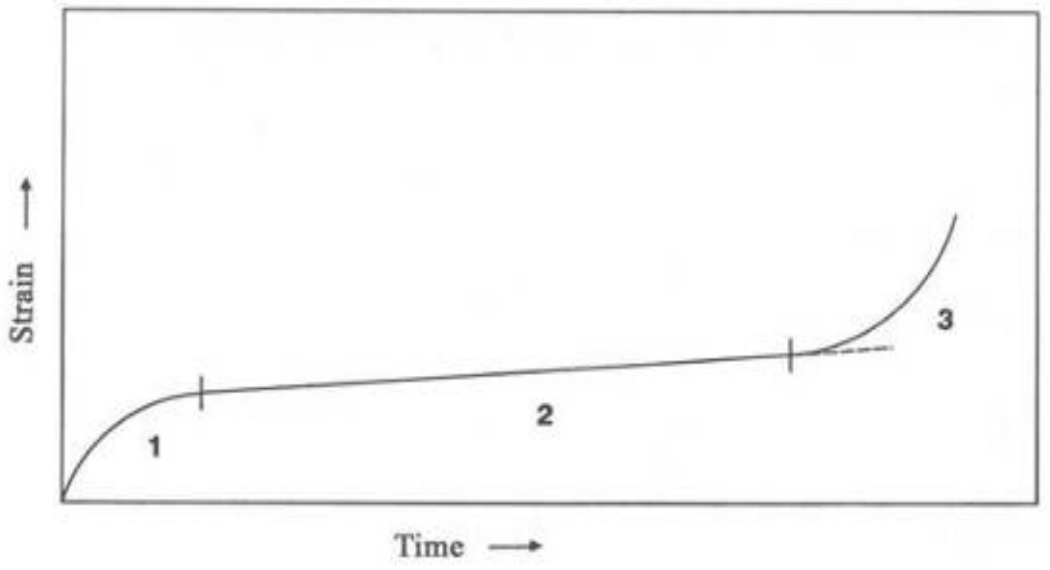

Figure 10. Typical creep curve [12:42].

2.7 Previous Research

While little research has been done of N720/A composites with 0°/90° fiber orientation at elevated temperature and in oxidizing environment, what has been done is worthy of mention. Harlan [20] examined creep performance in air at 1200 °C and found it acceptable. Harlan [20] also found diminished creep lifetimes and increased creep rate in air at a higher 1330 °C temperature. The presence of steam significantly lowered creep resistance at both temperatures. The primary damage mechanism was fiber fracture [20:69-71]. Ruggles-Wrenn [55] extended Harlan's findings by identifying that the primary creep regime was very short and that linear secondary creep persisted to failure. Creep strains also exceeded failure strains obtained in tensile tests [55].

Mehrman [36] investigated the effect of prior fatigue of N720/A on creep performance at 1200 °C. Creep performance in air improved with prior fatigue. The amount of damage and time to failure was proportional to time at maximum stress. The

presence of steam degraded creep performance. Additionally, a qualitative Energy Dispersive X-ray Spectroscopy (EDS) analysis of fracture surfaces indicated that the silicon species from the N720 fibers migrated into the matrix. This depleted the mullite phase in the N720 fibers, reducing their creep resistance [36:83-84].

Siegert [58] examined creep performance of N720/A with ±45° fiber orientation at 1200 °C and confirmed the silicon species migration from fiber to matrix in steam. Siegert also found a qualitatively larger migration took place in argon environment than in steam [58:79-91]. Creep life also diminished when creep stress was larger.

2.8 Thesis Objective

Before advanced materials like N720/A can be used in practical applications their mechanical and chemical behavior under representative operating conditions must be thoroughly characterized. Only then can a safe operating regime and realistic life expectancy be determined. The focus of this effort is to characterize the creep behavior of N720/A ceramic matrix composite over the 1000-1100 °C temperature range in laboratory air and in steam. Oxide-oxide ceramic matrix composites exhibit excellent fatigue and durability, but relatively poor creep resistance. Since knowing creep rates is necessary to determine the limits of applicability of this CMC in real-life applications, this research is of particular importance.

III. Material and Specimens

3.1 Nextel™ 720/Alumina Ceramic Matrix Composite

The ceramic matrix composite studied in this research was Nextel 720/Alumina (N720/A), manufactured by Composite Optics, Inc. (COI) Ceramics, a division of ATK Space Systems. This oxide-oxide CMC consists of Nextel 720 fibers in a porous alumina matrix. The composite was supplied in the form of 12" x 12" panels. Each panel consisted of 12 0°/90° woven layers. The fibers were woven in an 8 harness satin weave.

The Nextel™ 720 fibers are manufactured by the Minnesota Mining and Manufacturing Company (3M™). The fiber is composed of 85% Al_2O_3 and 15% SiO_2 in the form of α-alumina and mullite [28]. The fabric was infiltrated with an alumina matrix (α-Al_2O_3) for a final fiber volume close to forty-five percent [67]. The representative properties of the N720/A composite used in this thesis are shown in Table 2.

Table 2. N720/A panel properties.

Panel	COI Serial #	Thickness (mm)	Fabric Volume (%)	Matrix Volume (%)	Porosity (%)	Density (g/cc)
1	6656-2	2.69	46.8	29.9	23.3	2.79
2	6656-1	2.54	49.2	28.3	22.5	2.80
3	4569	2.70	46.4	29.9	23.7	2.77

3.2 Composite Processing

Processing of the CMC using woven fiber plies involves several steps. Figure 11 schematically depicts steps of the CMC manufacturing process. First the fibers are woven into fabric. The fabric is first dipped in a slurry containing the powdered alumina matrix and an organic binder in a carrier liquid [27:204]. Dilute particles of alumina are precipitated out of the organic solution, forming a gel and infiltrating the fabric under low

temperature, low pressure conditions [12:23,125]. The gel dries forming the ceramic matrix. Finally, the composite is sintered [36:15].

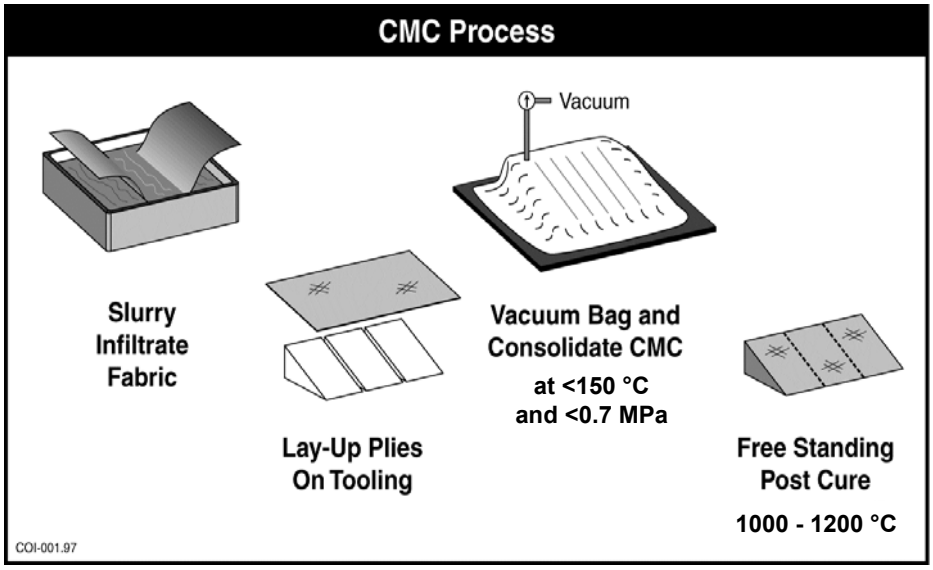

Figure 11. Representative steps of fabric-based CMC manufacturing process [27].

3.3 Test Specimen Geometry and Fabrication

The 12” x 12” panels were cut using water jet machining at the AFIT fabrication shop to the specifications in Figure 12. Plexiglas sheets sandwiched the panels while cutting to reduce fraying at the edges of the specimens. After machining, the specimens were cleaned to remove any residual debris from the water jet machining. The cut specimens were placed into an ultrasonic bath of deionized water for 20 min., then soaked in 200-proof ethyl alcohol for 20 min., and finally, dried in an Omegalux LMF-3550 Benchtop Muffler Furnace at 250 °C for 2 h.

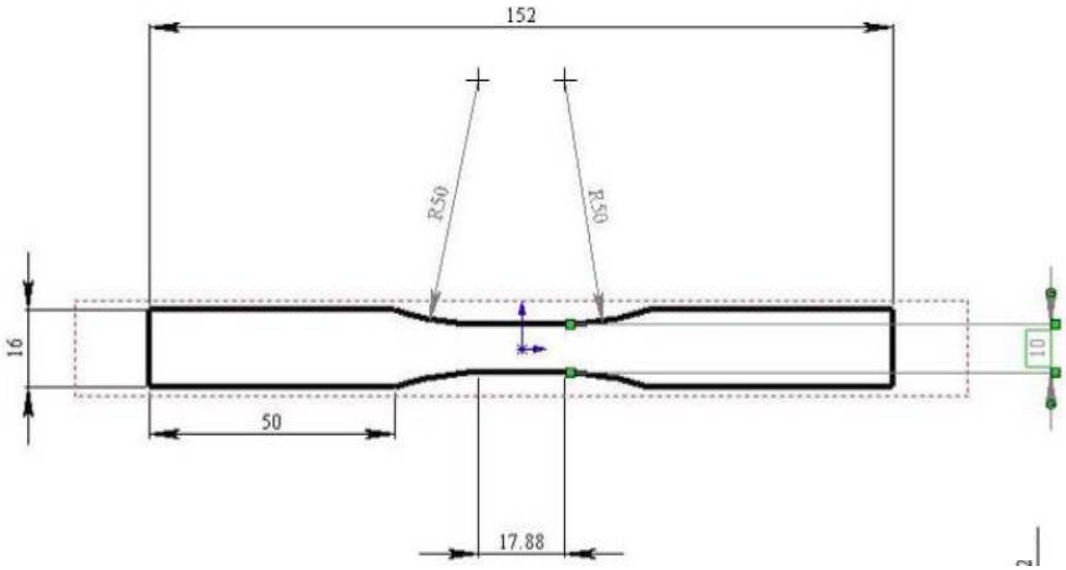

Figure 12. Uniaxial test specimen (dimensions in mm) [23].

IV. Experimental Arrangements and Test Procedures

4.1 Testing Equipment

4.1.1 Mechanical Testing Equipment

A vertically actuated, servo-hydraulic Material Test Systems (MTS) 810 Material Test System was used for all tests (see Figure 13), and an MTS Test Star IIs digital controller used for input signal generation and data acquisition. MTS System Software and Multi-Purpose Testware (MPT) were used to program and execute tests. MTS series 647 hydraulic wedge grips with a Surfalloy surface were used to grip specimens for testing. Grip pressure of 8 MPa was used in all tests. The grips were water cooled with a Neslab model HX-75 chiller. The Neslab HX-75 chiller continuously circulated 14 °C deionized water through the wedge grips to keep the wedges at temperatures under 177 °C.

Figure 13. MTS 810 Test Station.

The capacity of the test systems was 25 kN (5.5 kip). An MTS Force Transducer (Model 661.19E-04) was employed for force measurement. An LVDT internal to the test station was used to measure displacement. A low contact force, uniaxial, air-cooled, high temperature MTS Extensometer (Model 632.53E-14) was employed for strain measurement. Figure 14 shows a close-up of the transducer, top wedge grips, and extensometer.

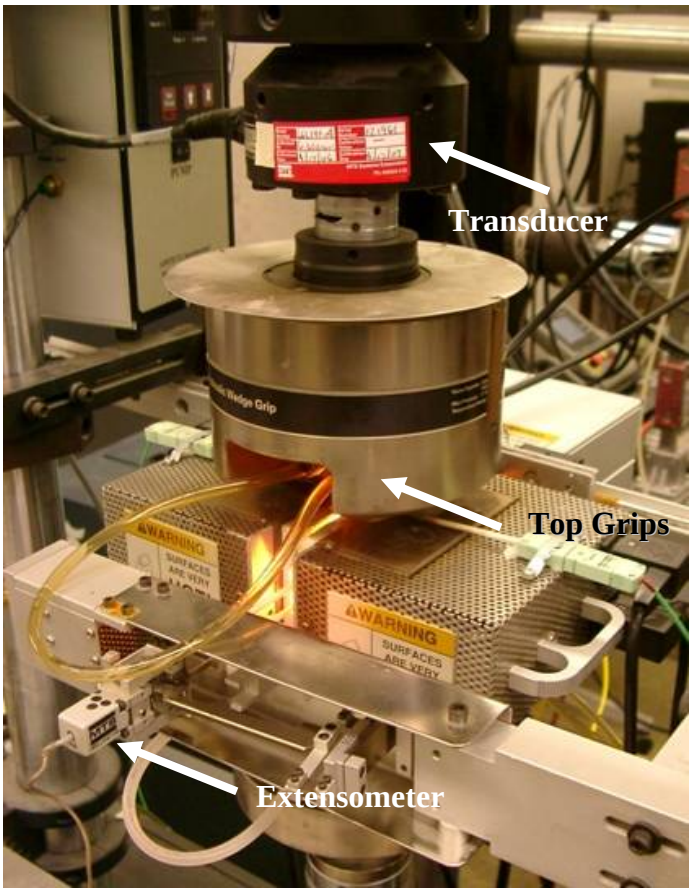

Figure 14. Test system close-up.

4.1.2 Environmental Testing Equipment

Several pieces of additional equipment were necessary to conduct tests at temperatures in the 800-1100 °C range, in laboratory air or in steam environment. The mechanical testing station was equipped with a compact, dual zone AMTECO Hot-Rail Furnace controlled by an MTS Model 409.83B Temperature Controller (see Figure 15).

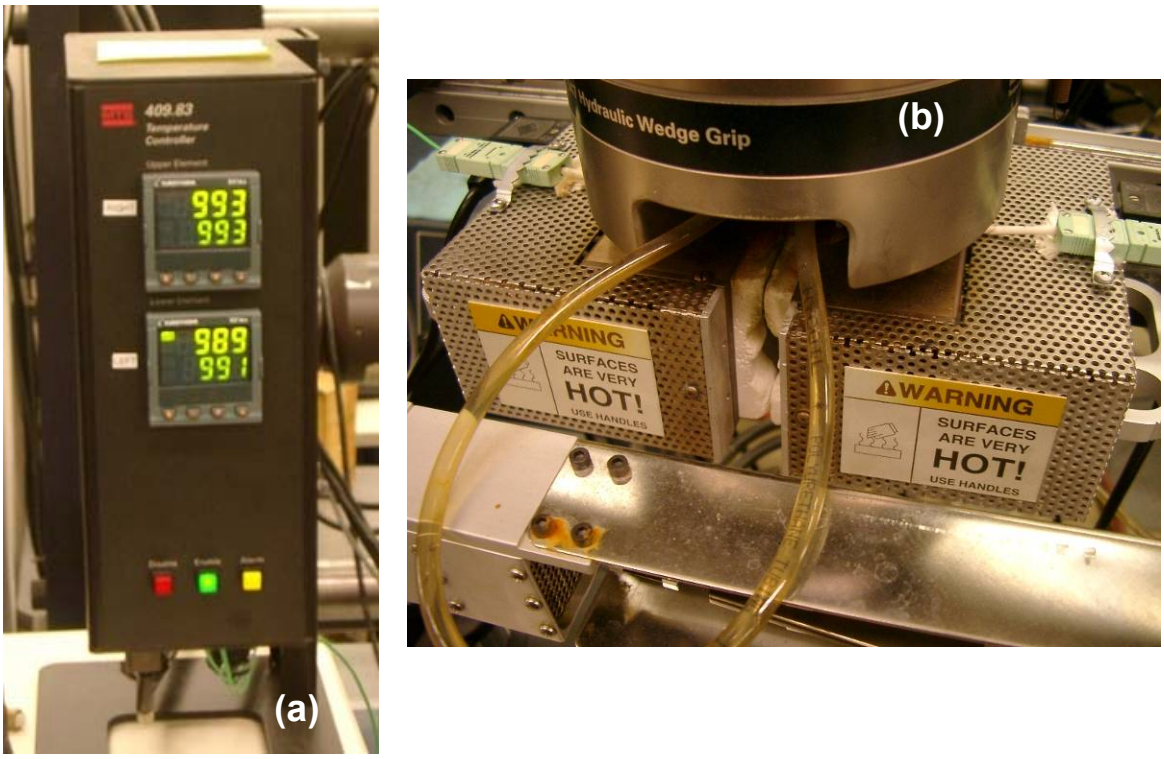

Figure 15. Heating equipment: (a) MTS temperature controller and (b) AMTECO Hot-Rail Furnace.

Each side of the furnace was fitted with an S-type thermocouple, which provided chamber temperature to the controller. Temperature set-point was provided via the Test Star II to the temperature controller, which applied a PID control algorithm to the furnace elements with a feedback loop from the control thermocouples. Note that the temperature measured by the control thermocouples was not the temperature of the specimen.

For testing in steam, continuous steam environment was provided by an AMTECO HRFS-STMGEN Steam Generation System, shown in Figure 16. Tests in steam employed an alumina susceptor, a cylinder with end caps, which fits inside the furnace. The specimen gauge section is located inside the susceptor, with the ends of the specimen passing through slots in the susceptor. Steam is introduced through a feeding tube in a continuous stream with a slight positive pressure, expelling the dry air and creating 100% steam environment inside the susceptor. The susceptor is shown in Figure 17.

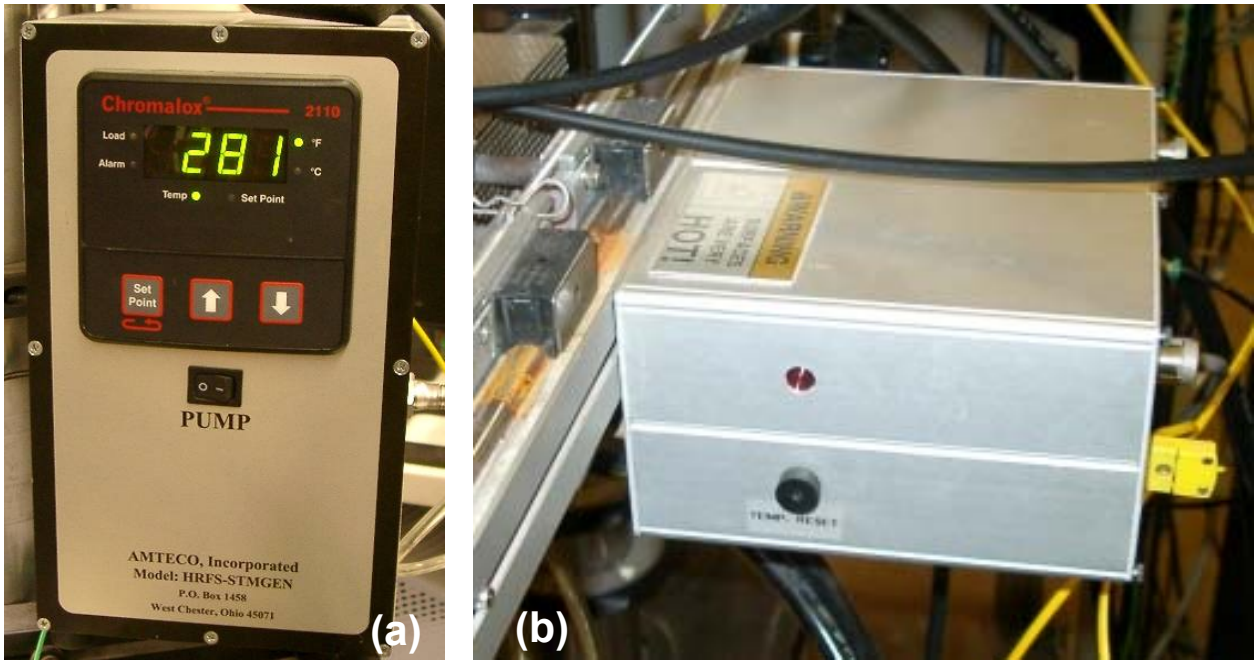

Figure 16. AMTECO Steam System: (a) pump and temperature controller and (b) heating unit.

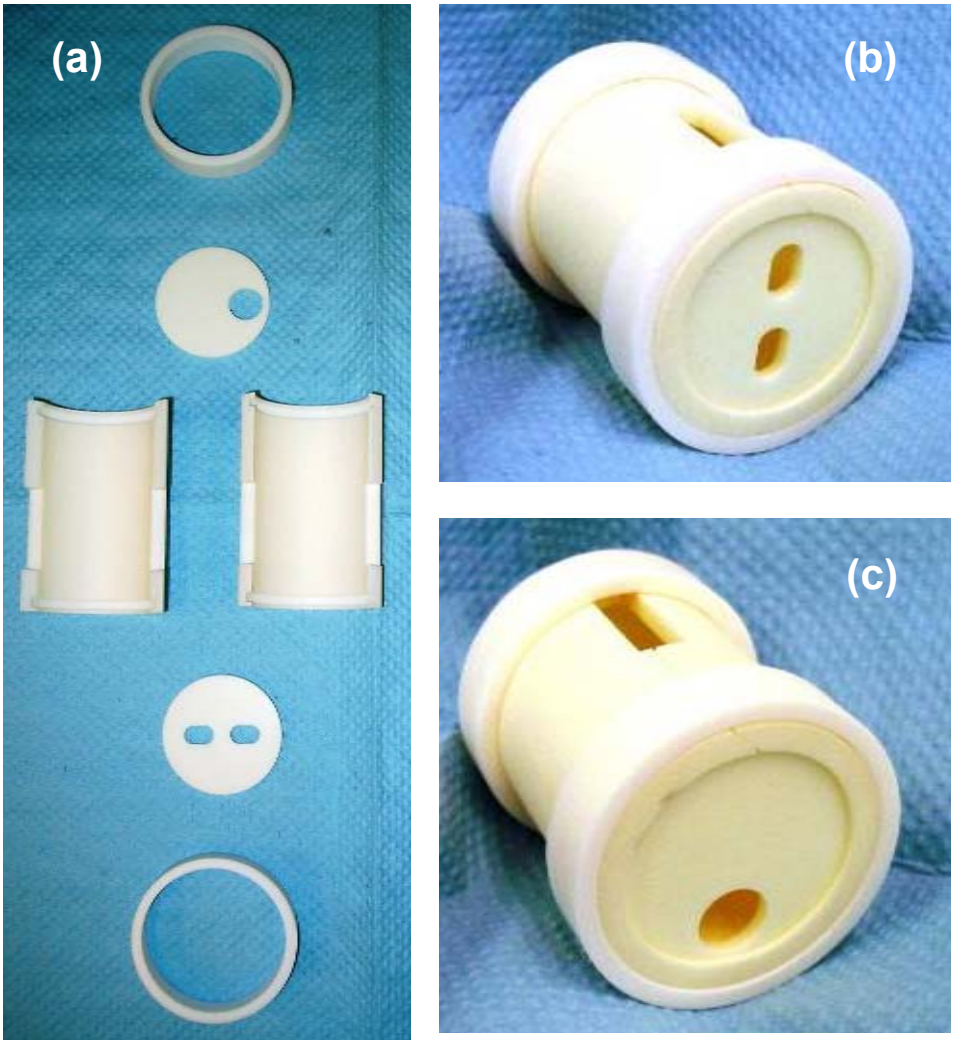

Figure 17. Susceptor views: (a) disassembled, (b) front view and (c) rear view.

4.1.3 Microstructural Characterization

Fracture surfaces of the failed specimens were examined at magnifications of up to 100X using a Zeiss Discovery V.12 optical microscope shown in Figure 18. Micrographs were taken with a Zeiss AxioCam HRc digital camera built into the microscope. Microstructural characterization at magnifications of up to 20,000X was

performed using an FEI FP 2011/11 Quanta 200 HV Scanning Electron Microscope (SEM), shown in Figure 19.

Figure 18. Zeiss optical microscope.

To create an image, SEMs use electron beams instead of light and magnetic fields to focus the beams instead of lenses. When the beam bombards the specimen, some electrons are reflected and some are absorbed. Furthermore, the beam causes the specimen to emit secondary electrons, photons, and even X-rays. The backscattered and emitted electrons are detected by a scintillation detector in the SEM and converted into a digital image signal for display on a computer screen [1].

The high vacuum mode of the SEM, which utilizes the process described above, requires conductive specimens. Non-conductive specimens build up a charge which

obscures resolution capability and can be damaging to equipment. The non-conductive specimens must be specially coated before use with the high vacuum mode.

Figure 19. FEI Quanta Scanning Electron Microscope (SEM) and EDAX X-Ray Analysis System.

The Environmental Scanning Electron Microscope (ESEM) mode allows non-conductive specimens to be imaged without special coating, which permits faster specimen preparation but incurs a resolution penalty. In ESEM, de-ionized water is used to create a gaseous environment in low vacuum inside the Quanta 200's specimen chamber. A Gaseous Secondary Electron Detector then detects cascade amplification, created when water vapor ionizes as the electron beam passes through it, to enhance the secondary electron signal. Water molecules become positive ions from secondary

electron emission and are attracted to the negatively charged surface of any non-conductive specimen. This minimizes resolution reduction effectively, but not entirely [1]. Magnification of 3000X was found to be the limiting condition for ESEM use.

4.2 Test Procedures

4.2.1 Mechanical Testing Equipment – Calibration

The MTS testing machine was aligned prior to all testing efforts using an MTS 609 Alignment Fixture with 12 strain gauges and MTS 709 Alignment Software. The machine was tuned for displacement control with no specimen and for force control using an actual test specimen. The extensometer was calibrated using standard procedures.

The furnace temperature controller was calibrated to maintain the desired test temperature of the specimen. A test specimen fitted with 2 R-type thermocouples was employed for calibration. It is shown in Figure 20.

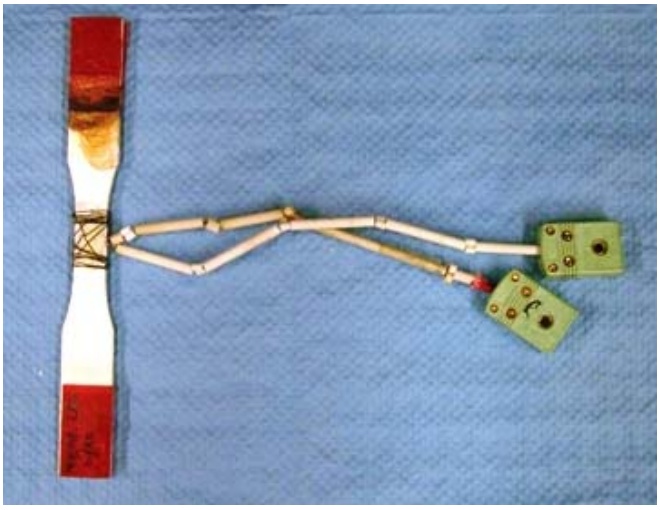

Figure 20. Temperature calibration specimen.

The thermocouples were mounted using two part Omega CC high temperature cement. After curing for 24 h, high temperature wire was wound around the cement for added assurance. The temperature calibration specimen was placed into the MTS machine and heated under zero load with the thermocouples connected to an Omega Engineering, Inc. OMNI-CAL-8A-110 portable temperature reader.

Oven temperature was slowly raised until the specimen temperature reached the desired level. The determined set-point was then used in actual tests. The temperature controller setting for testing in steam was determined by placing the specimen instrumented with thermocouples in steam environment and repeating the furnace calibration procedure.

To confirm the temperature controller settings, a portable multi-meter with a high temperature measuring wand was used to verify the specimen temperature. The set points determined in this effort are in agreement with those established by Siegert [58] but slightly lower than could be expected from those established by Harlan [20]. The oven temperature settings required to achieve test temperatures of 800, 900, 1000, and 1100 °C are shown in Table 3.

Table 3. Temperature Set-Points (°C).

Specimen Temperature	800	900	1000	1100
Oven Temperature (Air)	610 (Right) 622 (Left)	702 (R) 713 (L)	777 (R) 787 (L)	870 (R) 877 (L)
Oven Temperature (Steam)	707 (Right) 705 (Left)	802 (R) 800 (L)	894 (R) 892 (L)	993 (R) 991 (L)

4.2.2 Mechanical Testing – Preparation

In preparation for testing, fiberglass tabs were bonded to the grip section of the specimens with M-Bond 200 adhesive. The tabs were used to protect the specimen surface from crushing by the grips. A tabbed test specimen is shown in Figure 21.

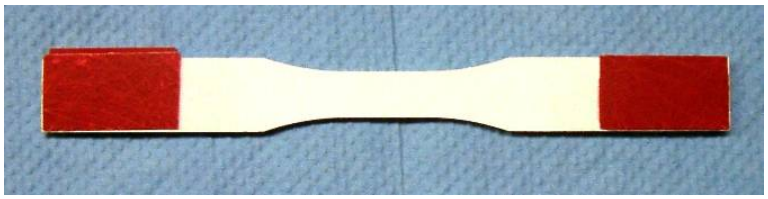

Figure 21. Tabbed Dogbone Test Specimen.

The specimen gauge section (i.e., width and thickness) was measured with Mitutoyo Corporation Digital Micrometers (Model NTD12-6"C) three to five times and an average taken. Based on these measurements, the cross-sectional area of the specimen was calculated. The cross-sectional area was used to calculate the load needed to attain the desired test stress level, using:

$$\sigma = \frac{P}{A} \tag{2}$$

where σ is stress in Pascals (Pa), P is load in Newtons (N), and A is cross-sectional area in meters squared (m^2).

While cross-sectional measurements were being taken the MTS machine was warmed up. The MTS function generator was used to cycle the actuator in displacement control mode at 0.1 Hz for 15 minutes.

A separate procedure was written for each test using an MPT Procedure Editor module. It allowed multiple channel data acquisition, sampling rate, and file saving formats. An example of a creep test procedure is shown in Figure 22.

The Neslab cooler was turned on and sufficient time was allowed to bring the cooling water down to the set temperature before testing. The temperature controller was verified to be in "enabled" mode with no error codes on its readouts. If the test required steam, the steam controller was turned on and allowed sufficient time to stabilize. The ceramic steam tube was inserted into the front of the steam pump. The pump itself was not turned on until just before test initiation.

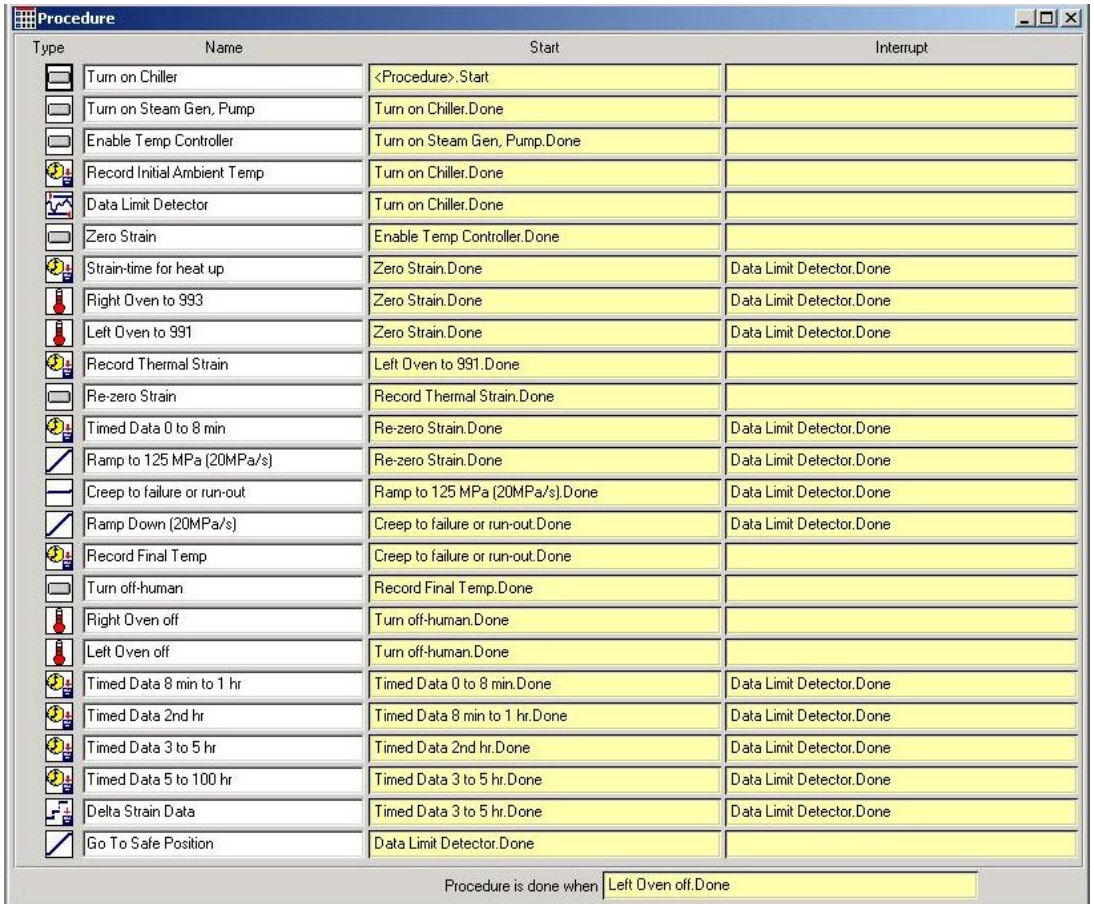

Figure 22. Sample MPT procedure.

Specimens were always secured into the top grips first while in displacement control mode. If the susceptor was needed it was assembled around the specimen prior to placing it in the grips. The bottom grips were closed only after switching into force control mode and setting force to 0 N. Next the ovens were slowly swung into place and the steam tube carefully fed into the back of the susceptor. Care had to be taken not to impact the edges of the susceptor hole because the material was very thin and brittle. The extensometer was placed through the susceptor slots or directly onto the specimen prior to closing the oven halves. Once this was accomplished the strain and displacement were both digitally zeroed with the MTS control software. The final step before starting a test was to set safety interlocks for displacement, force, and temperature to guard against equipment damage from an unexpected hydraulic power spike or power outage. In all tests the specimen was heated to test temperature in 30 min. and held at test temperature for an additional 15 min. prior to testing.

4.2.3 Monotonic Tensile Tests

All tensile tests were performed in laboratory air environment in displacement control with a constant displacement rate of 0.05 mm/s. Load, displacement, strain, time and temperature settings for both oven sides were collected at 20 Hz and recorded. Duration of all tensile tests to failure was approximately 10 seconds (s).

4.2.4 Creep-Rupture Tests

Creep rupture tests were conducted in load control in accordance with the procedure in ASTM Standard C 1337. The loading to creep stress level was accomplished at 20 MPa/s. Data was sampled at varying rates: at 20 Hz during the first 8 minutes of the test, at 6.67 Hz during the remainder of the first hour, once every 2 seconds during the second hour, every 10 seconds during hours 3-5, and every 3 minutes during the remaining 95 hours. Creep run-out was defined as 100 hours (h) at creep stress. Such run-out condition is commensurate with the material's expected service life in applications mentioned in Chapter II. Specimens that achieved run-out were unloaded to zero load at 20 MPa/s and subjected to tensile testing to failure to measure retained properties. It is noteworthy that in all tests reported herein, the failure occurred within the gauge section of the specimen.

4.2.5 Microstructural Characterization – Specimen Preparation

Since N720/A is non-conductive, failed specimens were prepared for viewing in the SEM using (1) carbon paint to ground it to aluminum mounting platforms for use in ESEM mode, and (2) coating them with carbon to provide a conductive surface compatible with high vacuum mode. An SPI-MODULE Control and Carbon Coater, shown in Figure 23, was used to coat specimens. The coater sent a charge through braided carbon rope that emitted carbon atoms in a controlled-vacuum chamber. Prior to coating or painting specimens were cut just below the damage zone with an MTI Corporation EC400 CNC Dicing/Cutting and 3.5-inch impregnated diamond blade, shown in Figure 24.

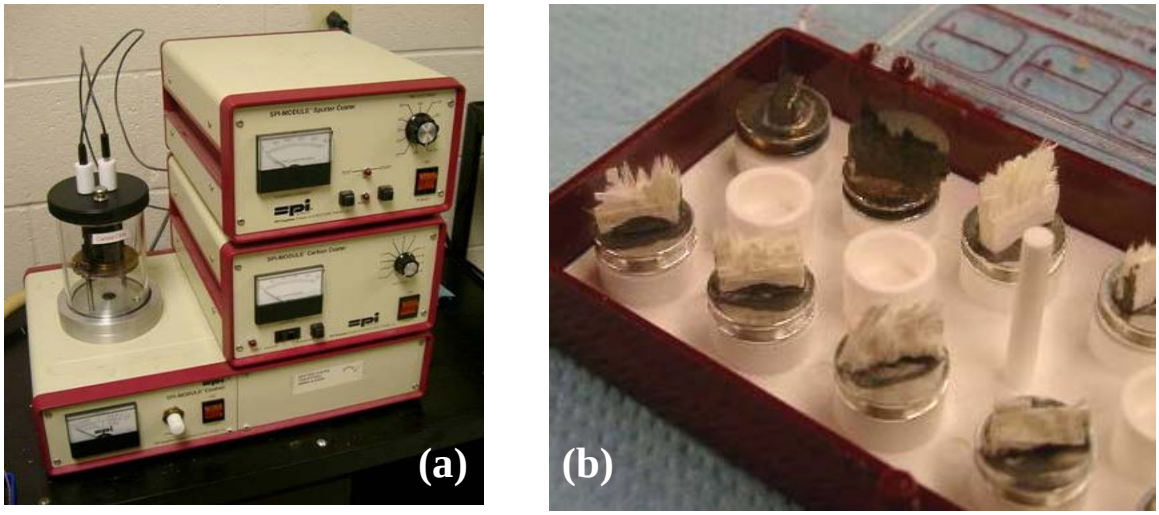

Figure 23. (a) SPI Carbon Coating System and (b) carbon-painted and carbon-coated fracture surface specimens.

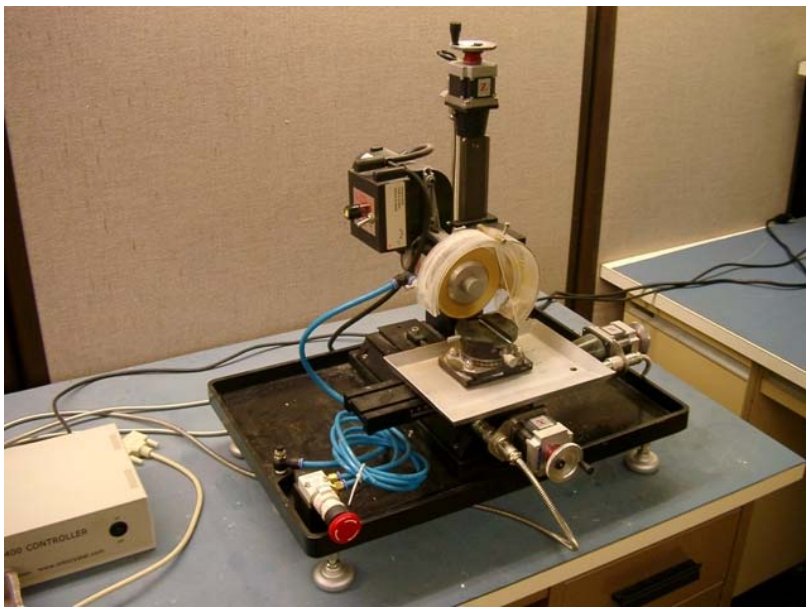

Figure 24. CNC saw.

V. Results and Discussion

The tests performed during the course of this research are summarized in Table 4, where specimen number, panel number, loading type and test environment are given together with the maximum stress level for each test. Specimen numbers contain reference to the panel number. For example, number P3-1 refers to specimen 1 from panel 3.

Table 4. Test Matrix

Specimen	Panel	Loading Type	Environment	Temperature (°C)	Maximum Stress (MPa)
P3-1	4569	Tensile	Air	800	197
P3-2	4569	Tensile	Air	900	189
P3-3	4569	Tensile	Air	1000	192
P3-4	4569	Tensile	Air	1100	191
P1-1	6656-2	Tensile	Air	900	164
P1-2	6656-2	Tensile	Air	900	159
P1-3	6656-2	Tensile	Air	1000	173
P1-4	6656-2	Tensile	Air	1100	167
P1-5	6656-2	Creep	Steam	1000	135
P1-6	6656-2	Creep	Steam	1000	150
P1-7	6656-2	Creep	Air	1000	150
P3-5	6656-2	Creep	Steam	1000	160
P2-1	6656-1	Creep	Steam	1100	100
P2-2	6656-1	Creep	Steam	1100	125
P2-3	6656-1	Creep	Steam	1100	150
P1-8	6656-2	Creep	Air	1100	150

5.1 Thermal Expansion

The coefficient of linear thermal expansion was calculated with a curve fit to the linear portion of the strain-temperature curve, for temperatures ≥ 400 °C, as shown in Harlan [20:44]. The linear portion of the ε - T curve was assumed to behave according to the linear relationship

$$\varepsilon_{th} = \alpha \cdot \Delta T \tag{3}$$

where ε_{th} is the thermal strain, α the coefficient of linear thermal expansion, and ΔT is the temperature change from room temperature, taken to be 23 °C. Expansion coefficients were similar for air or steam heat-up and for different end temperatures. Table 5 compares thermal strains and coefficients of linear thermal expansion for several efforts.

Table 5. Thermal strain and coefficients of linear thermal expansion for the N720/A composite.

Specimen	Temperature (°C)	Thermal Strain (%)	Coefficient of Linear Thermal Expansion (10^{-6} K^{-1})
P3-1	800	0.440	[a]
P1-1	900	0.466	[a]
P3-2	900	0.476	[a]
P1-2	900	0.495	[a]
P1-3	1000	0.529	[a]
P1-7	1000	0.533	7.38
P3-3	1000	0.548	[a]
P1-5	1000	0.625	[a]
P3-5	1000	0.634	7.75
P1-6	1000	0.670	[a]
P1-4	1100	0.573	[a]
P3-4	1100	0.597	[a]
P1-8	1100	0.612	7.30
P2-2	1100	0.702	8.51
P2-3	1100	0.716	8.80
P2-1	1100	0.721	[a]

[a] Data not collected

Strain-temperature data was collected for select specimens to confirm that thermal measurements were consistent with those reported by Harlan [20], Mehrman [36], and Hetrick [23], whose average α 's were 7.20, 7.66, and 7.57 10^{-6} K^{-1}, respectively. For specimens where data was not collected, overall thermal strain values are consistent with those where detailed thermal strain- temperature data was collected.

5.2 Monotonic Tensile Tests

All monotonic tensile tests were performed in laboratory air on specimens cut from two panels. Table 6 compares results of monotonic tensile tests obtained in current research and those from prior efforts. The elastic moduli values compare well with those reported earlier (see Figure 25) [8].

Table 6. Ultimate tensile strength, elastic modulus, and failure strain, for N720/A at varying temperatures.

Source	Temperature (°C)	UTS (MPa)	Elastic Modulus (GPa)	Failure Strain (%)
Panel 4569	800	197	64.6	0.33
Panel 4569	900	189	61.4	0.34
Panel 6656-2 (2-panel average)	900	162	61.5	0.31
Panel 4569	1000	192	74.4	0.32
Panel 6656-2	1000	173	54.6	0.31
Panel 4569	1100	191	68.4	0.32
Panel 6656-2	1100	167	43.4	0.34
Harlan [20:45]	1200	192	74.7	0.38
Mehrman [36:33]	1200	186	77.7	0.37
COI [13]	1200	219	76.1	0.43
Harlan [20:46]	1330	120	43	1.68

Tensile stress-strain curves obtained at temperatures in the 800-1100 °C range are shown in Figure 26 together with the stress-strain curves at 1200 and 1330 °C from prior work [55]. The stress-strain curves obtained at 800-1100 °C are consistent with those at 1200 and 1300 °C.

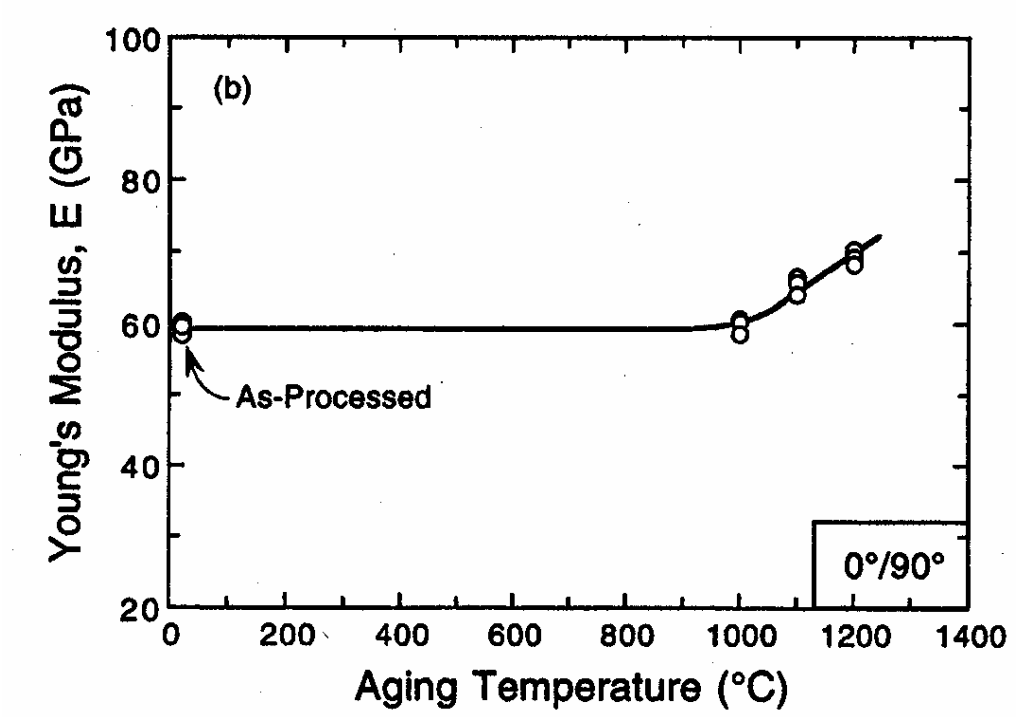

Figure 25. Young's modulus for N720/AS aged 1000 hours [8].

Note that the specimens from panel 6656-2 failed in the "shoulder" region, at relatively low ultimate strengths and with lower elastic moduli than expected from previous work. This may be attributed to a slight curvature noticed in panels 6656-2 and 6656-1. Any warp in a specimen would be translated into bending stress when gripped. Thus instead of uniaxial tension, the specimen would be subject to combined tension and bending. The curvature in the specimen is likely the cause of failure outside the gauge section and at a lower axial load. Note that specimens cut from panel 4569 exhibited higher UTS values and failed in the gauge section.

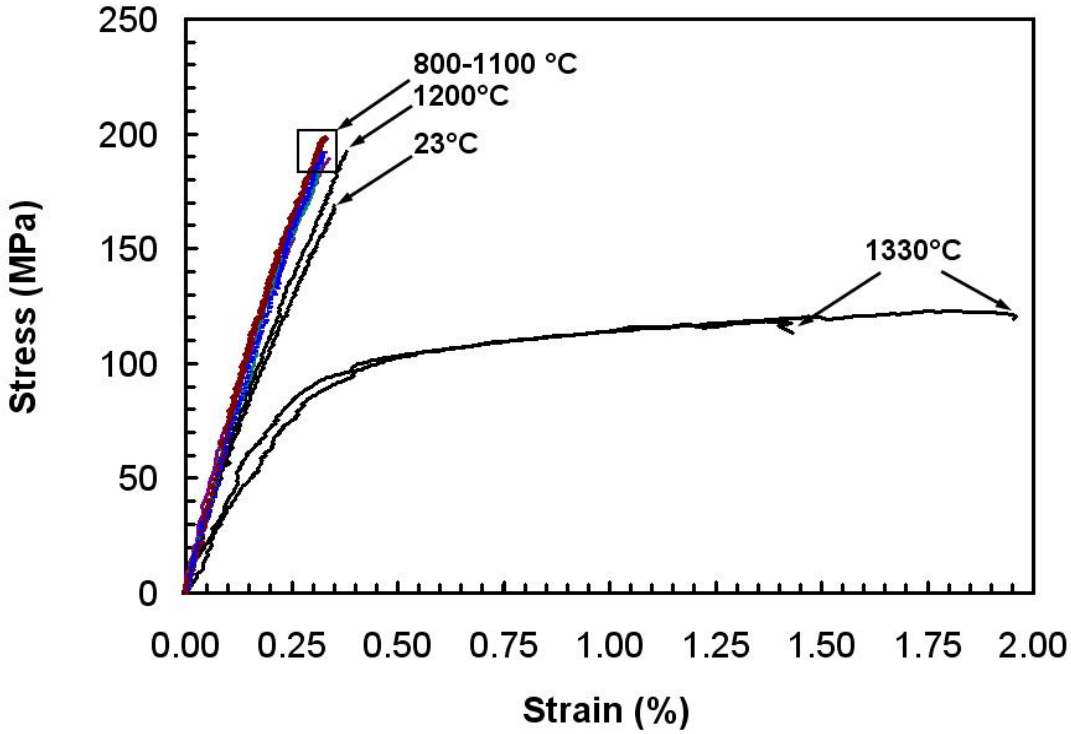

Figure 26. Tensile stress-strain curves for N720/A CMC at temperatures in the 800-1330 °C range. Data at 1200 and 1300 °C from Ref [55].

5.3 Creep Rupture Tests at 1000 °C

The total strain accumulated by each specimen during a test consisted of thermal strain, strain due to load-up to creep stress, and the actual creep strain. Creep run-out was achieved in all tests at 1000 °C with the exception of the 160 MPa test, which failed prematurely due to equipment malfunction, as shown in Table 7. Considering that the steady-state creep strain rate in the 160 MPa test was below 3.4e-8 s^{-1}, it is likely that this would have achieved creep run-out as well.

Creep strain vs. time curves obtained at 1000 °C are shown in Figure 27. Note that all creep strains remain below 0.2%. The presence of steam has some effect on creep strain; larger creep strains are produced at 150 MPa in steam than in air. However, the

creep lifetime does not appear to be significantly affected by the presence of steam and creep strains accumulated in steam still remain fairly low, less than or equal to 0.2%.

Table 7. Summary of creep-rupture results for the N720/A ceramic matrix composite.

Specimen	Temperature (°C)	Creep stress (MPa)	Creep strain (%)	Time to rupture (s)
Tests in laboratory air				
C2-1	1000	150	0.08	360,000[a]
C1-1	1100	150	0.10	360,000[a]
Tests in steam				
C2-2	1000	135	0.09	360,000[a]
C2-3	1000	150	0.17	360,000[a]
C2-4R	1000	160	0.13	144,000[b]
C1-3'	1100	100	0.47	360,000[a]
C1-2'	1100	125	0.50	193,313
C1-1'	1100	150	0.43	43,552

[a] Run-out. [b] Power failure.

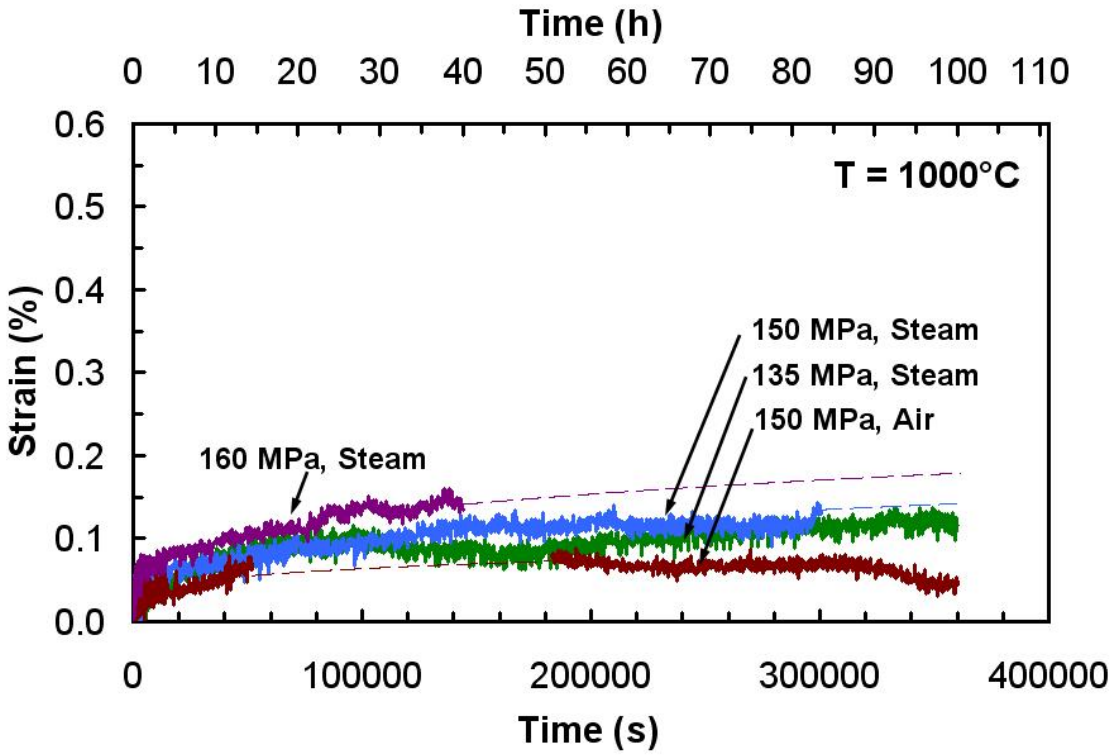

Figure 27. Creep strain vs. time results for Nextel 720/Alumina ceramic matrix composite at 1000 °C, in laboratory air and in steam environment.

5.4 Creep Rupture Tests at 1100 °C

Creep curves obtained at 1100 °C are presented in Figure 28. In air creep run-out stress was 150 MPa. In steam, creep run-out stress was only 100 MPa. Furthermore, the presence of steam significantly accelerated creep rates, which resulted in larger creep strains. Accelerated creep due to the presence of steam was also reported by Mehrman [36:61] and Ruggles-Wrenn et al [55].

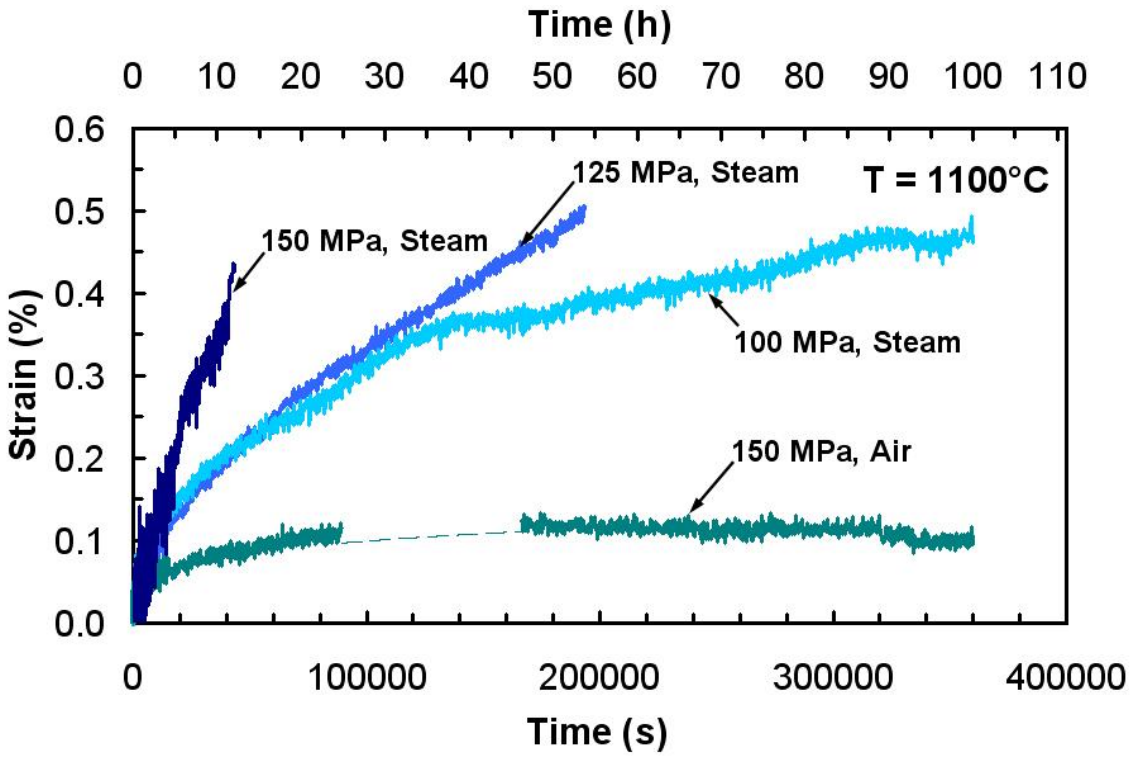

Figure 28. Creep strain vs. time curves for Nextel 720/Alumina ceramic matrix composite at 1100 °C in laboratory air and in steam environment.

5.5 Effect of Temperature on Creep Rupture Behavior

The effect of temperature on creep behavior is illustrated in Figure 29, where creep curves obtained at 1100 °C are shown together with those obtained at 1200 °C [20, 55]. Creep curves obtained at 1200 °C in both air and steam environments exhibit

primary, secondary, and tertiary creep, while only primary and secondary creep are observed in creep curves obtained at 1000 and 1100 °C. Creep strain accumulation at a given creep strain increases significantly with temperature. Creep strain accumulated at 135 MPa at 1000 °C in steam is < 0.2%. Creep strain accumulated at 1100 °C at a lower stress of 100 MPa is nearly 0.5%. Finally, creep strains accumulated at 100 MPa at 1200 °C in either air or steam exceed 1%. Harlan [20] reported creep strain accumulation of nearly 4% at 1330 °C for the creep stress of 100 MPa, in laboratory air.

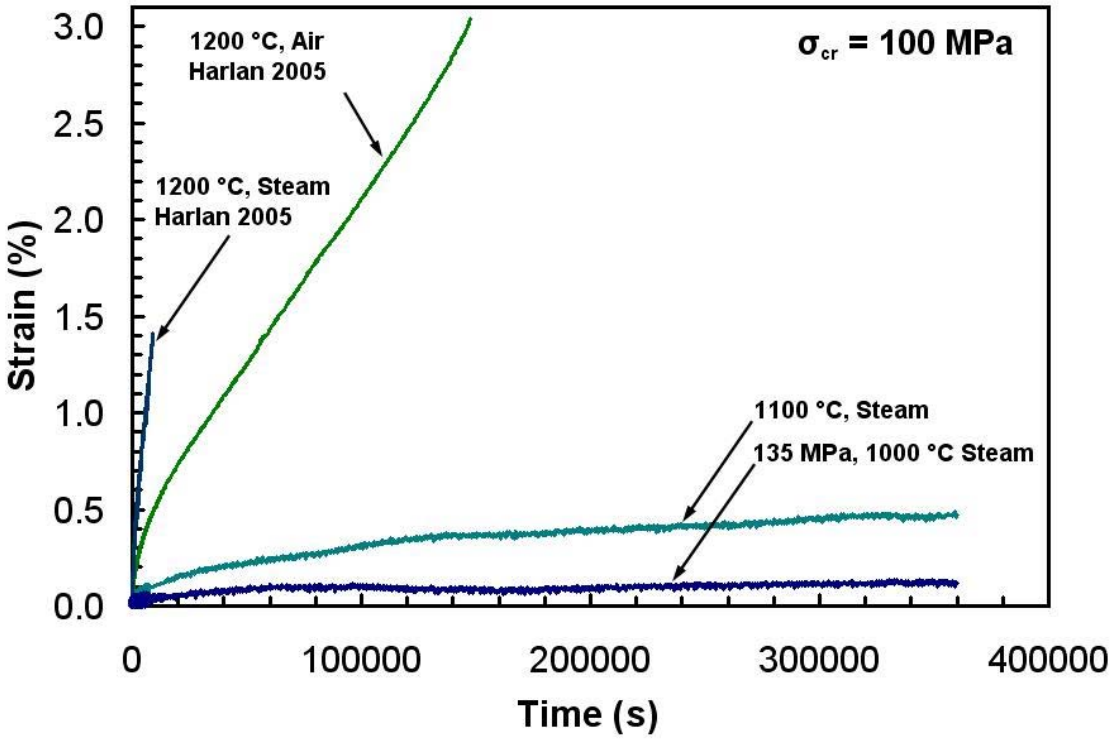

Figure 29. Creep strain vs. time curves at 1000, 1100, and 1200 °C in laboratory air and in steam environment. Data at 1200 °C from Harlan [20:48, 55].

Creep curves in Figure 29 are shown again in Figure 30 together with the creep curves obtained at 1330 °C for creep stress levels of 100 MPa [20]. The time scale in Figure 30 is reduced to clearly show the creep curves at 1330 °C.

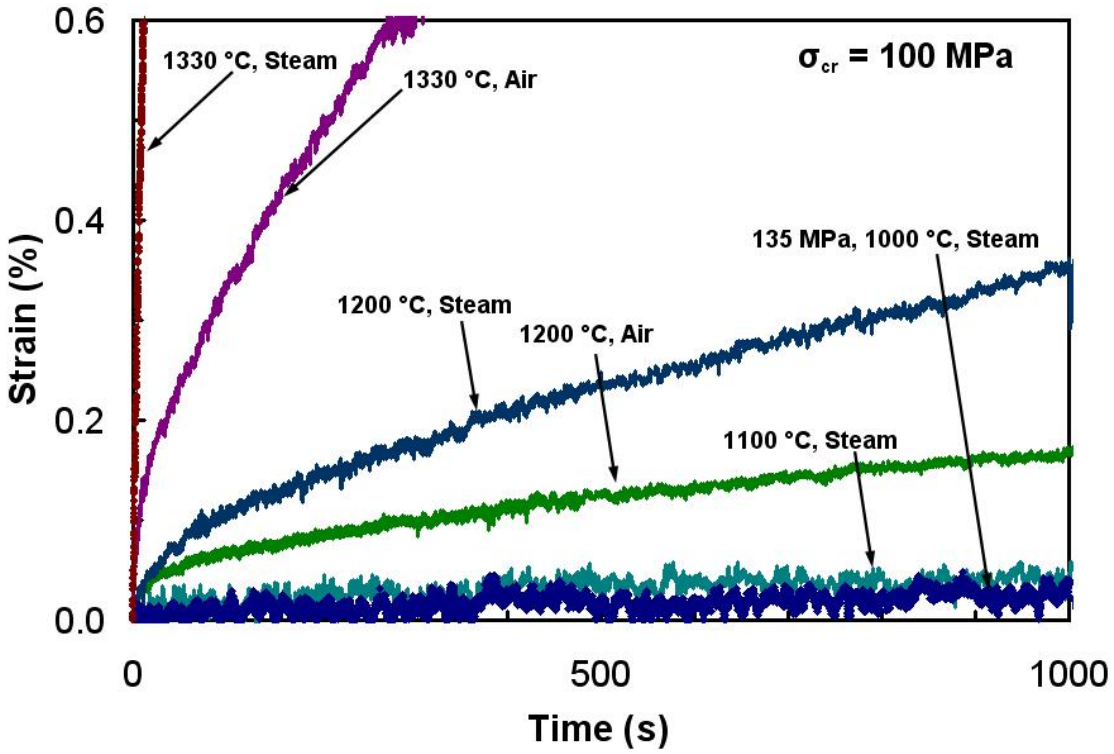

Figure 30. Creep strain vs. time curves for N720/A ceramic matrix composite at 1000, 1100, 1200, and 1330 °C in laboratory air and steam environments. Time scale is reduced to clearly show the creep curves at 1330 °C. Creep data at 1200 and 1330 °C from Harlan [20:48, 55, 57], Ruggles-Wrenn et al. [55].

Presented in Figure 31 is a plot of rupture strain vs. temperature. Results from Ref [20] at 1200 and 1330 °C are included for comparison. All data in Figure 31 are for the creep stress of 100 MPa, except a data point at 1000 °C, which was obtained at 135 MPa. Note that rupture strain increases with increasing temperature. It is also seen that larger strains were accumulated in air than in steam at a given temperature. This is likely due to the slower creep rates and longer creep lifetimes observed in air, which allowed for larger strain accumulation prior to rupture. The rupture time vs. temperature plot in Figure 32 further reveals that at a given temperature longer lifetimes were observed in air than in steam.

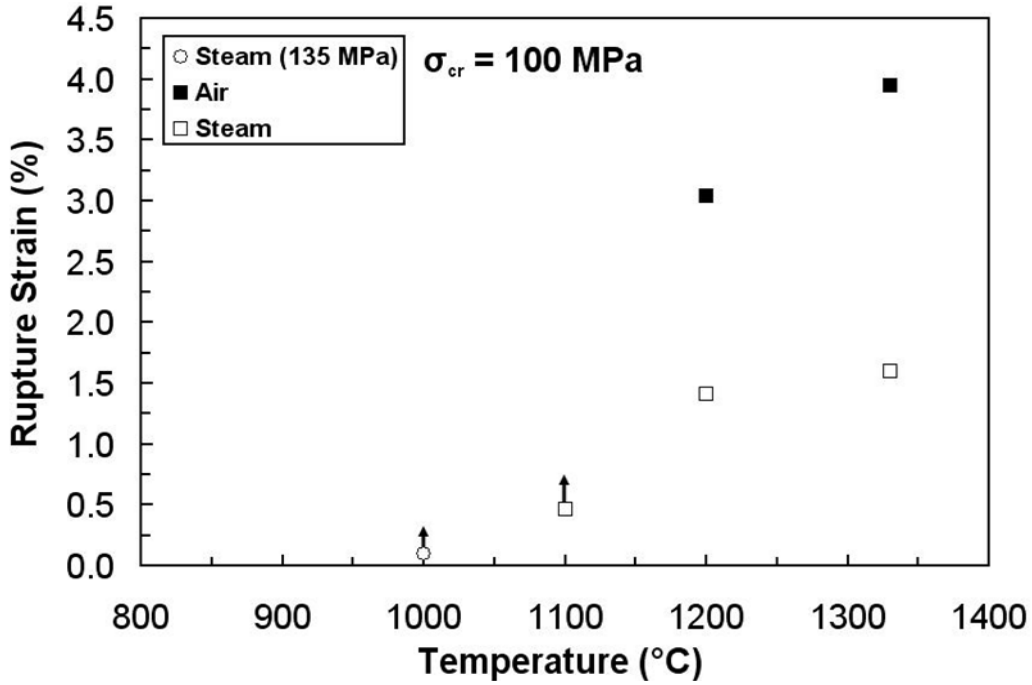

Figure 31. Rupture strain versus temperature for N720/Alumina ceramic matrix composite. Creep stress is 100 MPa. Data at 1200 and 1330 °C are from Harlan [20].

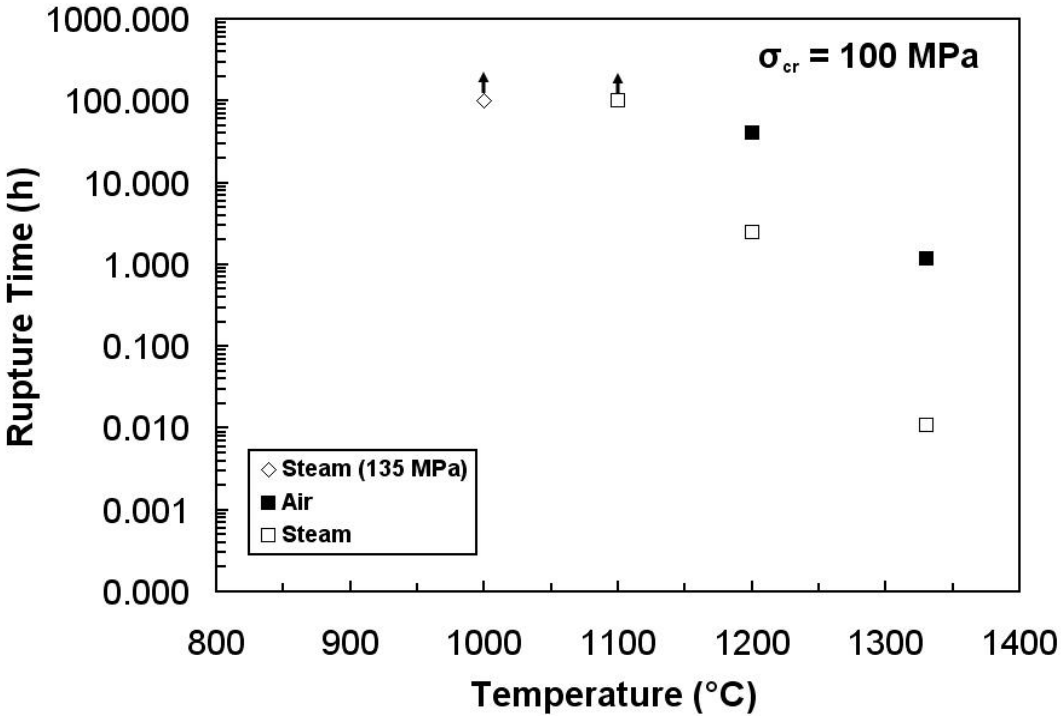

Figure 32. Rupture time versus temperature for N720/Alumina ceramic matrix composite. Creep stress is 100 MPa. Data at 1200 and 1330 °C are from Harlan [20].

The effect of temperature on creep rupture strain as well as on creep lifetime was also assessed in creep tests conducted at 150 MPa, shown in Figure 33. It is noteworthy that for the creep stress level of 150 MPa, the presence of steam has a noticeable effect on creep life as well as on creep strain accumulation at 1100 °C. Recall that no such effect was observed at 1100 °C at 100 MPa.

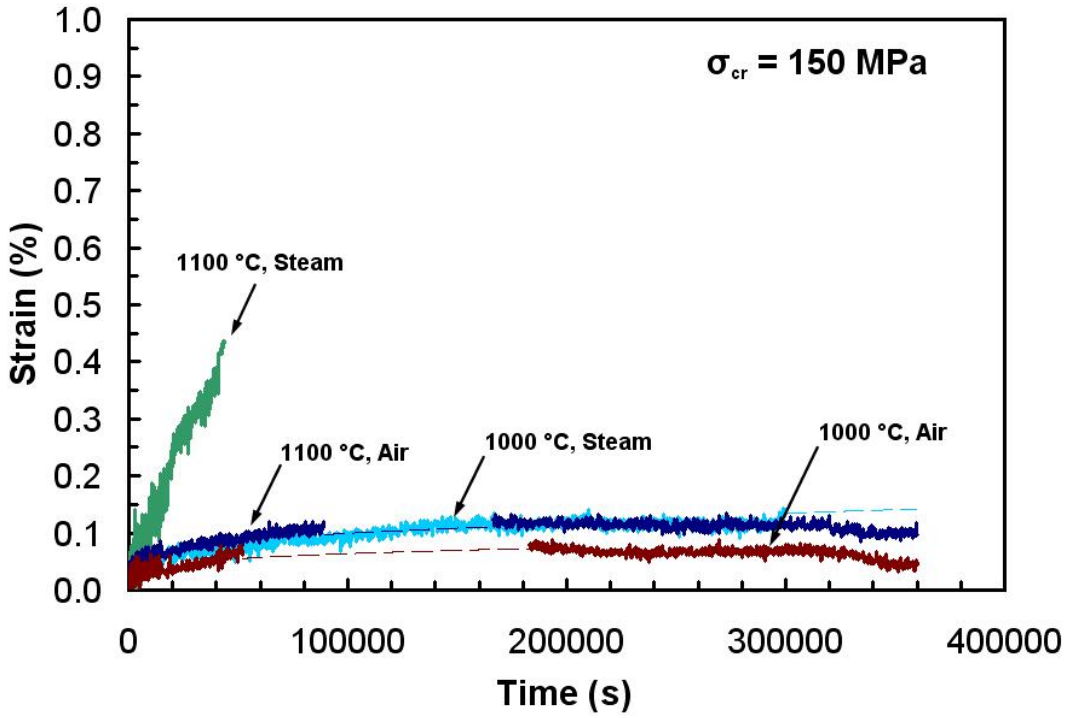

Figure 33. Creep strain vs. time curves for N720/Alumina ceramic matrix composite at 1000 and 1100 °C in laboratory air and steam environments.

At 1100 °C creep run-out was achieved in all 100 MPa tests, regardless of test environment. In contrast, creep run-out at 150 MPa was achieved only in air environment. The 150 MPa creep test conducted at 1100 °C in steam survived only 12.1 hours. Creep strain accumulated at 1100 °C at 150 MPa in steam was ~0.43%, while

only a low 0.1% strain was accumulated in air. Creep curves in Figure 33 are shown again in Figure 34 together with the creep curves obtained by Harlan [20] at 1200 °C for creep stress levels of 150 MPa. The time scale in Figure 34 is reduced to clearly show the creep curves at 1200 °C.

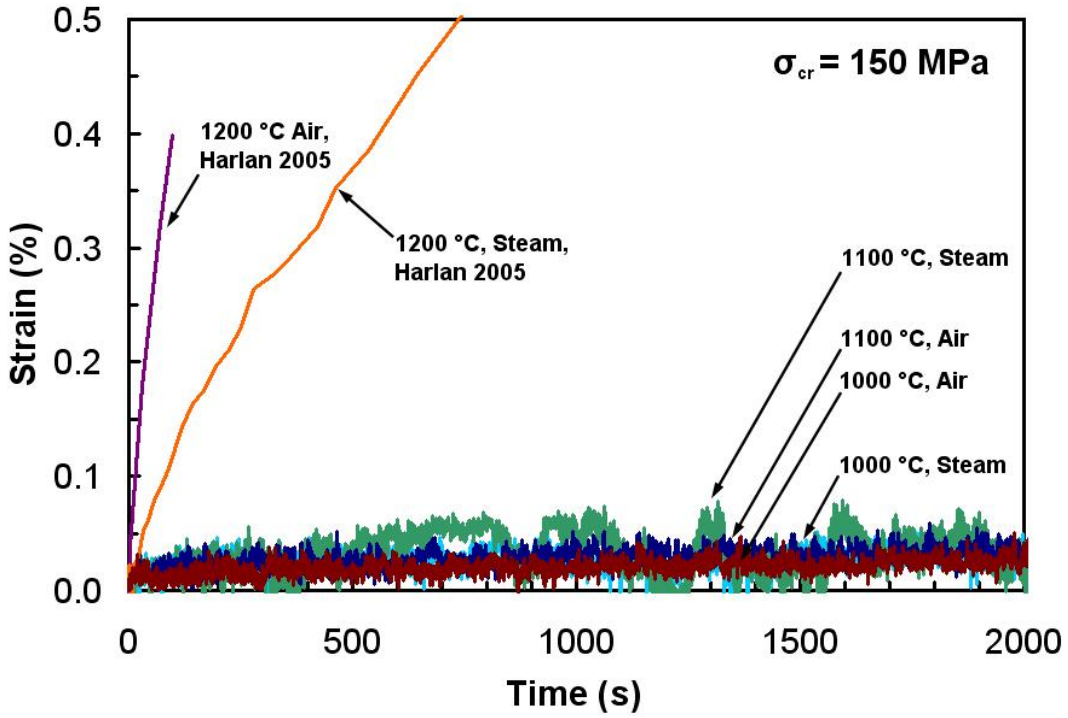

Figure 34. Creep strain vs. time curves for N720/Alumina ceramic matrix composite at 1000, 1100, and 1200 °C in laboratory air and steam environments. Time scale is reduced to clearly show the creep curves at 1200 °C. Creep data at 1200 °C from Harlan [20:48, 55], Ruggles-Wrenn et al. [55].

In tests that achieved run-out, larger creep strains were accumulated in steam than in air at the same applied stress. The presence of steam accelerates creep rates thereby increasing creep strain accumulation for a given period of time. This is illustrated in Figure 35 and Figure 36, where rupture strain and rupture time, respectively, are plotted vs. temperature. It is noteworthy that at 1000 °C creep run-out was achieved at 150 MPa

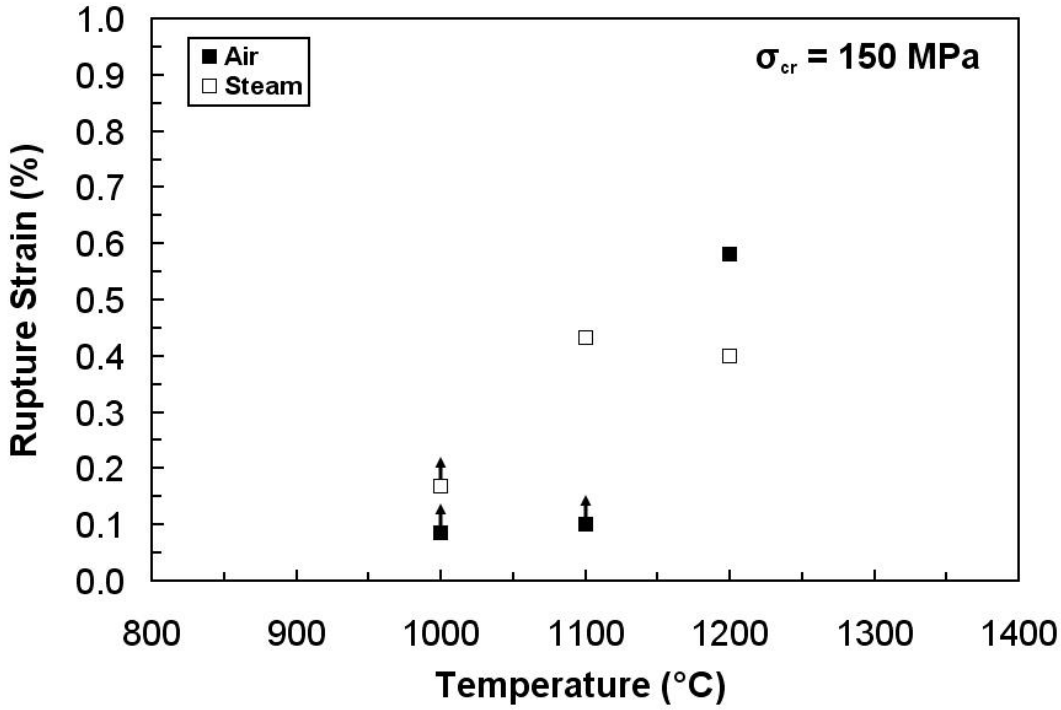

Figure 35. Rupture strain versus temperature for N720/Alumina ceramic matrix composite. Creep stress is 150 MPa. Data at 1200 °C is from Harlan [20].

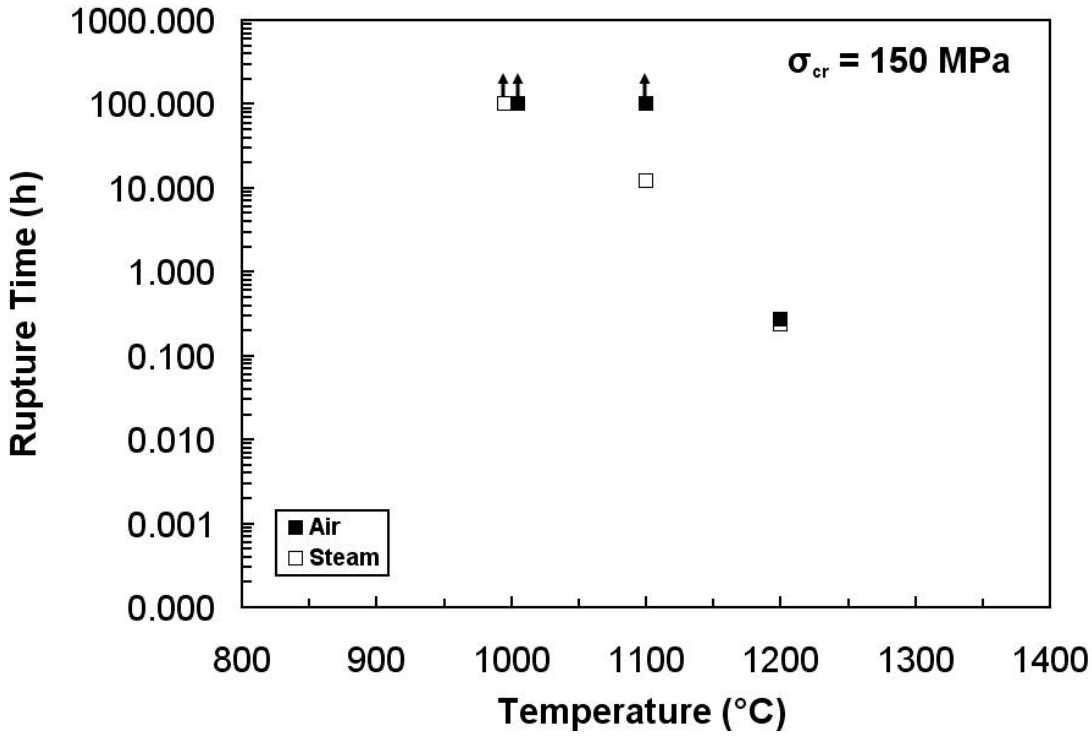

Figure 36. Rupture time versus temperature for N720/Alumina ceramic matrix composite. Creep stress is 150 MPa. Data at 1200 °C is from Harlan [20].

in both air and in steam. At 1100 °C, a degrading effect of steam environment is seen. Creep run-out at 150 MPa is achieved in air, but not in steam. At 1200 °C, creep resistance of the material is considerably degraded by exposure to temperature- creep run-out is not achieved in either air or steam.

Minimum creep rate was reached in all tests. All tests exhibited short primary creep followed by secondary creep until failure. It was possible to fit the creep results with a temperature independent Norton-Bailey equation of the form:

$$\dot{\varepsilon} = A_o \sigma^n \tag{4}$$

Where A_o is a temperature-dependent coefficient that accounts for the activation energy and other variables in the full form of the power law in Equation (1), and σ is the applied stress [9:140, 19:954].

Wilson and Visser studied the creep rate of Nextel 720 fiber alone at 1100 and 1200 °C. Those results are also plotted in Figure 37, with the dotted lines showing creep stress adjusted for a fiber volume, V_f, of 22%, the volume of fibers in the loading direction. At 1000 and 1100 °C, creep rates obtained in air are what may be expected from fibers alone at 1100 °C. However, creep rates obtained at 1000 °C in steam are nearly an order of magnitude higher than creep rates expected from fibers alone at 1100 °C. Creep rates obtained at 1100 °C in steam are 2 to 3 orders of magnitude higher than those expected from fibers alone. Similarly, results produced at 1200 °C in air are close to the rates obtained for fibers alone, although the stress exponent appears to be considerably higher, possibly due to the contribution from the matrix. At 1200 °C creep rates increase by a factor of 100 in the presence of steam.

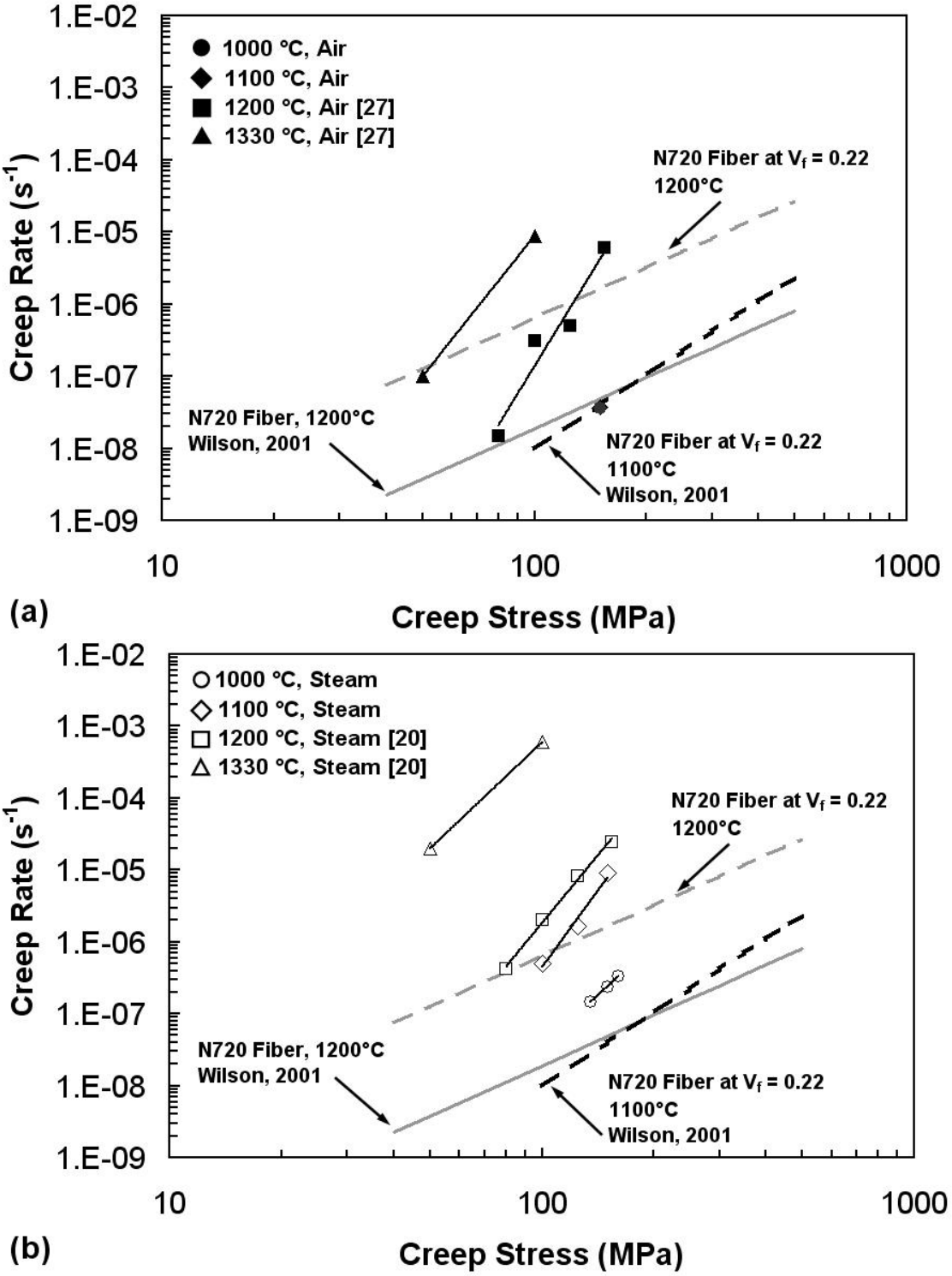

Figure 37. Minimum creep rate as a function of applied stress for N720/A ceramic matrix composite in the 1000-1330 °C temperature range in (a) laboratory air and (b) in steam. Data for Nextel 720 fibers (Wilson [67]) and data at 1200 and 1330 °C from Harlan [20:58] are also shown.

The effect of temperature on minimum creep rates is further illustrated in Figure 38. It is seen that minimum creep rates increase with temperature as well as with applied stress. Similar observations were reported earlier by Ruggles-Wrenn et al. [55]. Results in Figure 38 reveal that at 150 MPa in air environment creep rate remains relatively independent of temperature for $T \leq 1100$ °C. However, creep rate increases by at least 2 orders of magnitude as the temperature increases from 1100 to 1200 °C. Such dramatic increase in creep rate is observed at a lower temperature of 1100 °C in steam environment. In steam, creep rate increases by nearly 2 orders of magnitude as the temperature increases from 1000 to 1100 °C. In steam increase in creep rate with temperature is also seen at the creep stress level of 100 MPa (see Figure 38(b)). At this lower creep stress level, the effect of temperature is slightly less pronounced. An increase of 100 °C in temperature causes a nearly tenfold increase in creep rate.

At 1000 °C creep rates ranged from 10^{-8} to 10^{-7} s^{-1}. At 1100 °C, creep rates ranged from 10^{-8} to 10^{-6} s^{-1}. Harlan [20] reported creep rates in the 10^{-8} -10^{-5} s^{-1} range at 1200 °C and in the 10^{-7} - 10^{-5} s^{-1} range at 1330 °C.

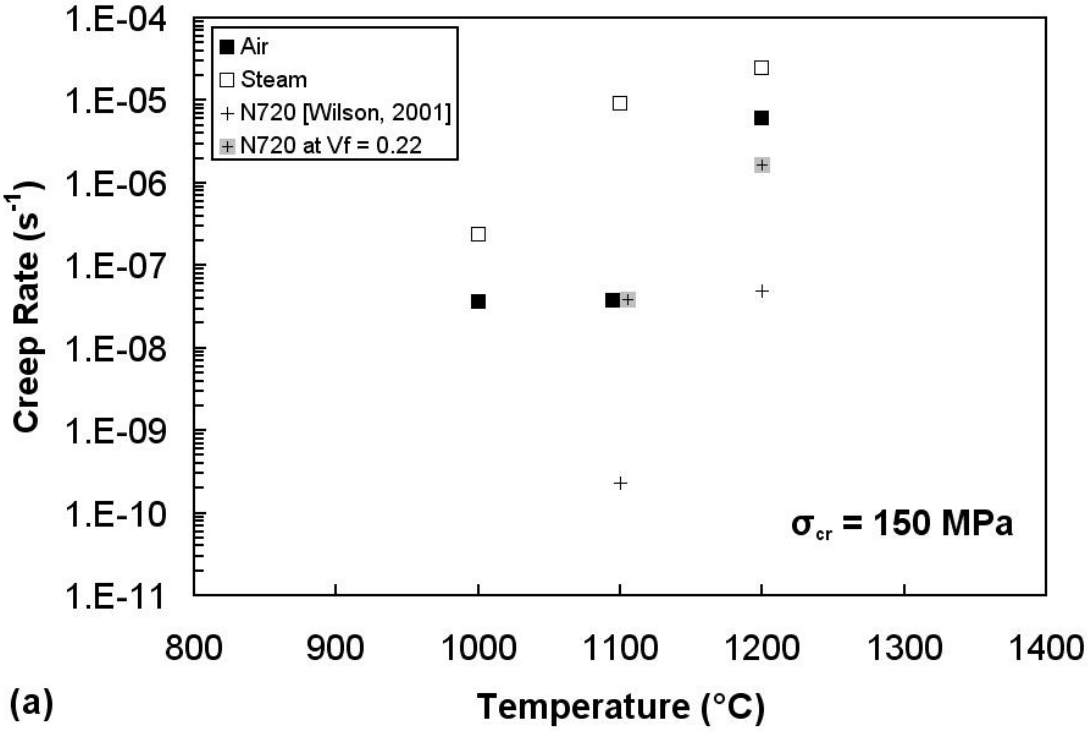

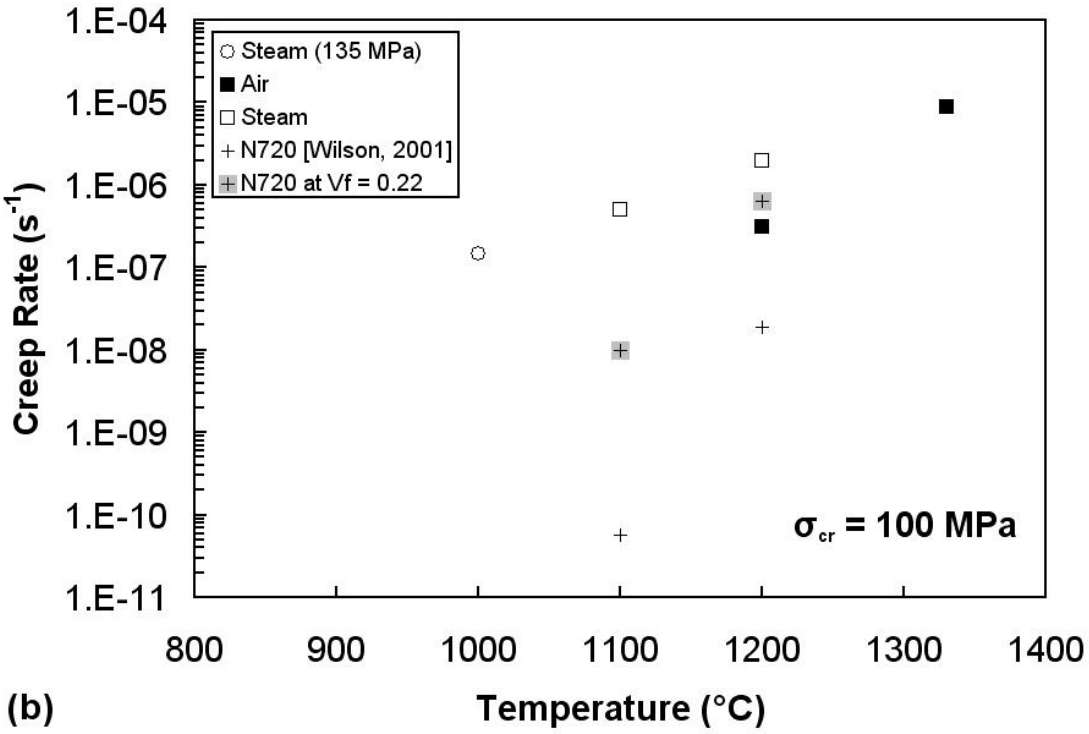

Figure 38. Minimum creep rate as a function of temperature for N720/A ceramic matrix composite in the 1000-1330 °C temperature range at (a) 150 MPa and (b) 100 MPa. Data for Nextel 720 fibers (Wilson [67]) and data at 1200 and 1330 °C from Harlan [20:58] are also shown.

5.6 Retained Properties

Retained strength and stiffness of the specimens that achieved run-out are summarized in Table 8. Tensile stress-strain curves obtained for the N720/A specimens subjected to prior creep are presented in Figure 39 together with the stress-strain curves for the as-processed material.

Strength retention values in Table 8 were obtained by comparing the UTS of pre-crept specimens with the UTS of as-processed material from the same panel. Stiffness retention values were obtained by comparing the post-creep modulus of a given specimen to the elastic modulus measured during load-up to creep stress of that same specimen.

Results in Table 8 reveal that at 1000 °C the composite retained at least 100% of its tensile strength, when compared to the 166 MPA average UTS of tensile specimens taken from the same panel. It is also seen that while the moduli of specimens subjected to prior creep in steam were reduced by 17 and 32%, respectively, the specimen pre-crept in air retained ~100% of its stiffness.

Table 8. Retained properties of N720/A specimens subjected to prior creep at elevated temperatures.

Specimen	Condition of Prior Creep Test	Creep Stress (MPa)	Retained Strength (MPa)	Retained Modulus (GPa)	Initial Modulus (GPa)	Failure Strain (%)	Strength Retention (%)	Modulus Retention (%)
P1-5	Steam, 1000 °C	135	174	56.7	68.0	0.30	104.8	83.4
P1-6	Steam, 1000 °C	150	195	50.8	74.6	0.37	117.5	68.1
P1-7	Air, 1000 °C	150	170	64.3	64.6	0.24	102.4	99.5
P2-1	Steam, 1100 °C	100	160	53.6	68.6	0.30	97.0	78.1
P1-8	Air, 1100 °C	150	186	60.0	61.7	0.35	112.0	97.2

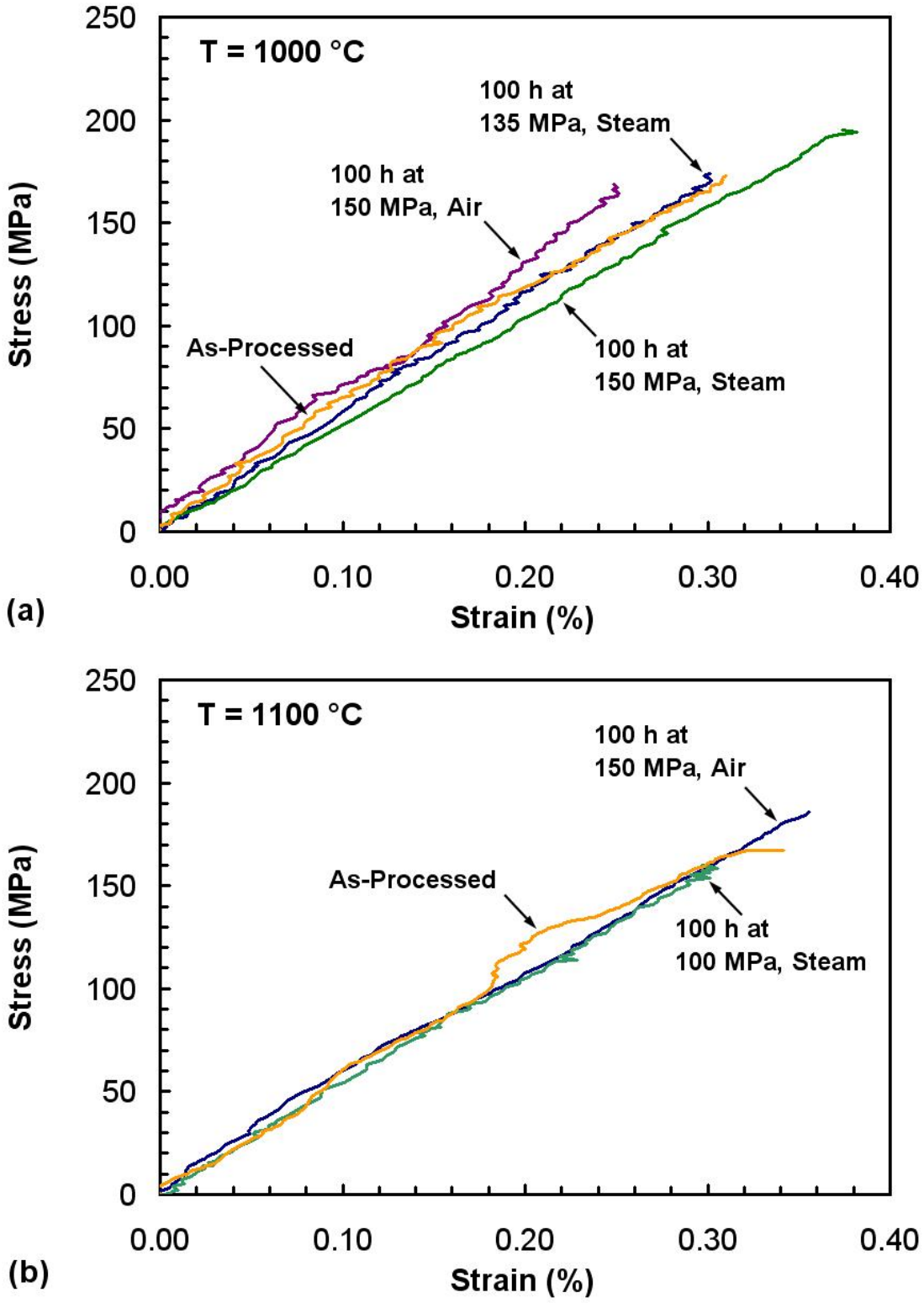

Figure 39. Effects of prior creep on tensile stress-strain behavior of N720/A ceramic matrix composite at (a) 1000 °C and (b) 1100 °C.

Similarly, prior creep at 1100 °C caused little to no reduction in specimen strength. The specimen pre-crept in air retained 97% of its tensile strength, while the specimen pre-crept in steam retained 112% of its tensile strength. The modulus reduction was ~22% for the specimen subjected to prior creep in steam. In the case of the specimen subjected to prior creep in air, stiffness reduction was insignificant at ~3%.

5.7 Composite Microstructure

Composite microstructure and fracture surfaces of all tested specimens were examined using optical and scanning electron microscopes. Microstructural investigation is conducted in order to illuminate damage and degradation mechanisms behind mechanical performance.

5.7.1 Optical Microscopy

Fracture surfaces obtained in tension tests at 800, 900, 1000 and 1100 °C are shown in Figure 40. All fracture surfaces in Figure 40 exhibit similar trends. The fracture plane is not well defined. The fibers in the 0° tows exhibit random failure producing fiber "pull-out". The 0° fiber tows also break over a wide range of axial locations, in general spanning the specimen width. Note that all specimens in Figure 40 produced damage zones of about 6 mm in length.

Fracture surfaces of N720/A specimens tested in creep at 100 MPa in steam at 1000, 1100, 1200 and 1330 °C are shown in Figure 41(a-d), respectively. The fracture planes are not well defined. The fibers in the 0° tows exhibit random failure producing brushy fracture surfaces. It is noteworthy that the average fiber pull-out length and the size of the damage zone appear to decrease with increasing temperature.

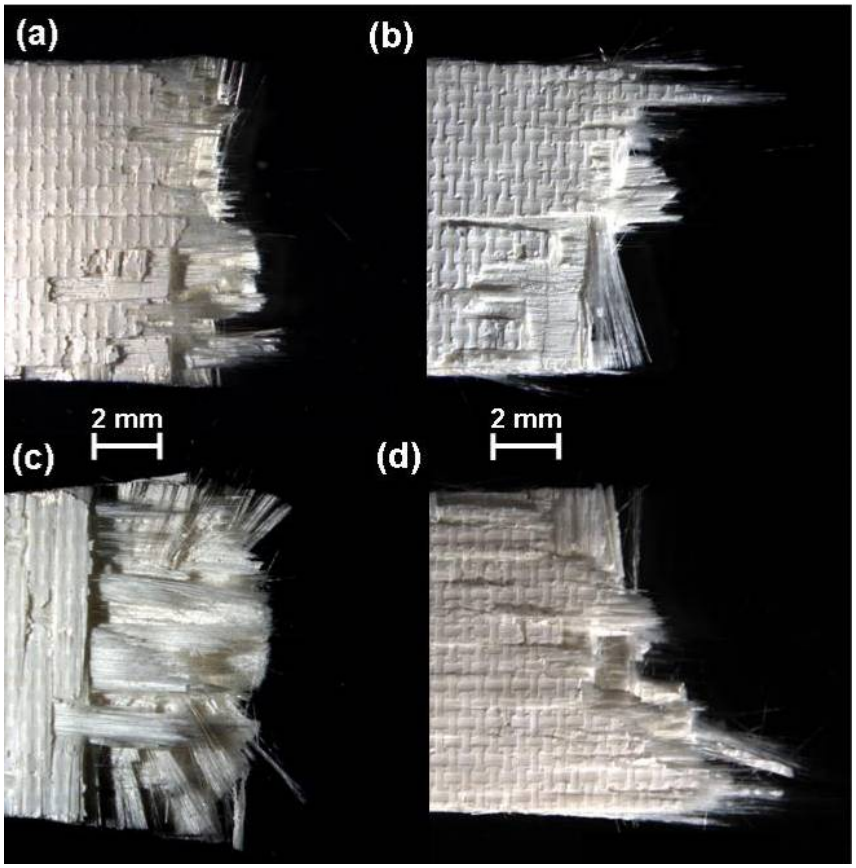

Figure 40. Fracture surfaces of the N720/A specimens tested in tension to failure in laboratory air at: (a) 800, (b) 900, (c) 1000, and (d) 1100 °C.

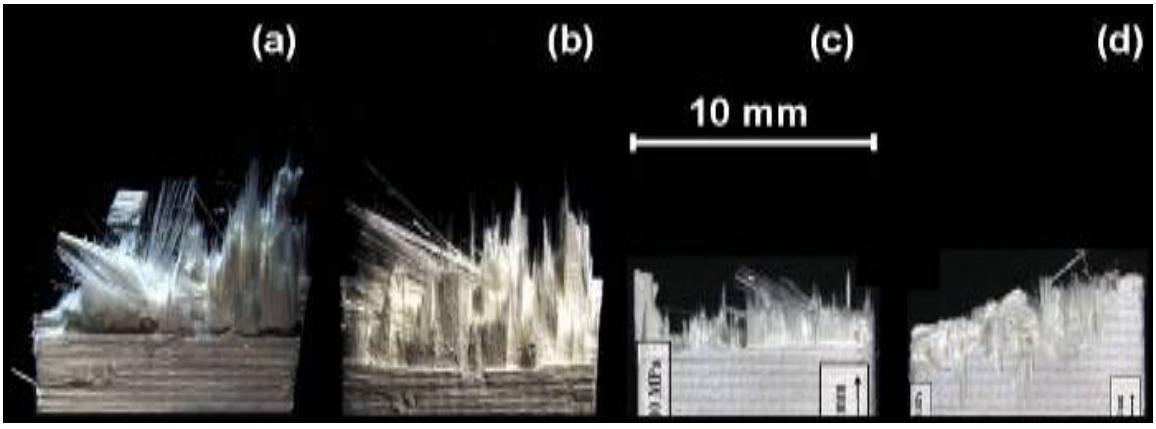

Figure 41. Fracture surfaces of N720/A specimens tested in creep at 135 MPa in steam at (a) 1000 °C, and 100 MPa in steam at (b) 1100, (c) 1200, and (d) 1330 °C. Fiber pull-out length decreases with increasing temperature. Micrographs of specimens tested at 1200 and 1330 °C from Harlan [20].

Fracture surfaces of the N720/A specimens tested in creep at 150 MPa in steam at 1000, 1100 and 1200 °C are shown in Figure 42(a-c), respectively. As was the case in the 100 MPa tests, the fracture planes obtained at 150 MPa show randomly distributed fiber failure and pull-out of both individual fibers and fiber tows. Likewise, the average length of fiber pull-out produced at 150 MPa appears to decrease with increasing temperature.

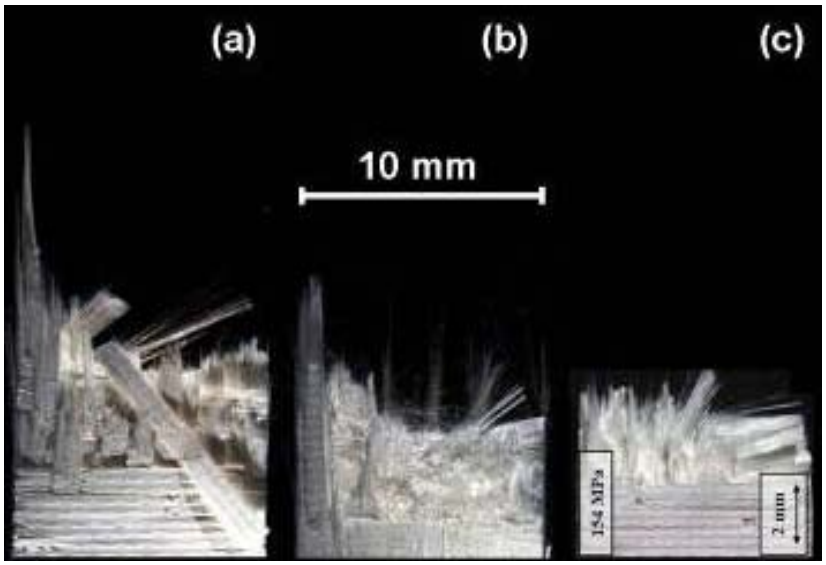

Figure 42. Fracture surfaces of N720/A specimens tested in creep at 150 MPa in steam at (a) 1000, (b) 1100, and (c) 1200. Fiber pull-out length decreases with increasing temperature. Micrograph of specimen tested at 1200 °C from Harlan [20].

Note that all specimens tested at 1000 °C and the specimen tested at 100 MPa at 1100 °C achieved creep run-out and were subsequently subjected to tensile tests to failure. The average length and degree of fiber pull-out is very similar in each. Their damage zone lengths are similar to the tensile tests at the same temperatures, but brushier. The 90° fiber bundles can be seen at varying states of pull-out, particularly in Figure

42(a), where an entire 90° bundle has been pulled out as the 0° degree bundles in the same layers fractured.

The 150 MPa test at 1100 °C in steam produced a flatter fracture surface than other tests conducted at $T \leq 1100$ °C. It failed after 12.1 hours. However, even its flatter fracture surface is brushier than those produced in creep tests at 1200 and 1330 °C [20]. Figure 41c and d, and Figure 42c failed after 2.5 hours, 98 seconds, and 39 seconds, respectively. They exhibit markedly flatter fracture surfaces and shorter damage zones than the specimens tested at lower temperatures.

Comparing fracture surfaces of specimens in both Figure 41 and Figure 42and the corresponding test durations, it appears longer lifetimes and longer damage zones are correlated. This has been reported previously [36]. The temperature increase from 1100 to 1200 °C appears to cause degradation in creep performance, as seen in creep test results reported in earlier sections. The difference between creep performance at 1000 and that at 1100 °C is not as large but exists, and is especially pronounced at higher stress levels.

Figure 43 shows fracture surfaces of N720/A specimens tested in creep at 150 MPa in laboratory air at various temperatures. It is seen that fracture surfaces clearly become less brushy and damage zones become shorter as temperature increases. Furthermore, Figure 44 provides a side view of specimens tested in creep at 150 MPa in air and in steam at 1000 and 1100 °C. Damage zones produced in steam are shorter and the corresponding fracture surfaces are less brushy. The fracture surfaces obtained in air

are brushier and the damage zones are longer with gaps between successive 0° fiber bundles where the 90° bundles have been pulled out.

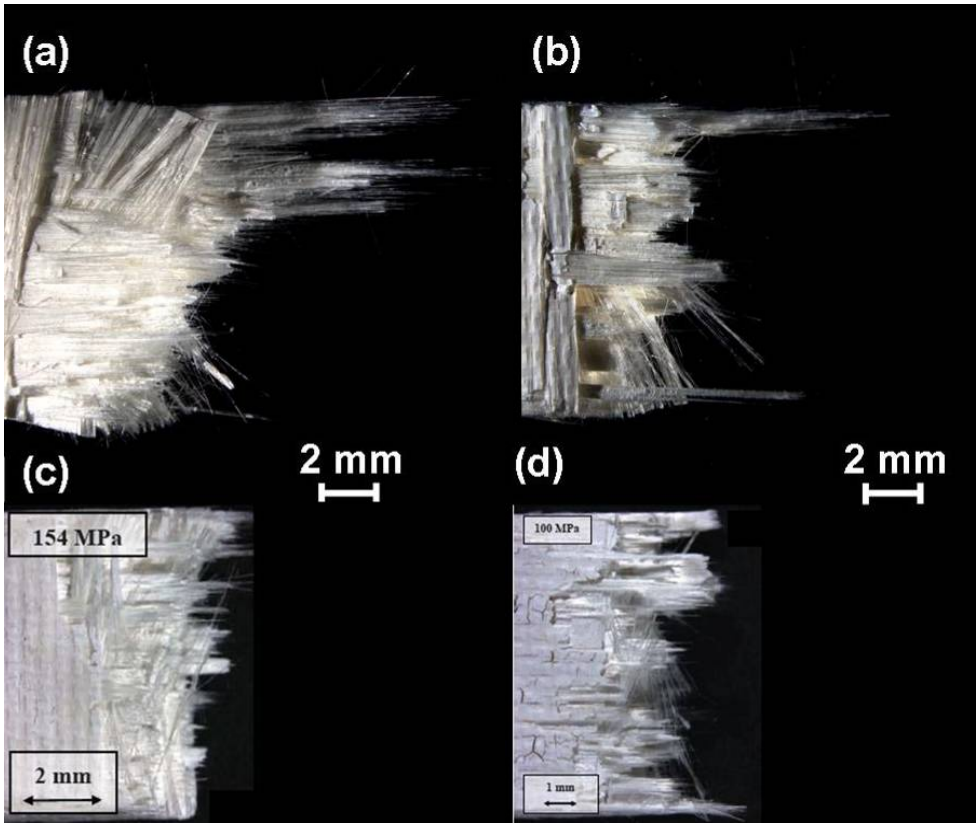

Figure 43. Fracture surfaces of N720/A specimens tested in creep at 150 MPa in laboratory air at (a) 1000, (b) 1100, (c) 1200, and (d) 1330 °C. Micrographs for 1200 and 1330 °C from Harlan [20].

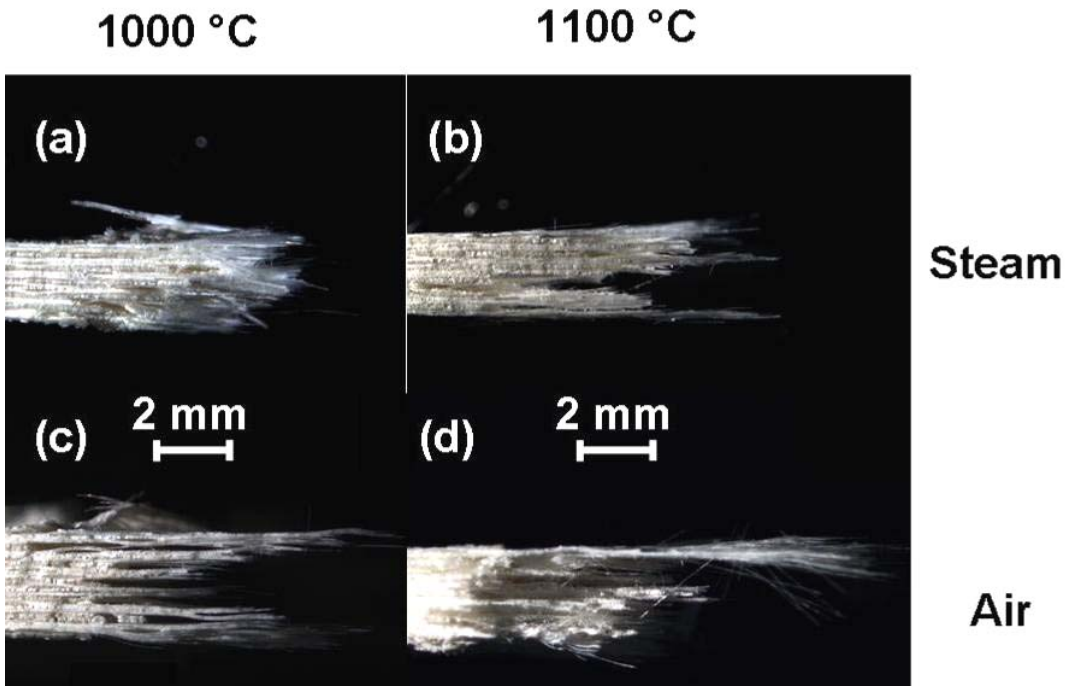

Figure 44. Side views of the fracture surfaces of N720/A specimens tested in creep at 150 MPa in laboratory air and steam at 1000 and 1100 °C.

Figure 45 reveals the overall reduction in "brushiness" and damage zone length with increasing creep stress for specimens tested at 1100 °C in steam at creep stress levels of 100, 125, and 150 MPa. The damage zone decreases with stress applied. As the applied stress increases, the ability for cracks to dissipate energy around fibers is diminished, and crack fronts propagate through fiber bundles, lowering the appearance of brushiness and individual fiber pull-out. Higher applied stress also shortens the specimen lifetime and consequently the time for strain accumulation, resulting in shorter damage zones.

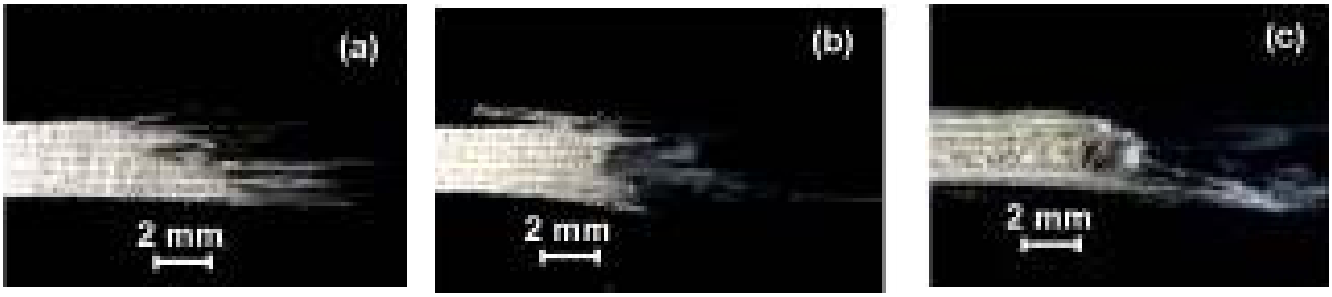

Figure 45. Side views of the fracture surfaces of N720/A specimens tested at 1100 °C in steam environment at: (a) 100, (b) 125, and (c) 150 MPa.

The physical effects of steam have been studied and chemical models formulated to describe the interaction of the water molecules in steam vapor with the Si-O bonds in silica glasses, particularly under load [39; 40]. Static fatigue of glass is a chemical process; crack growth is increased due to straining of the Si-O bonds at the crack tip in the presence of water molecules. This process is accelerated under stress [10, 11, 63-65]. Michalske formulated a qualitative chemical model to describe the interaction of H_2O molecules with the Si-O-Si bonds at crack tips [38]. A quantitative chemical-kinetics model for crack growth rate in silica glass as a function of stress has also been developed, according to which the crack growth rate increases exponentially with stress intensity, in a stress-corrosion mechanism [38-39]. The strain from applied stress accelerates the water-silica interaction. When no stress is applied, the Si-O bond that would be strained due to stress corrosion in the presence of H_20 is inert. Strained bonds react up to 8 times faster, the reaction rate increasing exponentially with stress [10, 11, 63-66]. This increased reaction rate may be one of the causes of accelerated fracture of Si-O_2-containing Nextel 720 fibers at high temperatures in steam.

5.7.2 Scanning Electron Microscopy

While optical micrographs are useful for providing macroscopic views of specimens and fracture surface topography, SEM micrographs allow observation of the composite microstructure at greater magnifications.

An overview of typical phenomena will be covered first. The granular nature of the alumina matrix in N720/A is visible in the matrix-rich region shown in Figure 46(a). Matrix micro-cracks are seen in Figure 46(b). Figure 47(b) highlights the effect of the strong bond between fiber and matrix. Large amounts of matrix material are still bonded to fibers even after pull-out.

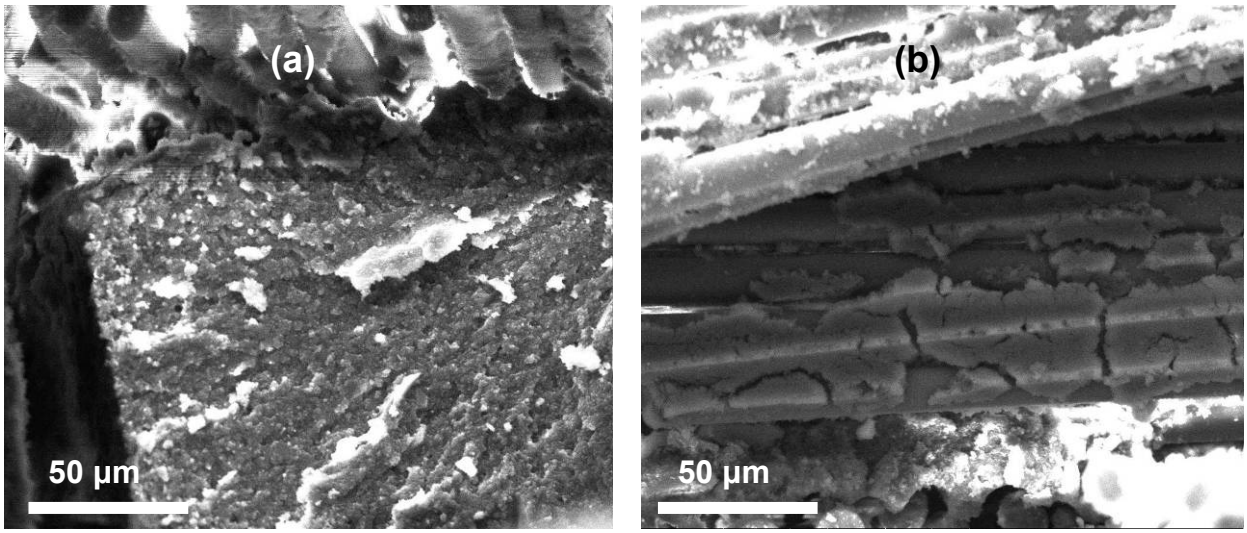

Figure 46. Fracture surfaces of the N720/A specimens tested in creep at 150 MPa at 1100 °C in (a) air and (b) steam, showing: (a) matrix-rich area (b) micro-cracking in the matrix surrounding 90° fibers.

The general scale of ~10 µm diameter fiber compared to the ~0.5 µm matrix grains is apparent in Figure 47(a-d), showing the details of the fracture surface of the N720/A specimen tested in creep at 150 MPa at 1000 °C in steam. Fiber pullout, seen in

Figure 47(a), is mostly clean but some pieces of the matrix do still adhere to the fiber surfaces. This can be seen at greater magnification in Figure 47(c) and (d).

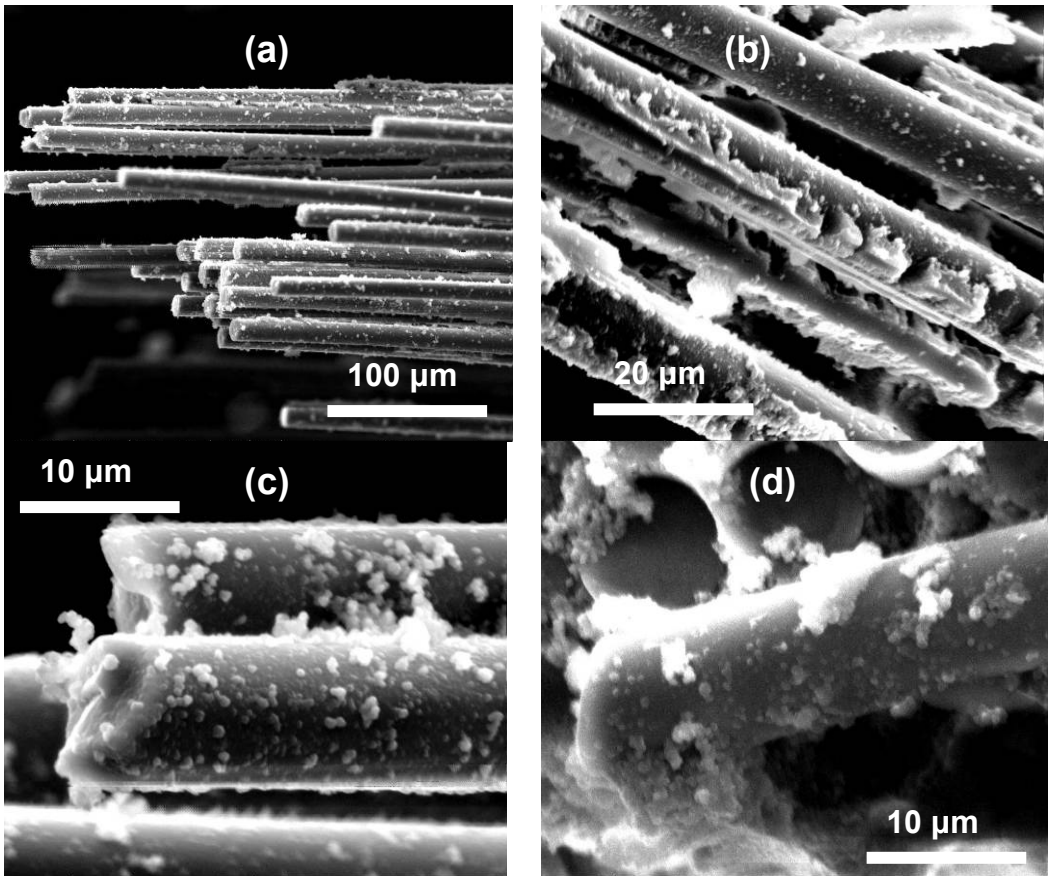

Figure 47. Details of fracture surface of the N720/A specimen tested in creep at 150 MPa at 1000 °C in steam. (a) Pull-out of individual fibers, (b) matrix material bonded to pulled-out fibers, (c) and (d) individual matrix grains on pulled-out fibers.

Figure 48 shows the key damage propagation mechanism in porous matrix composites at two magnifications: crack is propagating through the matrix and around fibers. As stress is applied, the crack fronts propagate through the porous matrix, dissipating energy in the process. In some areas, the matrix has formed "troughs" where the fiber has pulled away and a crack formed (see Figure 48(b)).

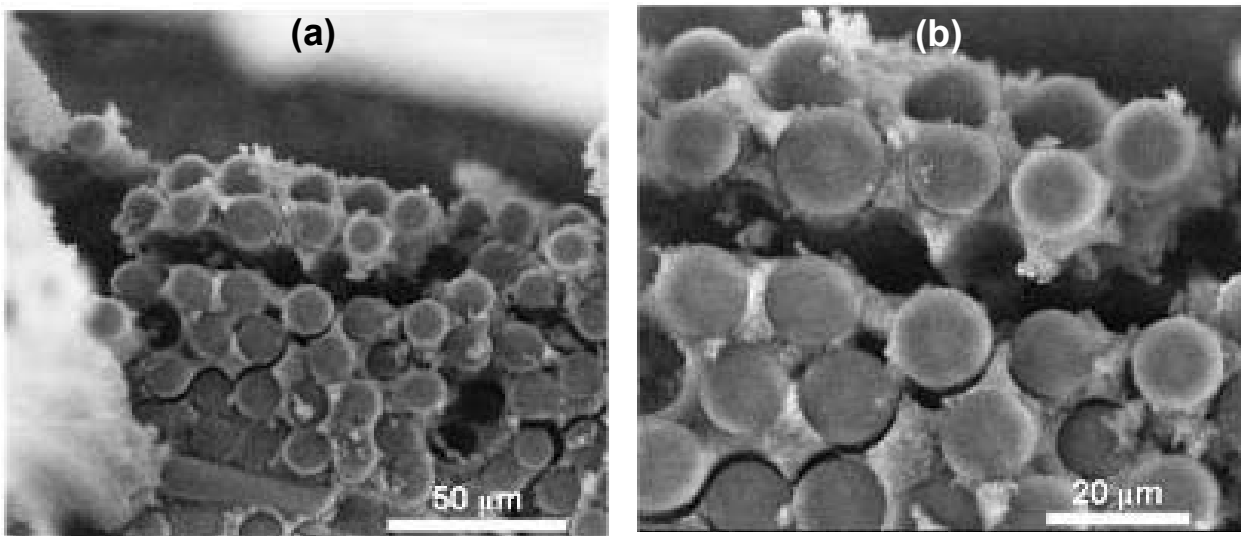

Figure 48. Details of fracture surface of the N720/A specimen tested in creep at 125 MPa at 1100 °C in steam. Crack propagation around 0° fibers is seen.

This may be indicative of additional matrix sintering. As the porous matrix undergoes additional sintering, the matrix porosity decreases. Thus, instead of fragmentizing when pulled away from fibers, the matrix retains its shape due to increased density. Carelli et al. [7] found that matrix porosity in N720/AS was reduced six percent after only a ten minute no-load exposure at 1200 °C.

The SEM micrographs in Figure 49 show fracture surfaces of three specimens, tested in creep at 100, 125, and 150 MPa in steam at 1100 °C. While all fracture surfaces contain a mix of brushy fiber failure with pull-out and planar coordinated fracture, the balance between the two shifts from predominantly fibrous failure to flat, coordinated fracture as the stress increases. This is consistent with previous research [23:54]. The effects of steam are also consistent with earlier observation [36:73].

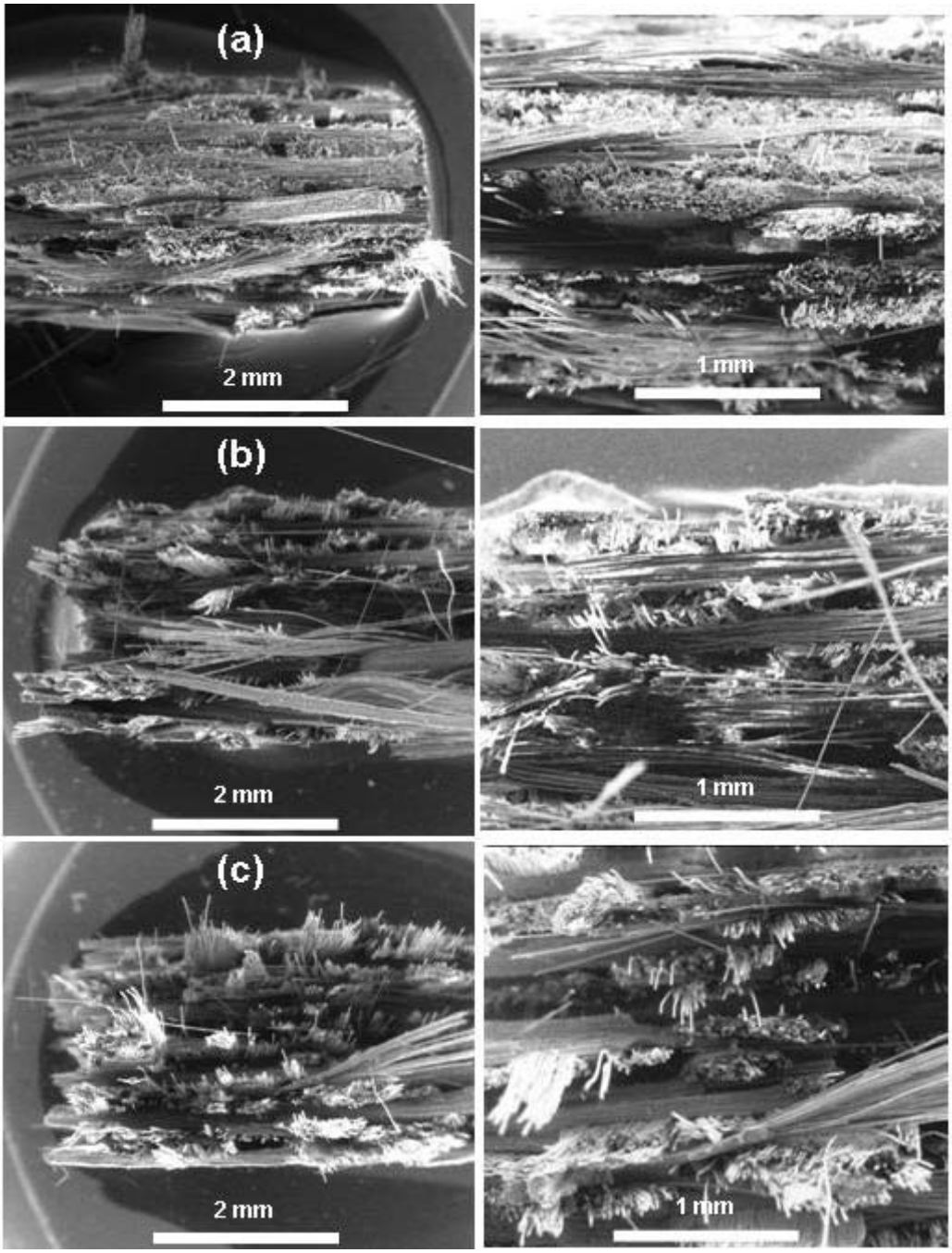

Figure 49. Fracture surfaces of the N720/A specimens tested in creep at 1100 °C in steam environment at (a) 150 MPa, (b) 125 MPa, and (c) 100 MPa.

Figure 50 and Figure 51 show fracture surfaces of four specimens tested in creep at 150 MPa. The specimens tested in air exhibit relatively more fiber pull-out than the specimens tested in steam. Furthermore, specimens tested in air show a greater average length of fiber pull-out.

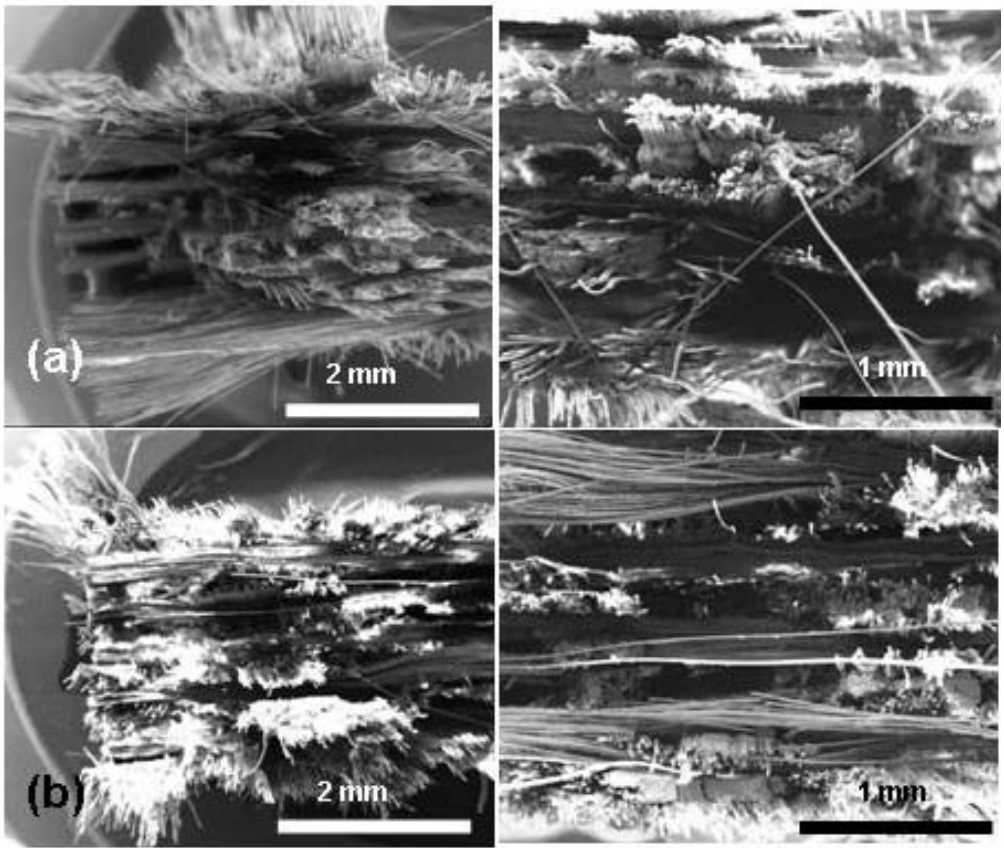

Figure 50. Fracture surfaces of N720/A specimens tested in creep at 150 MPa at (a) 1000 °C in air, (b) 1100 °C in air

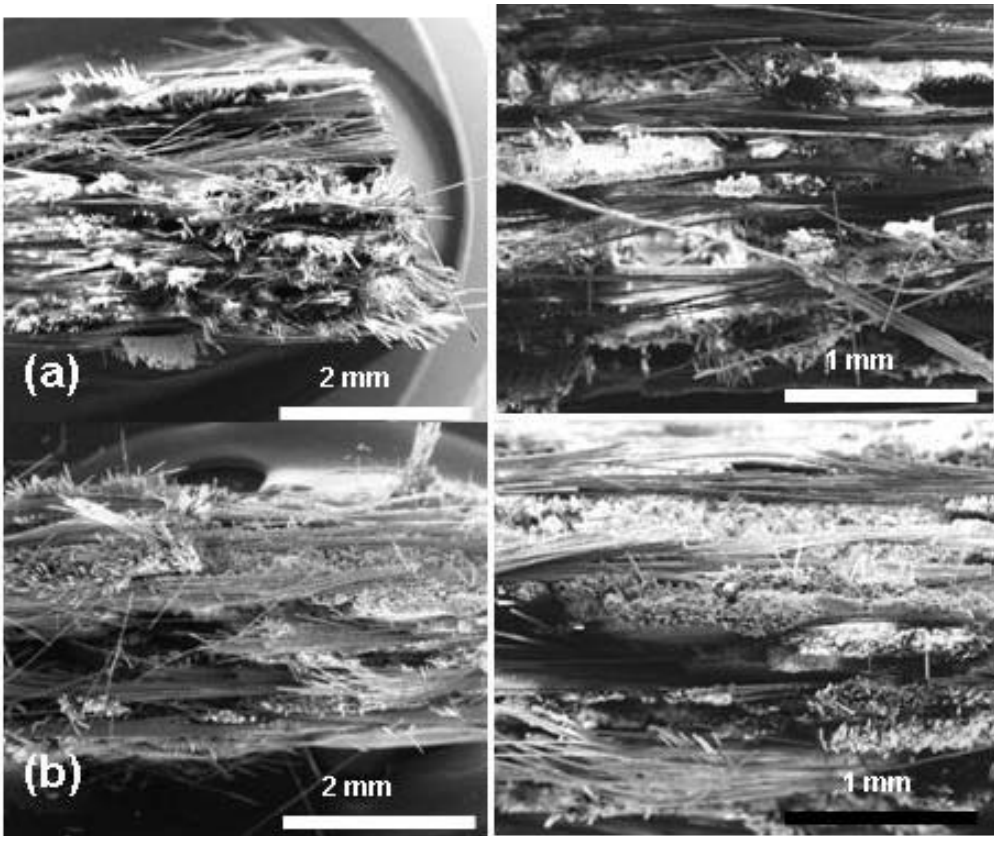

Figure 51. Fracture surfaces of N720/A specimens tested in creep at 150 MPa at (a) 1000 °C in steam, and (d) 1100 °C in steam.

The overall appearance of the fracture surfaces of specimens that achieved run-out and failed in subsequent residual tensile tests was predominantly brushy with clean fiber pull-out (Figure 52a and b). A higher magnification view is provided in Figure 52(c). Matrix particles are visible around the fibers' edges. The lack of a single plane or planes of fracture is evidence that no single crack caused specimen failure.

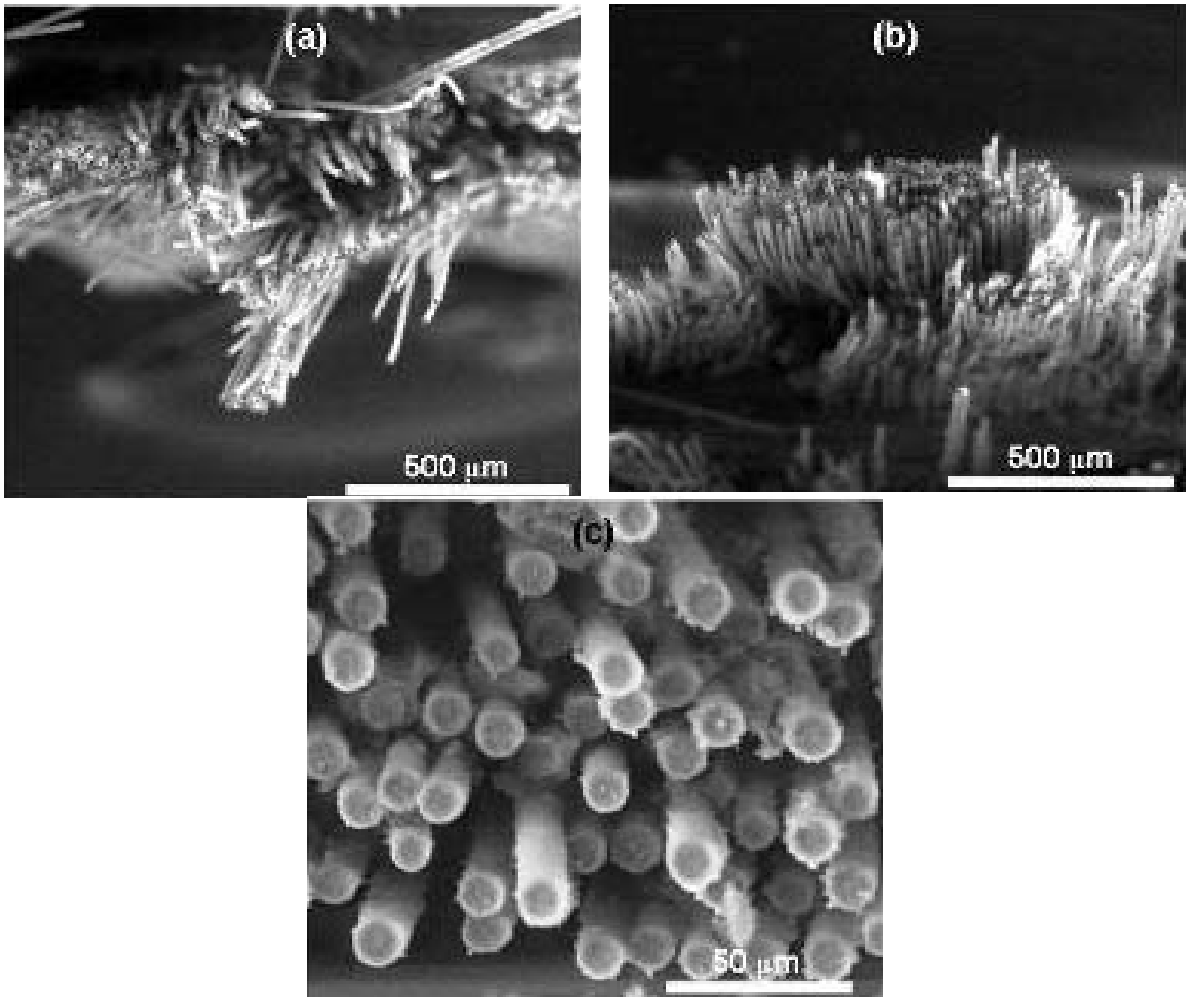

Figure 52. Fiber pull-out typical of run-out specimens tested for retained strength following creep tests: (a) at 150 MPa at 1000 °C in air and (b), (c) at 100 MPa at 1100 °C in steam.

Coordinated fracture surfaces, identified by planar areas where fibers appear to have broken in coordinated fashion, are more dominant in specimens that had shorter lifetimes and are indicative of diminished damage tolerance as seen in Figure 53(a-d).

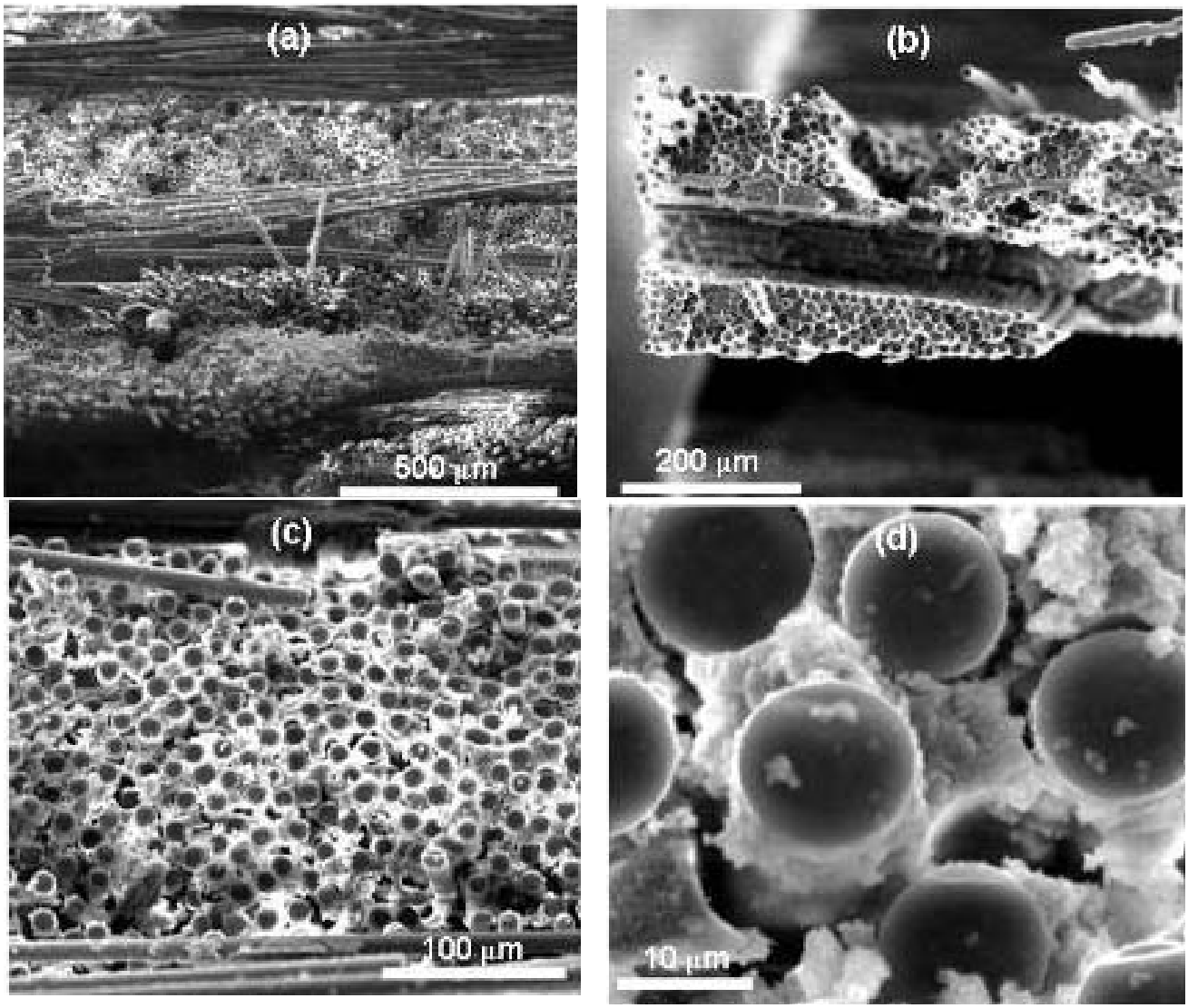

Figure 53. Typical coordinated fracture topography of N720/A specimens tested in creep at: (a) 150 MPa at 1100 °C in steam, (b) 125 MPa at 1100 °C in steam, (c) 150 MPa at 1100 °C in steam, and (d) 150 MPa at 1100 °C in steam.

Figure 53(a) shows the fracture surface of a specimen tested in creep at 150 MPa in steam at 1100 °C. Figure 53(c) and (d) show details of the same fracture surface. Even when coordinated fiber failure dominates, crack propagation around fibers is still visible- see Figure 53(d). In Figure 53(b) a 90° bundle between two 0° bundles has pulled out leaving an impression behind.

Regions of planar fracture are also present in run-out specimens, albeit in lesser quantities than in the specimens that failed in creep. Figure 54a shows the fracture surface of a run-out specimen tested in creep at 150 MPa in air at 1100 °C. The fracture surface in Figure 54(a) is similar to the one in Figure 53(b). Figure 54(b) shows a trough in a matrix-rich area where a fiber has pulled out and matrix particles shaken loose by fracture have fallen in.

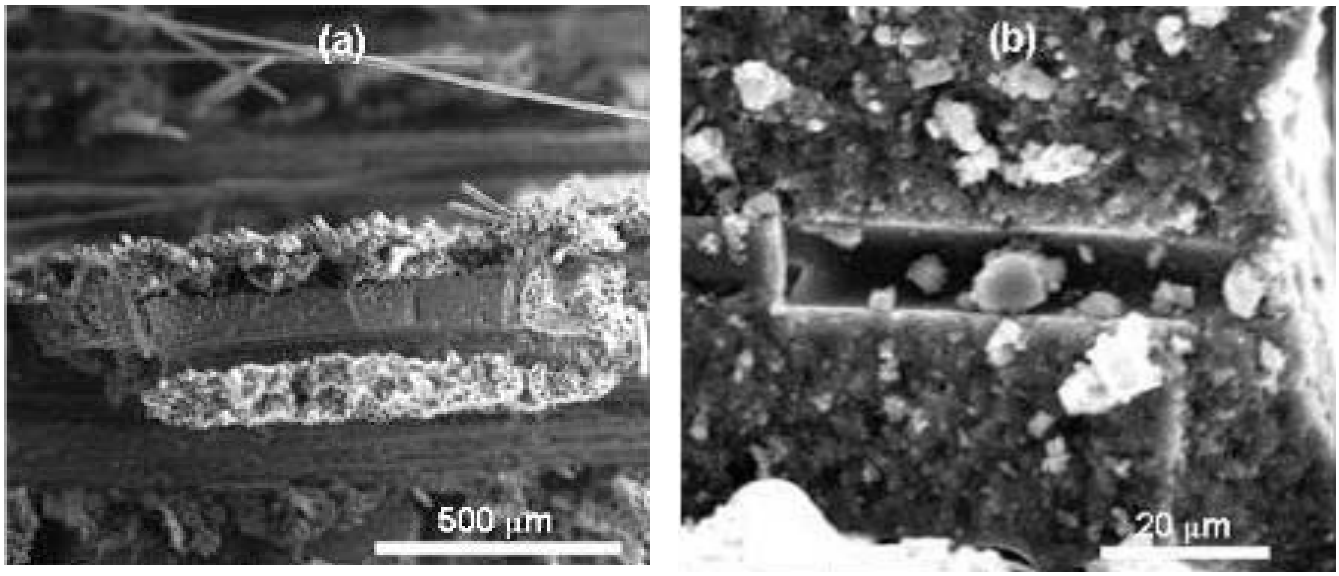

Figure 54. Fracture surfaces of the N720/A specimen tested in creep at 150 MPa in air at 1100 °C showing: (a) coordinated fracture and (b) matrix trough formed when 0° fiber pulled out with loose matrix particles in it.

Coordinated fracture is evidence of a single crack front propagating, through both matrix and fibers, and a trait of less damage tolerant material with denser matrices. Additional sintering during high temperature exposure can densify an Al_2O_3 matrix [7; 17; 18]. Since damage tolerance is largely dependent on matrix porosity additional matrix sintering can degrade composite durability.

Just as run-out specimens exhibit planar fracture, specimens that failed in creep also show some degree of fiber pull-out. Figure 55(a) and (b) show details of the fracture surface of a specimen tested in creep at 125 MPa at 1100 °C in steam. A fiber bundle that pulled out and then fractured across a planar surface is seen in Figure 55(a). Figure 55(b) shows fiber pull-out continued in one portion of the bundle after planar fracture splits the rest of the bundle farther down. Figure 55(c) shows matrix material still attached to the pulled out fibers due to the strong fiber-matrix interface.

The effect of temperature alone between 1000 and 1100 °C was not distinguishable in SEM images, as it was between varying stresses and environmental conditions.

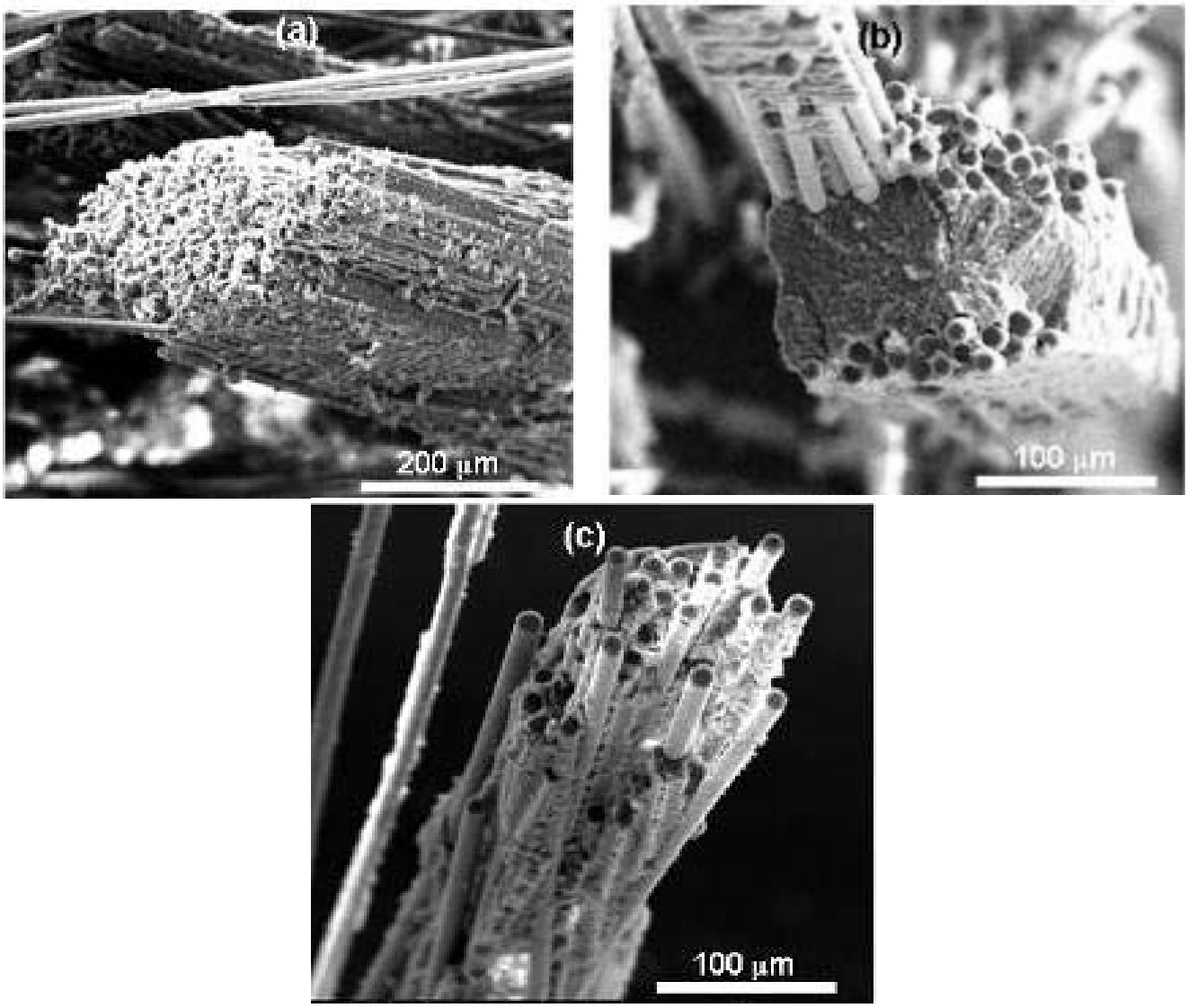

Figure 55. Fracture surfaces that exhibit fiber pull-out and coordinated fracture of N720/A specimens tested in creep at (a), (b) 125 MPa at 1100 °C in steam and (c) 150 MPa at 1100 °C in steam.

VI. Conclusions and Recommendations

Monotonic tensile tests were performed in air at temperatures ranging from 800 to 1100 °C. The average modulus of 67 GPa, ultimate tensile strength of ~190 MPa, and qualitative shape of stress-strain curves were consistent with Harlan and Carelli's findings [20:43; 8].

Creep tests were conducted at 1000 and 1100 °C in air and steam. Tests conducted at 1000 °C at stresses of 135 and 150 MPa achieved run-out in air and steam. In all tests at 1000 °C, creep strain accumulation was less than 0.2%. A test at 160 MPa in steam was prematurely ended due to equipment malfunction. Considering the data recorded prior to shutdown, the 160 MPa test was expected to achieve a 100-h run-out as well.

At 1100 °C in steam creep run-out stress was 100 MPa. Tests at 125 and 150 MPa did not achieve run-out. While strain accumulation and creep rates at 1100 °C were greater than those at 1000 °C, creep strains accumulated in all tests at 1100 °C were less than 0.6%.

Creep strain rates at 1000 °C ranged from 10^{-8} to 10^{-7} s^{-1}. At 1100 °C, creep strain rates were an order of magnitude higher, ranging from 10^{-8} to 10^{-6} s^{-1}. Creep strain rates at 1200 and 1330 °C were 10^{-8} -10^{-5} s^{-1} and 10^{-7} - 10^{-5} s^{-1}, respectively [20]. The presence of steam accelerated creep strain accumulation. Accumulated strain decreased with creep stress and temperature.

At 1000 °C creep run-out stress was 150 MPa (~80% UTS) in both laboratory air and in steam. At 1100 °C, creep run-out stress was 150 MPa in laboratory air, but only 100 MPa (~52% UTS) in steam. Recall that at 1200 °C creep run-out was 80 MPa in air [20:70]. At 1200 °C in steam, creep run-out was not achieved even at the low stress of 80 MPa.

Creep tests that achieved run-out were subjected to tensile tests to failure in order to determine retained strength and stiffness. All specimens retained 100% of their tensile strength. Specimens tested in air retained nearly 100% of their elastic modulus. In the case of specimens tested in steam modulus loss of ~25% was observed.

Specimens tested in steam produced flatter fracture surfaces and shorter damage zones than those tested in air at the same temperature. Furthermore, uncorrelated fiber fracture and brushy failure surfaces were more pronounced in specimens tested at a lower temperature at a given creep stress. Invariably, longer damage zones and brushier failure surfaces accompanied longer specimen lifetimes. Similar observations were reported by Mehrman [37].

At a given temperature, fracture surfaces had larger regions of planar fracture with more coordinated fiber failure as the applied stress increased. In general the run-out specimens that were subsequently failed in tension tests produced brushier fracture surfaces with longer fiber pull-out lengths than specimens that failed in creep in less than 100 hours.

The degradation of creep performance of N720/A at 1000 and 1100 °C may be attributable to several factors. Additional matrix sintering at higher temperatures, which

causes a reduction in matrix porosity, results in a less damage tolerant composite and promotes an earlier, more brittle failure. Stress corrosion of the N720 fibers, accelerated in the presence of steam under stress, is also possible. Finally, mullite depletion in the N720 fibers due to leeching out of Si species in the presence of steam at elevated temperature may be another factor contributing to the poor creep performance of N720/A CMC in steam [7; 23; 52; 58; 62].

Several additional analysis methods may be beneficial. The first is matrix hardness characterization using a nanoindenter. Sintering increases matrix hardness-comparing as-processed matrix hardness to high temperature and stress aged matrix hardness would allow a method for quantifying how much sintering occurs.

Transmission Electron Microscope (TEM) analysis would allow examination of fracture surfaces at much higher magnifications than SEM imaging. Actual grain size and shape could be viewed, offering insight into how N720 fiber grain structure changes, potentially depleting the mullite phase. A TEM would also permit a quantitative Energy Dispersive X-ray Spectroscopy (EDS) system analysis. EDS analysis would compare the chemical make-up of samples to each other, in steam, air, and as processed material, which in turn would definitively establish the stability of the mullite phase in the fibers.

Finally, a three-dimensional (3-D) SEM would allow a more detailed understanding of fracture surfaces, because a third dimension could truly be incorporated into imaging, an option not available in a 2-D SEM. Using a 3-D SEM, a Focused Ion Beam (FIB) for real-time micro cross-sectioning would allow the subsurface characteristics to be examined as well. Additionally, the ability to more fully

comprehend how fracture surface characteristics are spatially related to each other in three dimensions would allow a 3-D reconstruction of crack tip geometry, and 3-D porosity characterization and quantification. These results would be useful in analyzing the effects of additional matrix sintering.

Appendix A. Additional SEM Micrographs

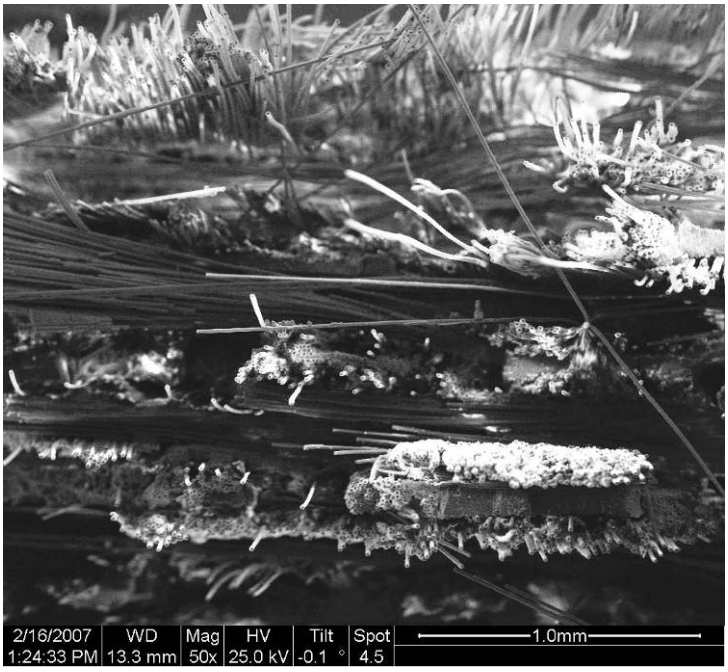

Figure 56. Fracture surface of N720/A specimen tested in creep at 150 MPa in air at 1000 °C.

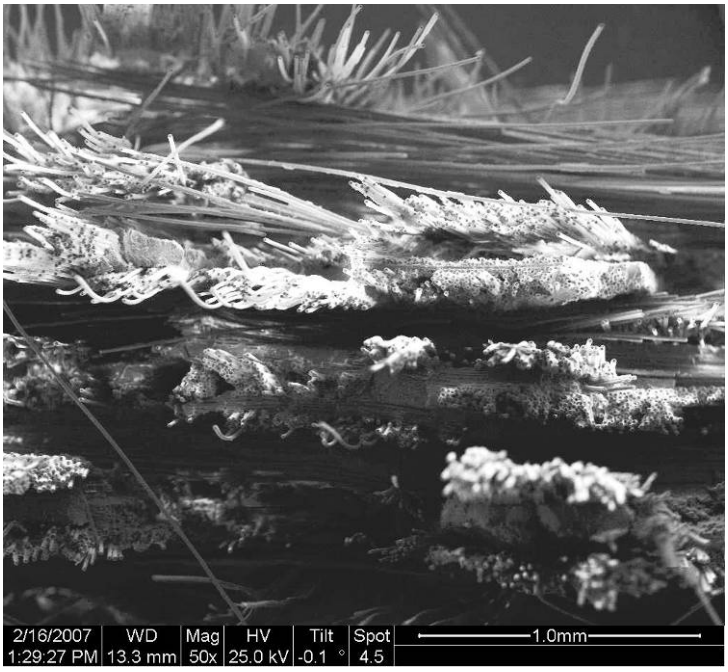

Figure 57. Fracture surface of N720/A specimen tested in creep at 150 MPa in air at 1000 °C.

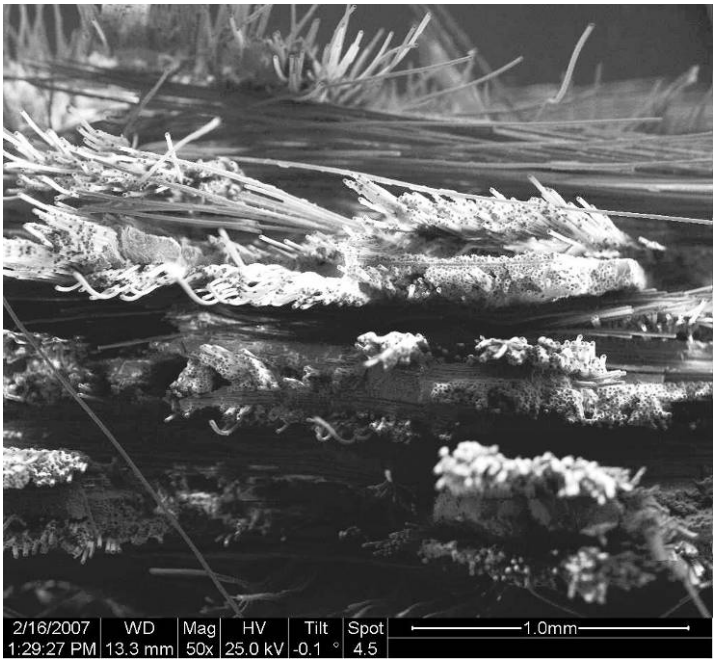

Figure 58. Fracture surface of N720/A specimen tested in creep at 150 MPa in air at 1000 °C.

Figure 59. Fracture surface of N720/A specimen tested in creep at 150 MPa in air at 1000 °C.

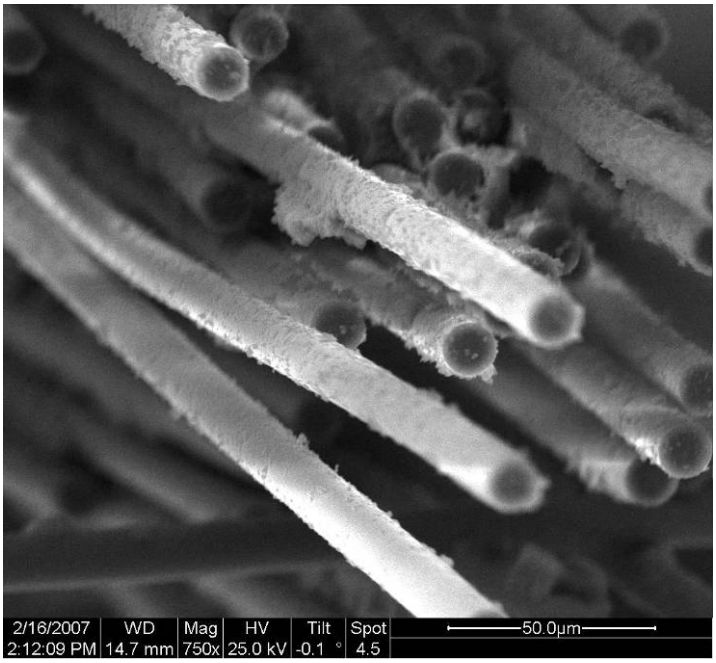

Figure 60. Fracture surface of N720/A specimen tested in creep at 150 MPa in air at 1000 °C.

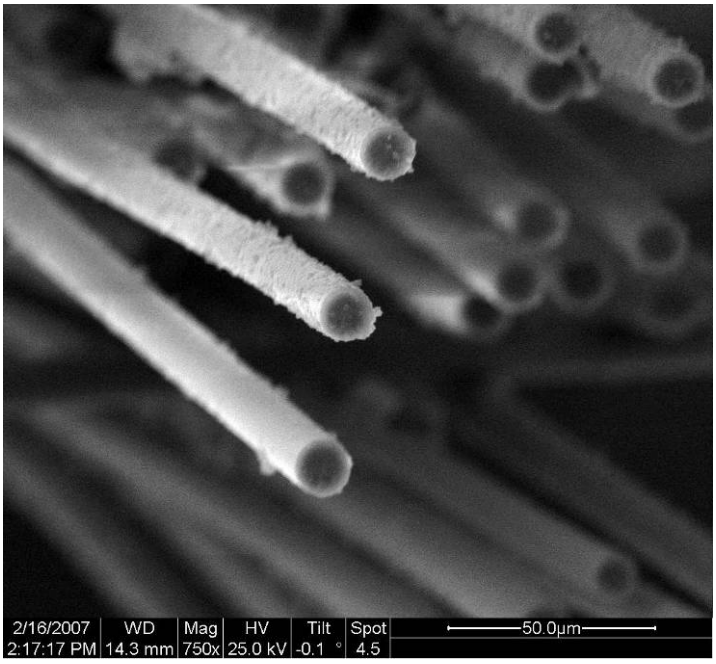

Figure 61. Fracture surface of N720/A specimen tested in creep at 150 MPa in air at 1000 °C.

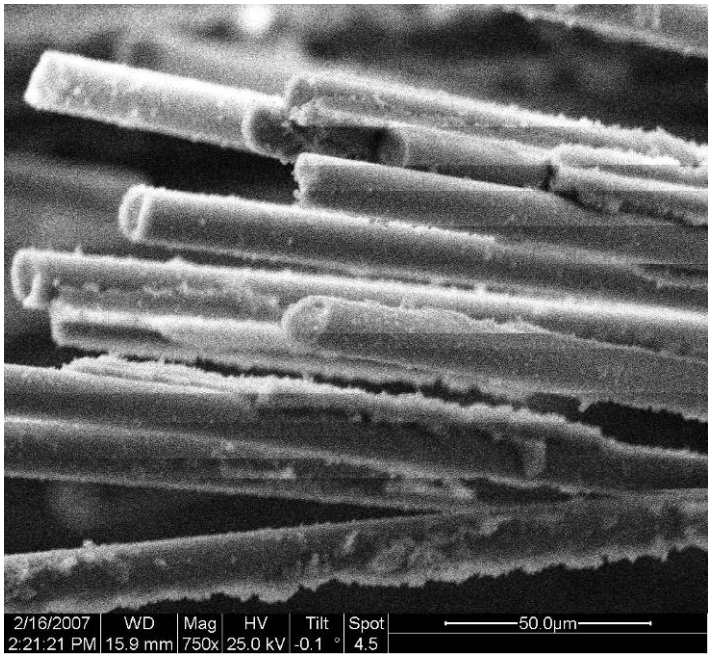

Figure 62. Fracture surface of N720/A specimen tested in creep at 150 MPa in air at 1000 °C.

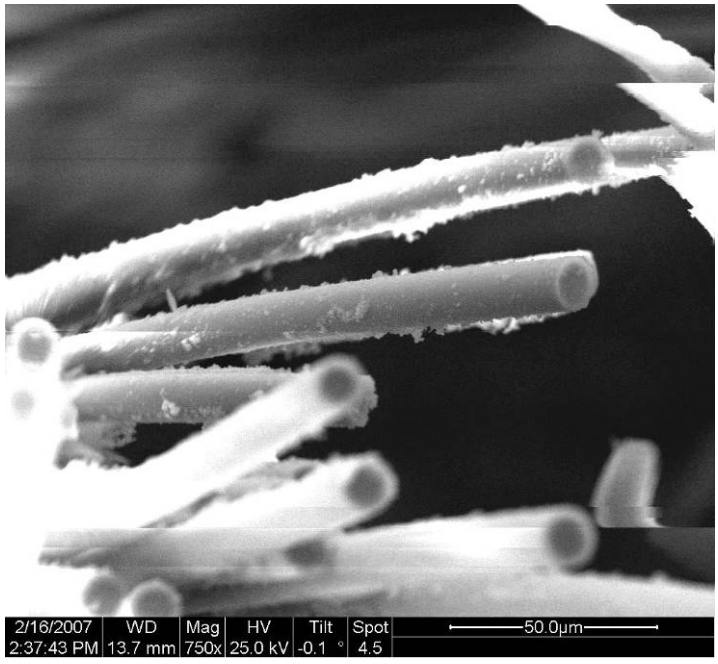

Figure 63. Fracture surface of N720/A specimen tested in creep at 150 MPa in air at 1000 °C.

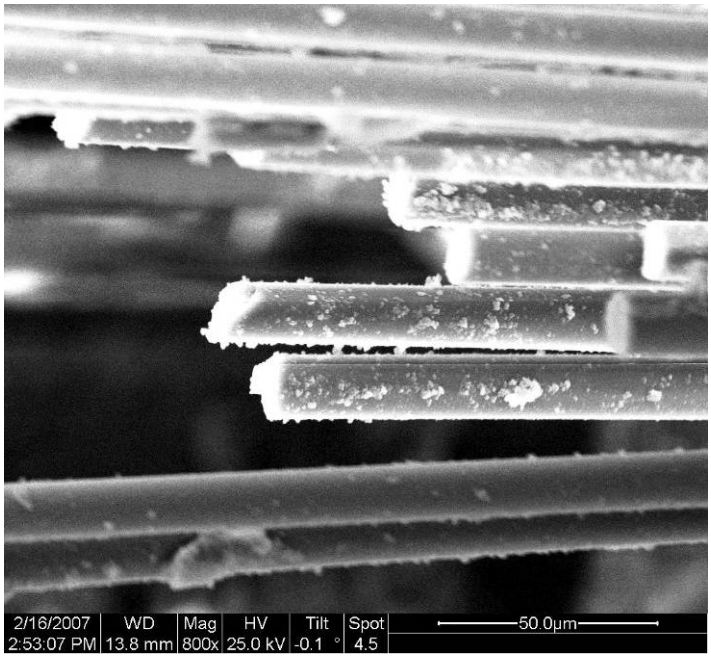

Figure 64. Fracture surface of N720/A specimen tested in creep at 150 MPa in air at 1000 °C.

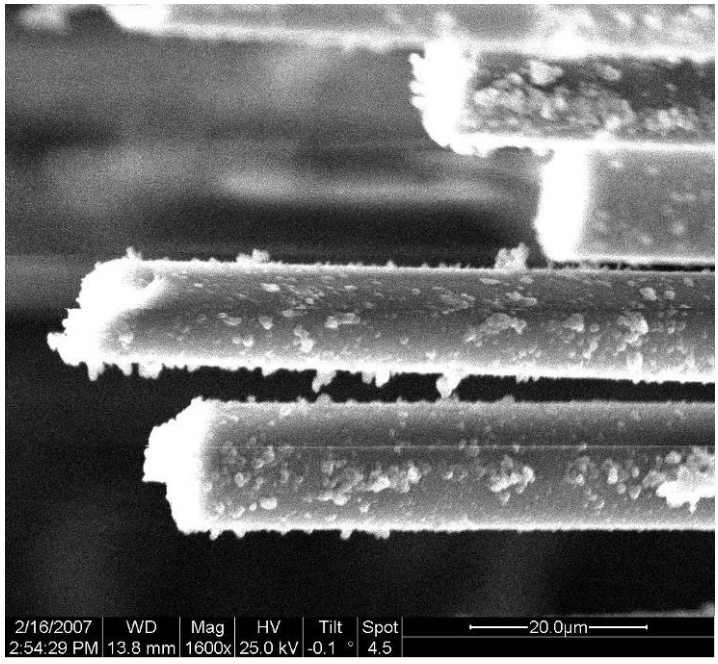

Figure 65. Fracture surface of N720/A specimen tested in creep at 150 MPa in air at 1000 °C.

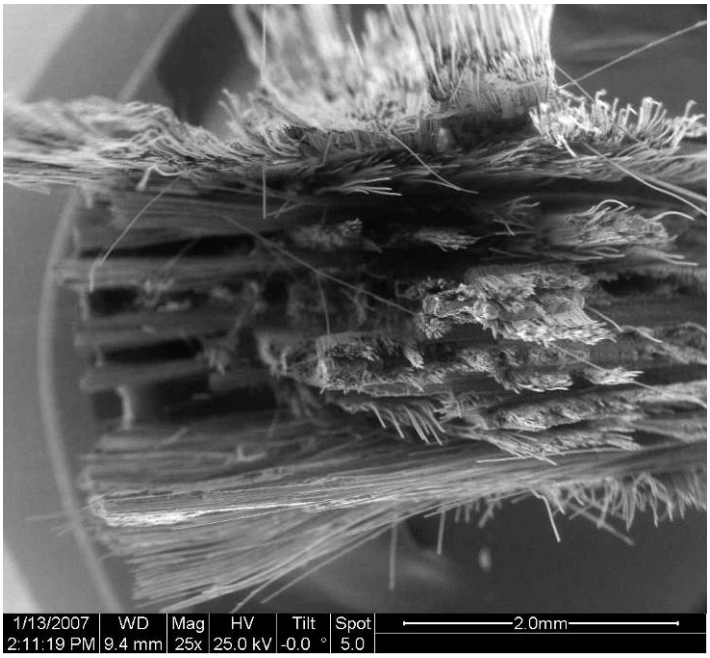

Figure 66. Fracture surface of N720/A specimen tested in creep at 150 MPa in air at 1000 °C.

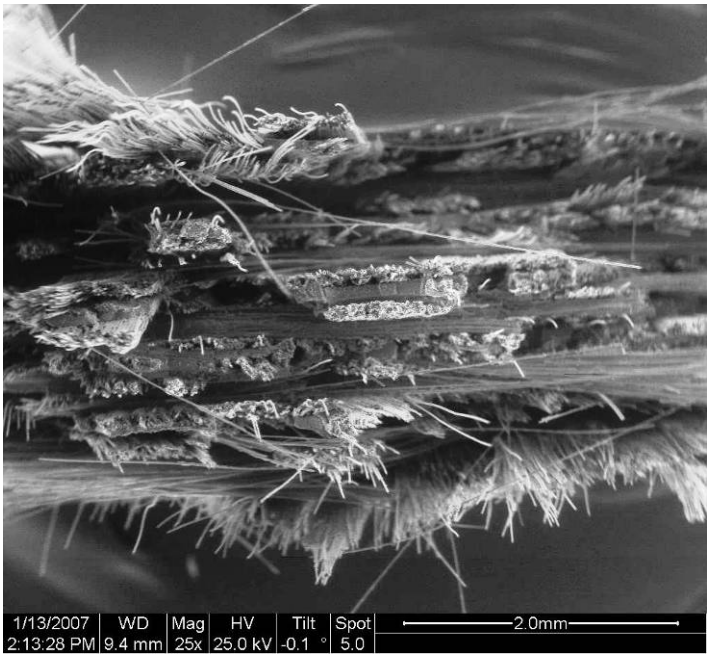

Figure 67. Fracture surface of N720/A specimen tested in creep at 150 MPa in air at 1000 °C.

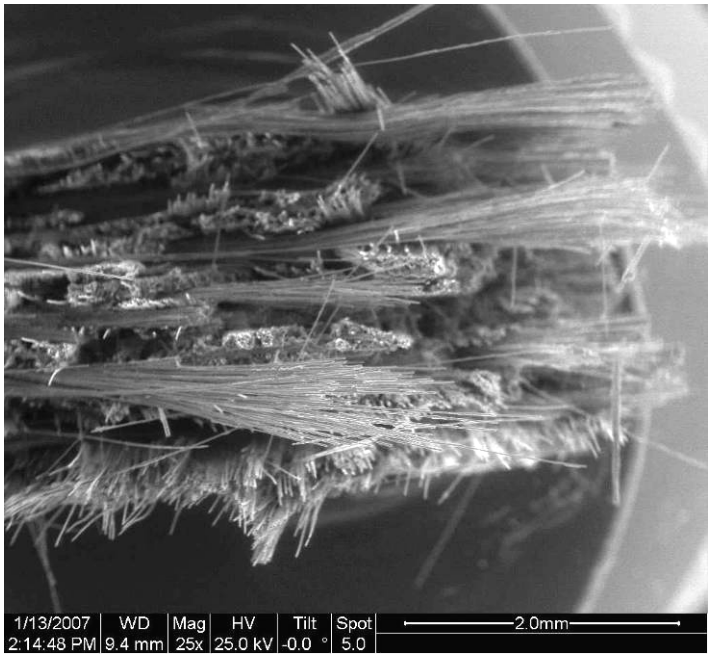

Figure 68. Fracture surface of N720/A specimen tested in creep at 150 MPa in air at 1000 °C.

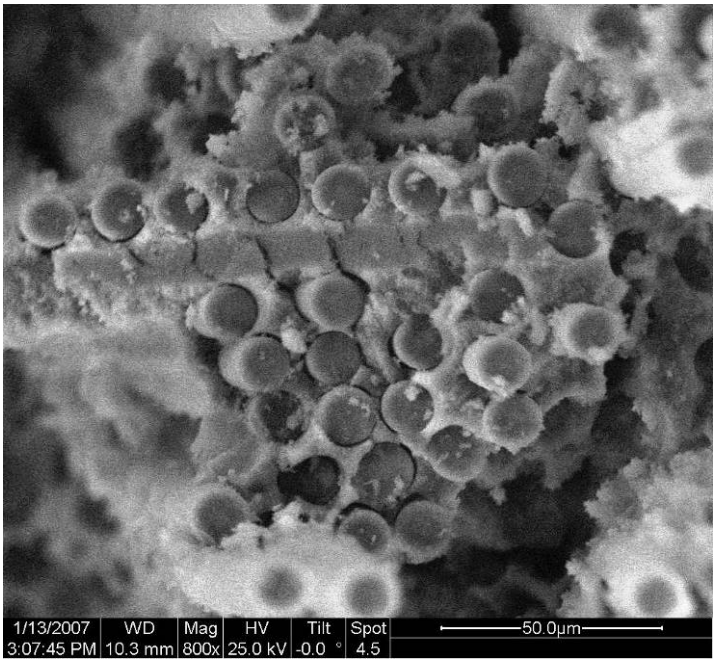

Figure 69. Fracture surface of N720/A specimen tested in creep at 150 MPa in air at 1000 °C.

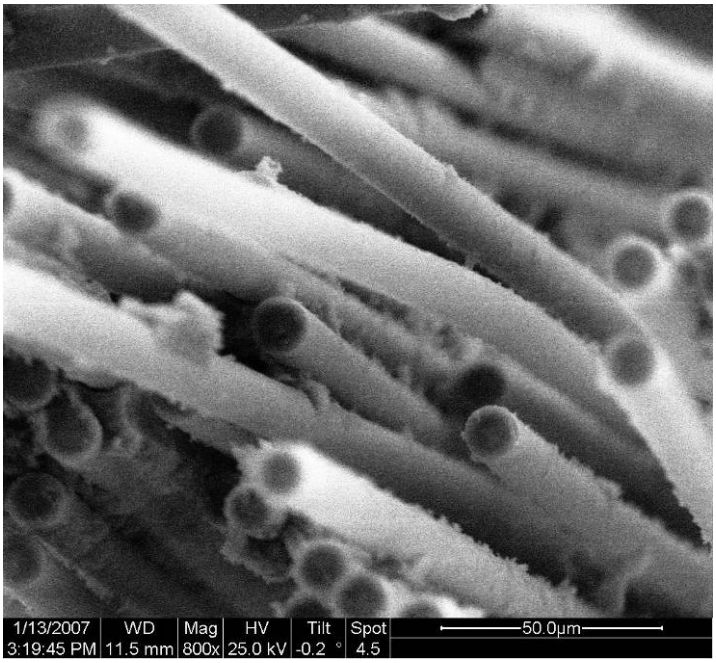

Figure 70. Fracture surface of N720/A specimen tested in creep at 150 MPa in air at 1000 °C.

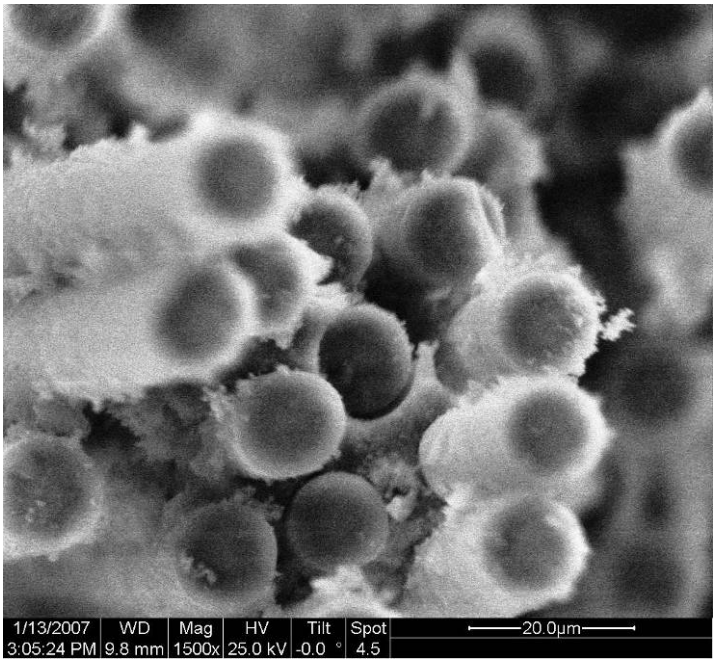

Figure 71. Fracture surface of N720/A specimen tested in creep at 150 MPa in air at 1000 °C.

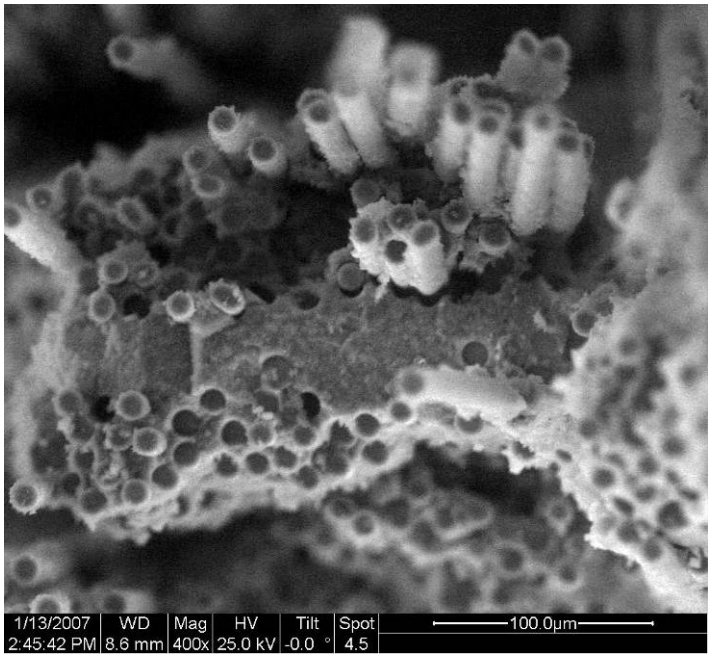

Figure 72. Fracture surface of N720/A specimen tested in creep at 150 MPa in air at 1000 °C.

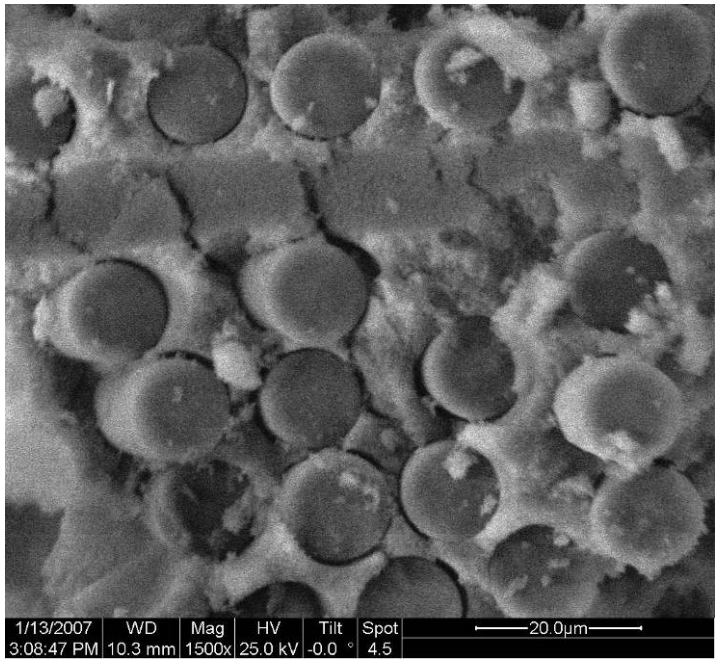

Figure 73. Fracture surface of N720/A specimen tested in creep at 150 MPa in air at 1000 °C.

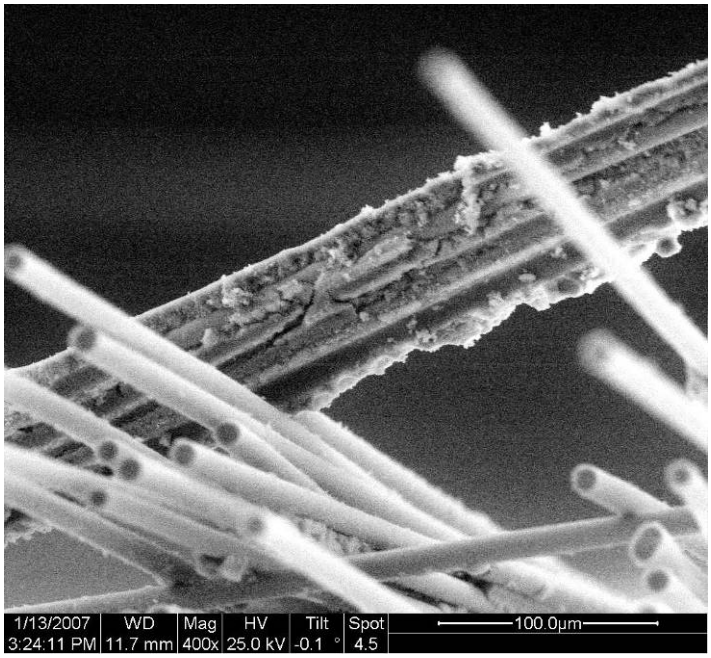

Figure 74. Fracture surface of N720/A specimen tested in creep at 150 MPa in air at 1000 °C.

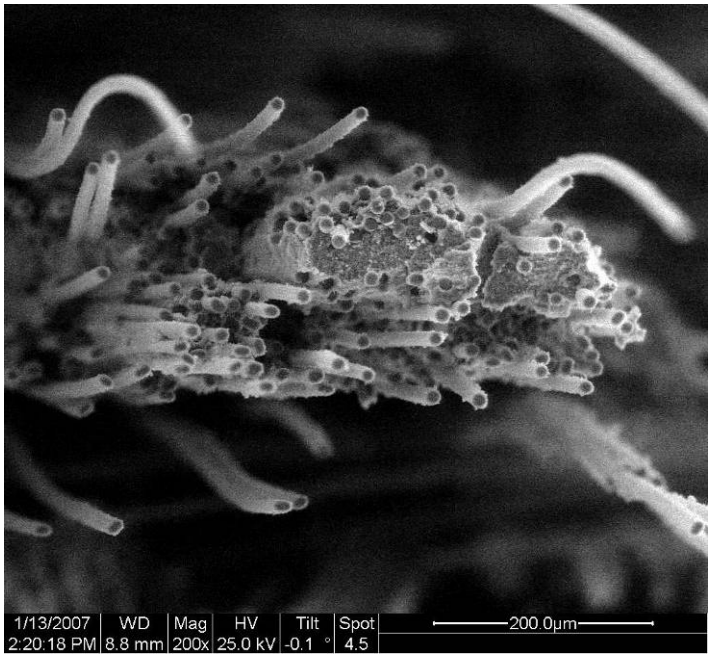

Figure 75. Fracture surface of N720/A specimen tested in creep at 150 MPa in air at 1000 °C.

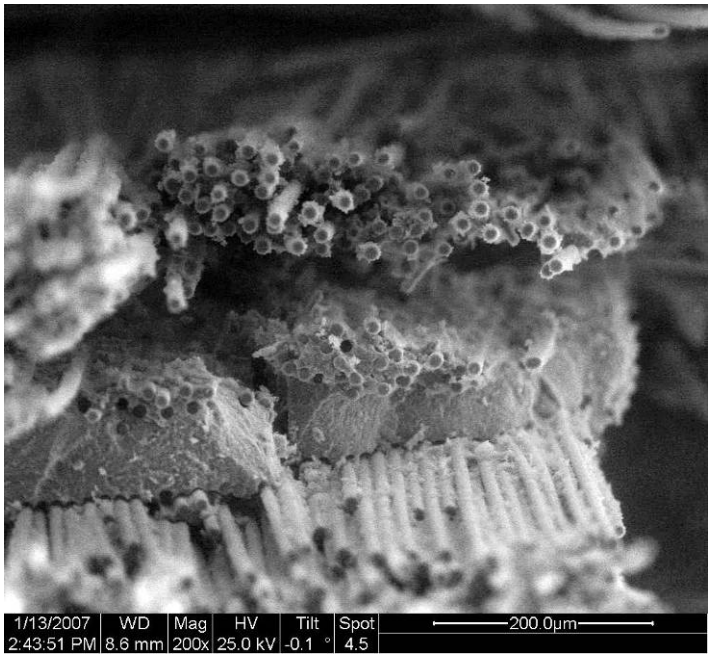

Figure 76. Fracture surface of N720/A specimen tested in creep at 150 MPa in air at 1000 °C.

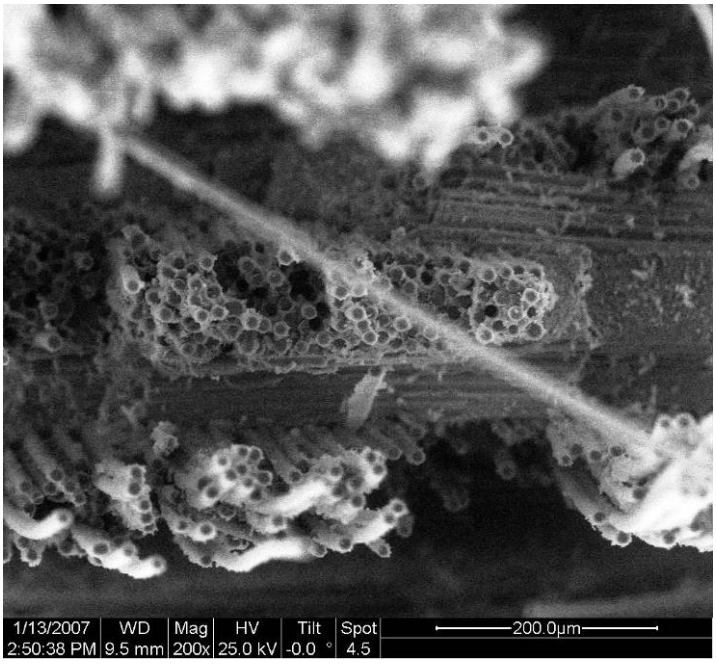

Figure 77. Fracture surface of N720/A specimen tested in creep at 150 MPa in air at 1000 °C.

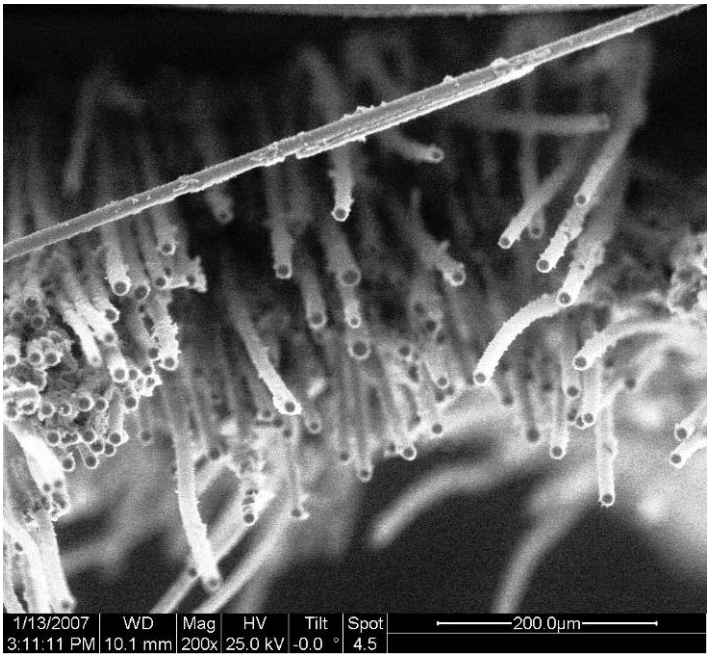

Figure 78. Fracture surface of N720/A specimen tested in creep at 150 MPa in air at 1000 °C.

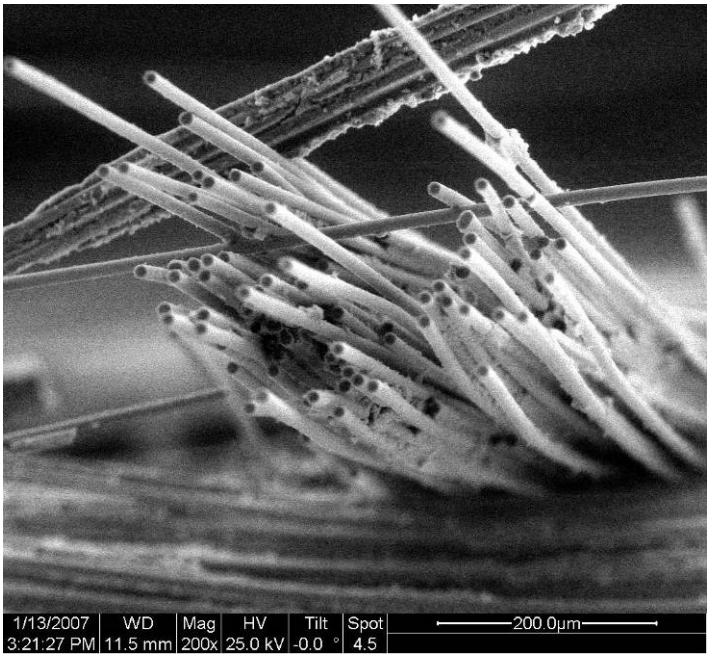

Figure 79. Fracture surface of N720/A specimen tested in creep at 150 MPa in air at 1000 °C.

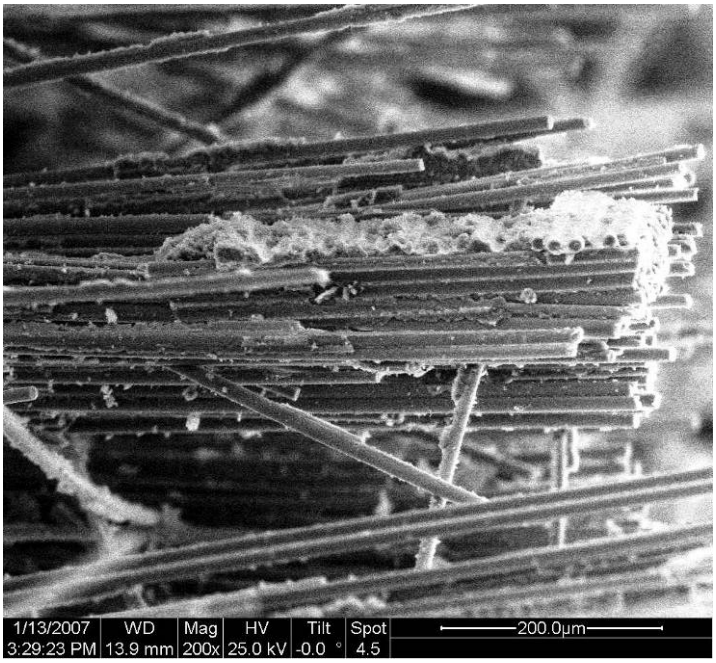

Figure 80. Fracture surface of N720/A specimen tested in creep at 150 MPa in air at 1000 °C.

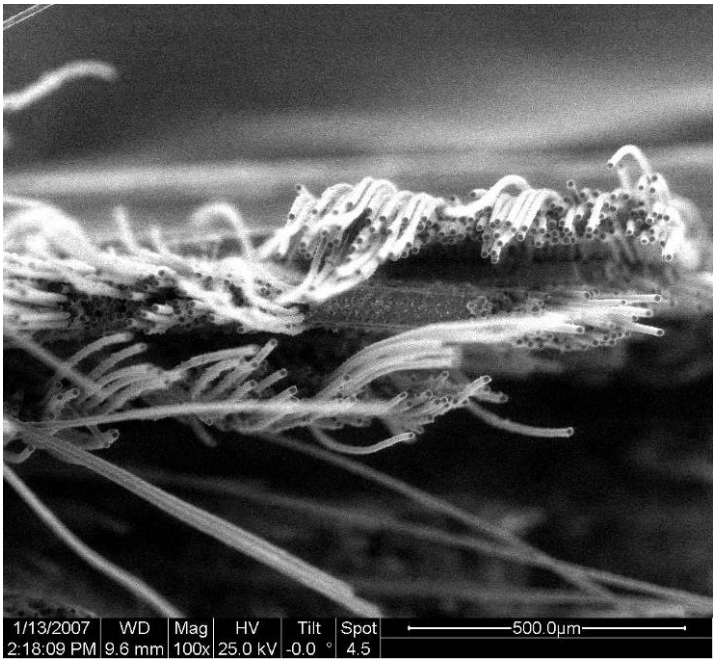

Figure 81. Fracture surface of N720/A specimen tested in creep at 150 MPa in air at 1000 °C.

Figure 82. Fracture surface of N720/A specimen tested in creep at 150 MPa in air at 1000 °C.

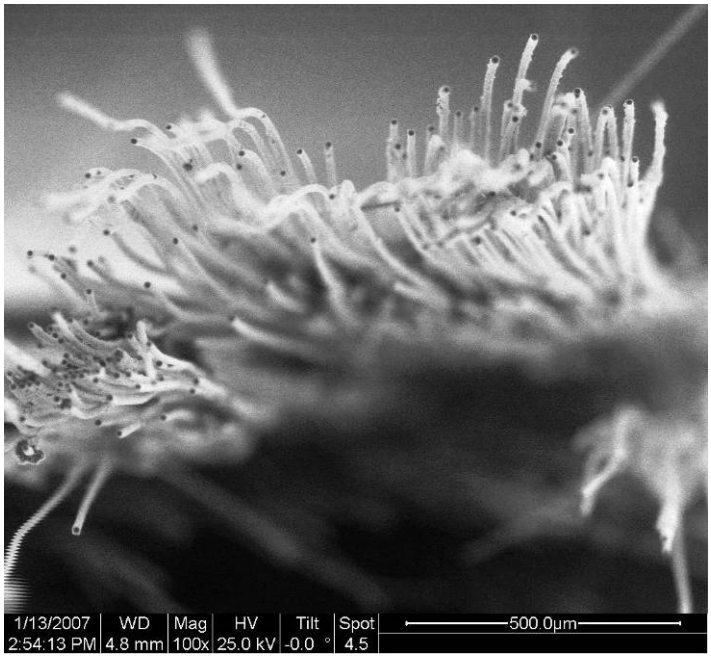

Figure 83. Fracture surface of N720/A specimen tested in creep at 150 MPa in air at 1000 °C.

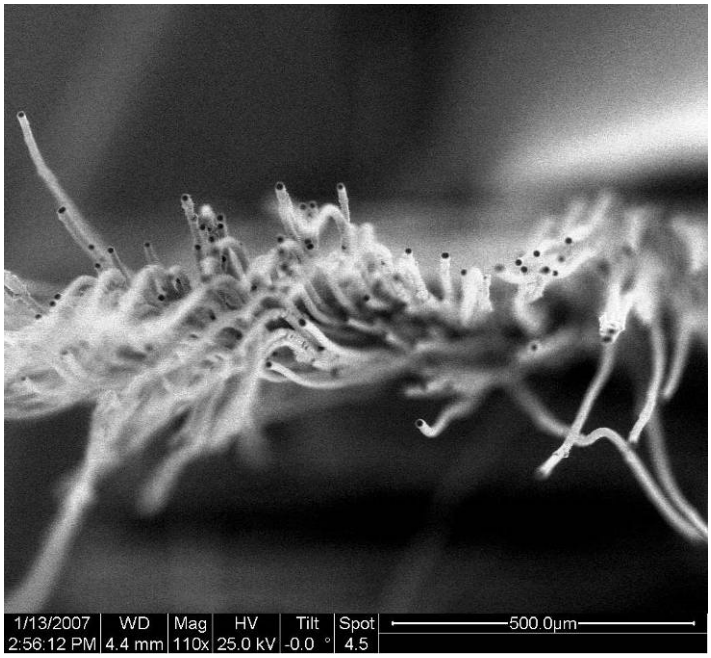

Figure 84. Fracture surface of N720/A specimen tested in creep at 150 MPa in air at 1000 °C.

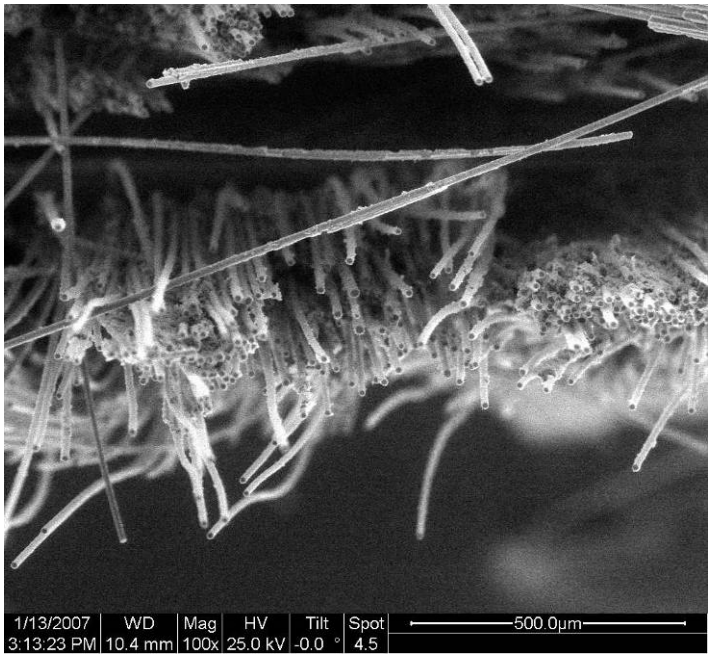

Figure 85. Fracture surface of N720/A specimen tested in creep at 150 MPa in air at 1000 °C.

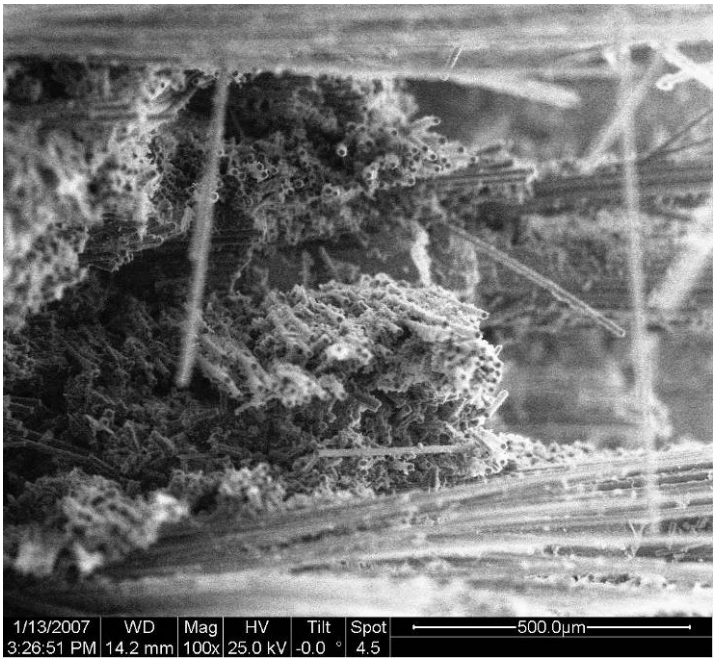

Figure 86. Fracture surface of N720/A specimen tested in creep at 150 MPa in air at 1000 °C.

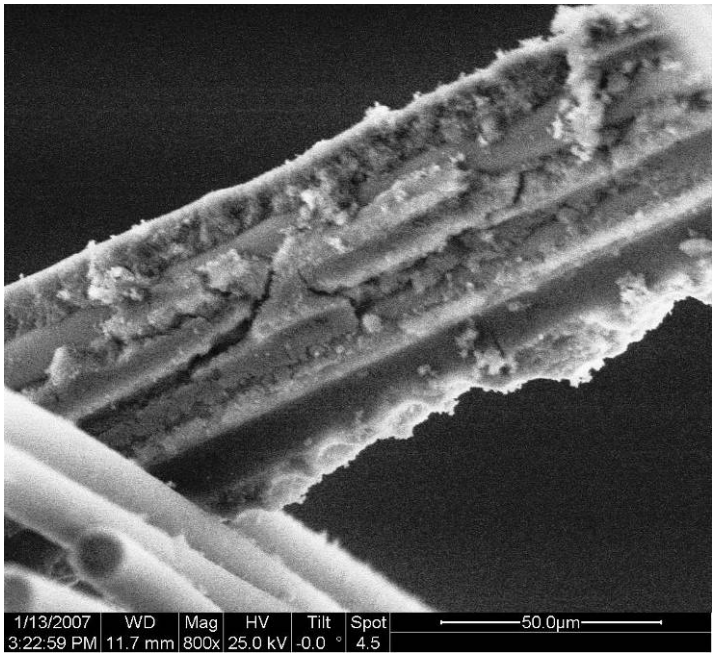

Figure 87. Fracture surface of N720/A specimen tested in creep at 150 MPa in air at 1000 °C.

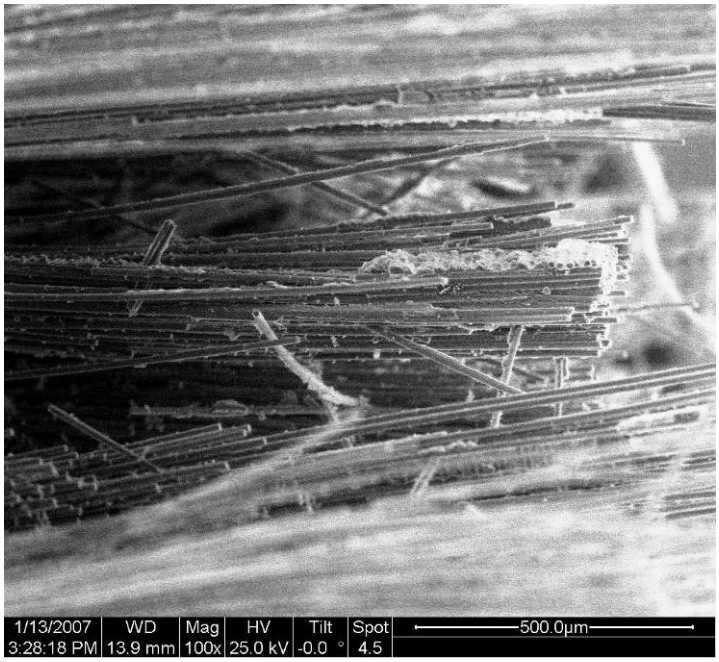

Figure 88. Fracture surface of N720/A specimen tested in creep at 150 MPa in air at 1000 °C.

Figure 89. Fracture surface of N720/A specimen tested in creep at 150 MPa in air at 1000 °C.

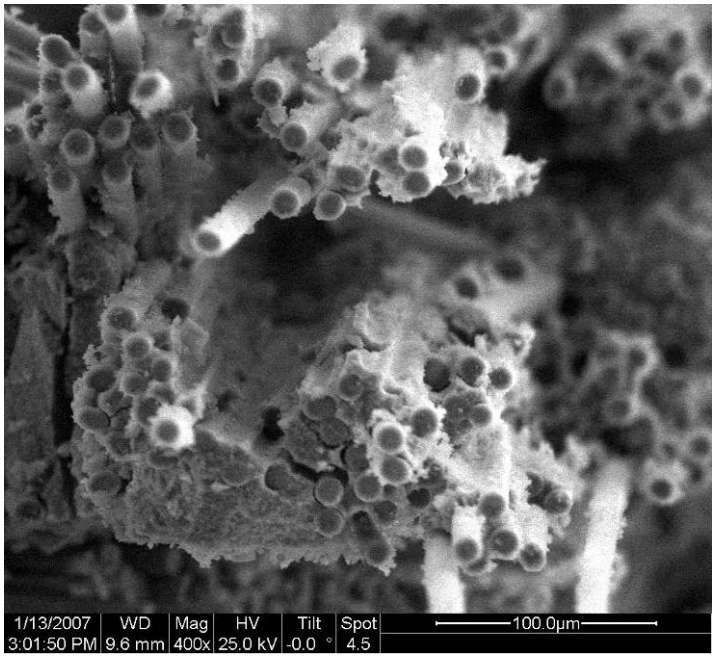

Figure 90. Fracture surface of N720/A specimen tested in creep at 150 MPa in air at 1000 °C.

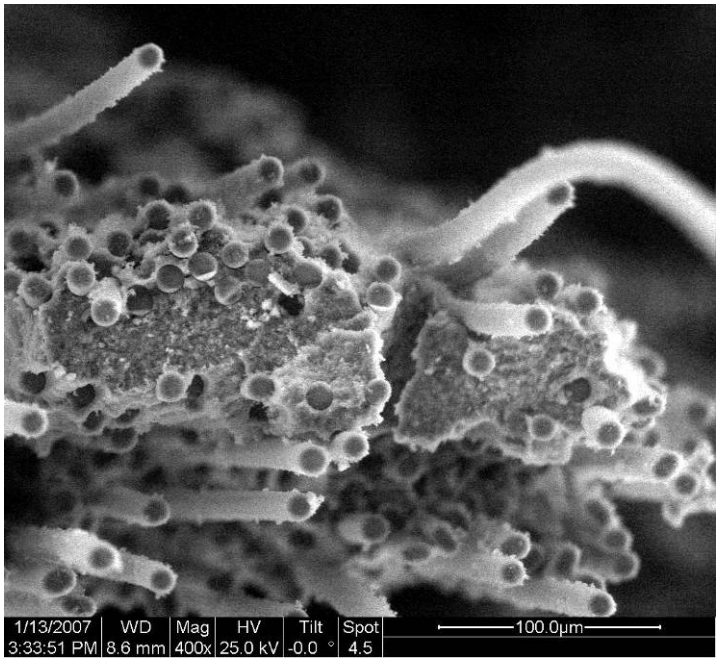

Figure 91. Fracture surface of N720/A specimen tested in creep at 150 MPa in air at 1000 °C.

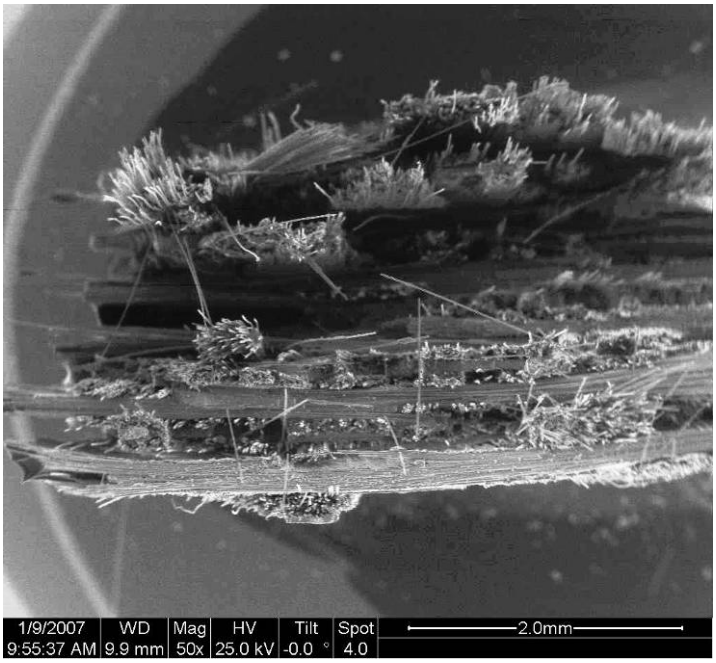

Figure 92. Fracture surface of N720/A specimen tested in tension in air at 1000 °C.

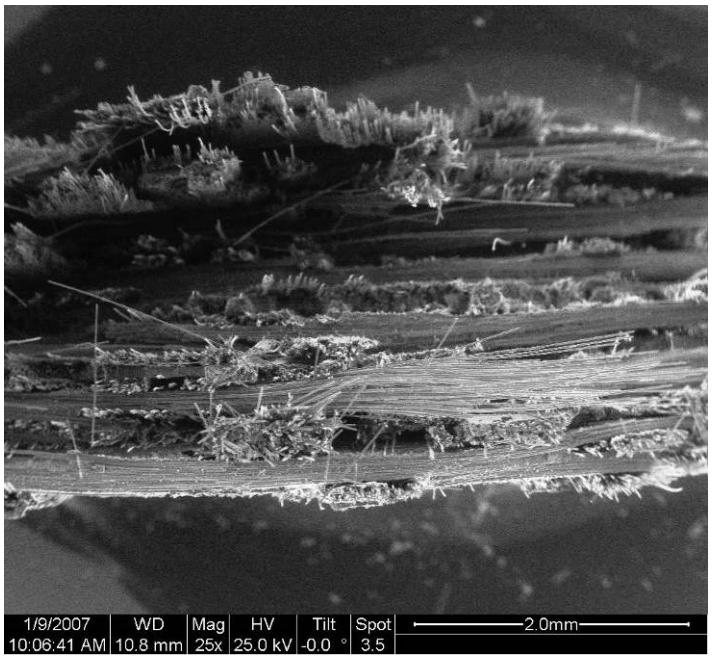

Figure 93. Fracture surface of N720/A specimen tested in tension in air at 1000 °C.

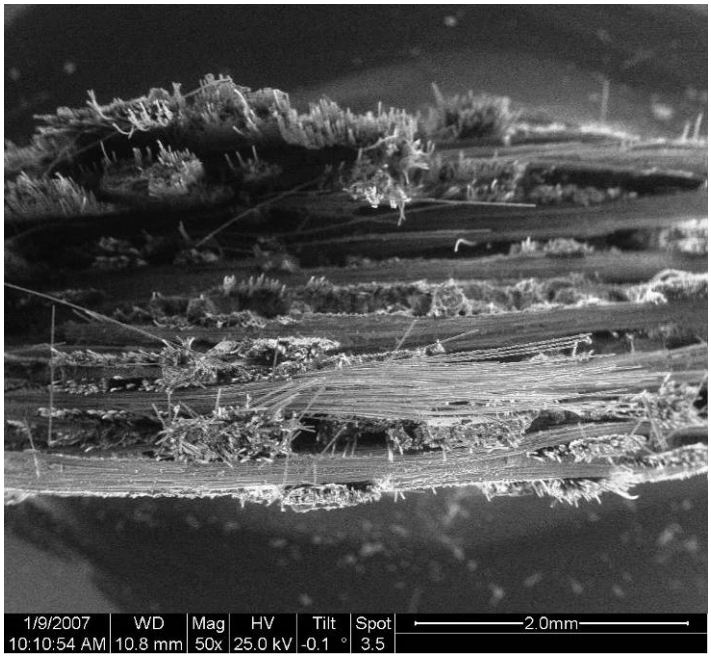

Figure 94. Fracture surface of N720/A specimen tested in tension in air at 1000 °C.

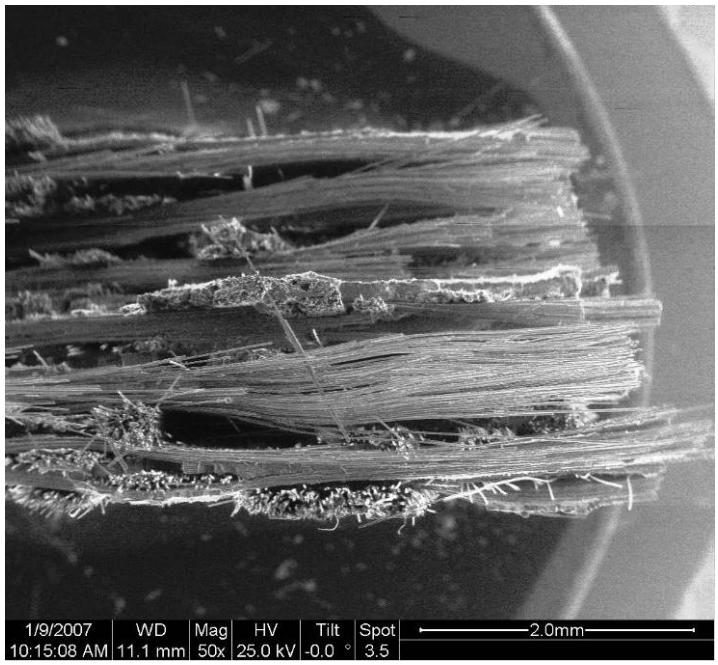

Figure 95. Fracture surface of N720/A specimen tested in tension in air at 1000 °C.

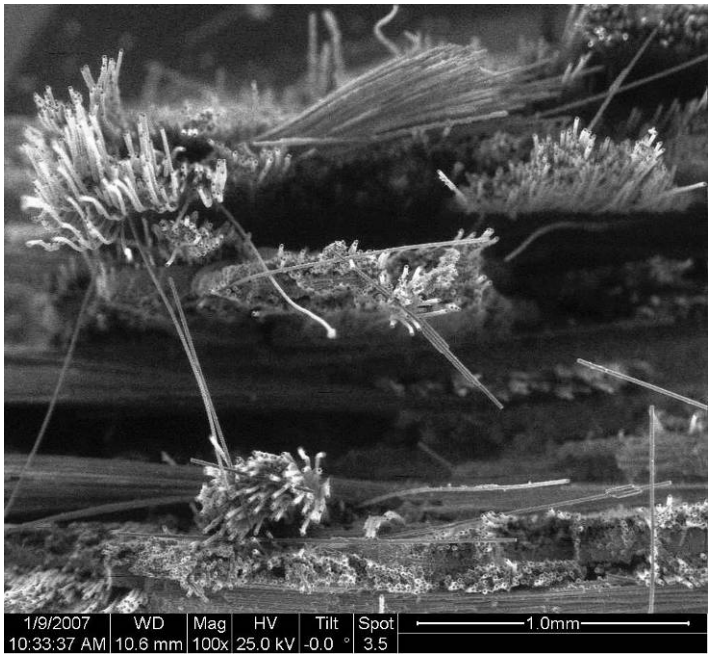

Figure 96. Fracture surface of N720/A specimen tested in tension in air at 1000 °C.

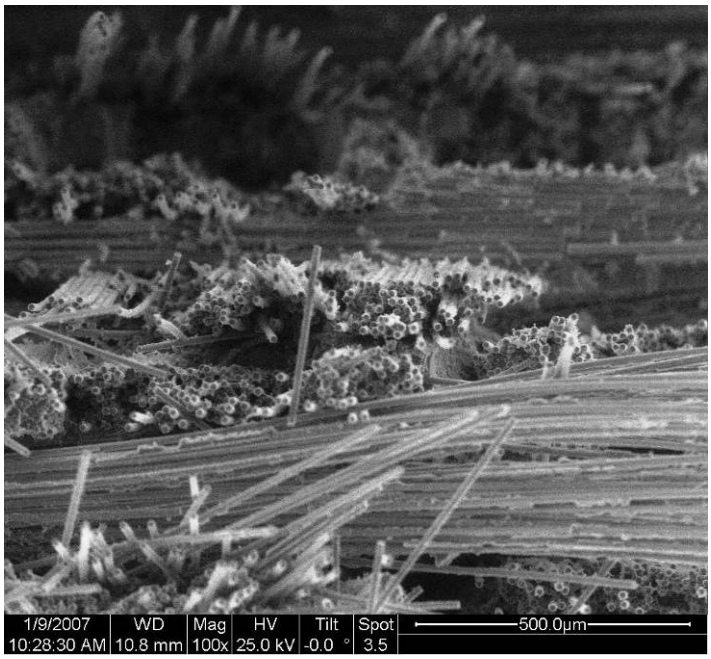

Figure 97. Fracture surface of N720/A specimen tested in tension in air at 1000 °C.

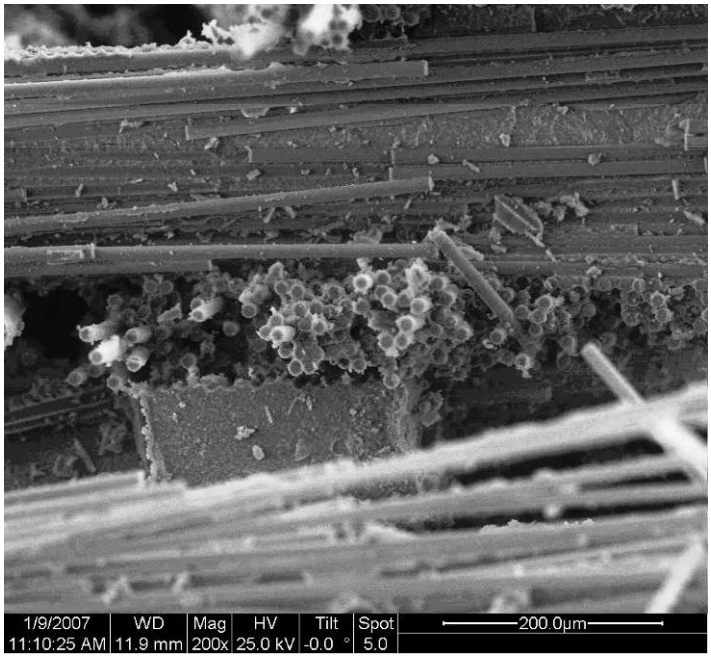

Figure 98. Fracture surface of N720/A specimen tested in tension in air at 1000 °C.

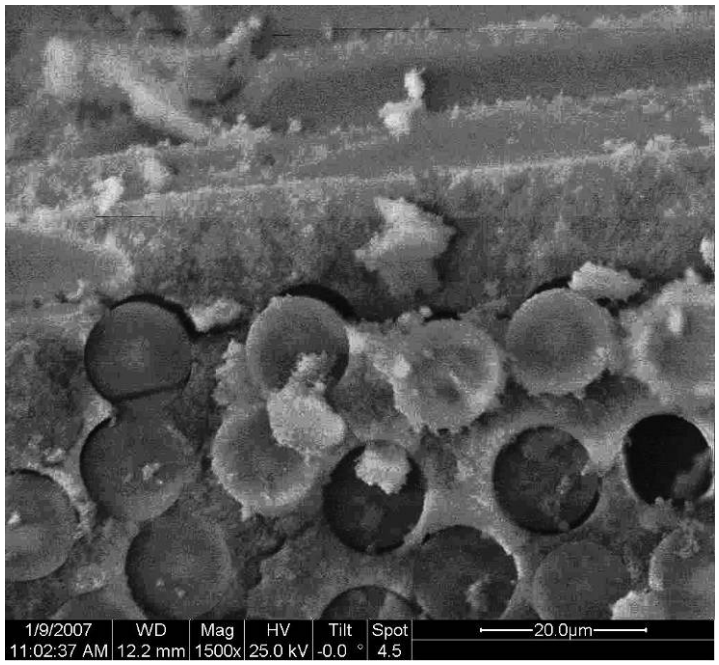

Figure 99. Fracture surface of N720/A specimen tested in tension in air at 1000 °C.

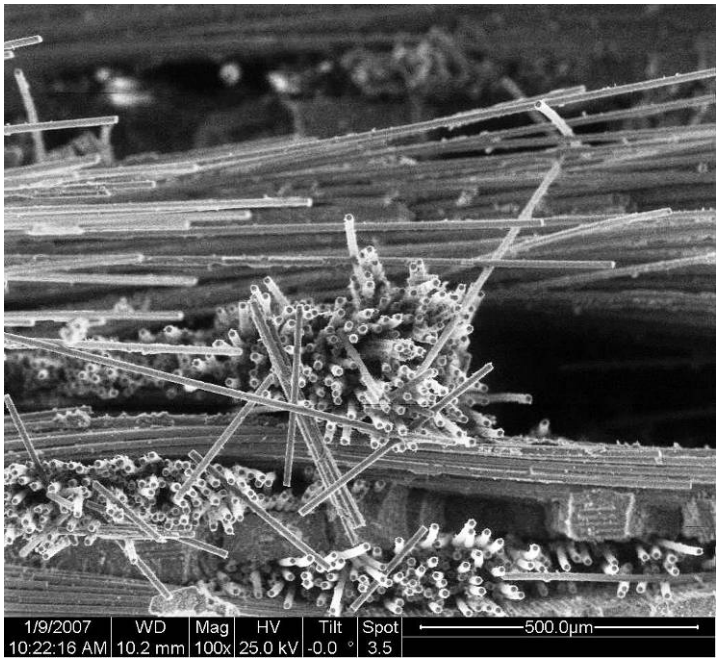

Figure 100. Fracture surface of N720/A specimen tested in tension in air at 1000 °C.

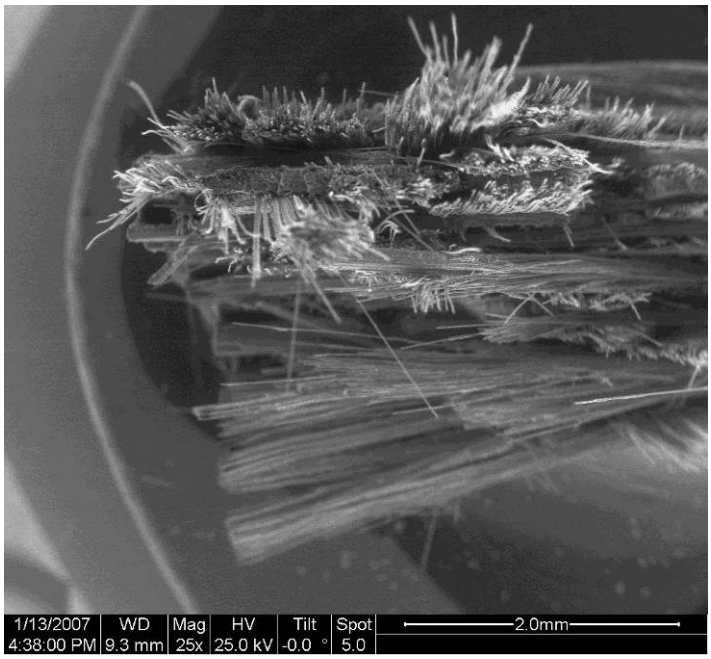

Figure 101. Fracture surface of N720/A specimen tested in creep at 135 MPa in steam at 1000 °C.

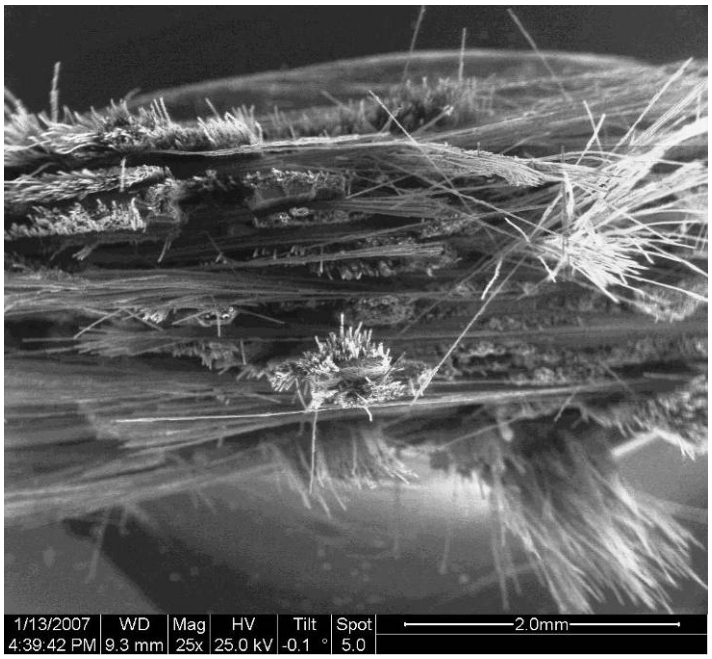

Figure 102. Fracture surface of N720/A specimen tested in creep at 135 MPa in steam at 1000 °C.

Figure 103. Fracture surface of N720/A specimen tested in creep at 135 MPa in steam at 1000 °C.

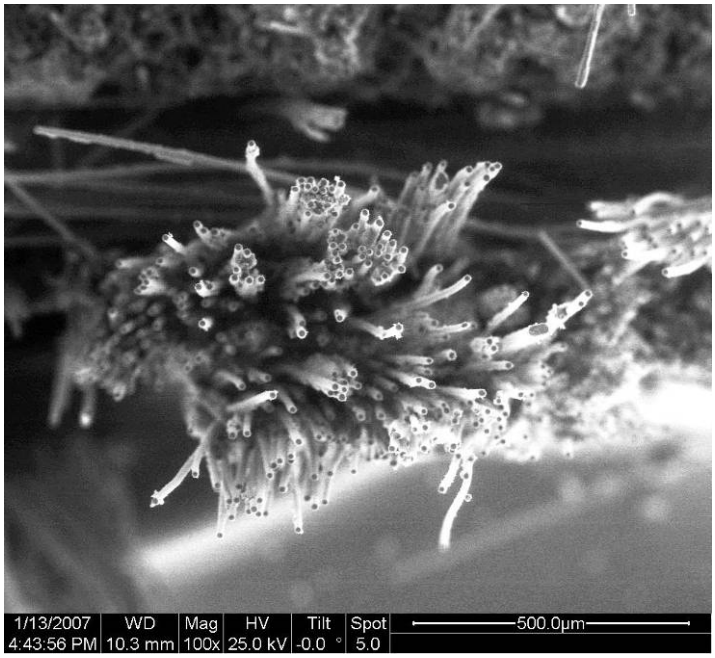

Figure 104. Fracture surface of N720/A specimen tested in creep at 135 MPa in steam at 1000 °C.

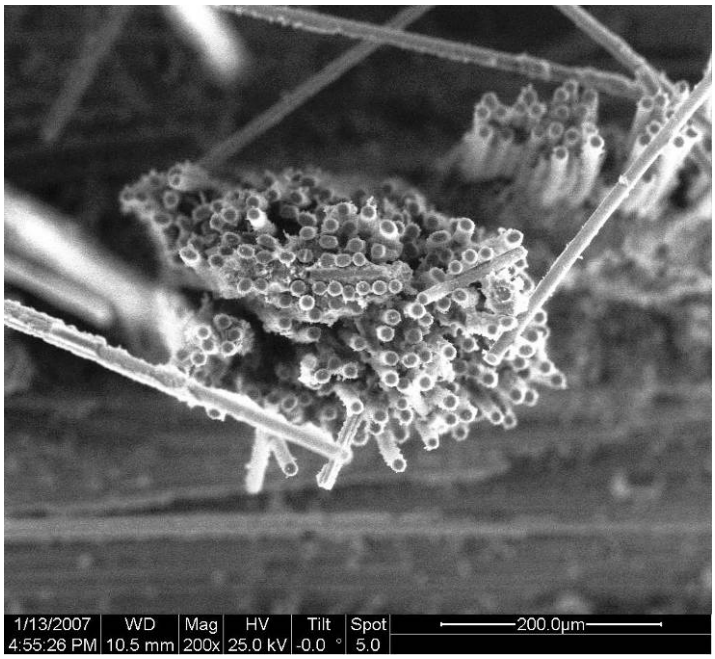

Figure 105. Fracture surface of N720/A specimen tested in creep at 135 MPa in steam at 1000 °C.

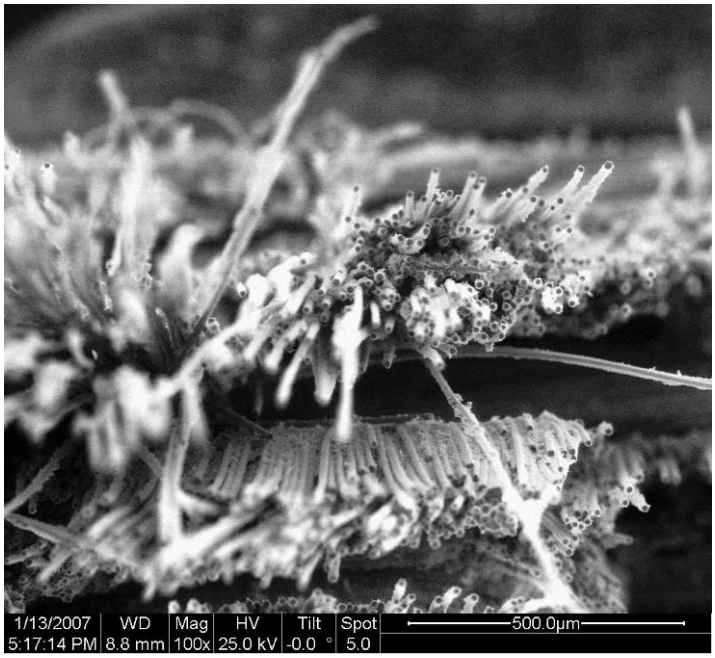

Figure 106. Fracture surface of N720/A specimen tested in creep at 135 MPa in steam at 1000 °C.

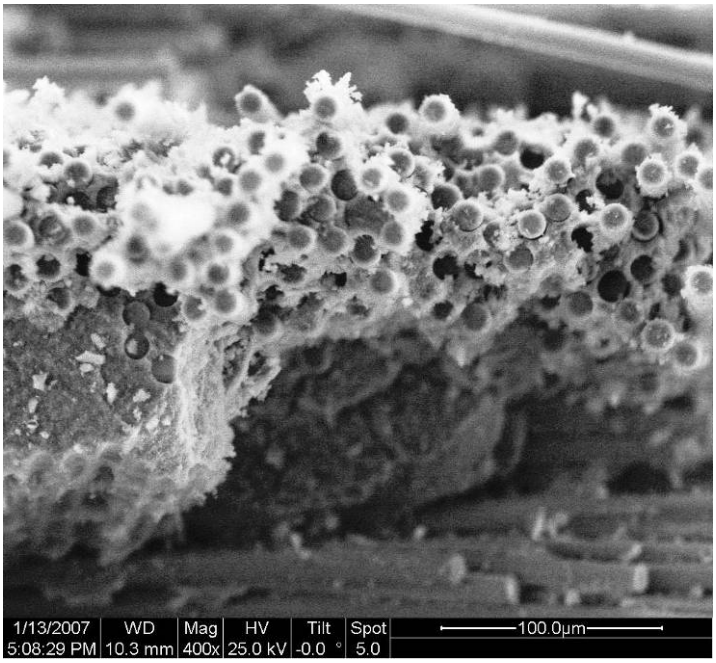

Figure 107. Fracture surface of N720/A specimen tested in creep at 135 MPa in steam at 1000 °C.

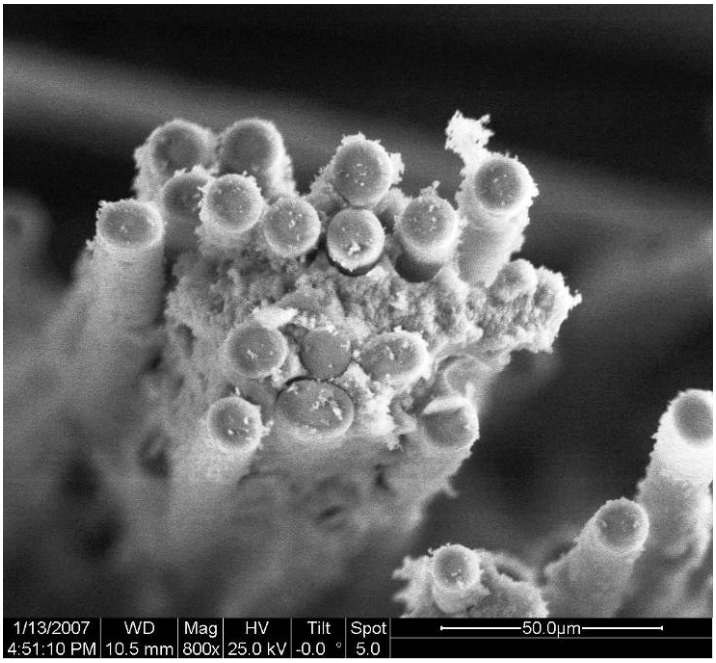

Figure 108. Fracture surface of N720/A specimen tested in creep at 135 MPa in steam at 1000 °C.

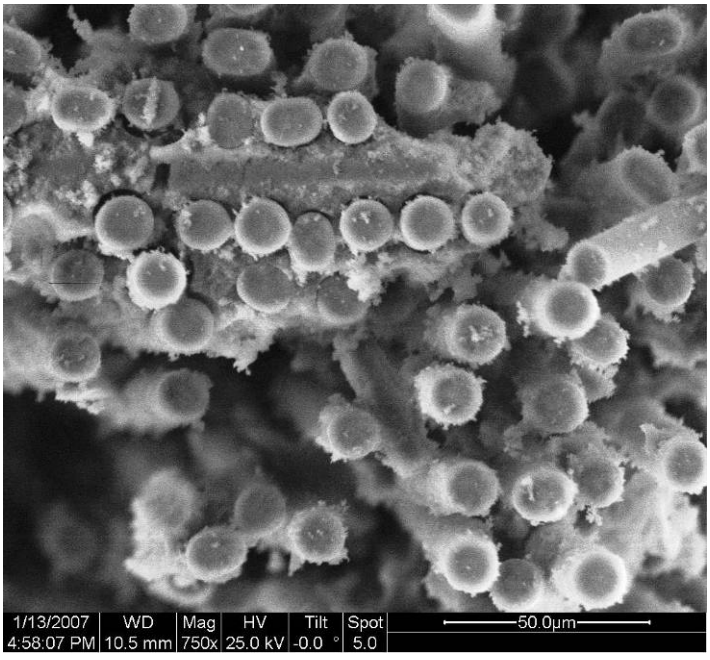

Figure 109. Fracture surface of N720/A specimen tested in creep at 135 MPa in steam at 1000 °C.

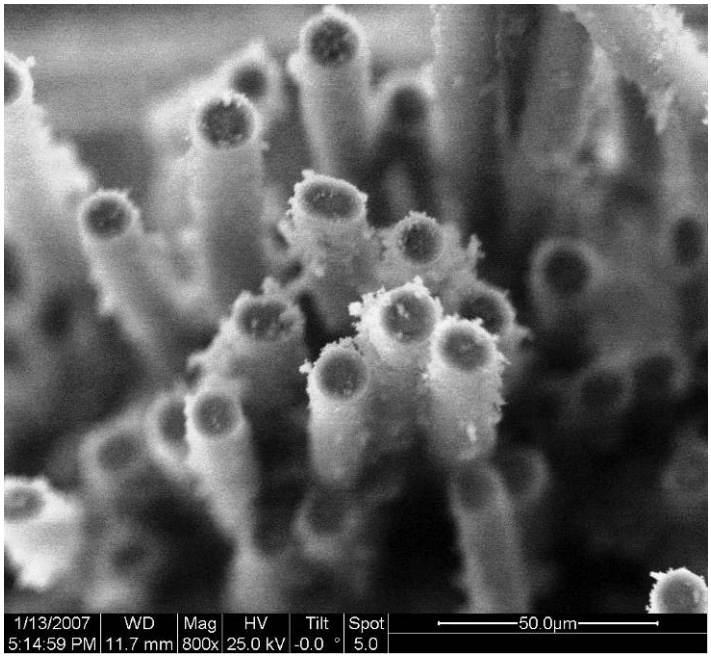

Figure 110. Fracture surface of N720/A specimen tested in creep at 135 MPa in steam at 1000 °C.

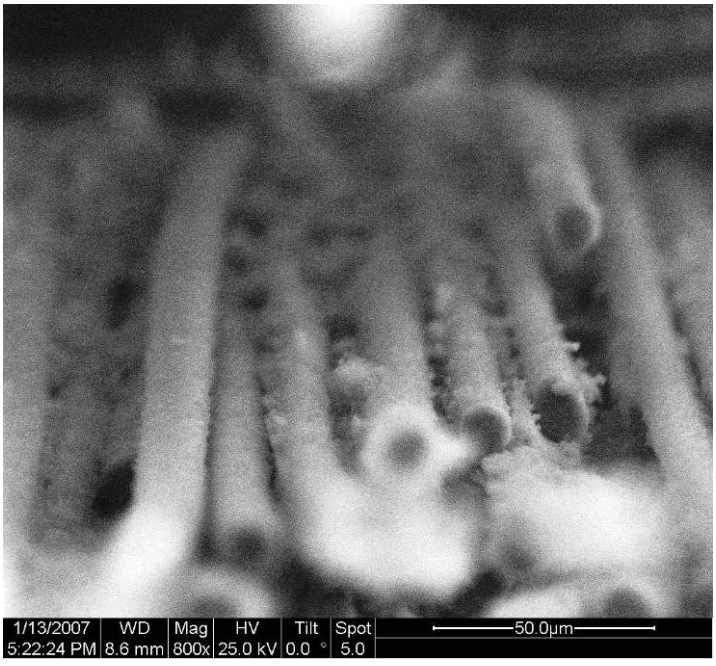

Figure 111. Fracture surface of N720/A specimen tested in creep at 135 MPa in steam at 1000 °C.

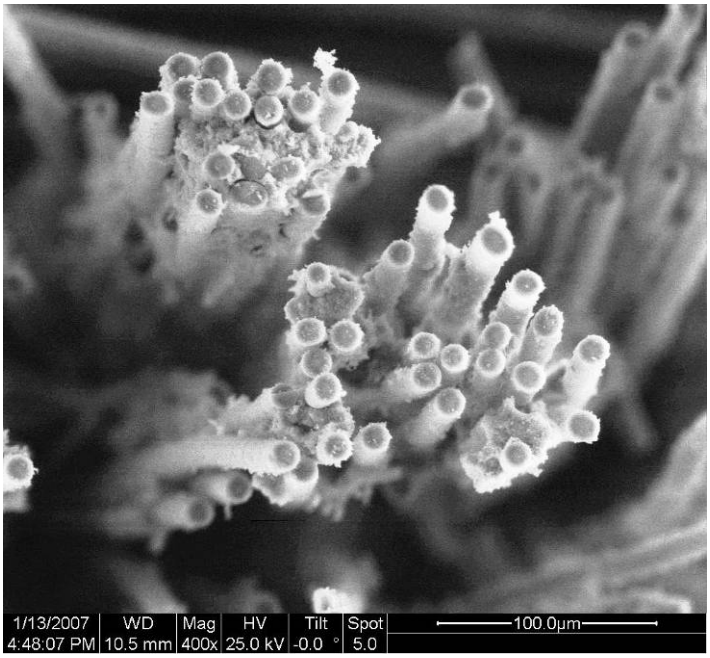

Figure 112. Fracture surface of N720/A specimen tested in creep at 135 MPa in steam at 1000 °C.

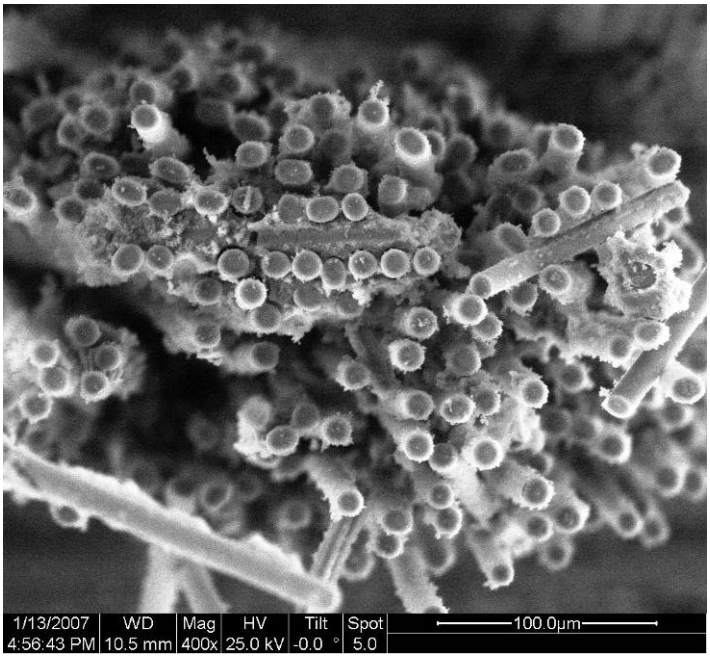

Figure 113. Fracture surface of N720/A specimen tested in creep at 135 MPa in steam at 1000 °C.

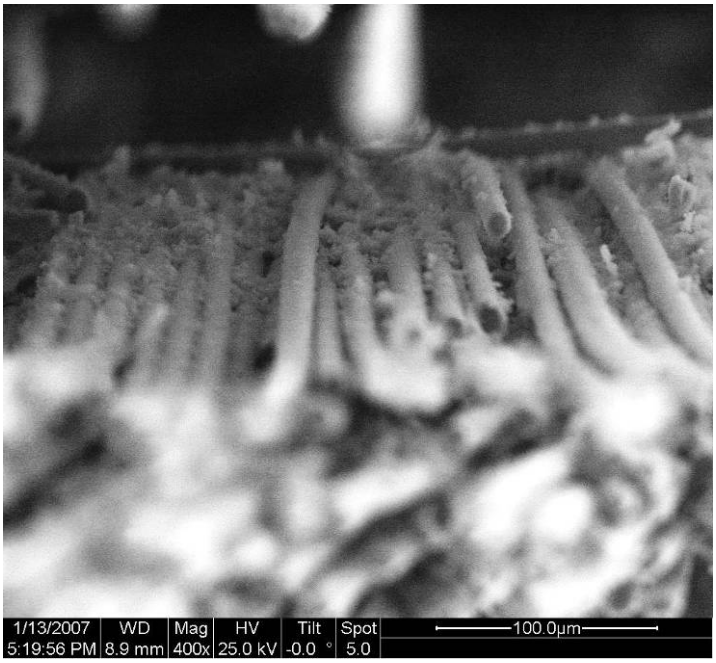

Figure 114. Fracture surface of N720/A specimen tested in creep at 135 MPa in steam at 1000 °C.

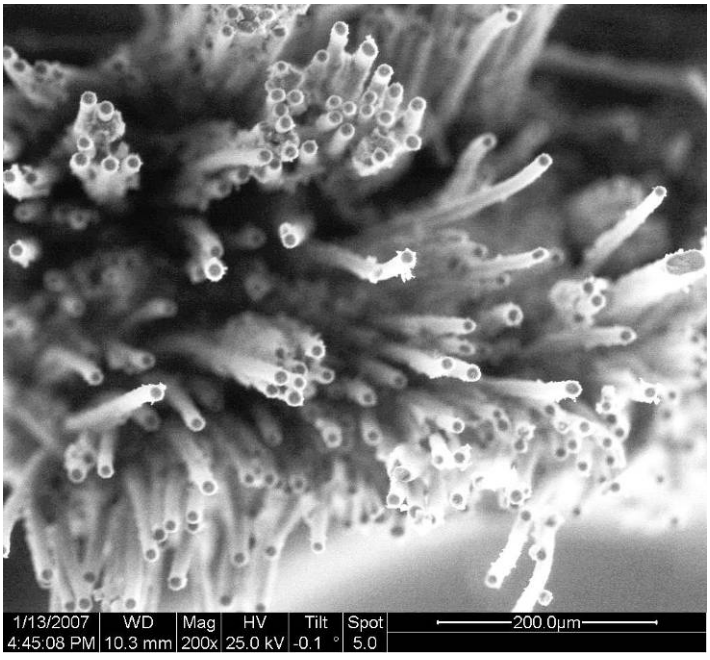

Figure 115. Fracture surface of N720/A specimen tested in creep at 135 MPa in steam at 1000 °C.

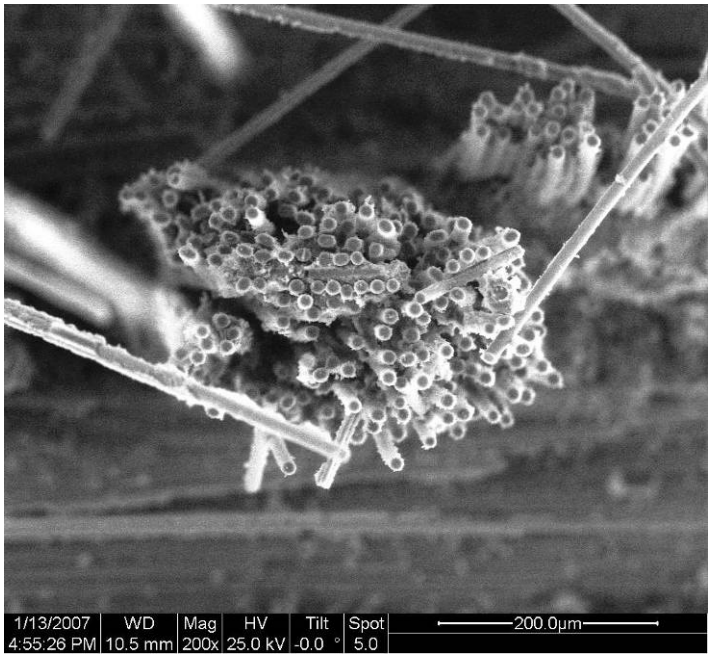

Figure 116. Fracture surface of N720/A specimen tested in creep at 135 MPa in steam at 1000 °C.

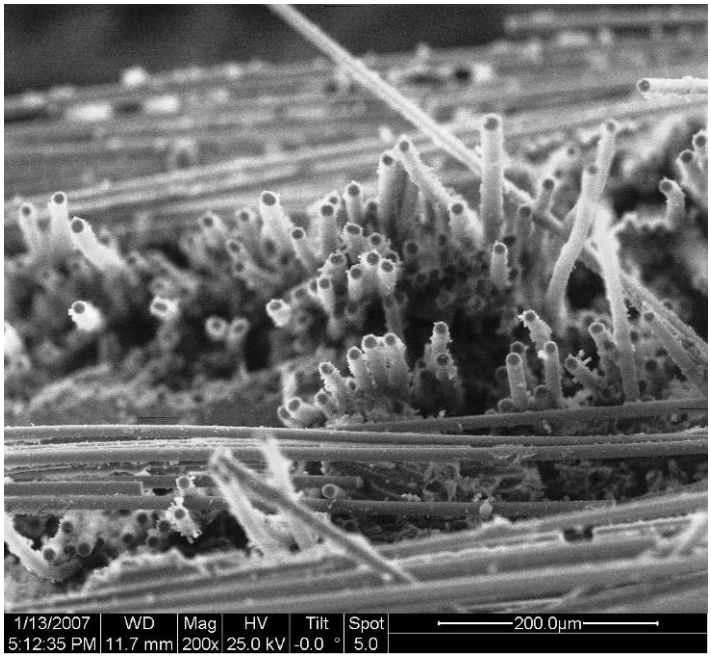

Figure 117. Fracture surface of N720/A specimen tested in creep at 135 MPa in steam at 1000 °C.

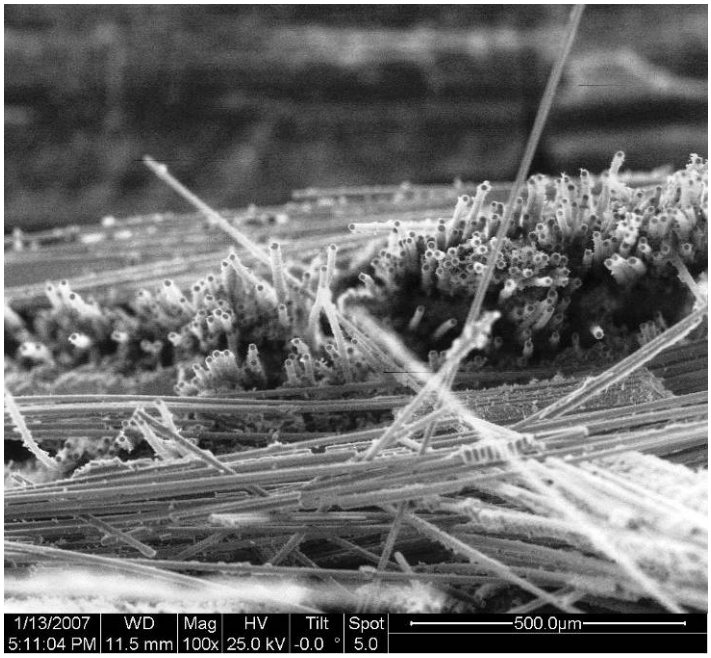

Figure 118. Fracture surface of N720/A specimen tested in creep at 135 MPa in steam at 1000 °C.

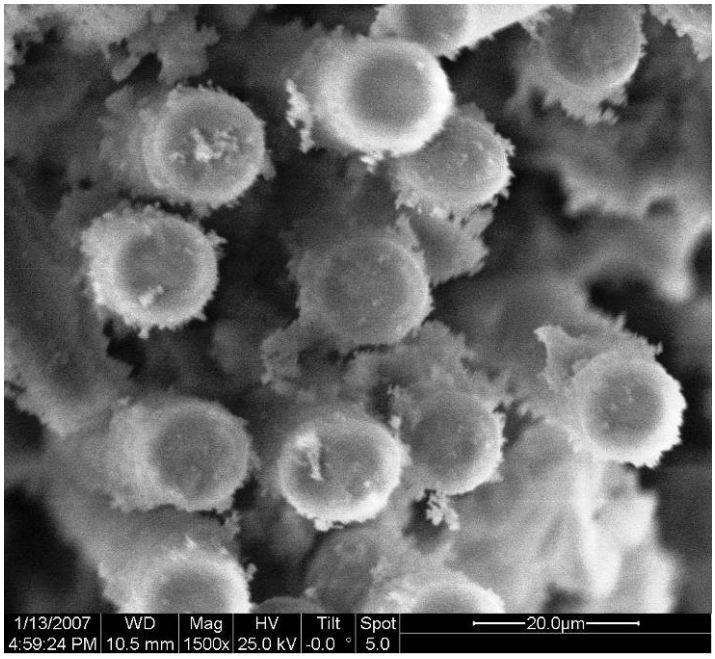

Figure 119. Fracture surface of N720/A specimen tested in creep at 135 MPa in steam at 1000 °C.

Figure 120. Fracture surface of N720/A specimen tested in creep at 150 MPa in steam at 1000 °C.

Figure 121. Fracture surface of N720/A specimen tested in creep at 150 MPa in steam at 1000 °C.

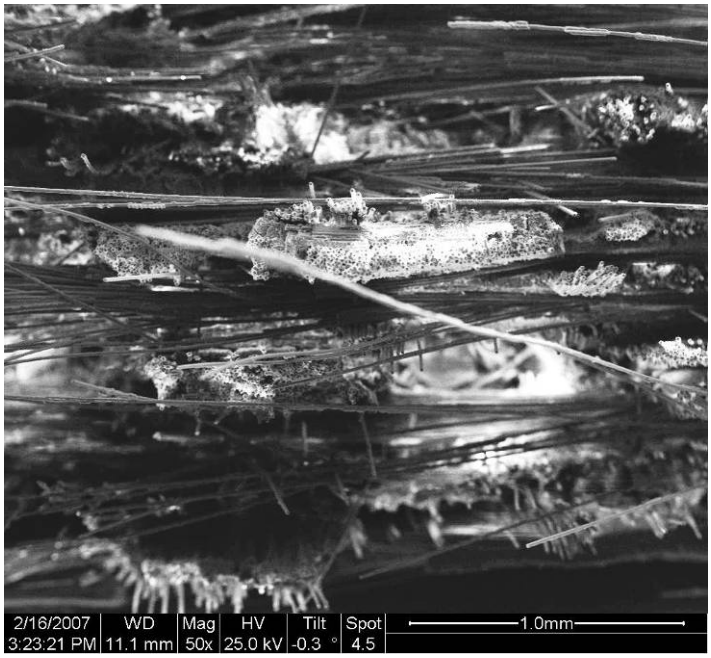

Figure 122. Fracture surface of N720/A specimen tested in creep at 150 MPa in steam at 1000 °C.

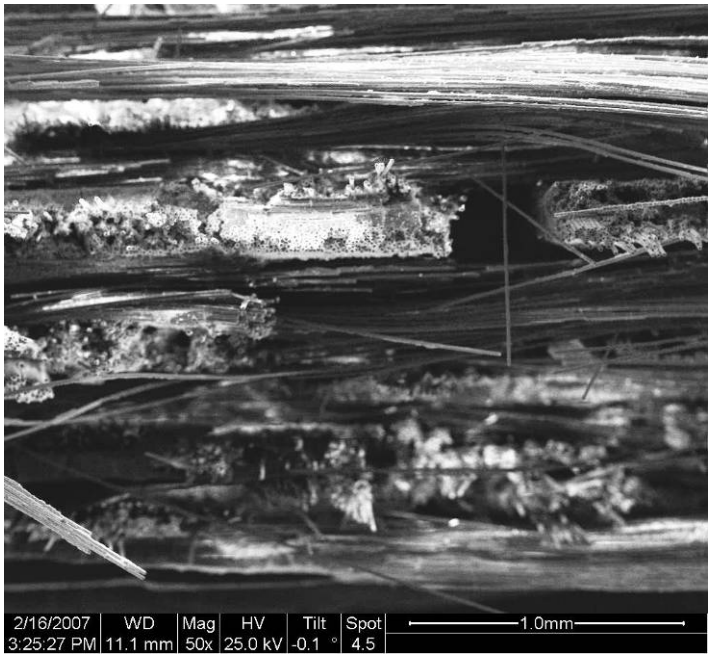

Figure 123. Fracture surface of N720/A specimen tested in creep at 150 MPa in steam at 1000 °C.

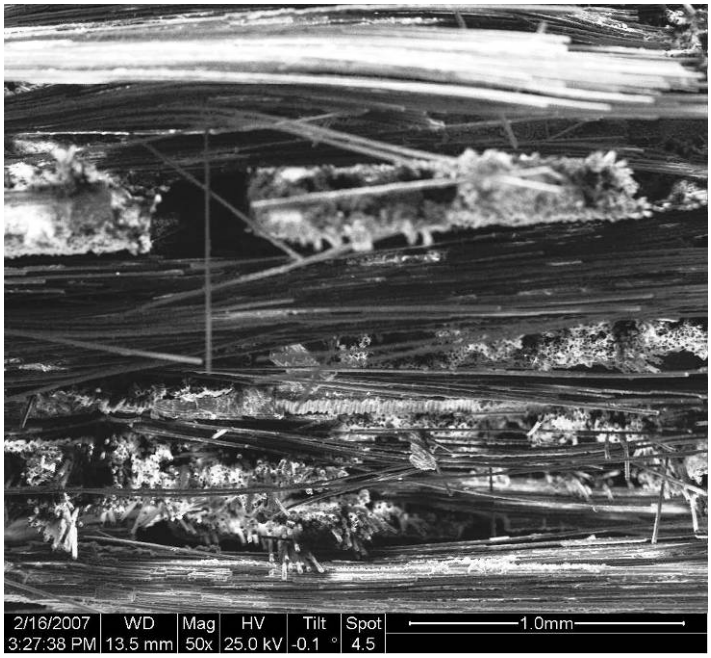

Figure 124. Fracture surface of N720/A specimen tested in creep at 150 MPa in steam at 1000 °C.

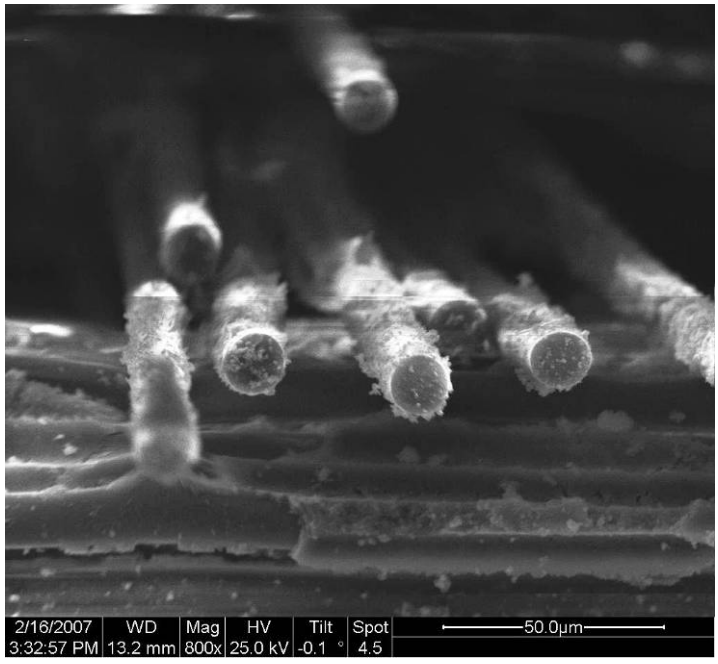

Figure 125. Fracture surface of N720/A specimen tested in creep at 150 MPa in steam at 1000 °C.

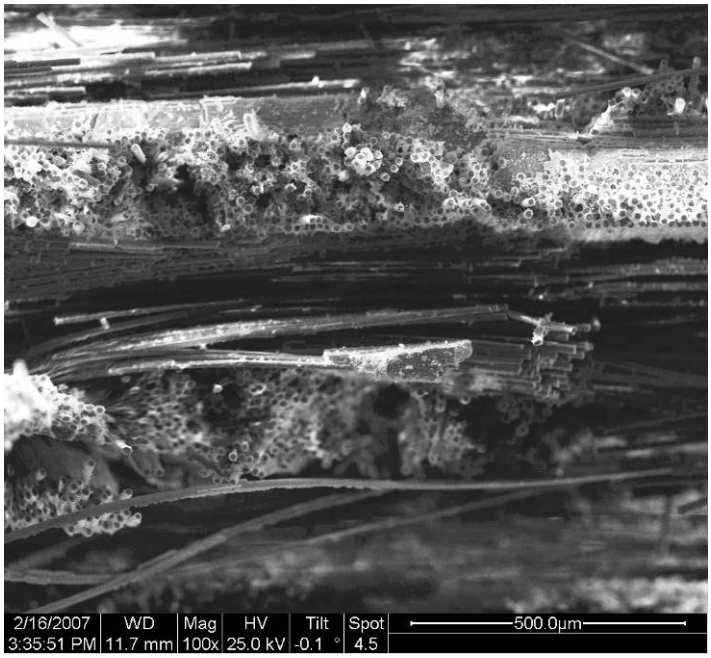

Figure 126. Fracture surface of N720/A specimen tested in creep at 150 MPa in steam at 1000 °C.

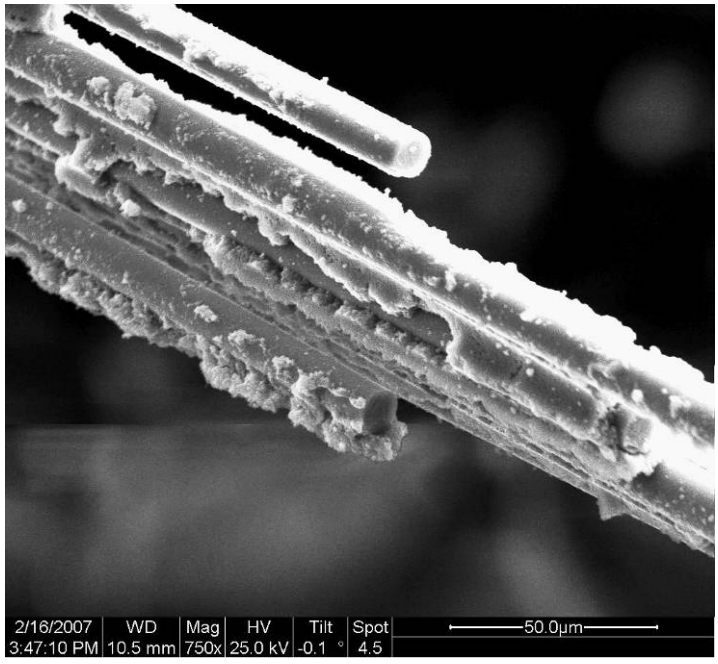

Figure 127. Fracture surface of N720/A specimen tested in creep at 150 MPa in steam at 1000 °C.

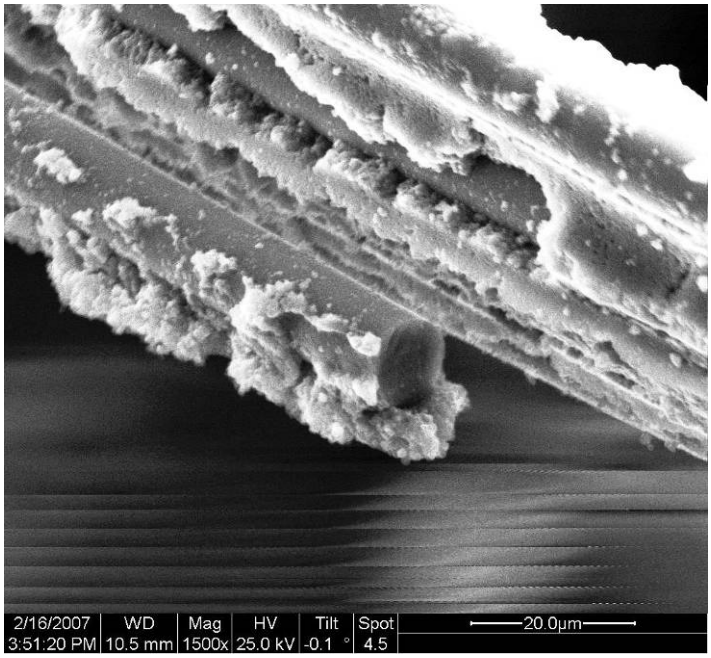

Figure 128. Fracture surface of N720/A specimen tested in creep at 150 MPa in steam at 1000 °C.

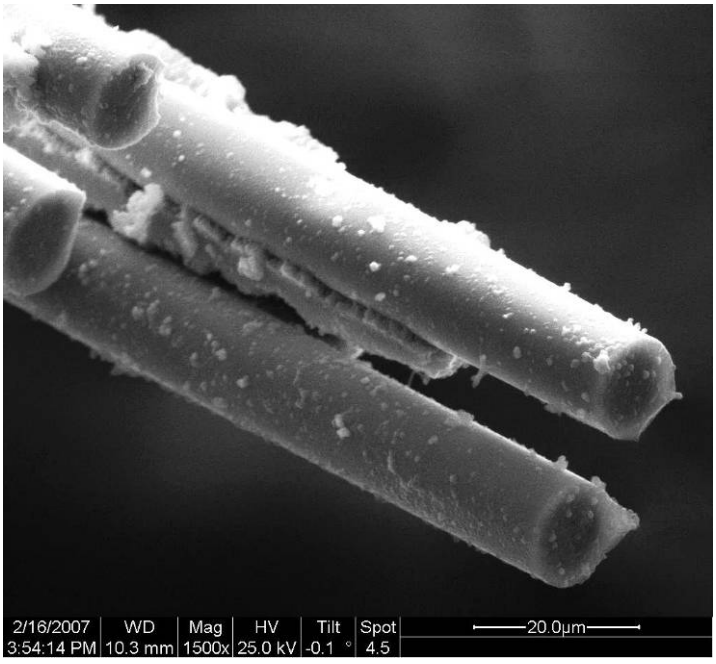

Figure 129. Fracture surface of N720/A specimen tested in creep at 150 MPa in steam at 1000 °C.

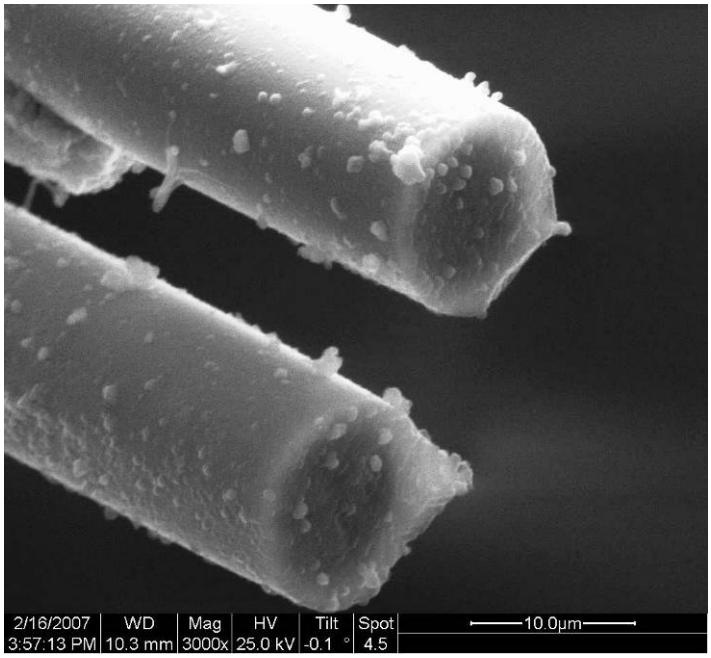

Figure 130. Fracture surface of N720/A specimen tested in creep at 150 MPa in steam at 1000 °C.

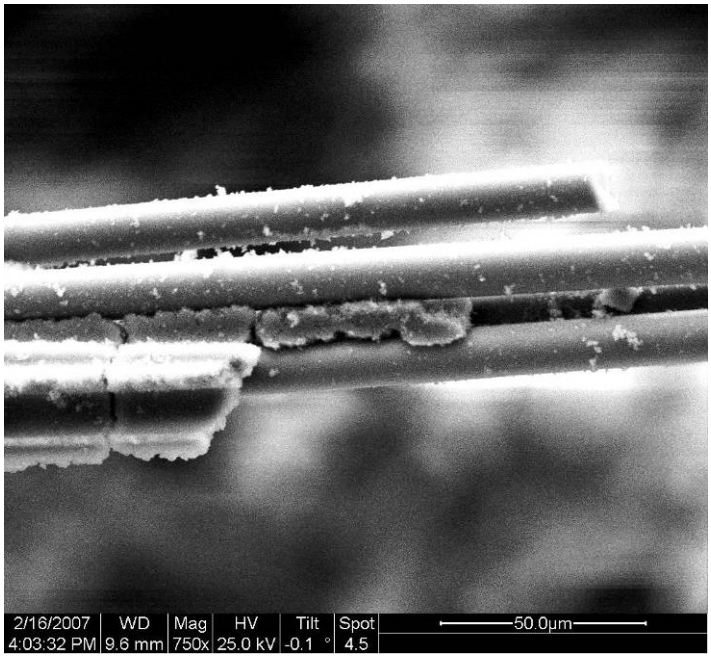

Figure 131. Fracture surface of N720/A specimen tested in creep at 150 MPa in steam at 1000 °C.

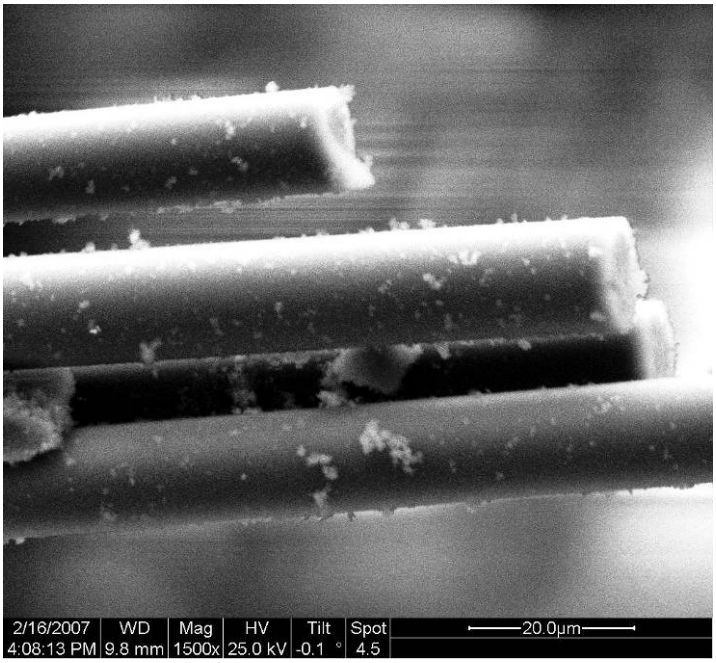

Figure 132. Fracture surface of N720/A specimen tested in creep at 150 MPa in steam at 1000 °C.

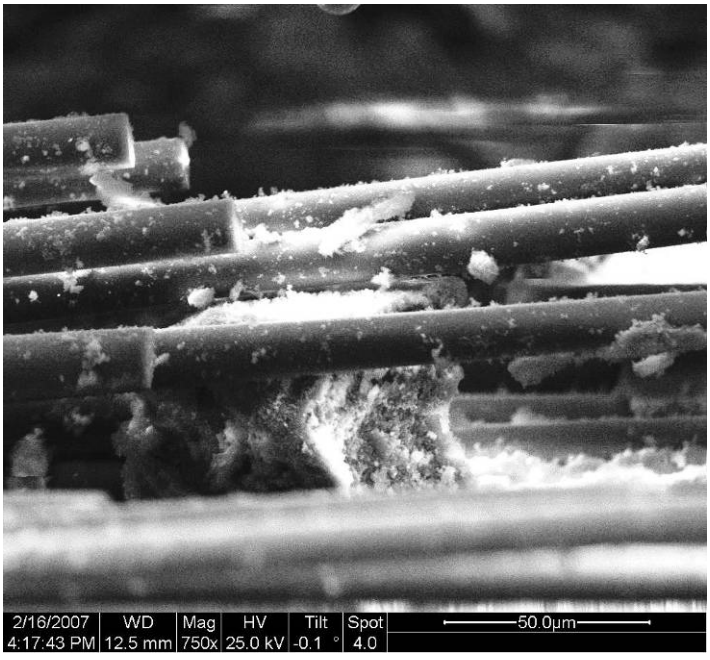

Figure 133. Fracture surface of N720/A specimen tested in creep at 150 MPa in steam at 1000 °C.

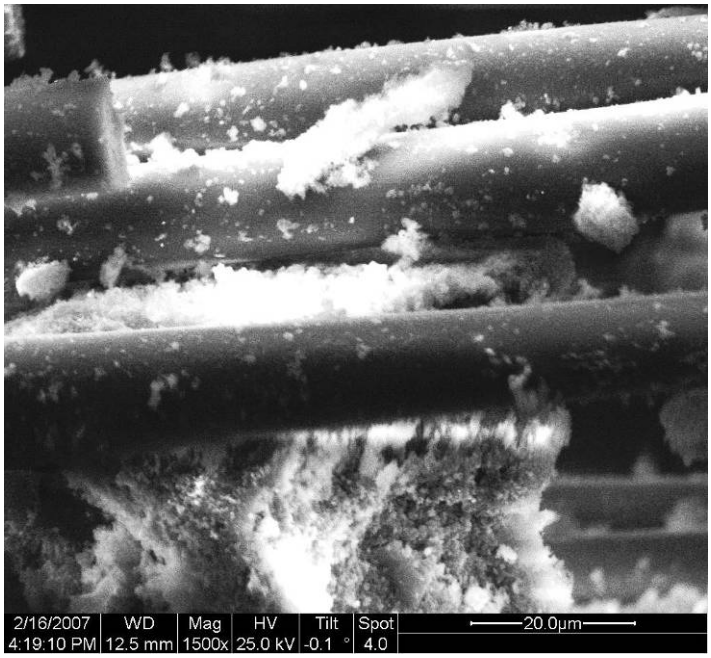

Figure 134. Fracture surface of N720/A specimen tested in creep at 150 MPa in steam at 1000 °C.

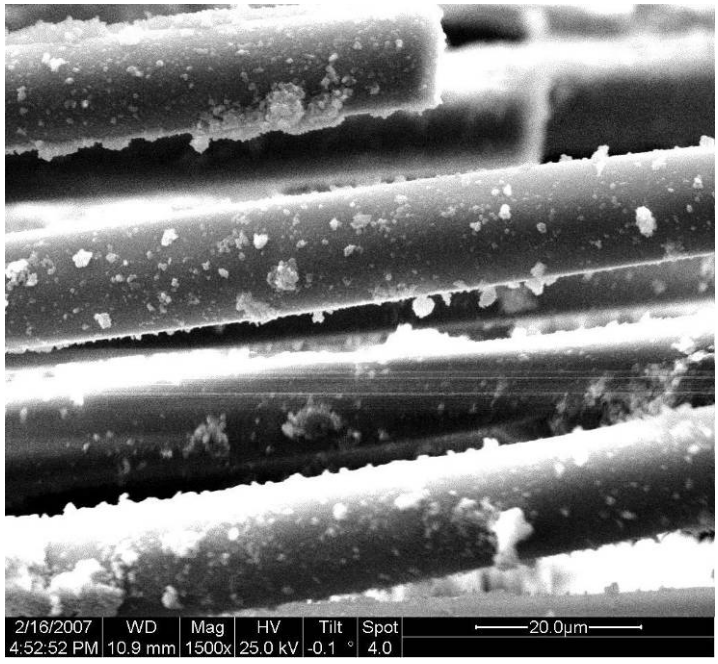

Figure 135. Fracture surface of N720/A specimen tested in creep at 150 MPa in steam at 1000 °C.

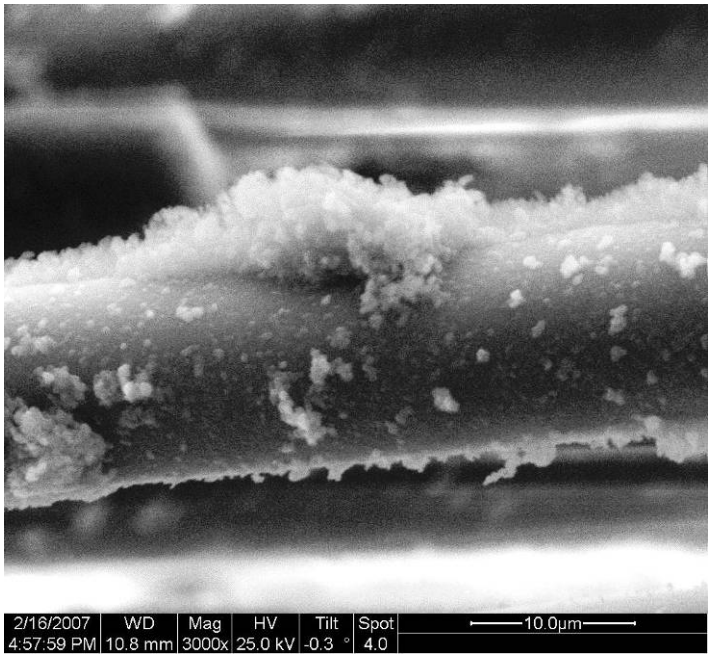

Figure 136. Fracture surface of N720/A specimen tested in creep at 150 MPa in steam at 1000 °C.

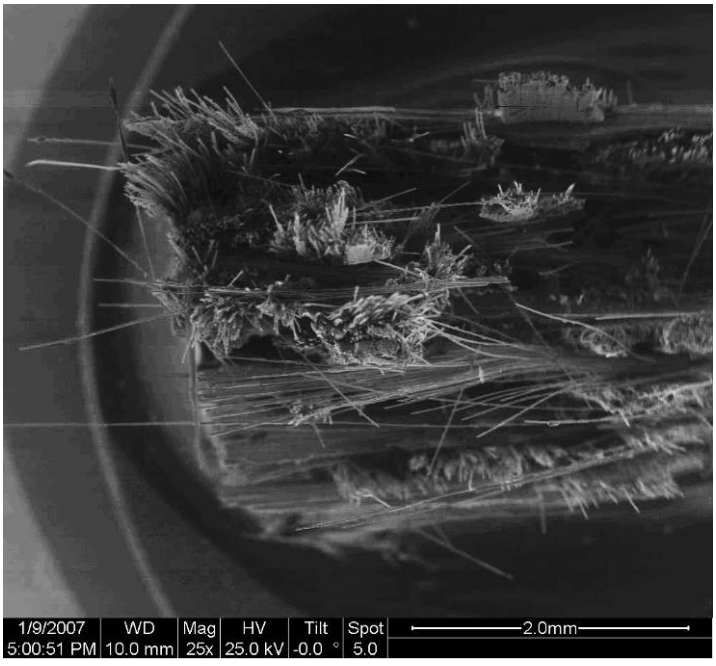

Figure 137. Fracture surface of N720/A specimen tested in creep at 150 MPa in steam at 1000 °C.

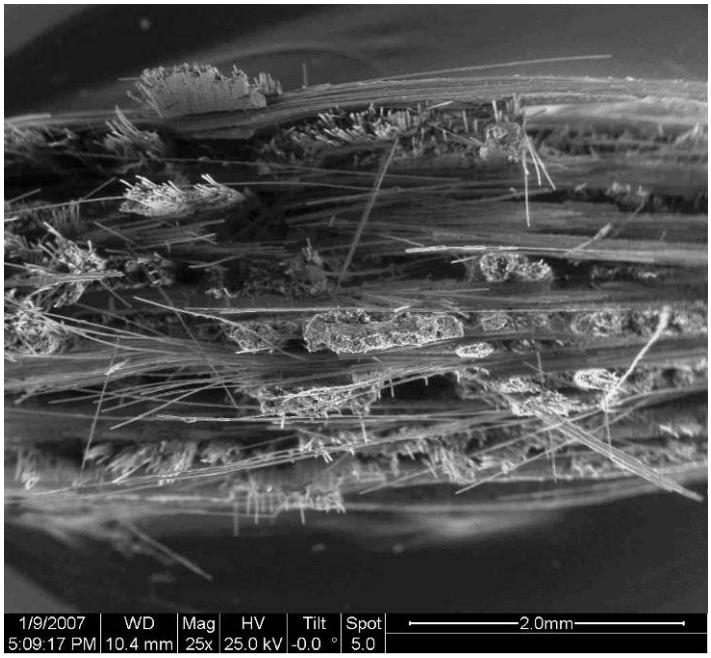

Figure 138. Fracture surface of N720/A specimen tested in creep at 150 MPa in steam at 1000 °C.

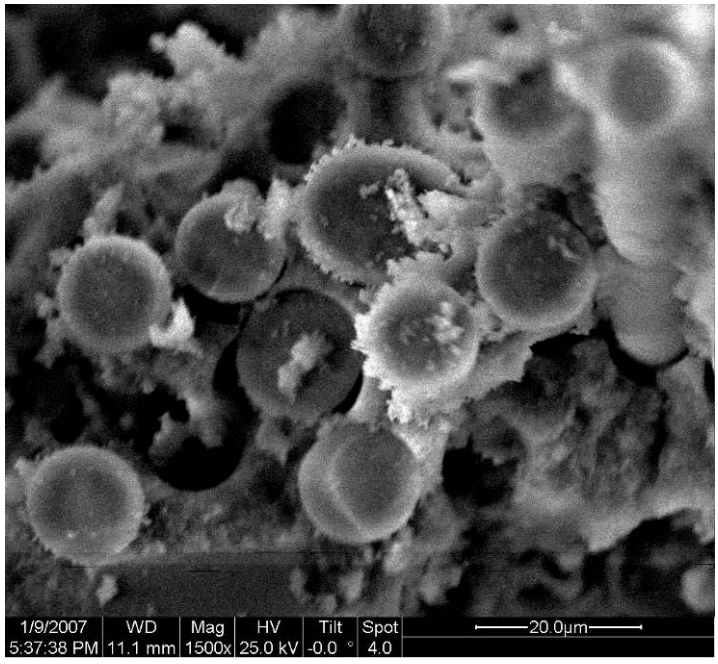

Figure 139. Fracture surface of N720/A specimen tested in creep at 150 MPa in steam at 1000 °C.

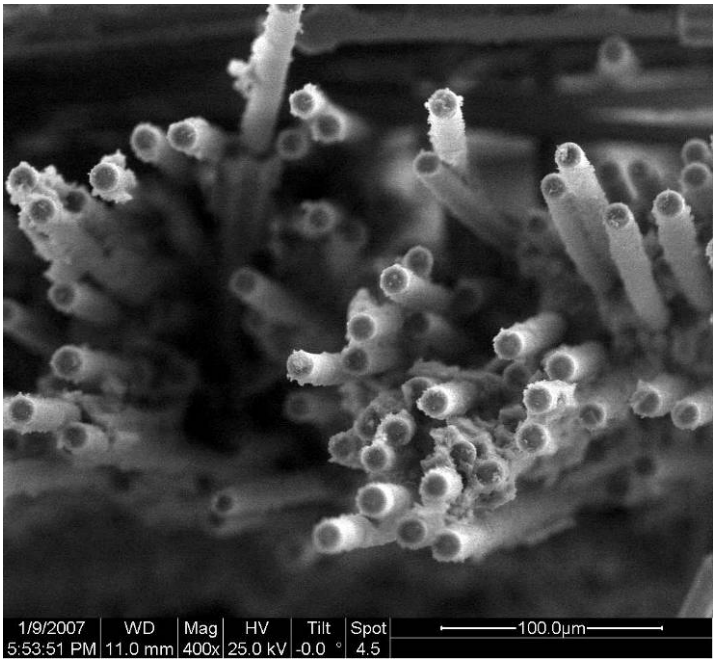

Figure 140. Fracture surface of N720/A specimen tested in creep at 150 MPa in steam at 1000 °C.

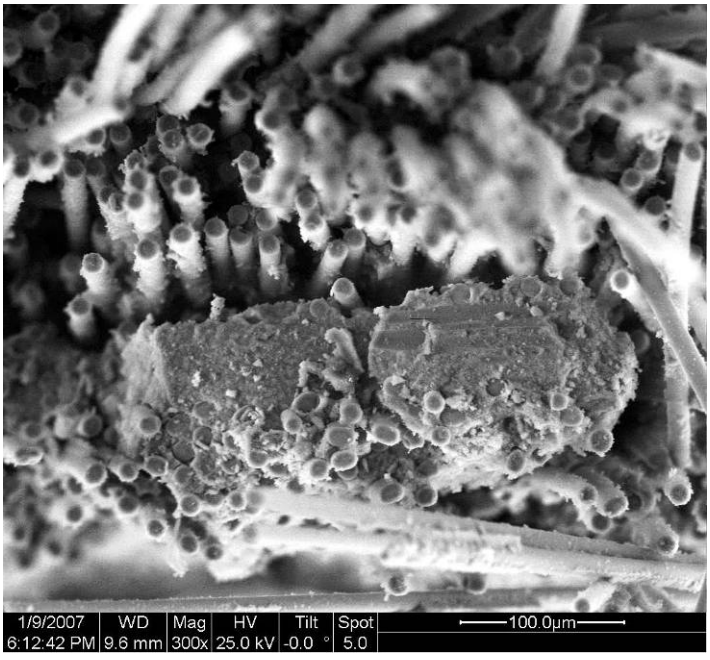

Figure 141. Fracture surface of N720/A specimen tested in creep at 150 MPa in steam at 1000 °C.

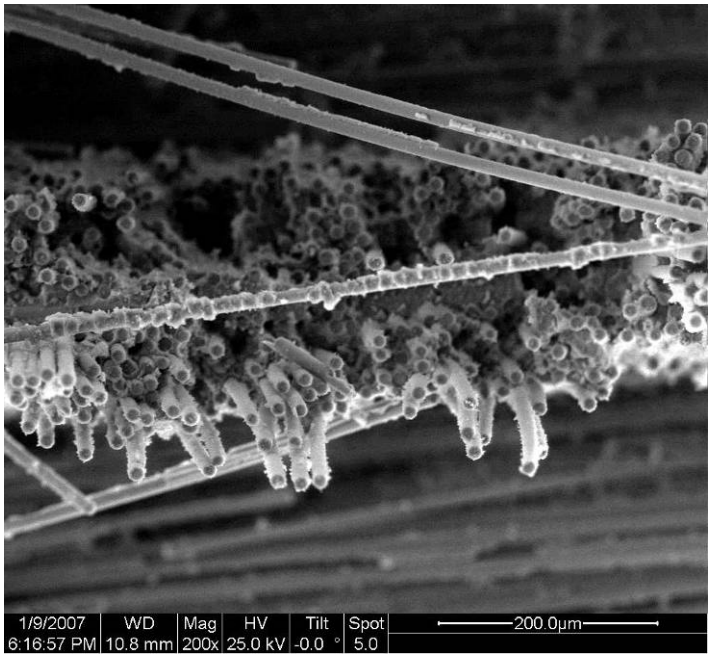

Figure 142. Fracture surface of N720/A specimen tested in creep at 150 MPa in steam at 1000 °C.

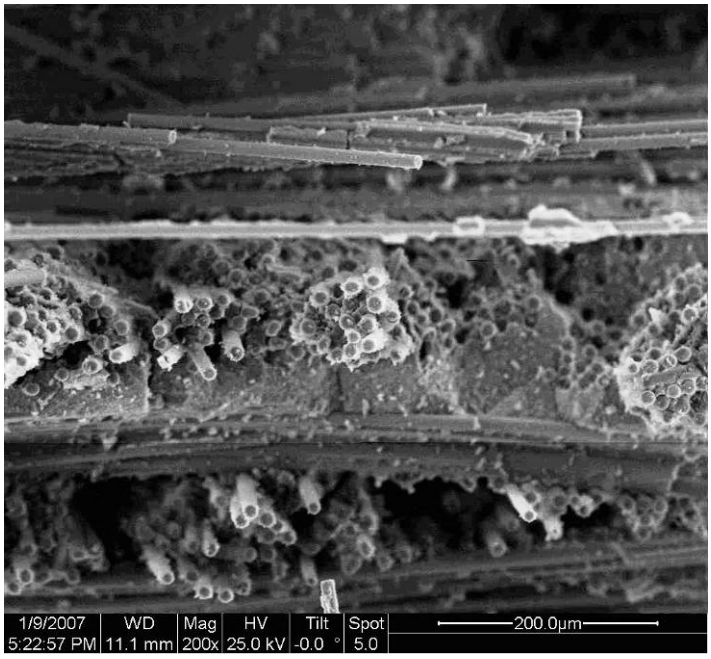

Figure 143. Fracture surface of N720/A specimen tested in creep at 150 MPa in steam at 1000 °C.

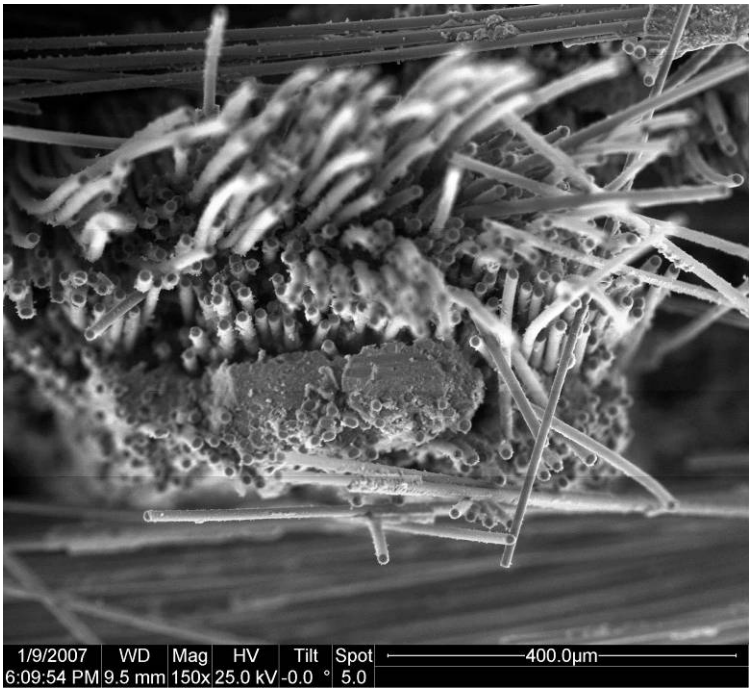

Figure 144. Fracture surface of N720/A specimen tested in creep at 150 MPa in steam at 1000 °C.

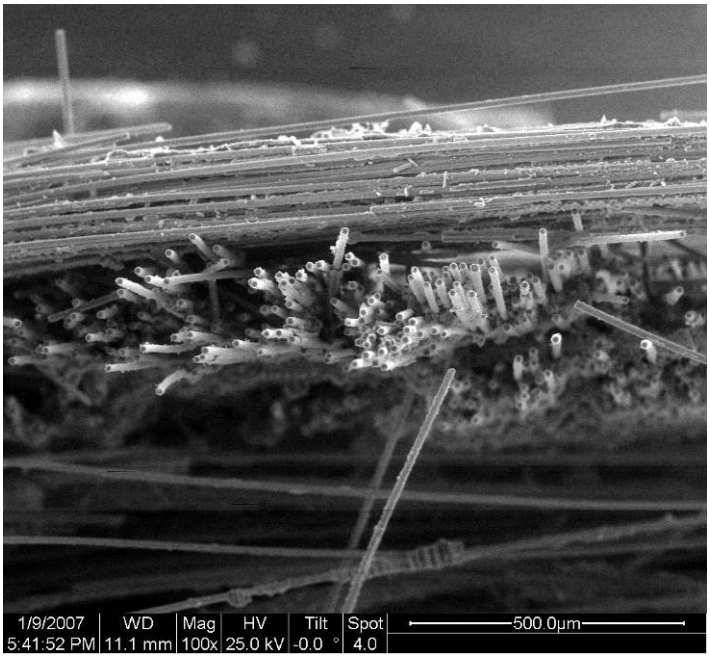

Figure 145. Fracture surface of N720/A specimen tested in creep at 150 MPa in steam at 1000 °C.

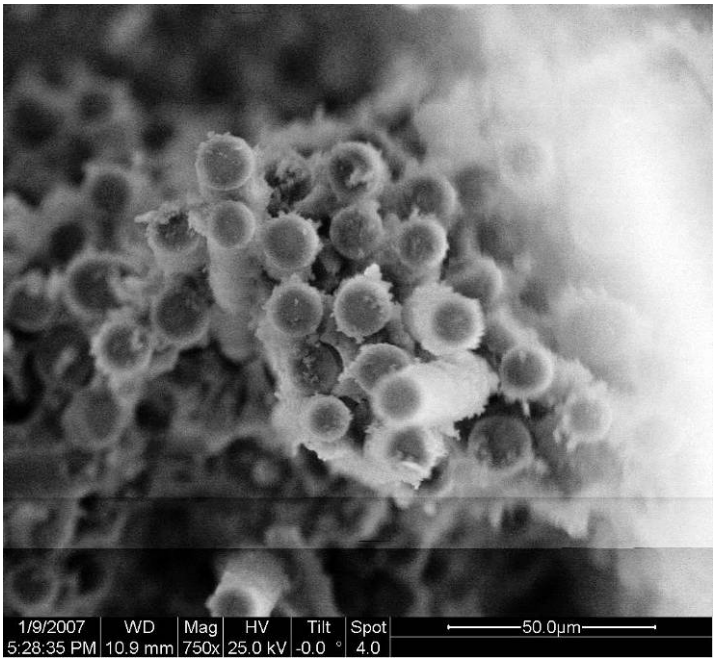

Figure 146. Fracture surface of N720/A specimen tested in creep at 150 MPa in steam at 1000 °C.

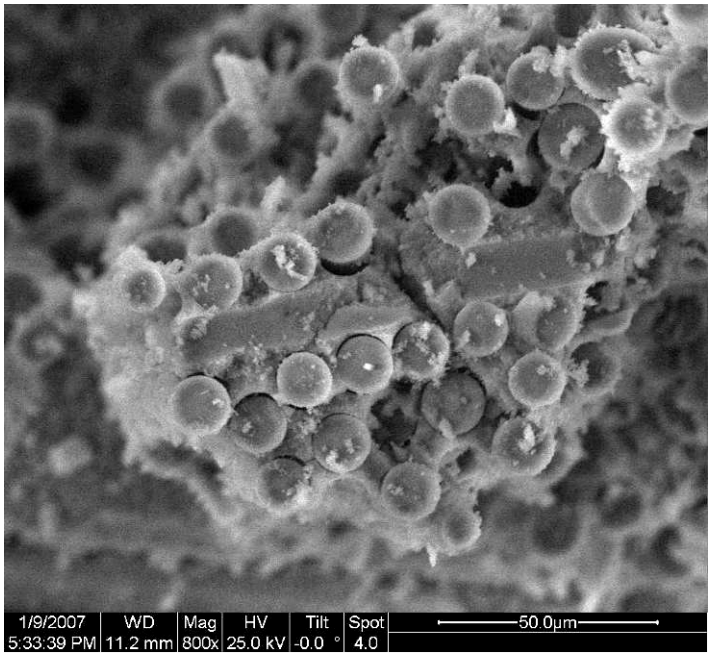

Figure 147. Fracture surface of N720/A specimen tested in creep at 150 MPa in steam at 1000 °C.

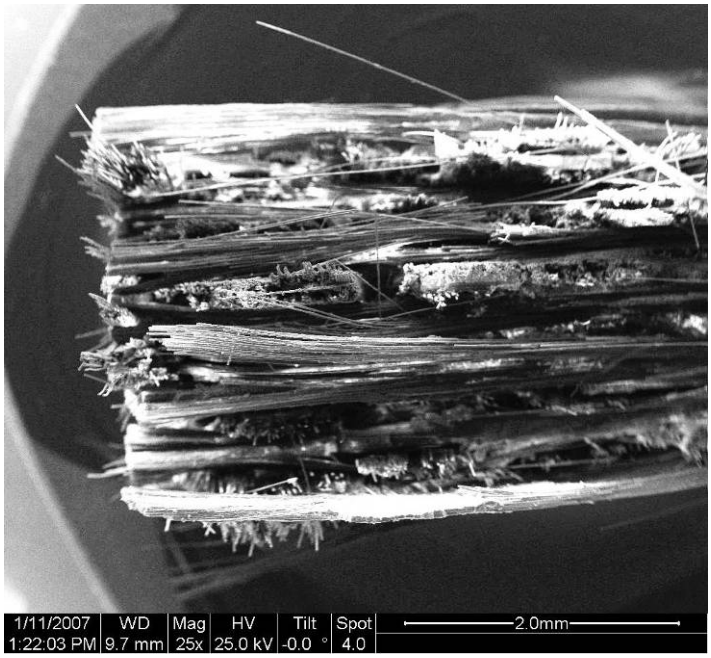

Figure 148. Fracture surface of N720/A specimen tested in creep at 150 MPa in steam at 1000 °C.

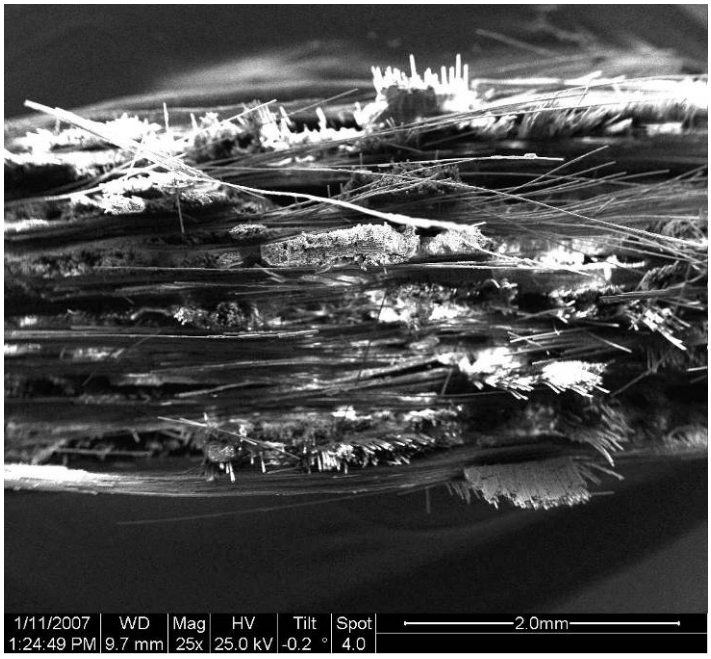

Figure 149. Fracture surface of N720/A specimen tested in creep at 150 MPa in steam at 1000 °C.

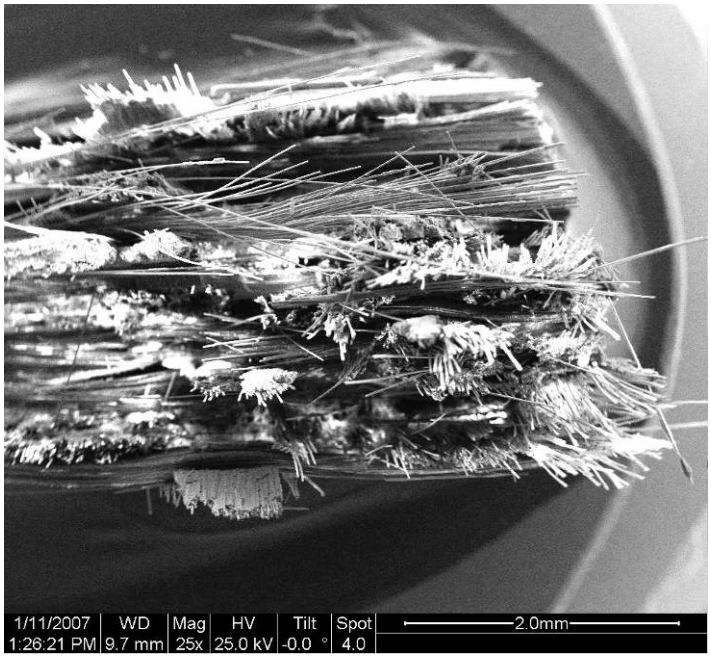

Figure 150. Fracture surface of N720/A specimen tested in creep at 150 MPa in steam at 1000 °C.

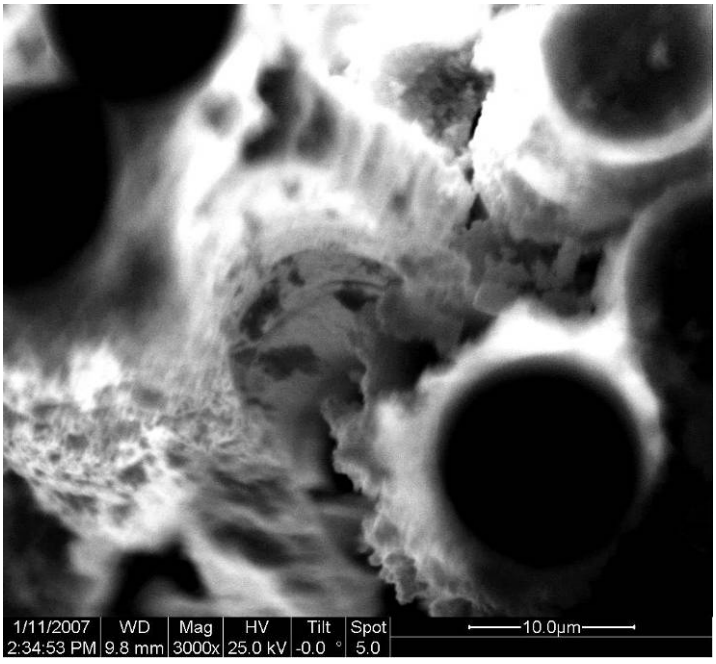

Figure 151. Fracture surface of N720/A specimen tested in creep at 150 MPa in steam at 1000 °C.

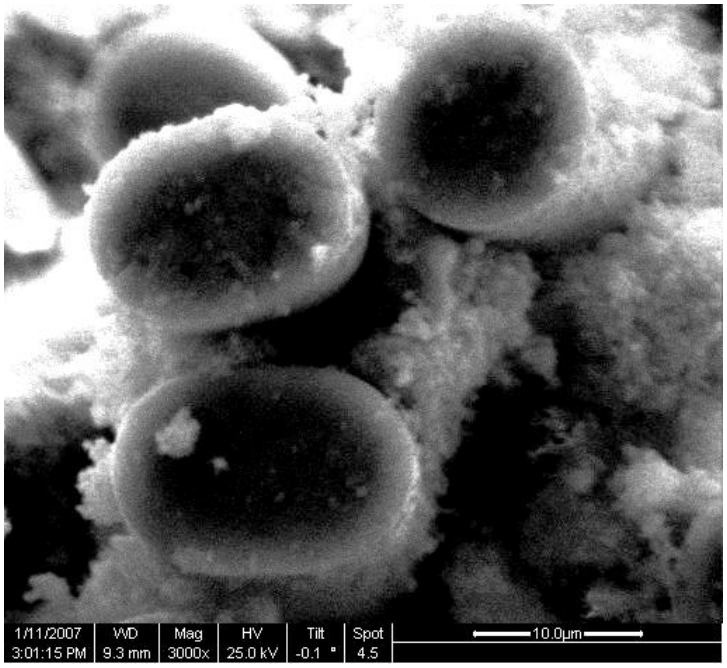

Figure 152. Fracture surface of N720/A specimen tested in creep at 150 MPa in steam at 1000 °C.

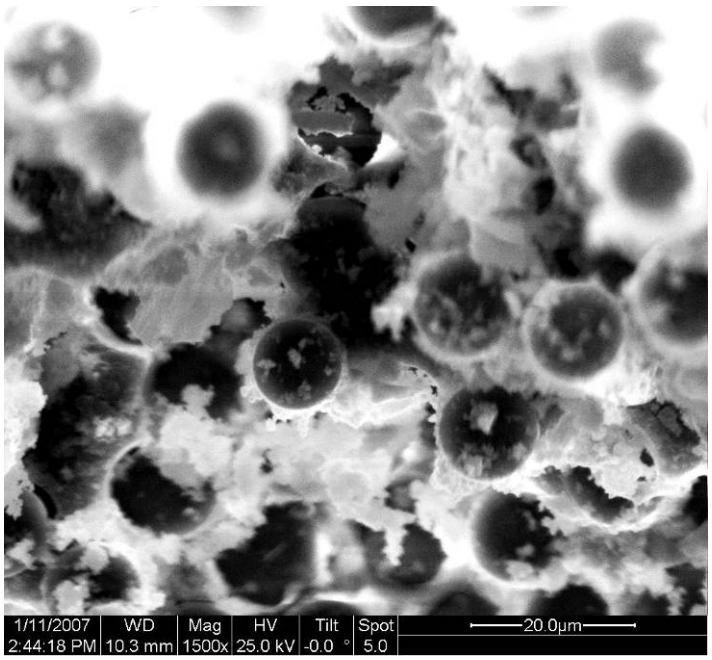

Figure 153. Fracture surface of N720/A specimen tested in creep at 150 MPa in steam at 1000 °C.

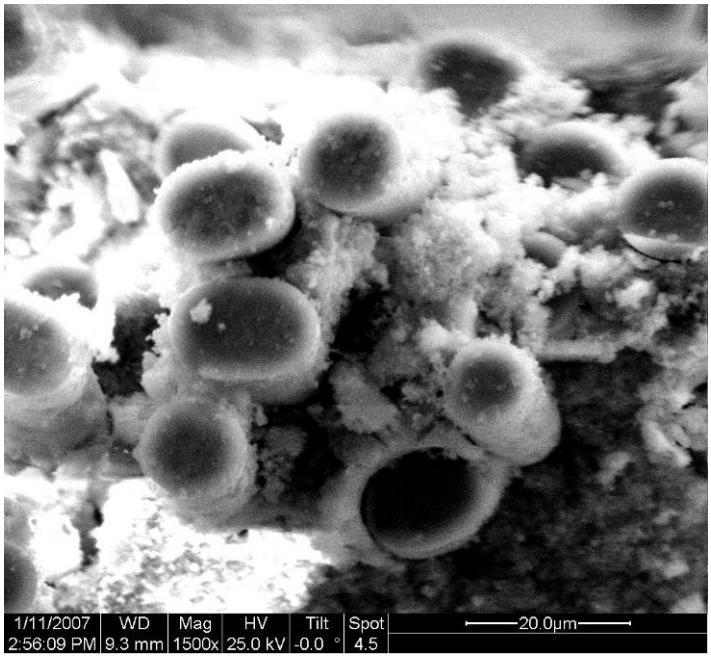

Figure 154. Fracture surface of N720/A specimen tested in creep at 150 MPa in steam at 1000 °C.

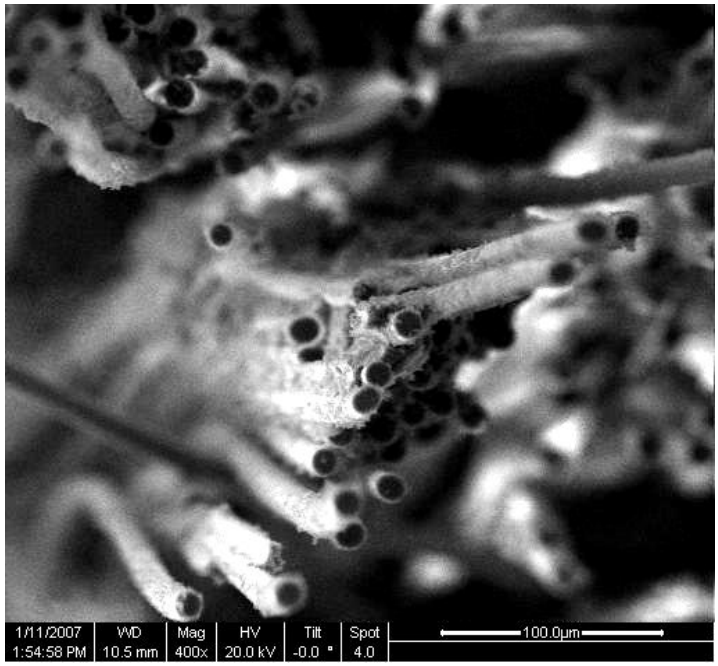

Figure 155. Fracture surface of N720/A specimen tested in creep at 150 MPa in steam at 1000 °C.

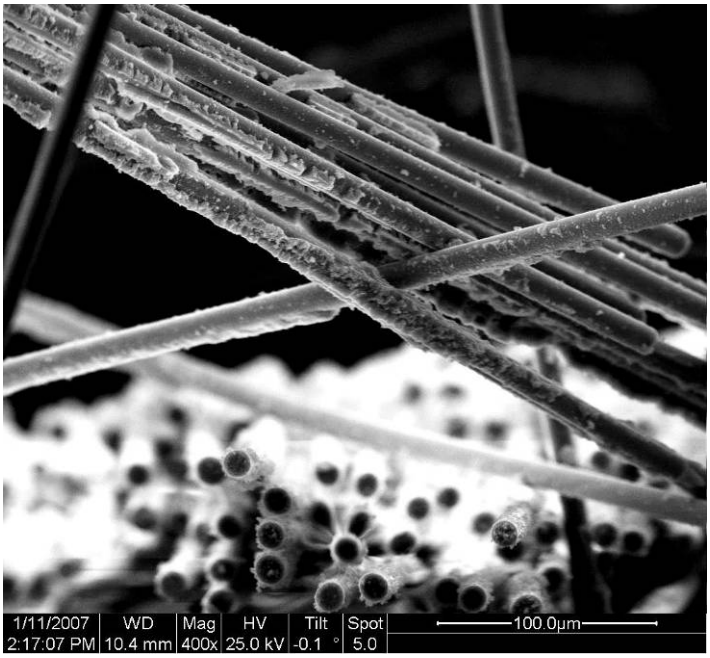

Figure 156. Fracture surface of N720/A specimen tested in creep at 150 MPa in steam at 1000 °C.

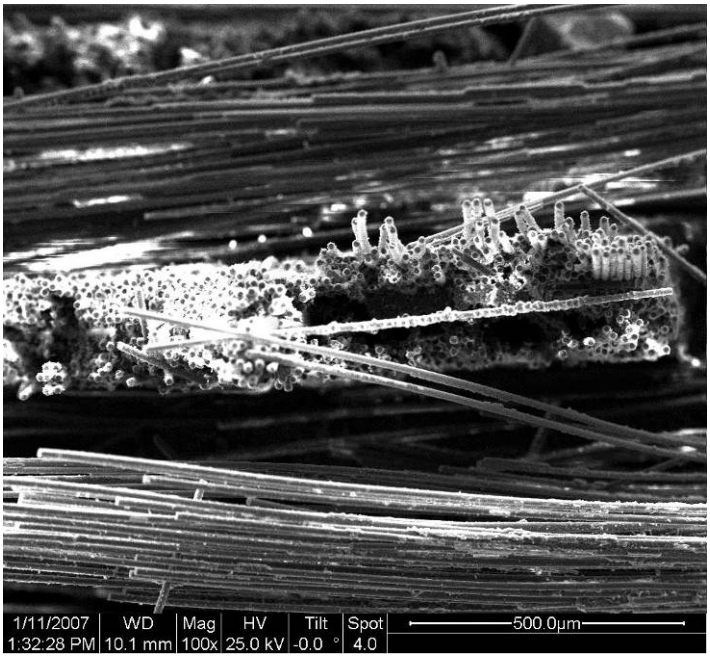

Figure 157. Fracture surface of N720/A specimen tested in creep at 150 MPa in steam at 1000 °C.

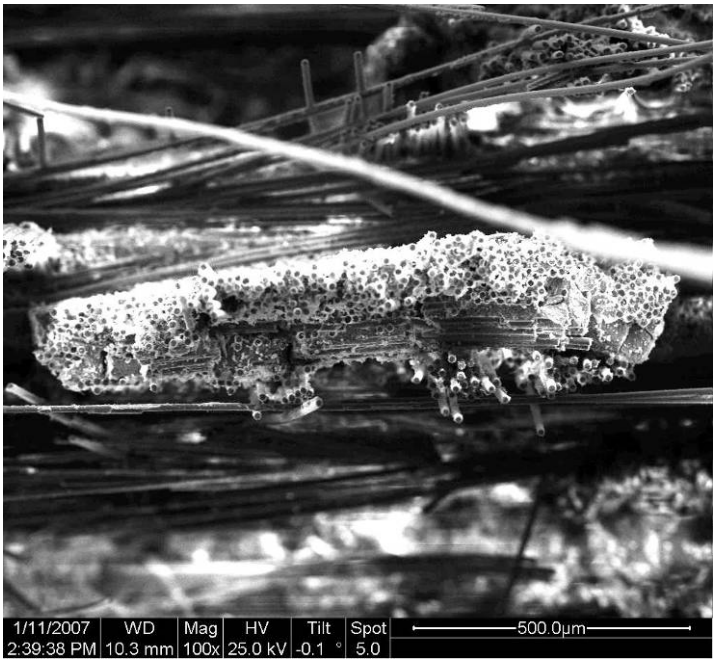

Figure 158. Fracture surface of N720/A specimen tested in creep at 150 MPa in steam at 1000 °C.

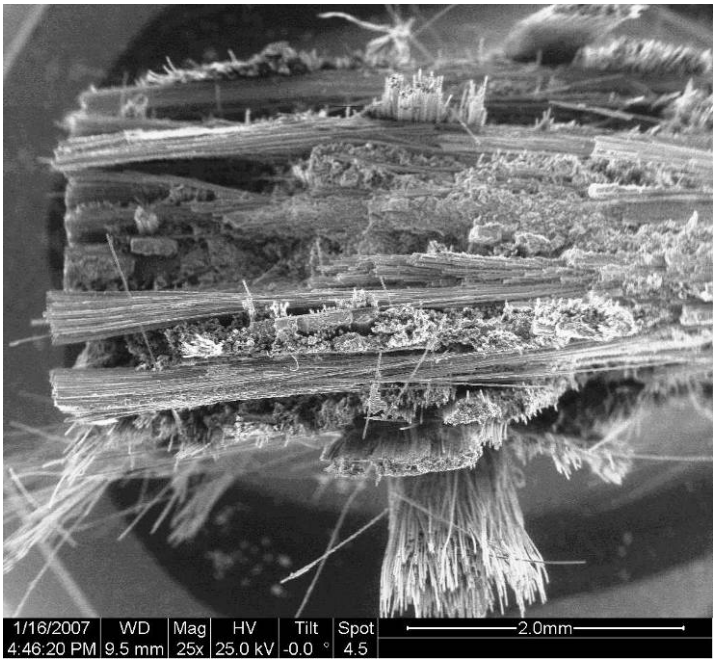

Figure 159. Fracture surface of N720/A specimen tested in creep at 160 MPa in steam at 1000 °C.

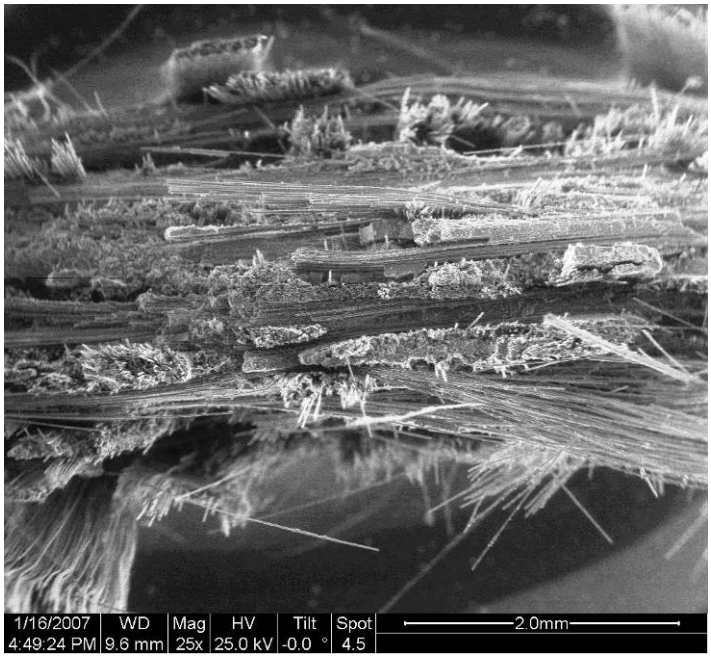

Figure 160. Fracture surface of N720/A specimen tested in creep at 160 MPa in steam at 1000 °C.

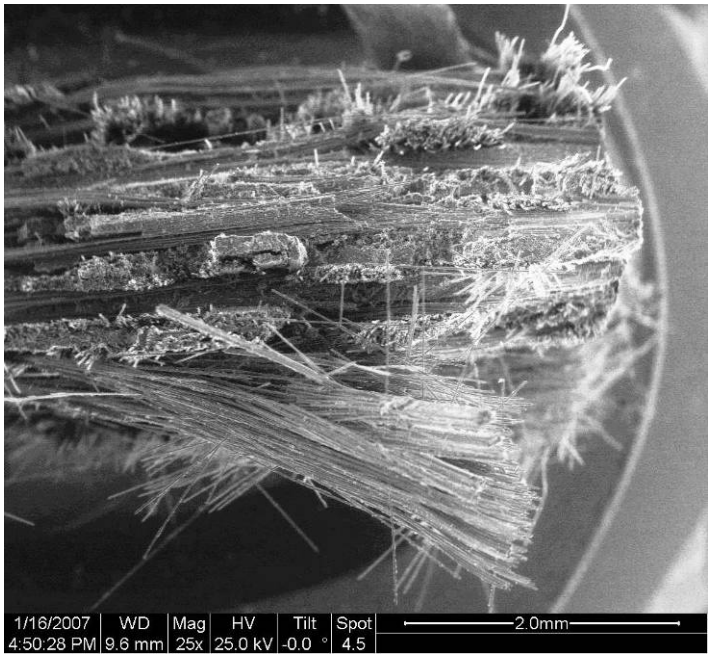

Figure 161. Fracture surface of N720/A specimen tested in creep at 160 MPa in steam at 1000 °C.

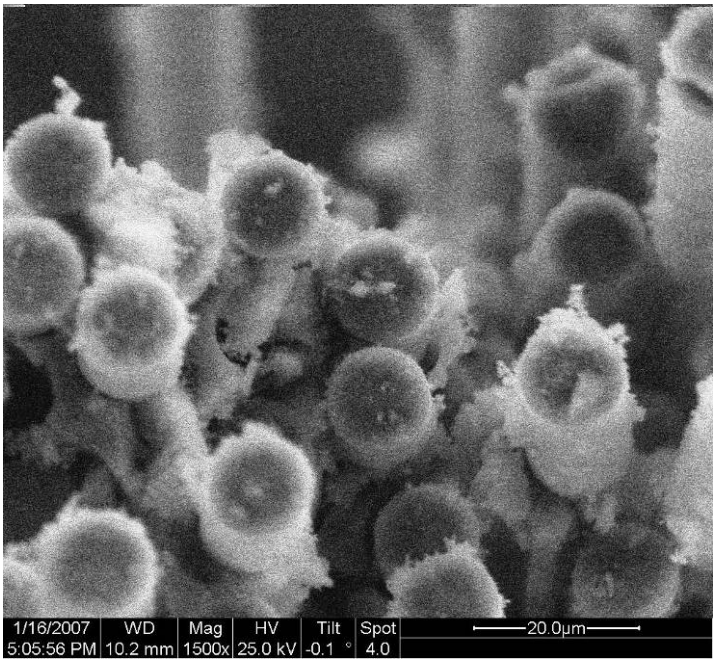

Figure 162. Fracture surface of N720/A specimen tested in creep at 160 MPa in steam at 1000 °C.

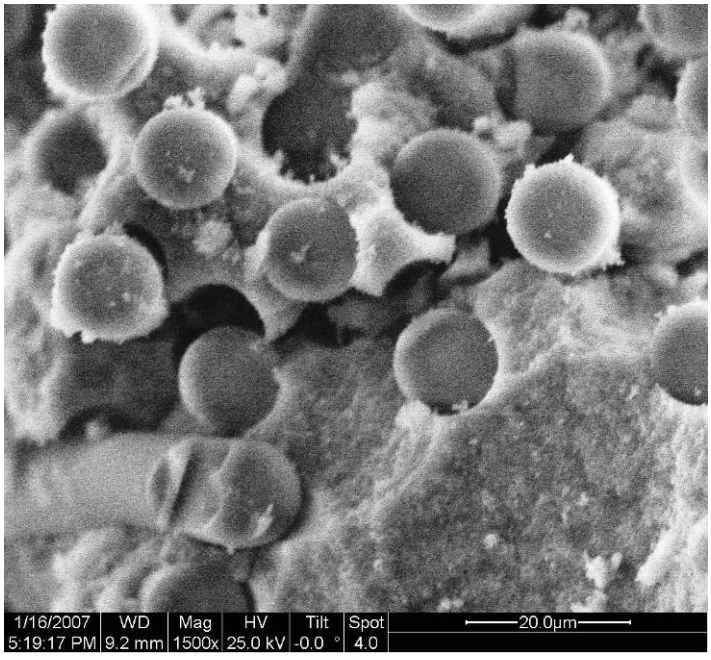

Figure 163. Fracture surface of N720/A specimen tested in creep at 160 MPa in steam at 1000 °C.

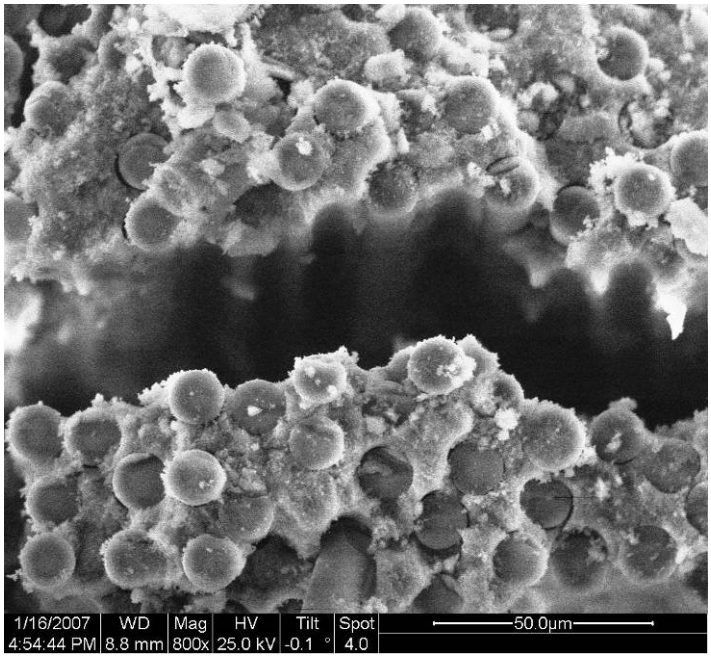

Figure 164. Fracture surface of N720/A specimen tested in creep at 160 MPa in steam at 1000 °C.

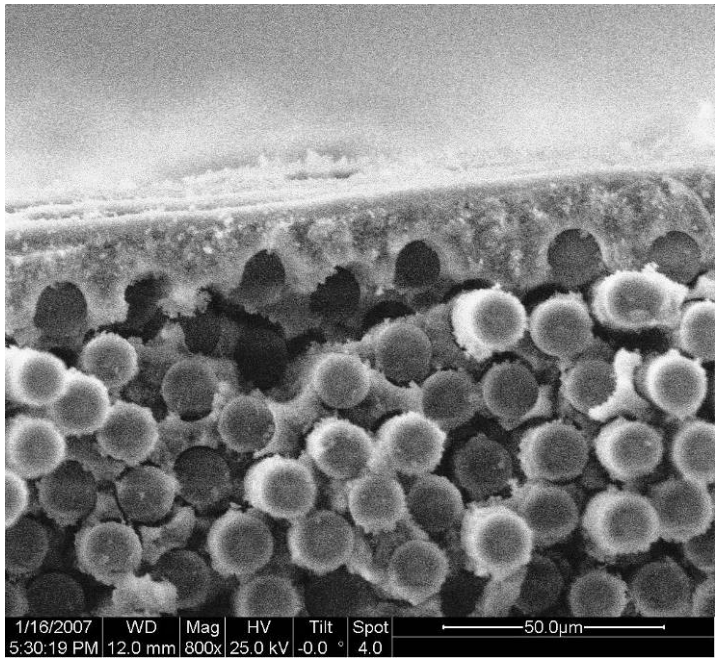

Figure 165. Fracture surface of N720/A specimen tested in creep at 160 MPa in steam at 1000 °C.

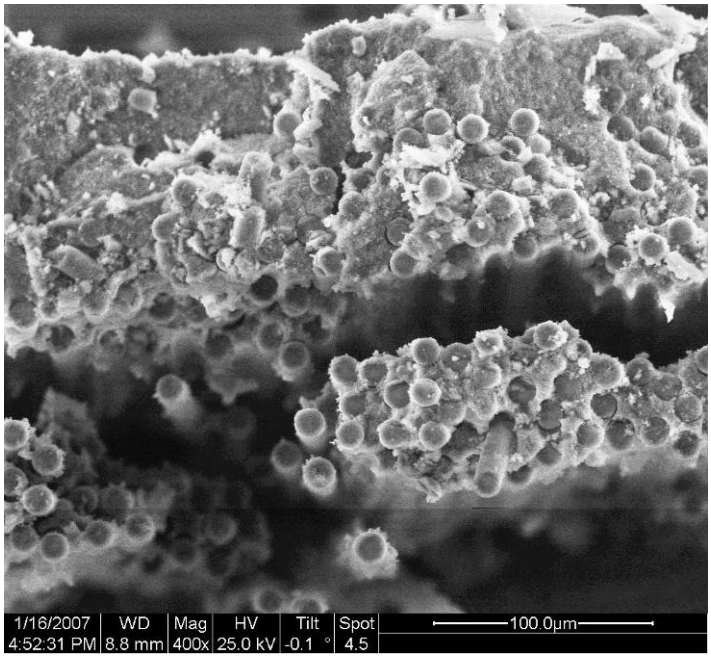

Figure 166. Fracture surface of N720/A specimen tested in creep at 160 MPa in steam at 1000 °C.

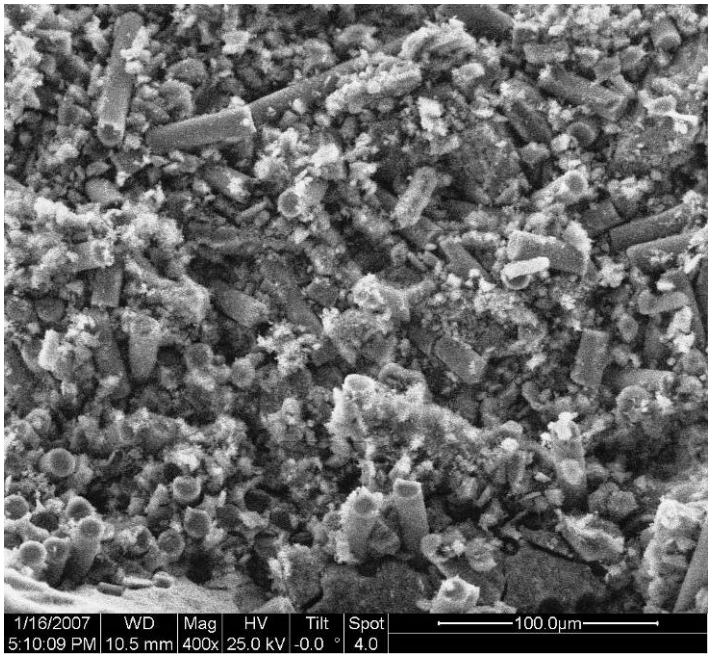

Figure 167. Fracture surface of N720/A specimen tested in creep at 160 MPa in steam at 1000 °C.

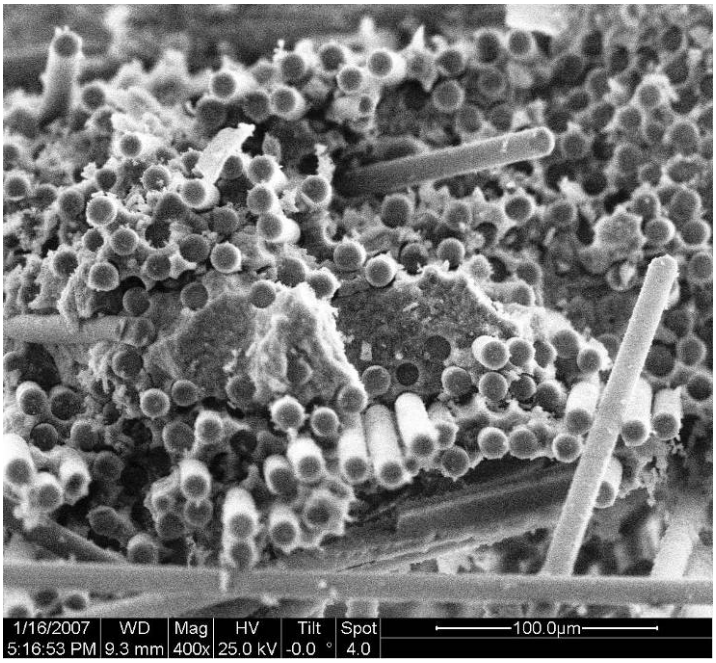

Figure 168. Fracture surface of N720/A specimen tested in creep at 160 MPa in steam at 1000 °C.

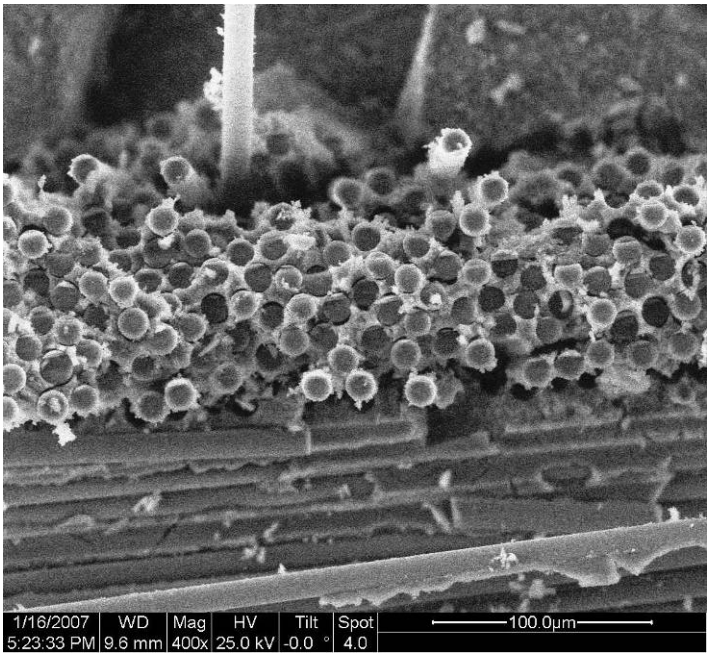

Figure 169. Fracture surface of N720/A specimen tested in creep at 160 MPa in steam at 1000 °C.

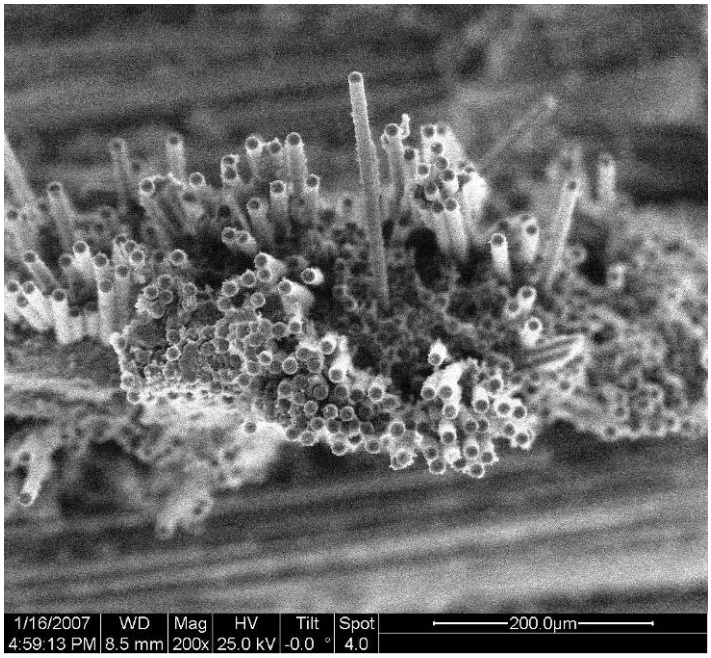

Figure 170. Fracture surface of N720/A specimen tested in creep at 160 MPa in steam at 1000 °C.

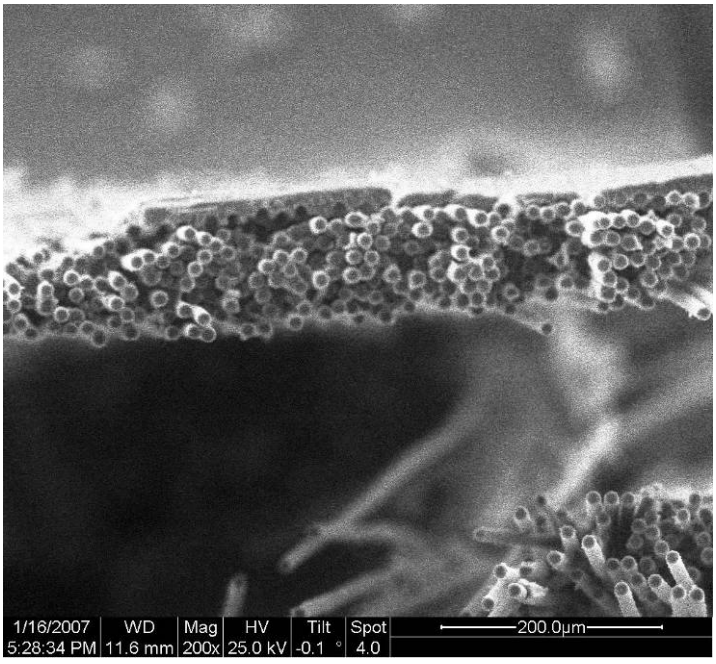

Figure 171. Fracture surface of N720/A specimen tested in creep at 160 MPa in steam at 1000 °C.

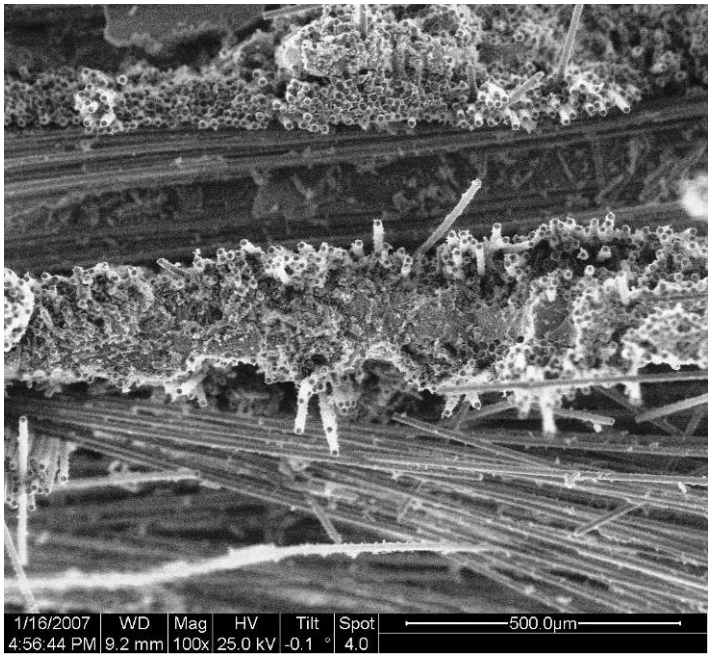

Figure 172. Fracture surface of N720/A specimen tested in creep at 160 MPa in steam at 1000 °C.

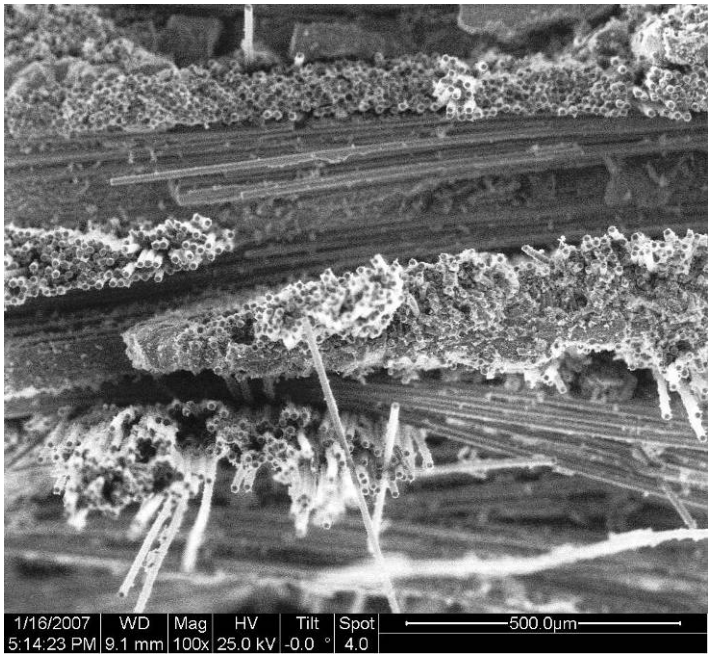

Figure 173. Fracture surface of N720/A specimen tested in creep at 160 MPa in steam at 1000 °C.

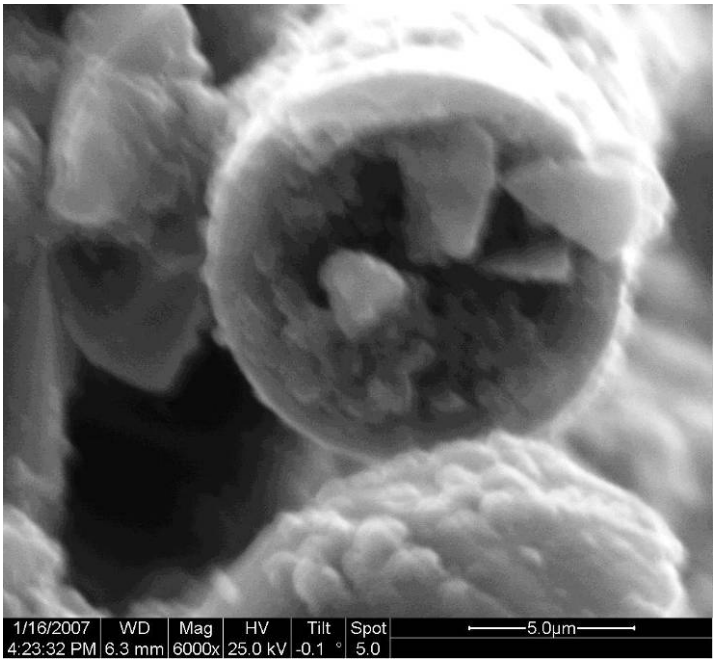

Figure 174. Fracture surface of N720/A specimen tested in creep at 160 MPa in steam at 1000 °C.

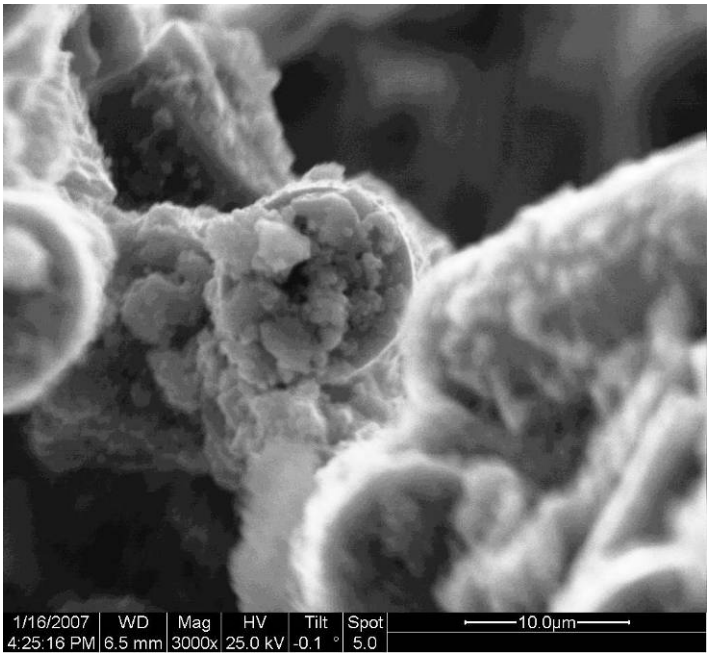

Figure 175. Fracture surface of N720/A specimen tested in creep at 160 MPa in steam at 1000 °C.

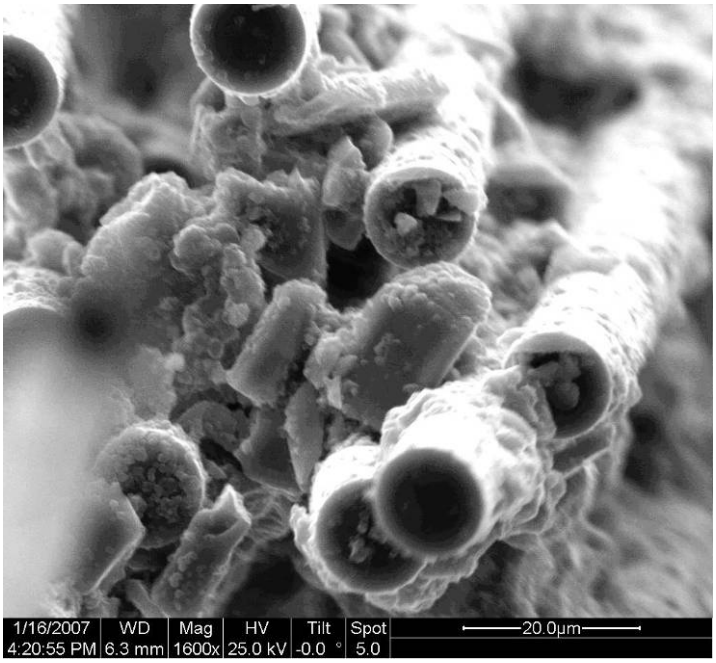

Figure 176. Fracture surface of N720/A specimen tested in creep at 160 MPa in steam at 1000 °C.

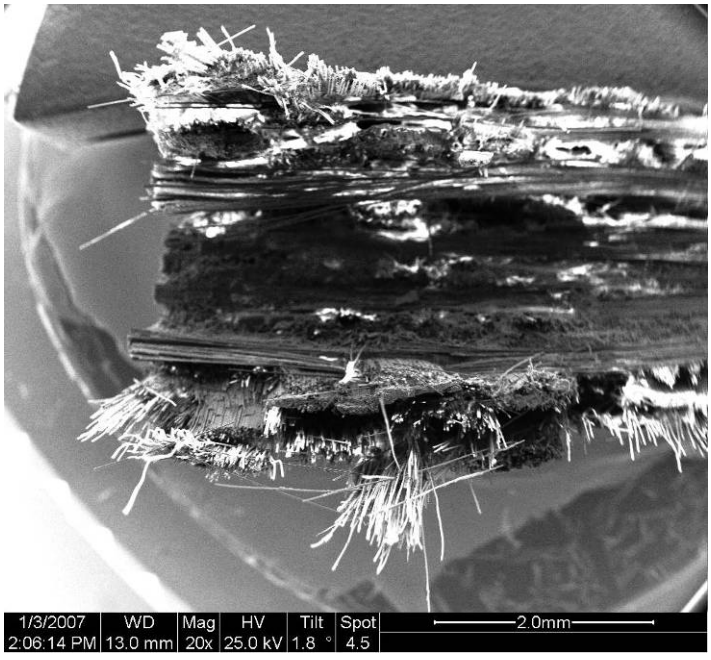

Figure 177. Fracture surface of N720/A specimen tested in creep at 160 MPa in steam at 1000 °C.

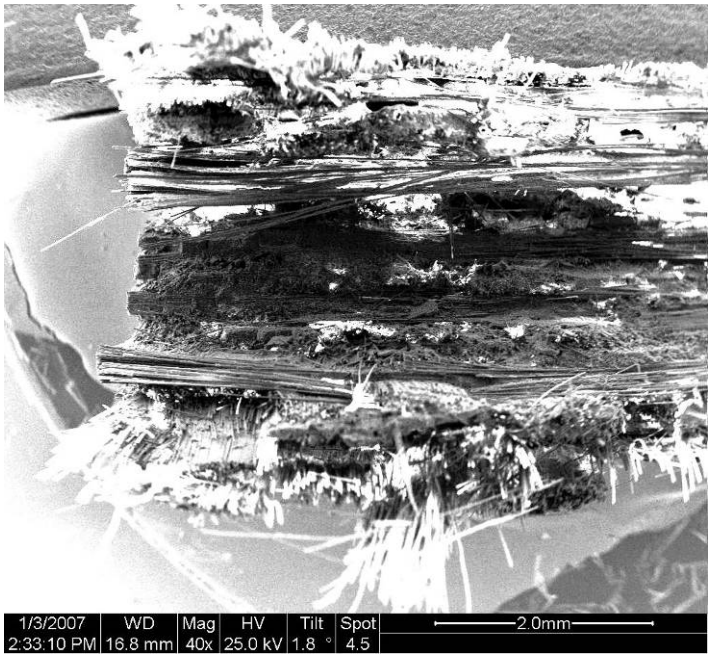

Figure 178. Fracture surface of N720/A specimen tested in creep at 160 MPa in steam at 1000 °C.

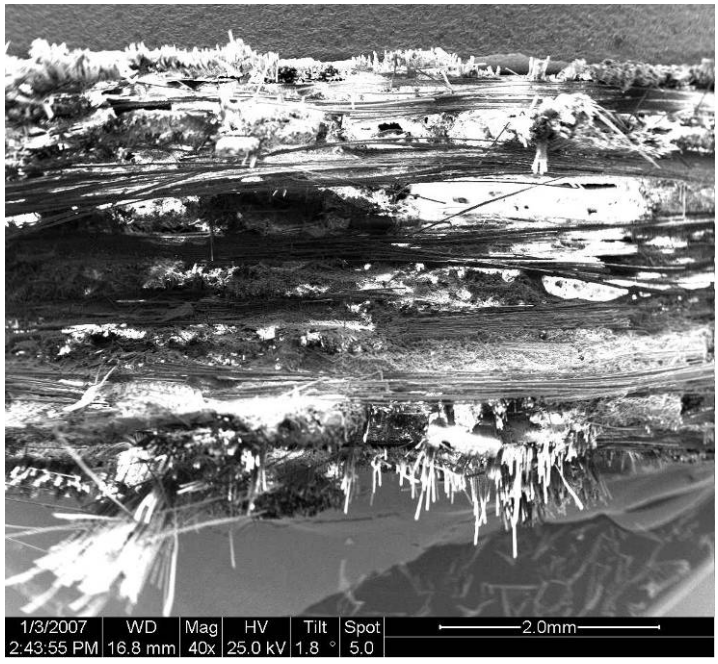

Figure 179. Fracture surface of N720/A specimen tested in creep at 160 MPa in steam at 1000 °C.

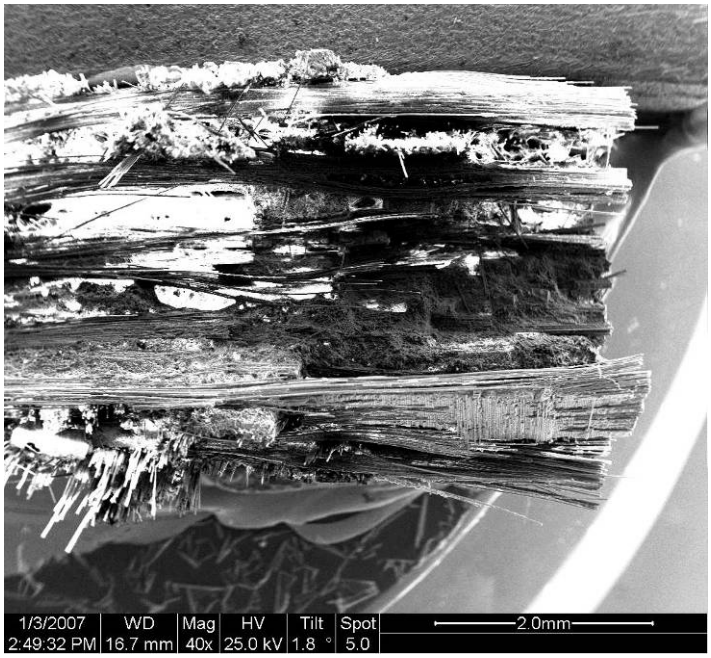

Figure 180. Fracture surface of N720/A specimen tested in creep at 160 MPa in steam at 1000 °C.

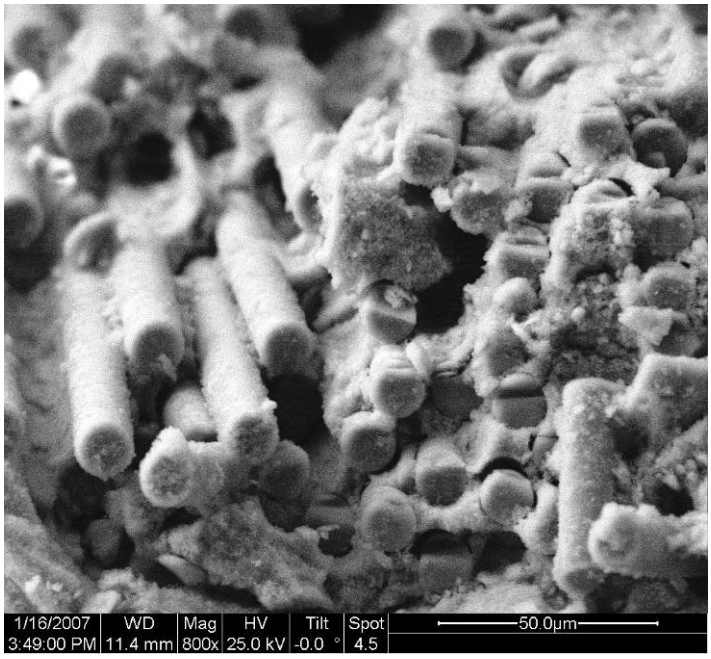

Figure 181. Fracture surface of N720/A specimen tested in creep at 160 MPa in steam at 1000 °C.

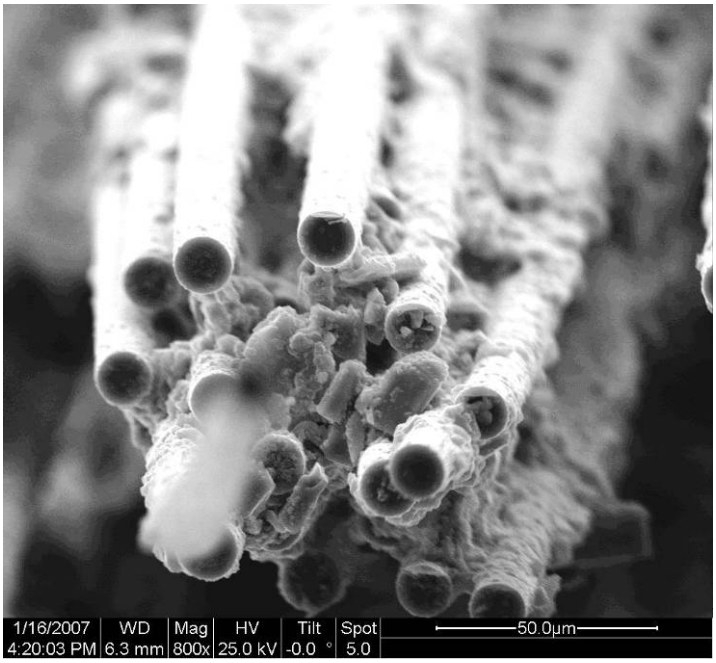

Figure 182. Fracture surface of N720/A specimen tested in creep at 160 MPa in steam at 1000 °C.

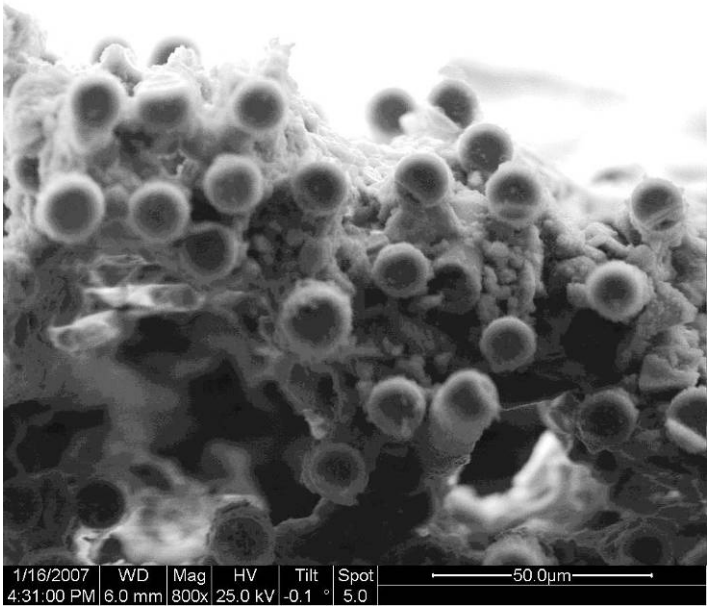

Figure 183. Fracture surface of N720/A specimen tested in creep at 160 MPa in steam at 1000 °C.

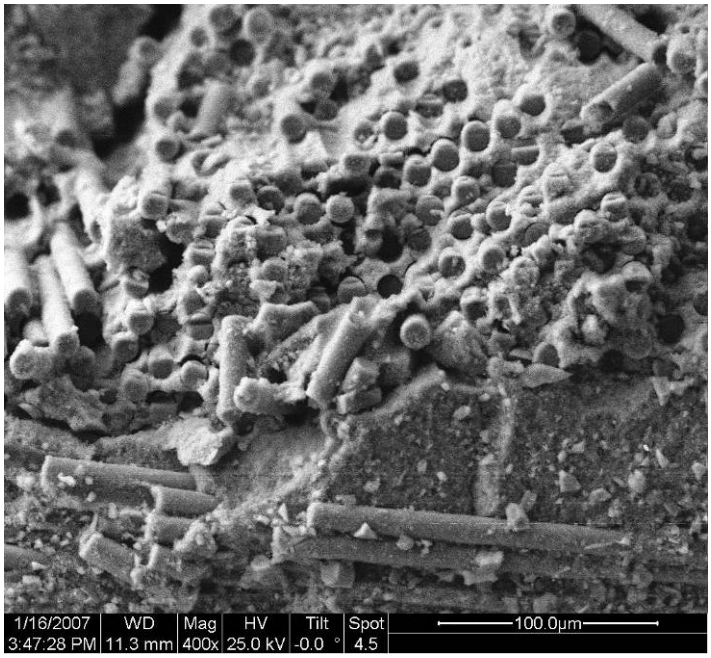

Figure 184. Fracture surface of N720/A specimen tested in creep at 160 MPa in steam at 1000 °C.

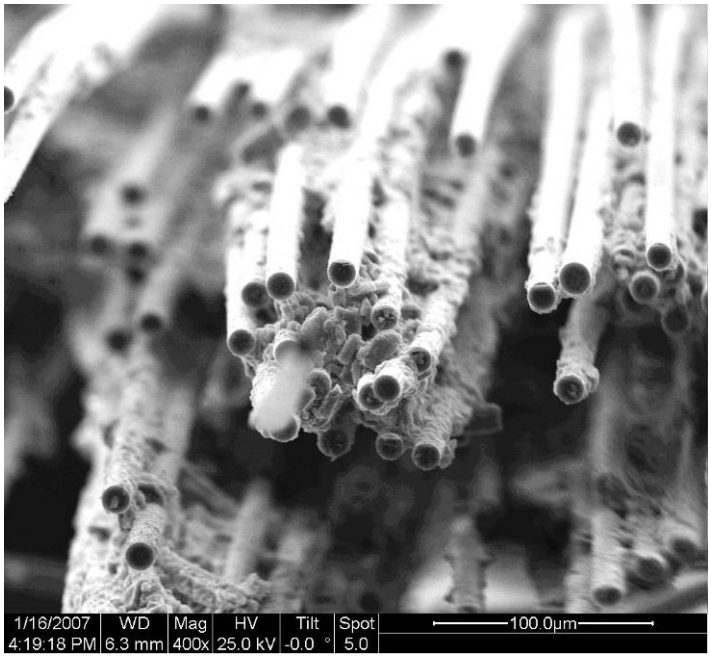

Figure 185. Fracture surface of N720/A specimen tested in creep at 160 MPa in steam at 1000 °C.

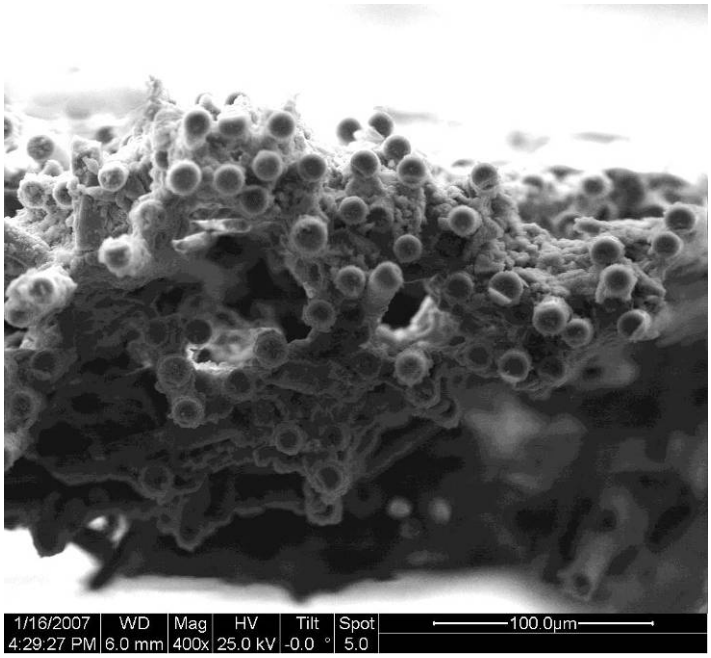

Figure 186. Fracture surface of N720/A specimen tested in creep at 160 MPa in steam at 1000 °C.

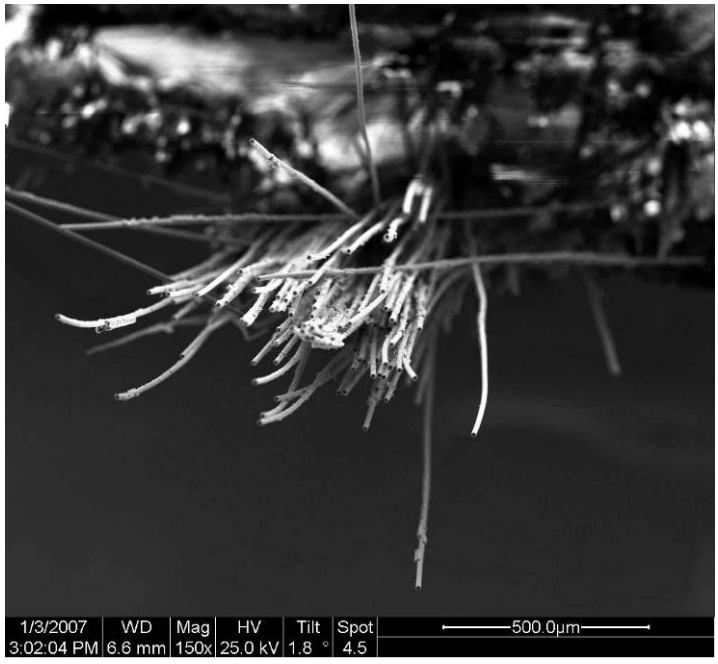

Figure 187. Fracture surface of N720/A specimen tested in creep at 160 MPa in steam at 1000 °C.

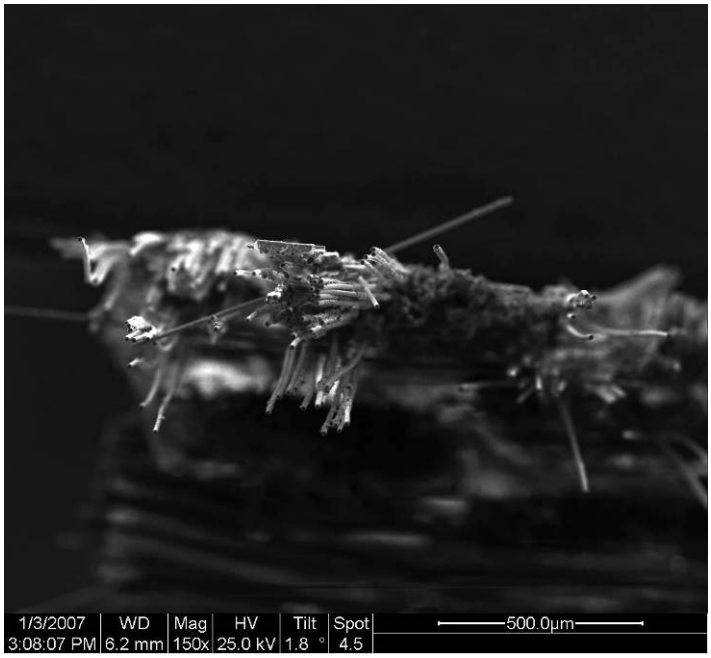

Figure 188. Fracture surface of N720/A specimen tested in creep at 160 MPa in steam at 1000 °C.

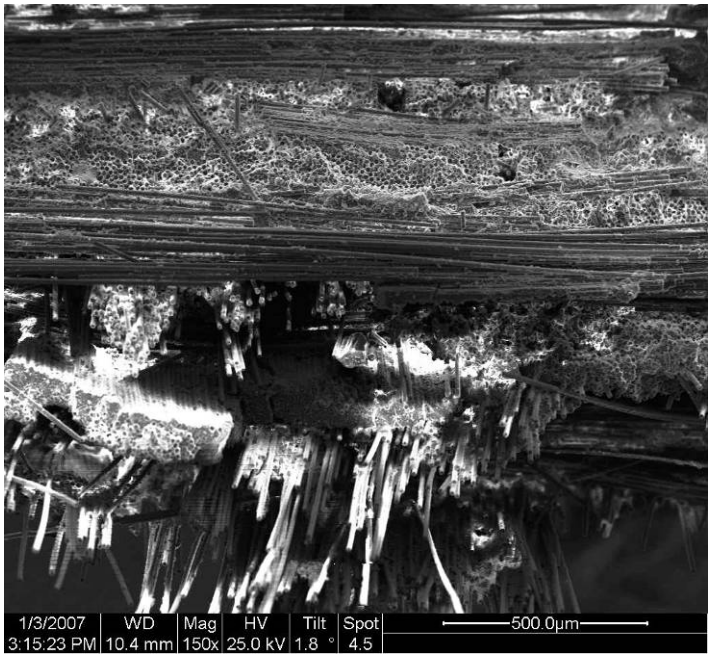

Figure 189. Fracture surface of N720/A specimen tested in creep at 160 MPa in steam at 1000 °C.

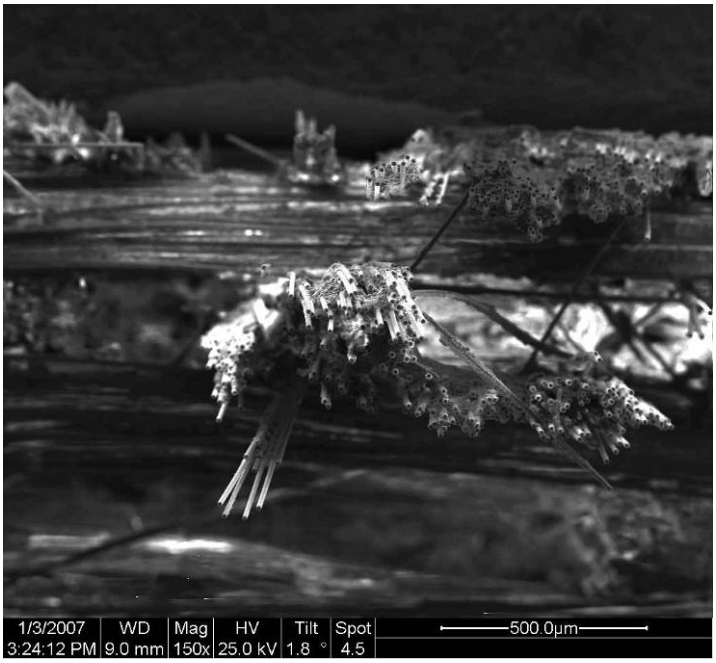

Figure 190. Fracture surface of N720/A specimen tested in creep at 160 MPa in steam at 1000 °C.

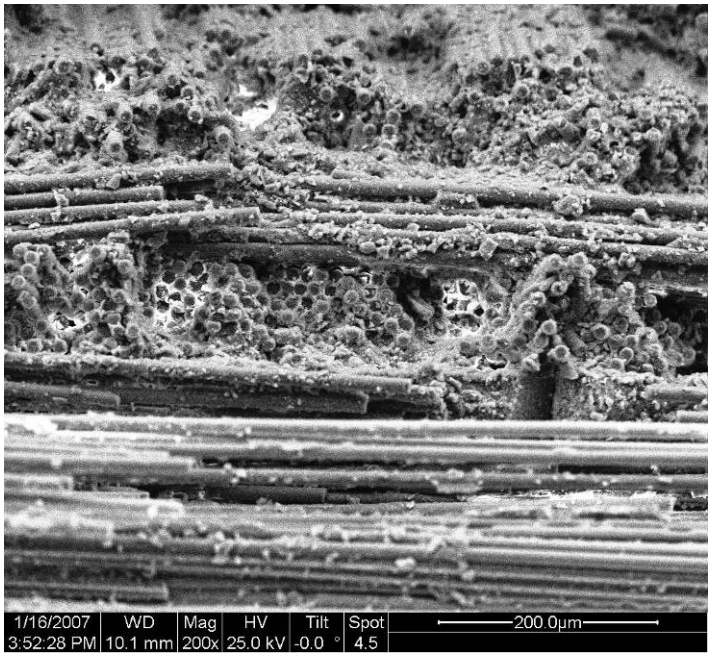

Figure 191. Fracture surface of N720/A specimen tested in creep at 160 MPa in steam at 1000 °C.

Figure 192. Fracture surface of N720/A specimen tested in creep at 160 MPa in steam at 1000 °C.

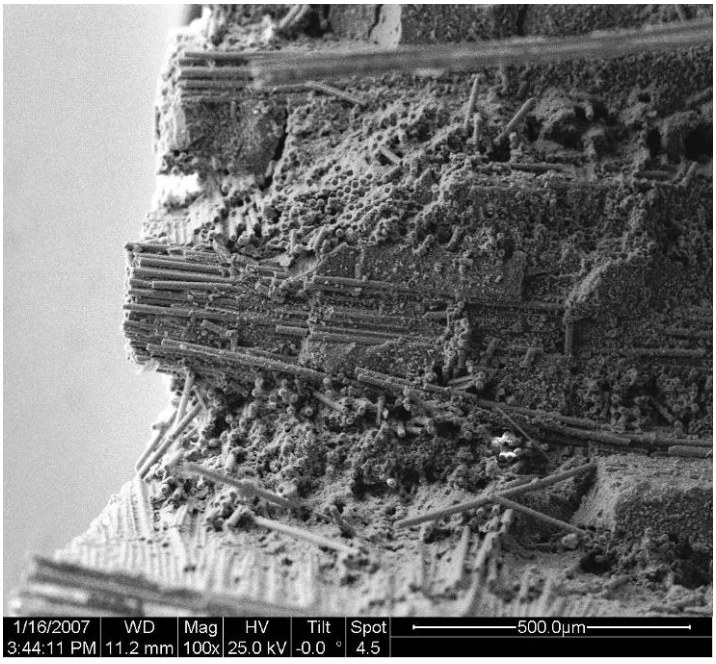

Figure 193. Fracture surface of N720/A specimen tested in creep at 160 MPa in steam at 1000 °C.

Figure 194. Fracture surface of N720/A specimen tested in creep at 160 MPa in steam at 1000 °C.

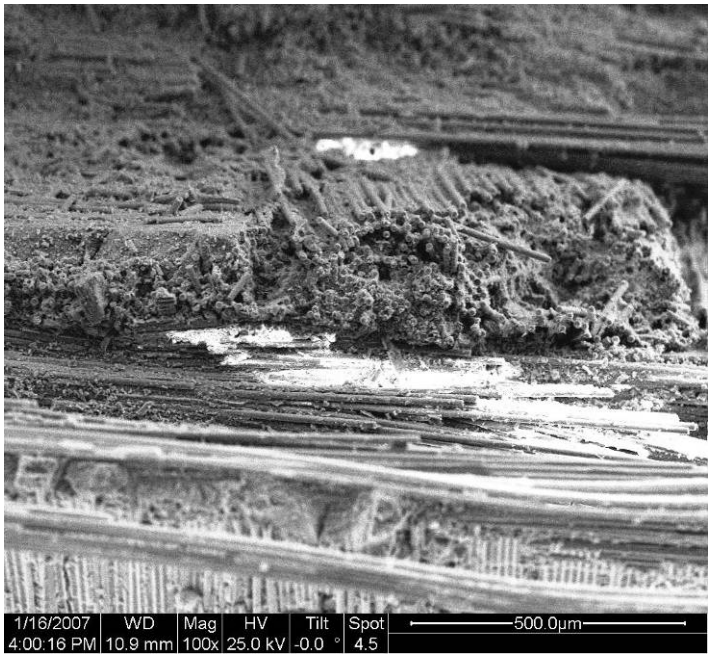

Figure 195. Fracture surface of N720/A specimen tested in creep at 160 MPa in steam at 1000 °C.

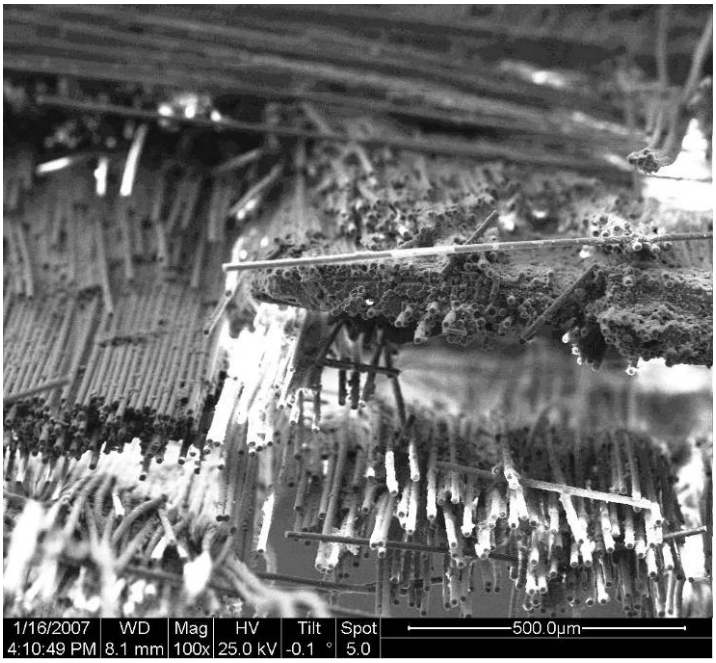

Figure 196. Fracture surface of N720/A specimen tested in creep at 160 MPa in steam at 1000 °C.

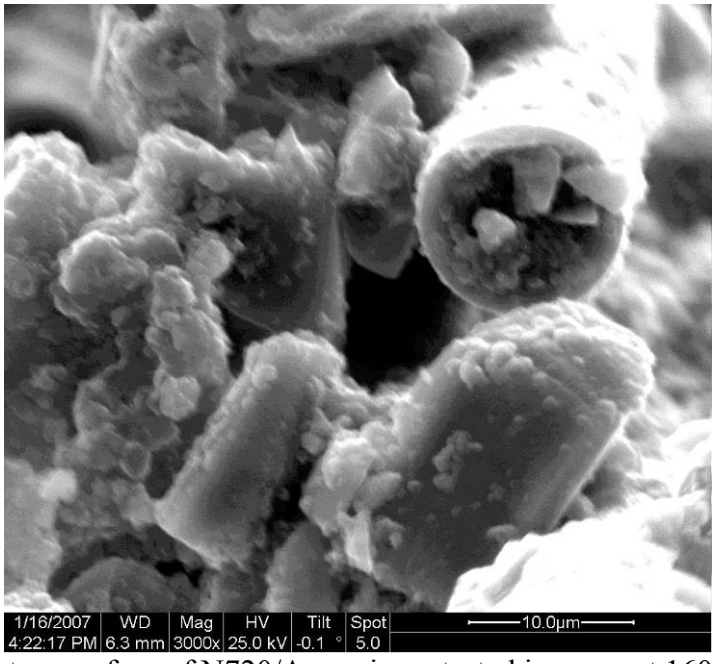

Figure 197. Fracture surface of N720/A specimen tested in creep at 160 MPa in steam at 1000 °C.

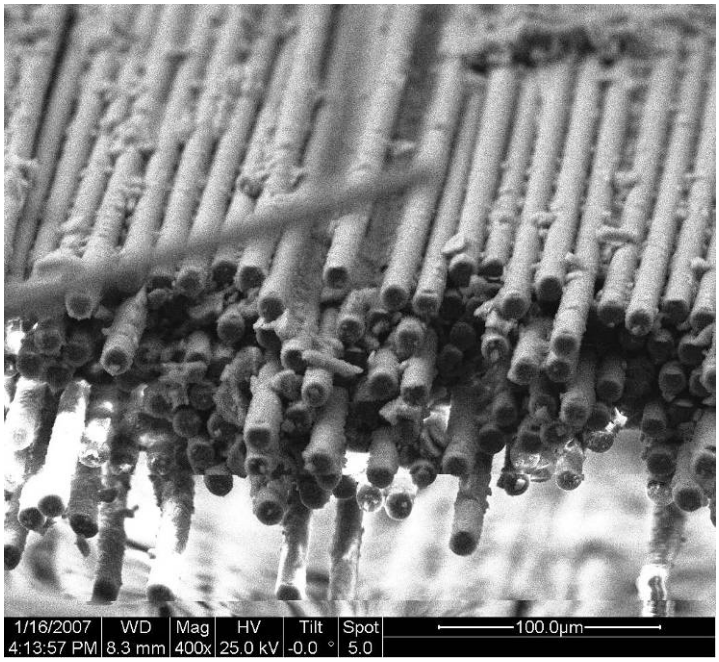

Figure 198. Fracture surface of N720/A specimen tested in creep at 160 MPa in steam at 1000 °C.

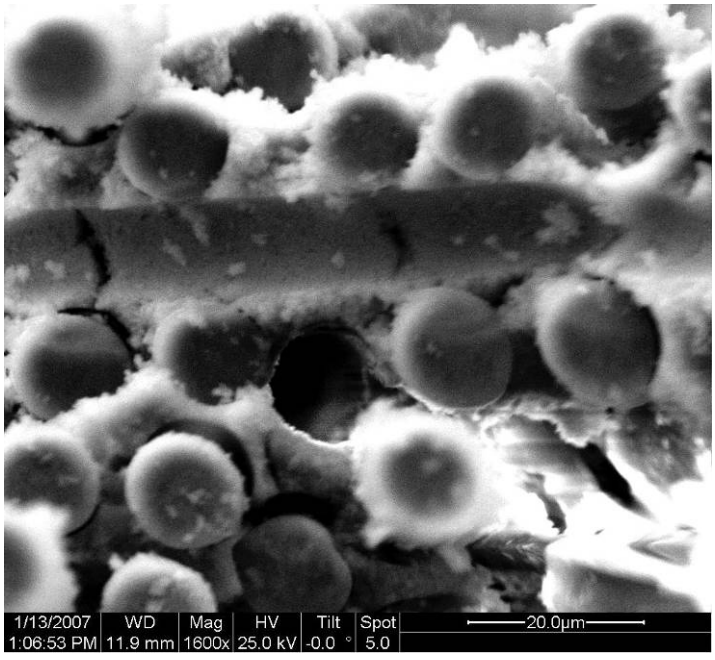

Figure 199. Fracture surface of N720/A specimen tested in creep at 150 MPa in air at 1100 °C.

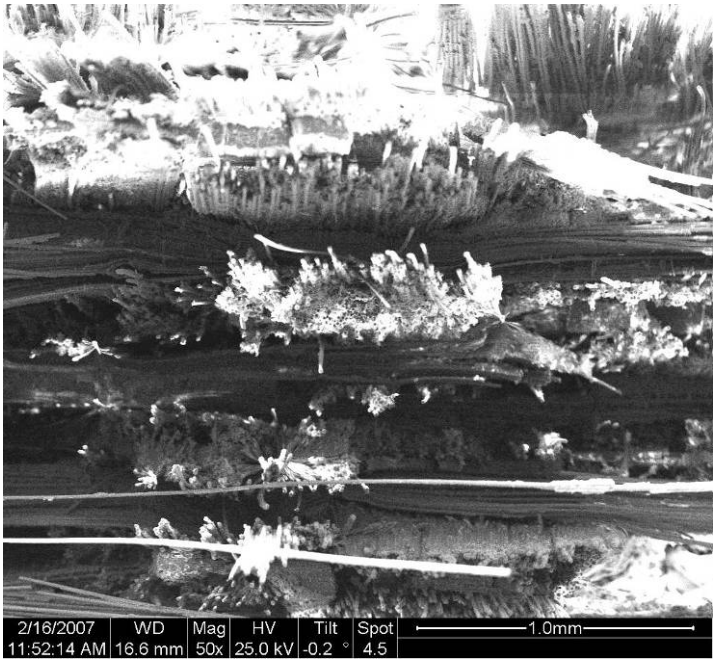

Figure 200. Fracture surface of N720/A specimen tested in creep at 150 MPa in air at 1100 °C.

Figure 201. Fracture surface of N720/A specimen tested in creep at 150 MPa in air at 1100 °C.

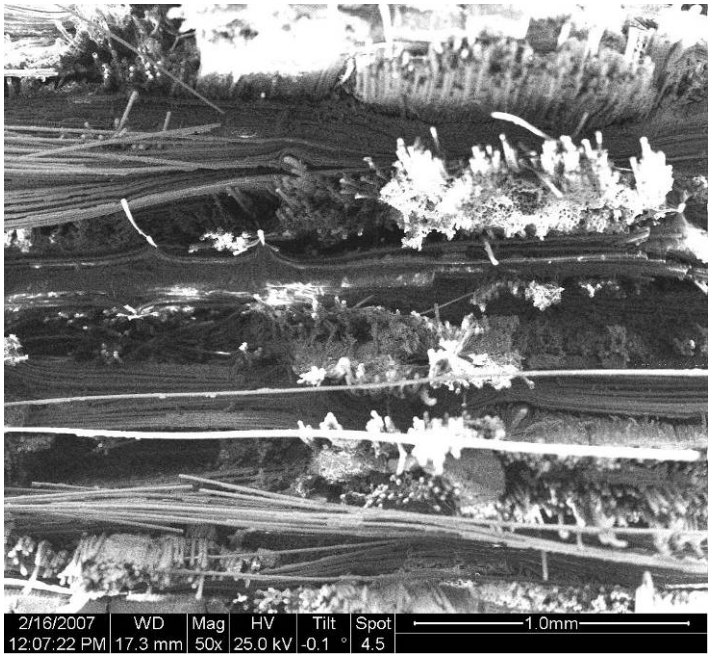

Figure 202. Fracture surface of N720/A specimen tested in creep at 150 MPa in air at 1100 °C.

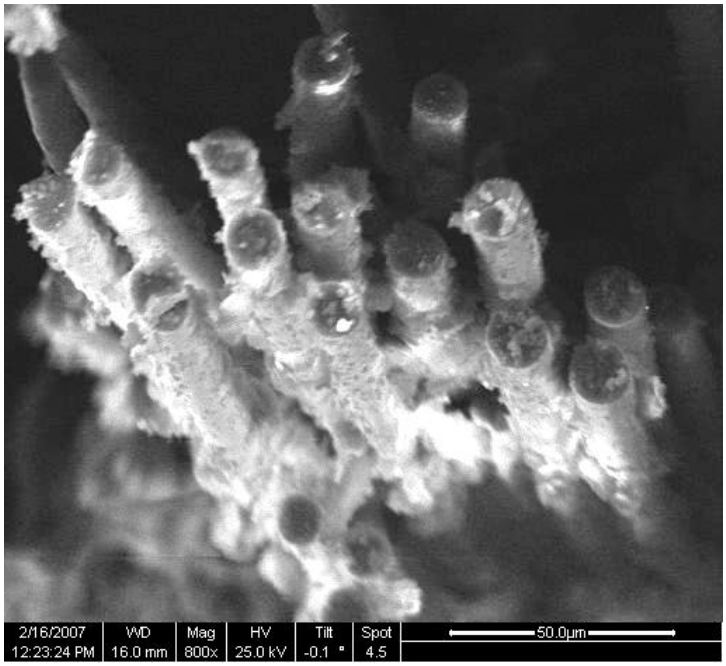

Figure 203. Fracture surface of N720/A specimen tested in creep at 150 MPa in air at 1100 °C.

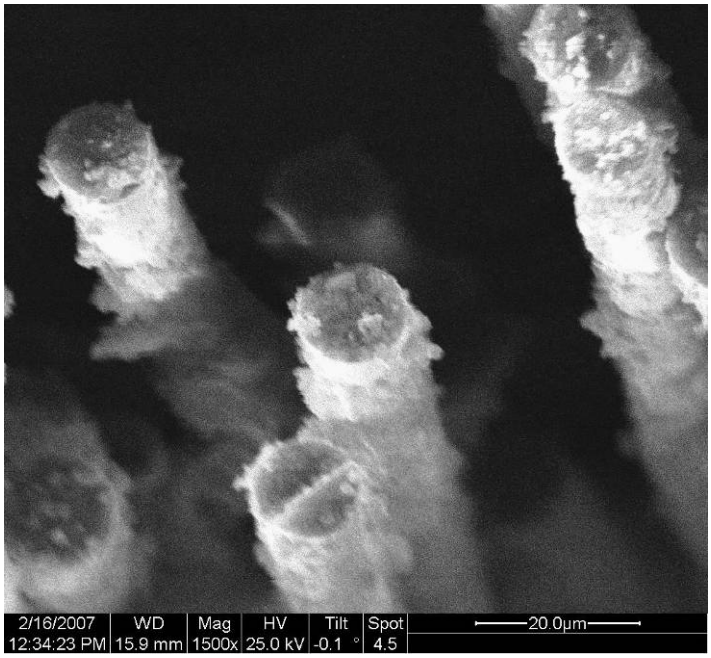

Figure 204. Fracture surface of N720/A specimen tested in creep at 150 MPa in air at 1100 °C.

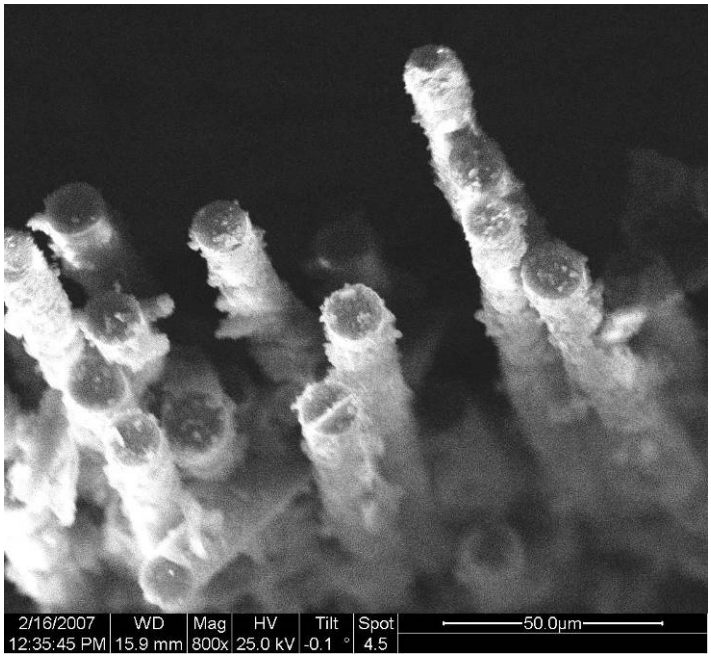

Figure 205. Fracture surface of N720/A specimen tested in creep at 150 MPa in air at 1100 °C.

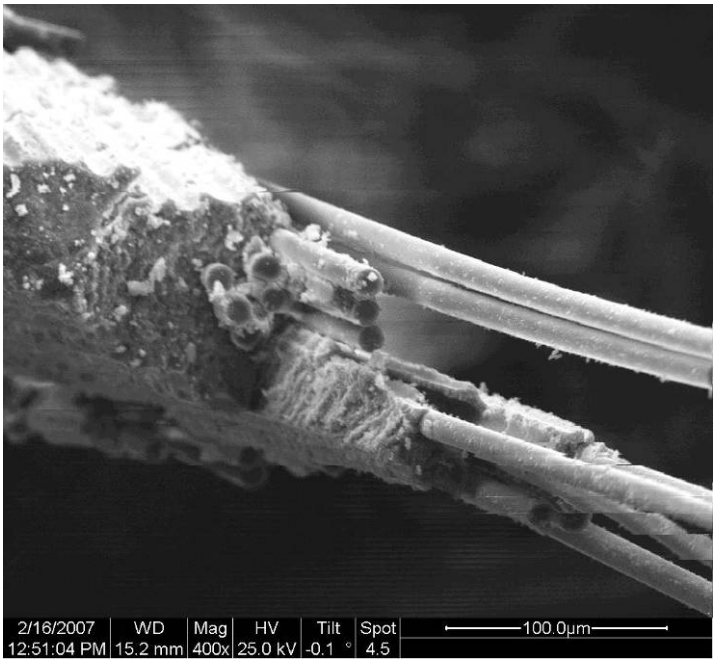

Figure 206. Fracture surface of N720/A specimen tested in creep at 150 MPa in air at 1100 °C.

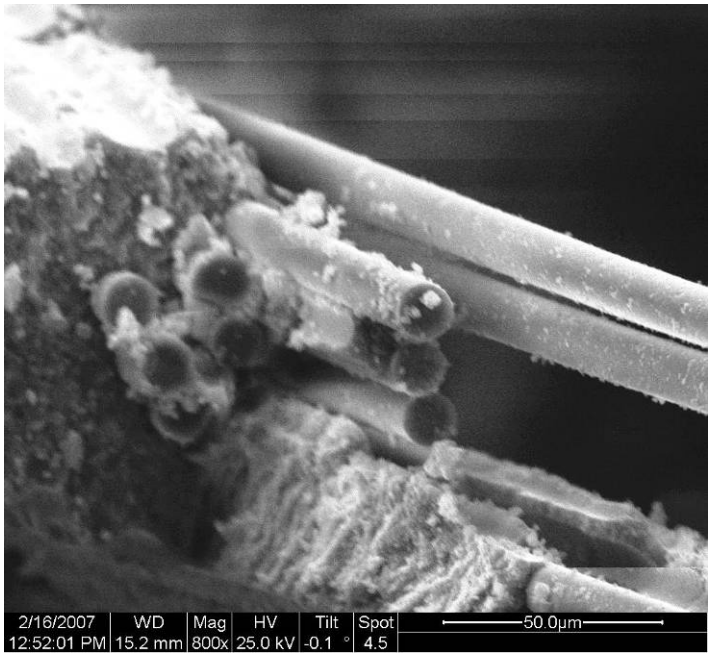

Figure 207. Fracture surface of N720/A specimen tested in creep at 150 MPa in air at 1100 °C.

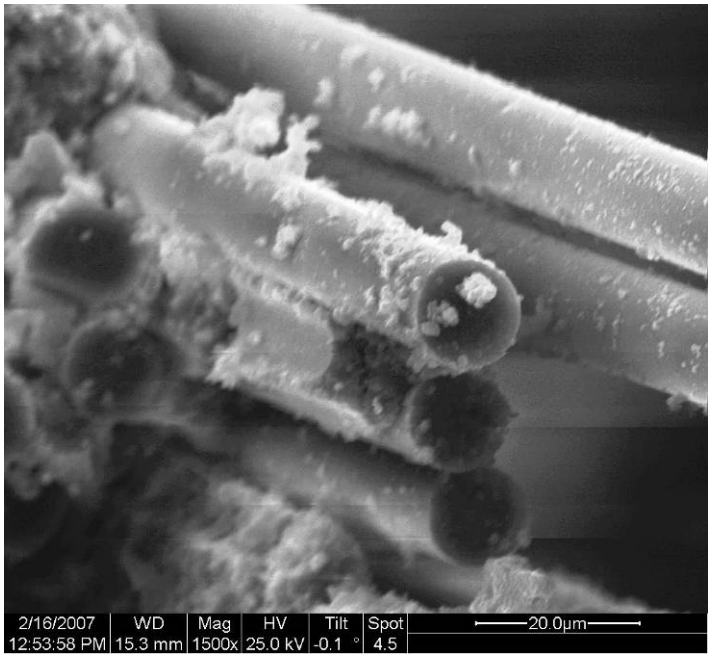

Figure 208. Fracture surface of N720/A specimen tested in creep at 150 MPa in air at 1100 °C.

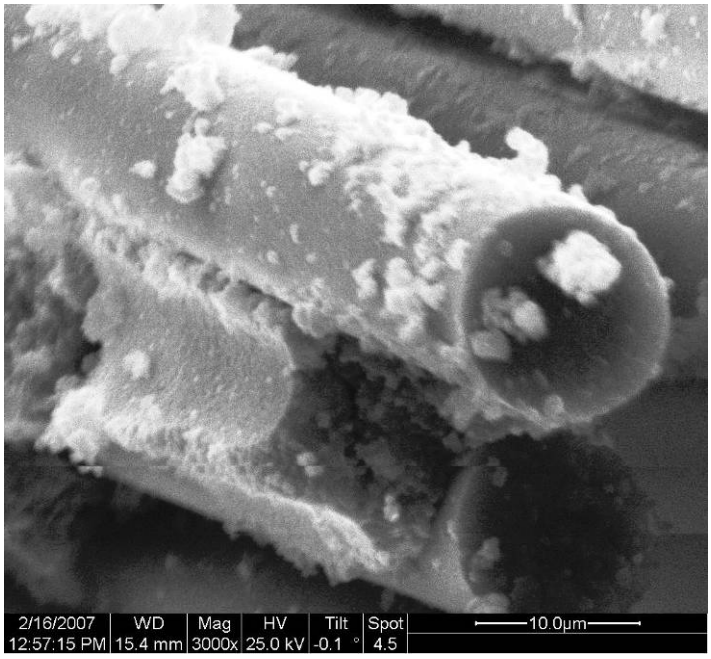

Figure 209. Fracture surface of N720/A specimen tested in creep at 150 MPa in air at 1100 °C.

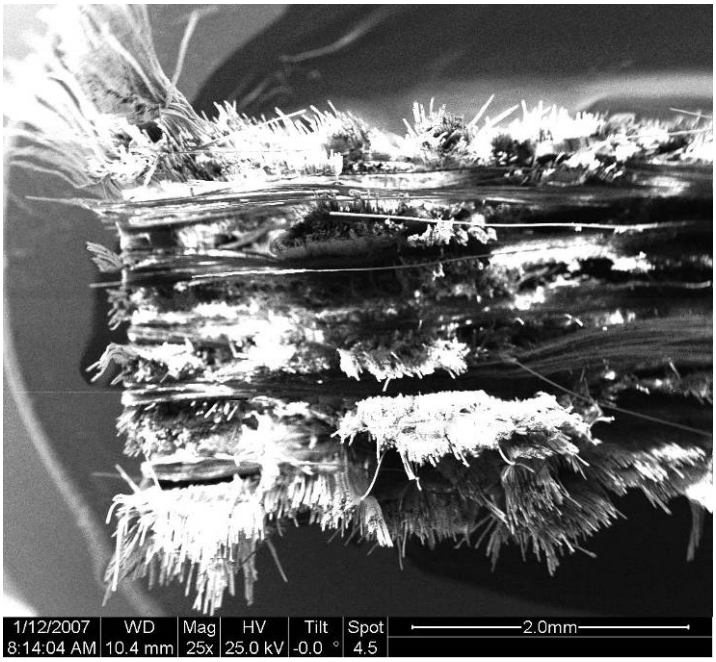

Figure 210. Fracture surface of N720/A specimen tested in creep at 150 MPa in air at 1100 °C.

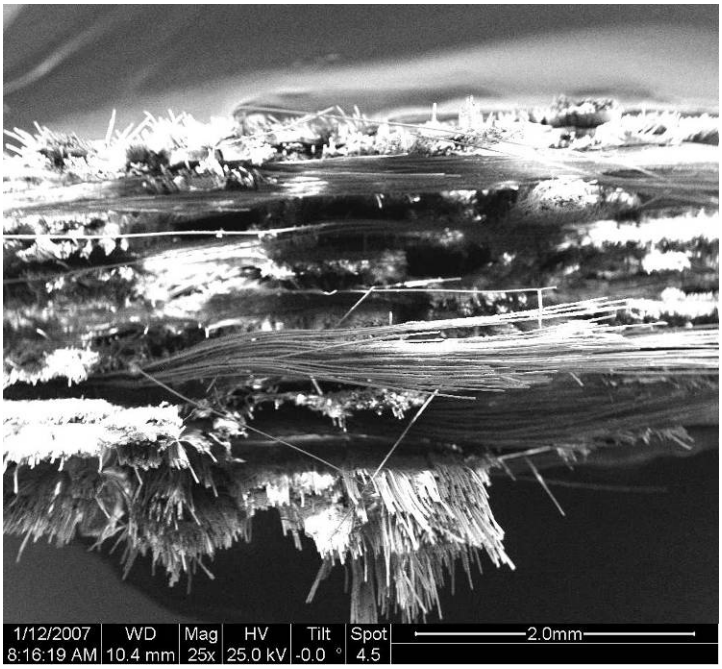

Figure 211. Fracture surface of N720/A specimen tested in creep at 150 MPa in air at 1100 °C.

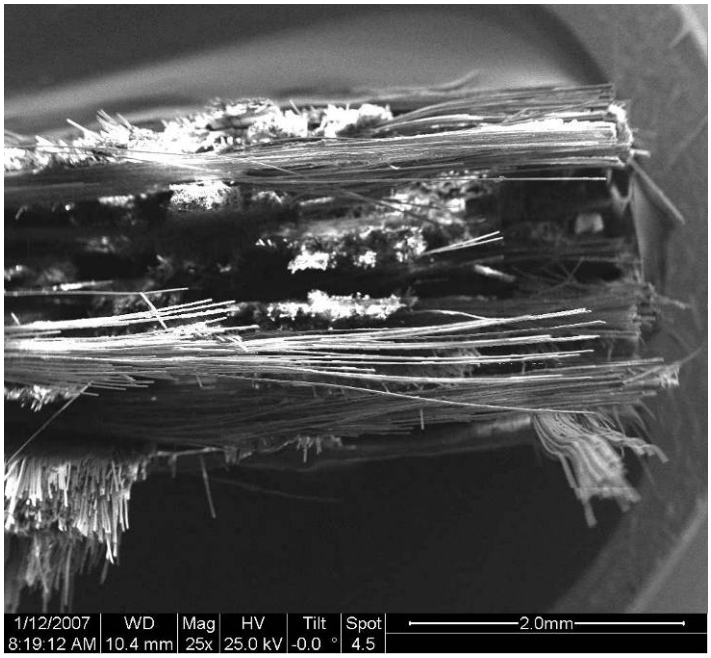

Figure 212. Fracture surface of N720/A specimen tested in creep at 150 MPa in air at 1100 °C.

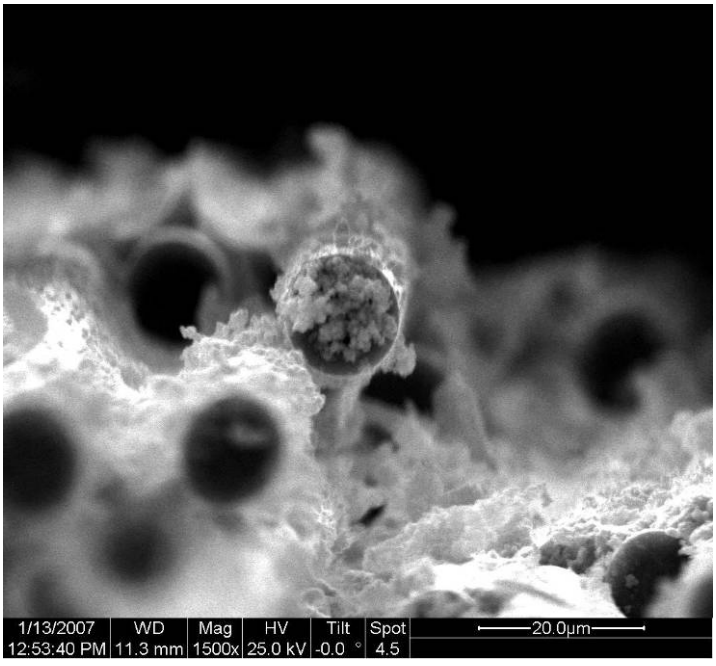

Figure 213. Fracture surface of N720/A specimen tested in creep at 150 MPa in air at 1100 °C.

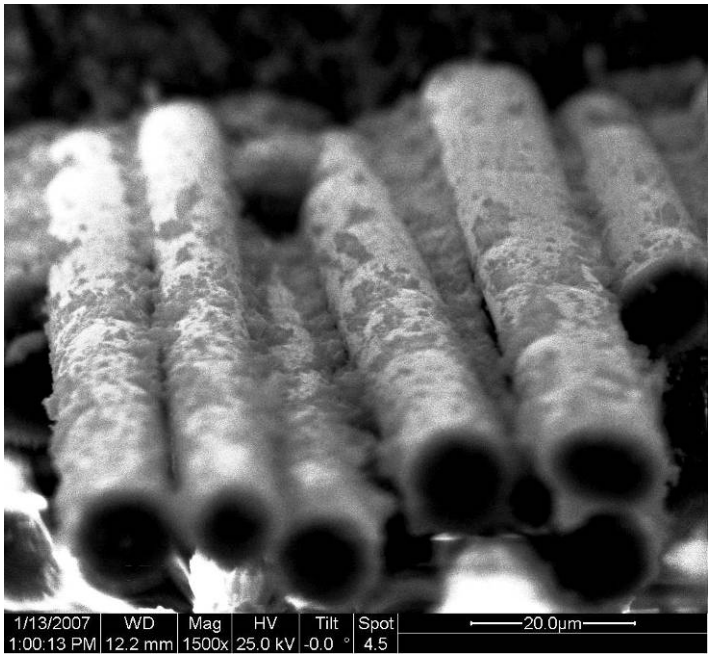

Figure 214. Fracture surface of N720/A specimen tested in creep at 150 MPa in air at 1100 °C.

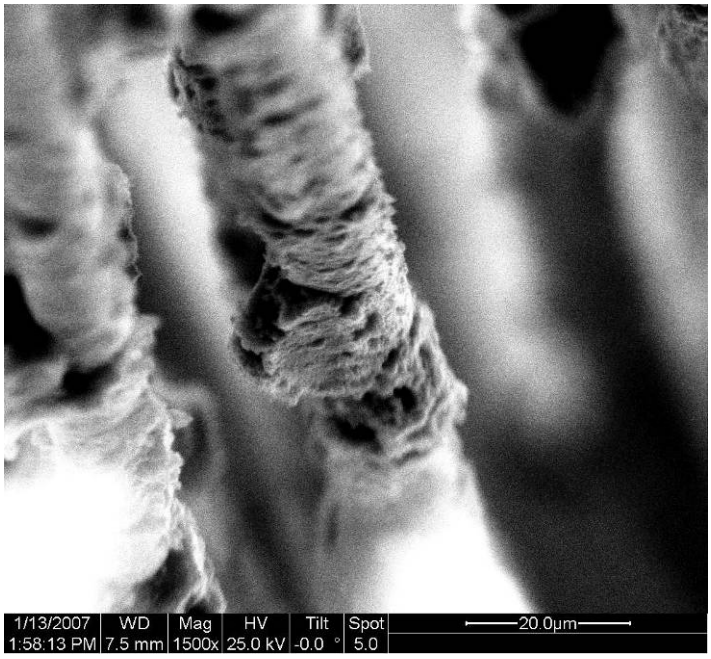

Figure 215. Fracture surface of N720/A specimen tested in creep at 150 MPa in air at 1100 °C.

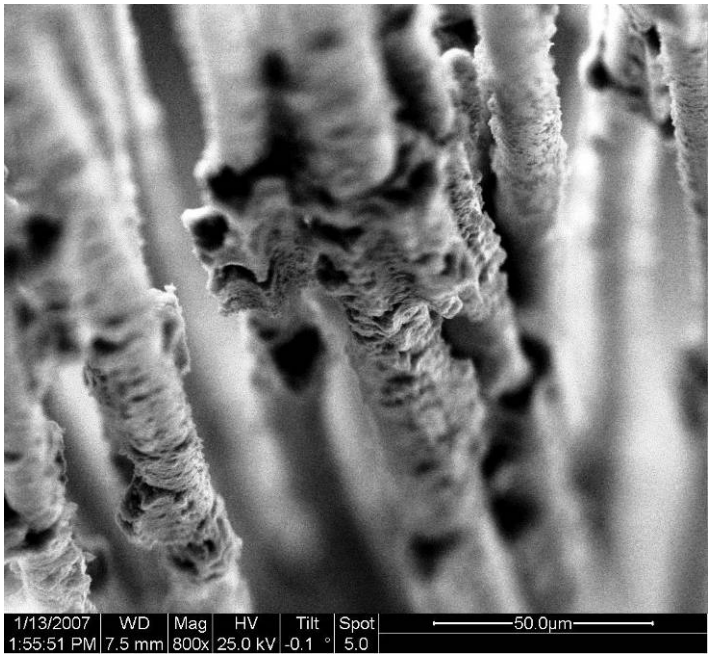

Figure 216. Fracture surface of N720/A specimen tested in creep at 150 MPa in air at 1100 °C.

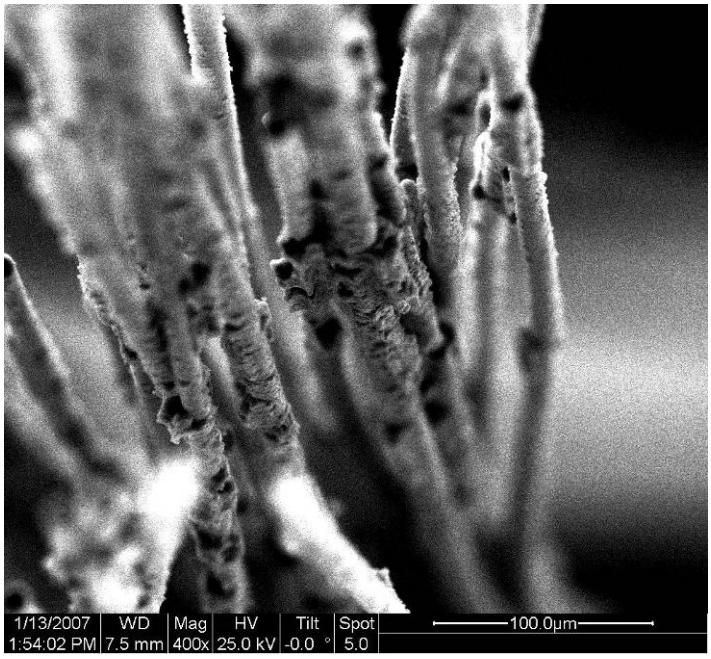

Figure 217. Fracture surface of N720/A specimen tested in creep at 150 MPa in air at 1100 °C.

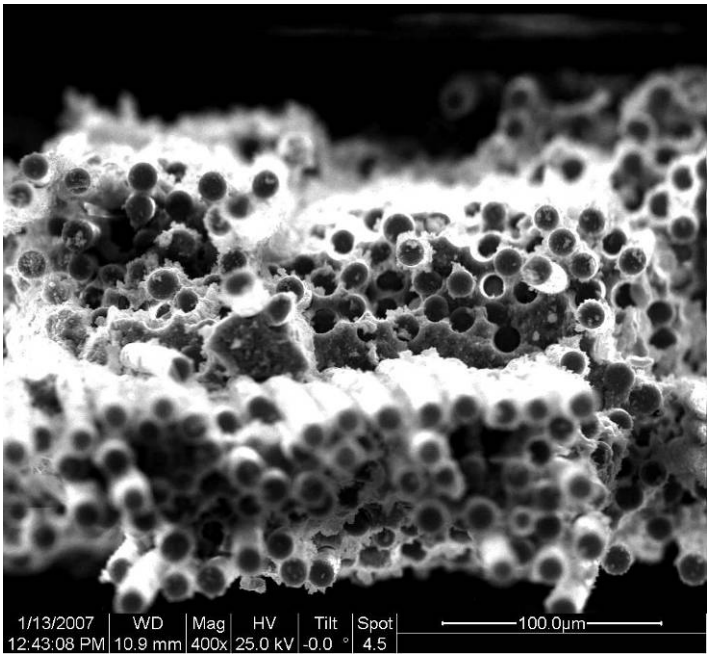

Figure 218. Fracture surface of N720/A specimen tested in creep at 150 MPa in air at 1100 °C.

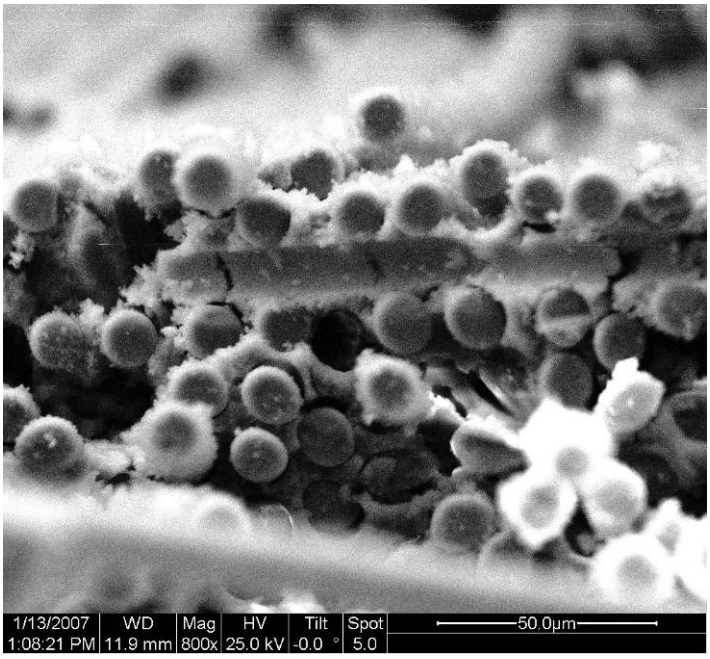

Figure 219. Fracture surface of N720/A specimen tested in creep at 150 MPa in air at 1100 °C.

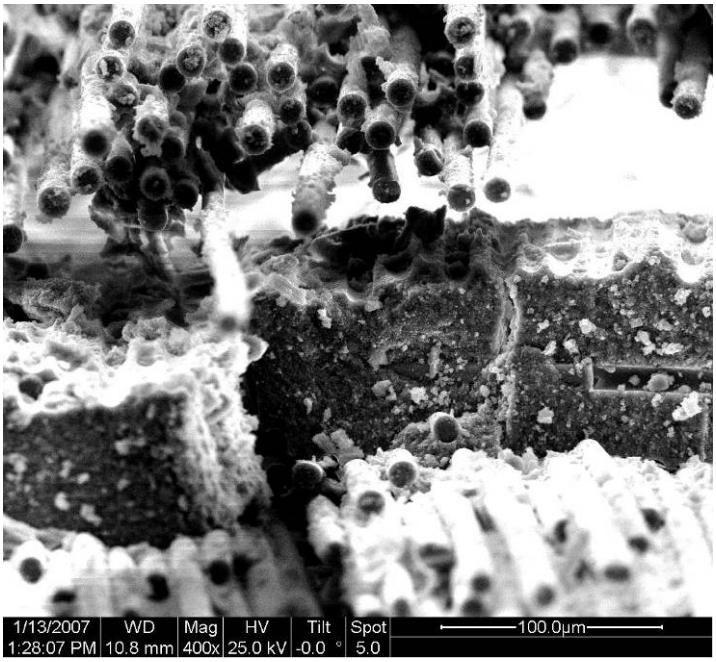

Figure 220. Fracture surface of N720/A specimen tested in creep at 150 MPa in air at 1100 °C.

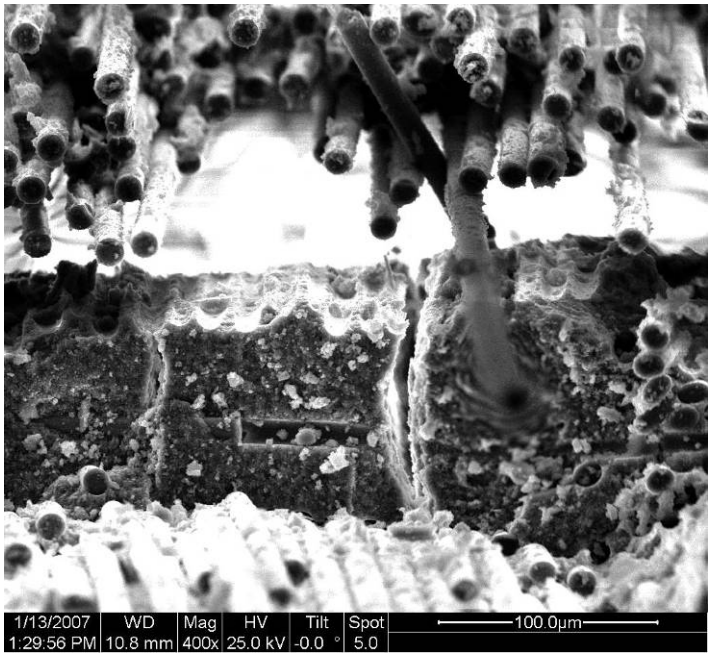

Figure 221. Fracture surface of N720/A specimen tested in creep at 150 MPa in air at 1100 °C.

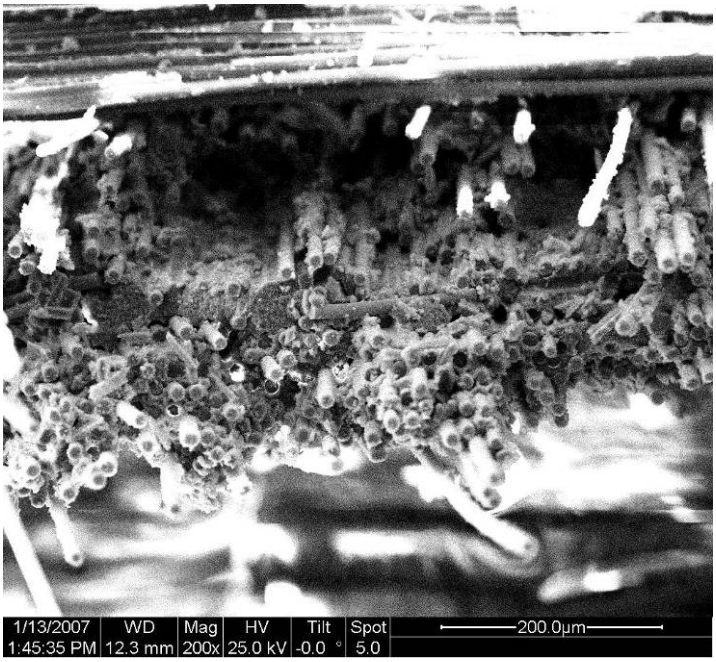

Figure 222. Fracture surface of N720/A specimen tested in creep at 150 MPa in air at 1100 °C.

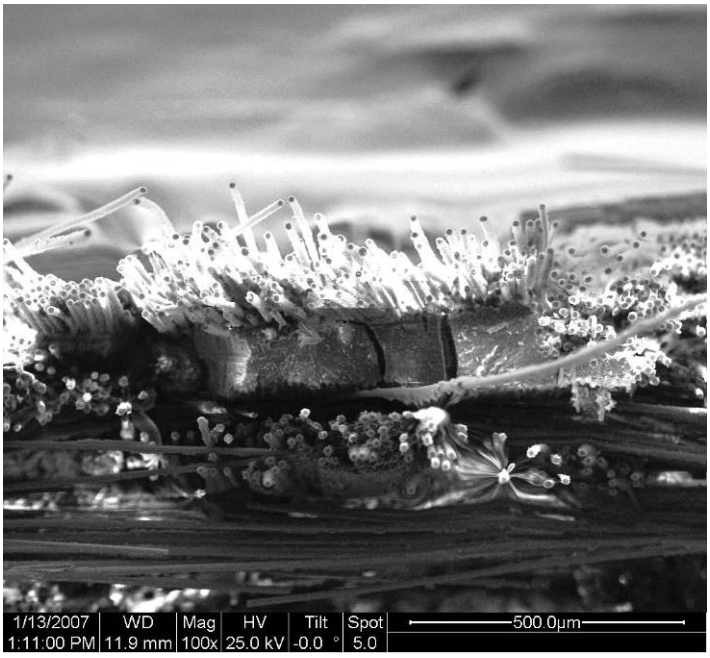

Figure 223. Fracture surface of N720/A specimen tested in creep at 150 MPa in air at 1100 °C.

Figure 224. Fracture surface of N720/A specimen tested in creep at 150 MPa in air at 1100 °C.

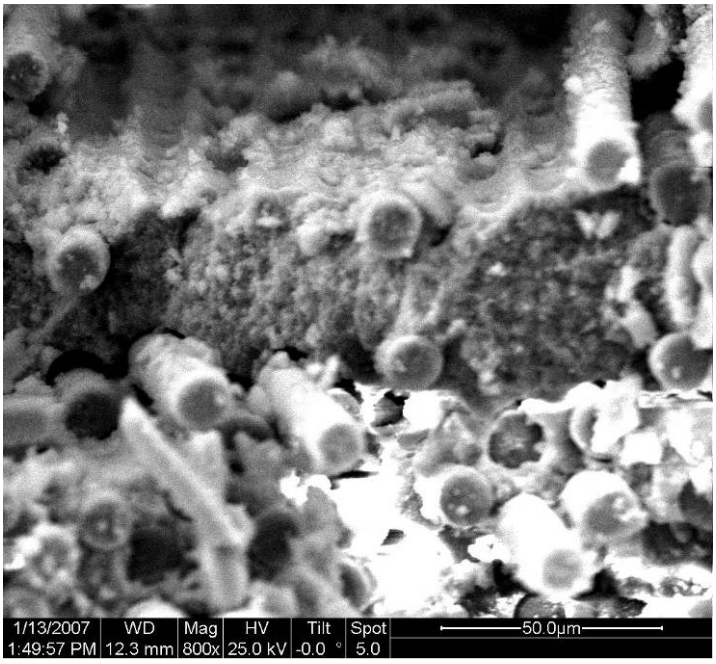

Figure 225. Fracture surface of N720/A specimen tested in creep at 150 MPa in air at 1100 °C.

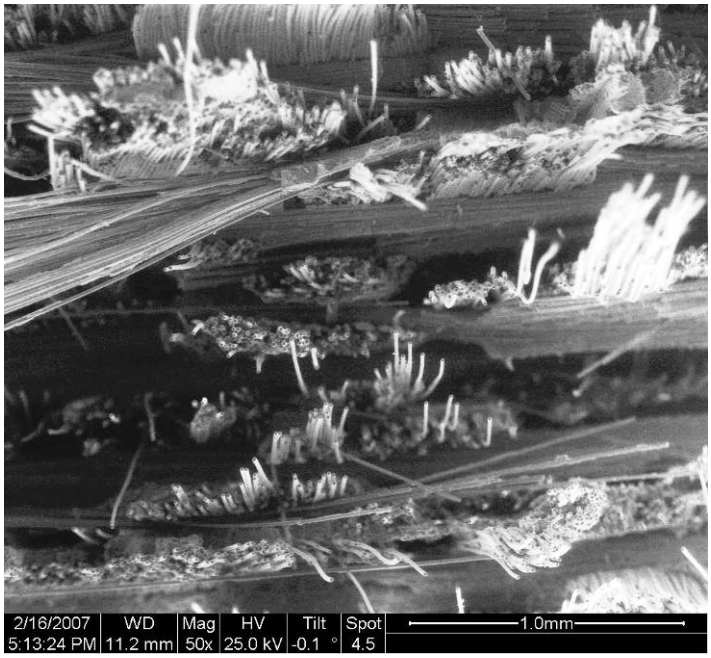

Figure 226. Fracture surface of N720/A specimen tested in creep at 100 MPa in steam at 1100 °C.

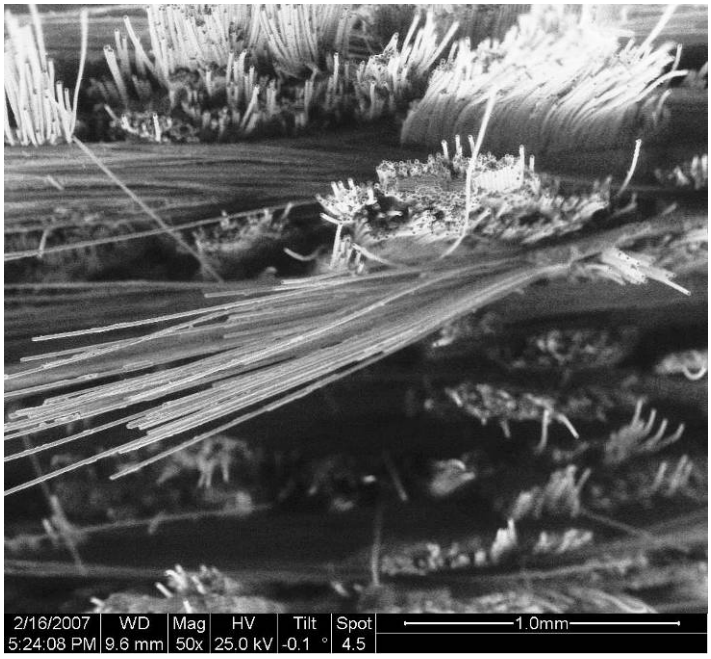

Figure 227. Fracture surface of N720/A specimen tested in creep at 100 MPa in steam at 1100 °C.

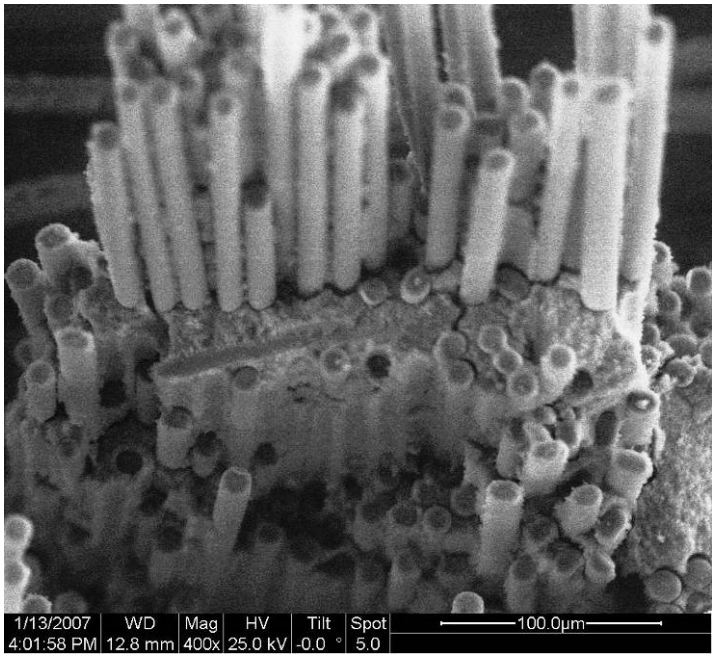

Figure 228. Fracture surface of N720/A specimen tested in creep at 100 MPa in steam at 1100 °C.

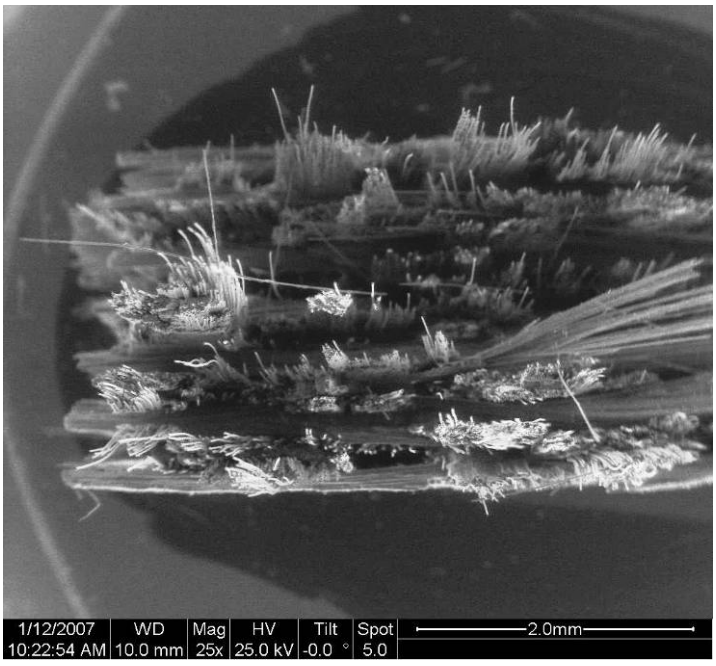

Figure 229. Fracture surface of N720/A specimen tested in creep at 100 MPa in steam at 1100 °C.

Figure 230. Fracture surface of N720/A specimen tested in creep at 100 MPa in steam at 1100 °C.

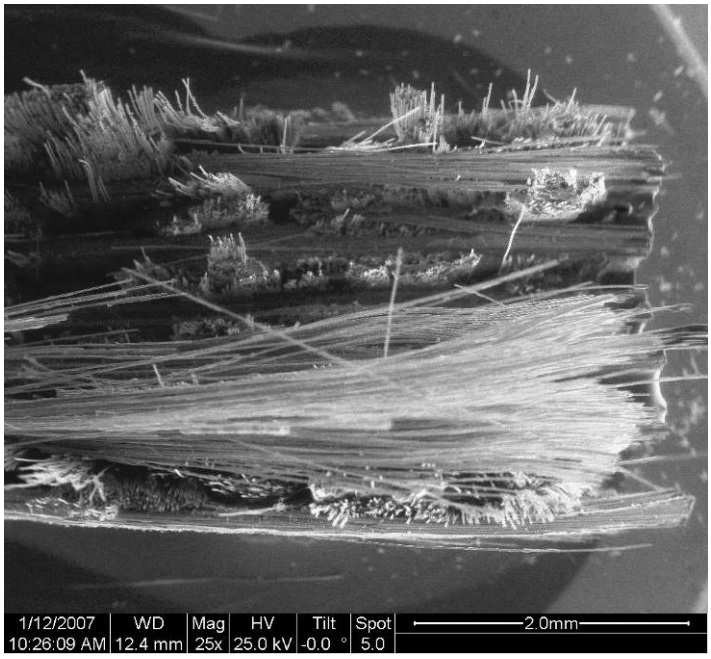

Figure 231. Fracture surface of N720/A specimen tested in creep at 100 MPa in steam at 1100 °C.

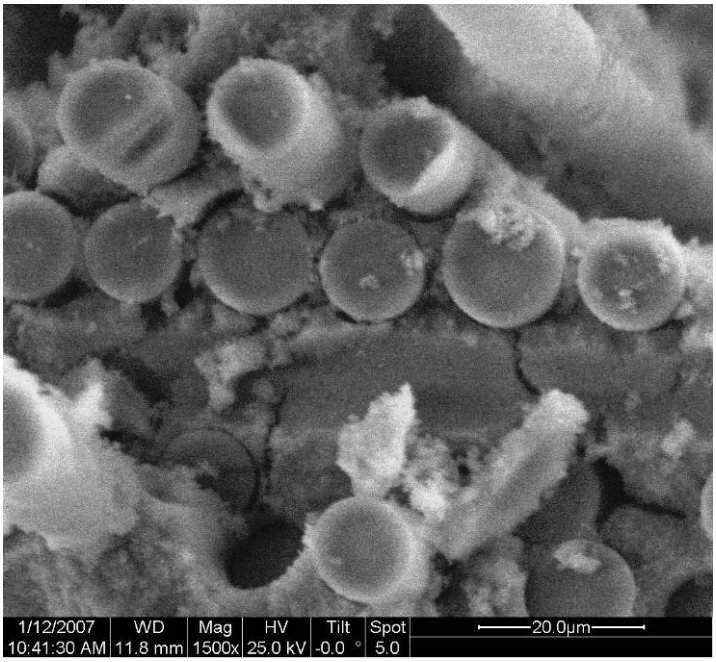

Figure 232. Fracture surface of N720/A specimen tested in creep at 100 MPa in steam at 1100 °C.

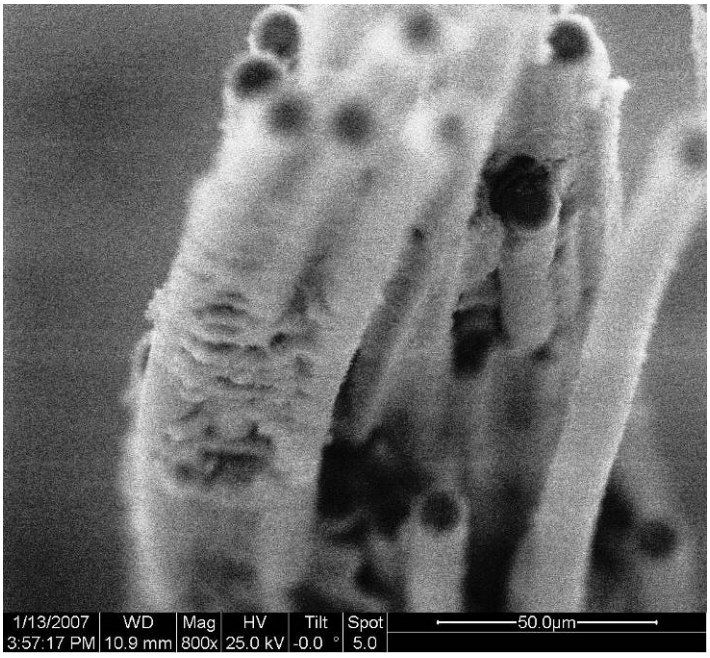

Figure 233. Fracture surface of N720/A specimen tested in creep at 100 MPa in steam at 1100 °C.

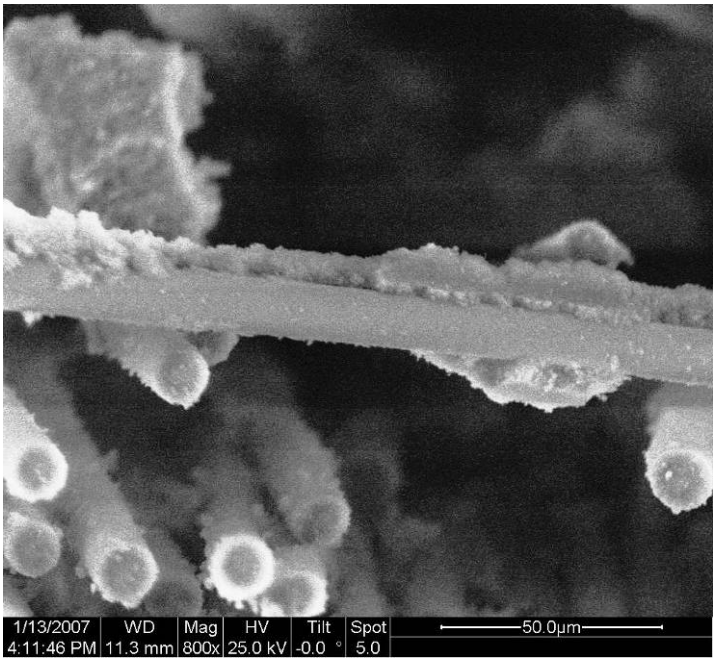

Figure 234. Fracture surface of N720/A specimen tested in creep at 100 MPa in steam at 1100 °C.

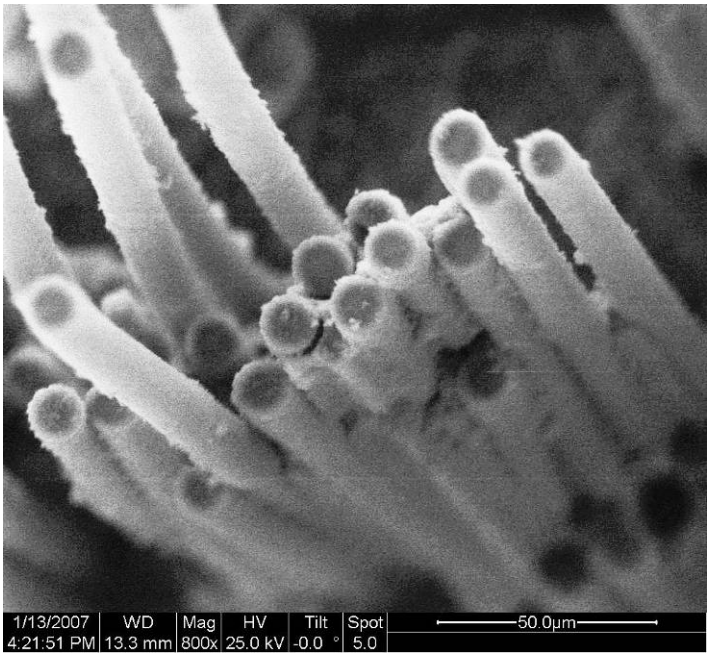

Figure 235. Fracture surface of N720/A specimen tested in creep at 100 MPa in steam at 1100 °C.

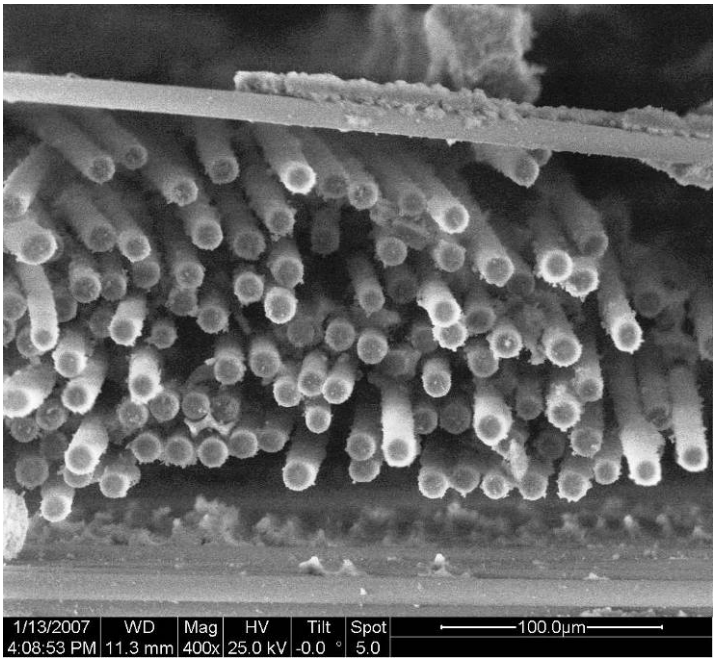

Figure 236. Fracture surface of N720/A specimen tested in creep at 100 MPa in steam at 1100 °C.

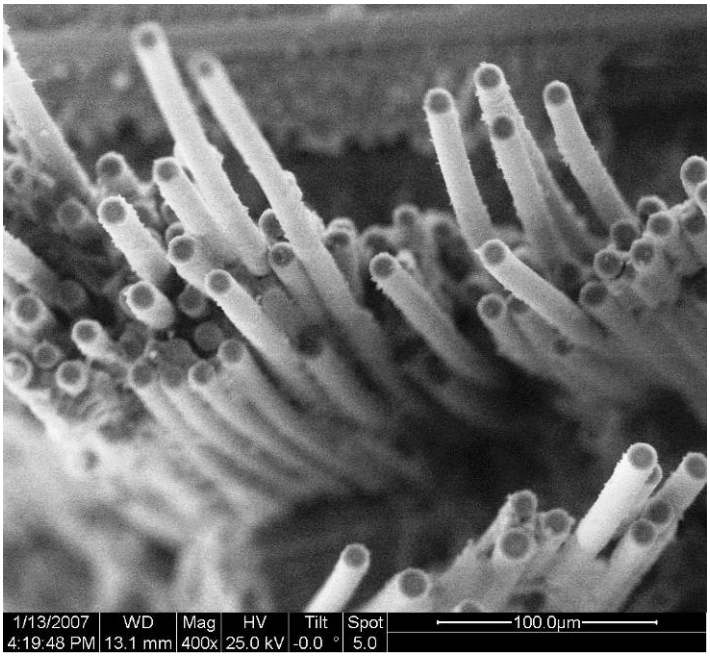

Figure 237. Fracture surface of N720/A specimen tested in creep at 100 MPa in steam at 1100 °C.

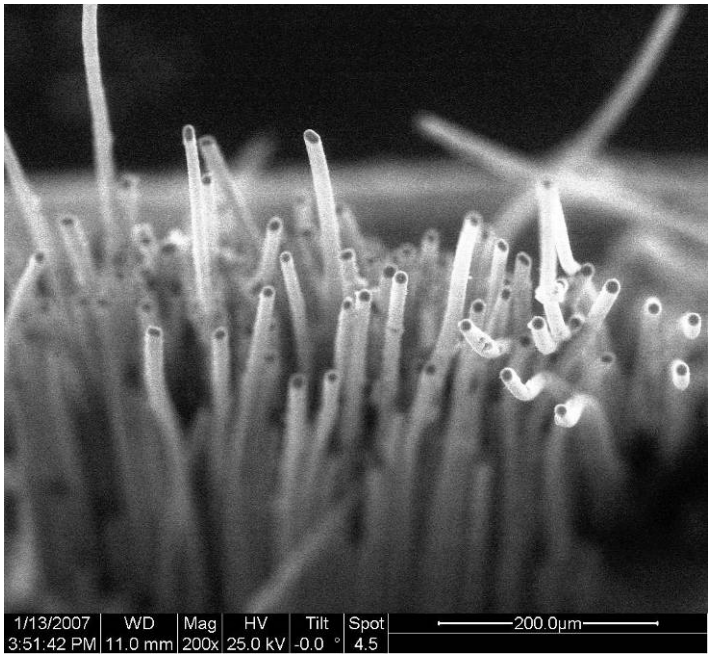

Figure 238. Fracture surface of N720/A specimen tested in creep at 100 MPa in steam at 1100 °C.

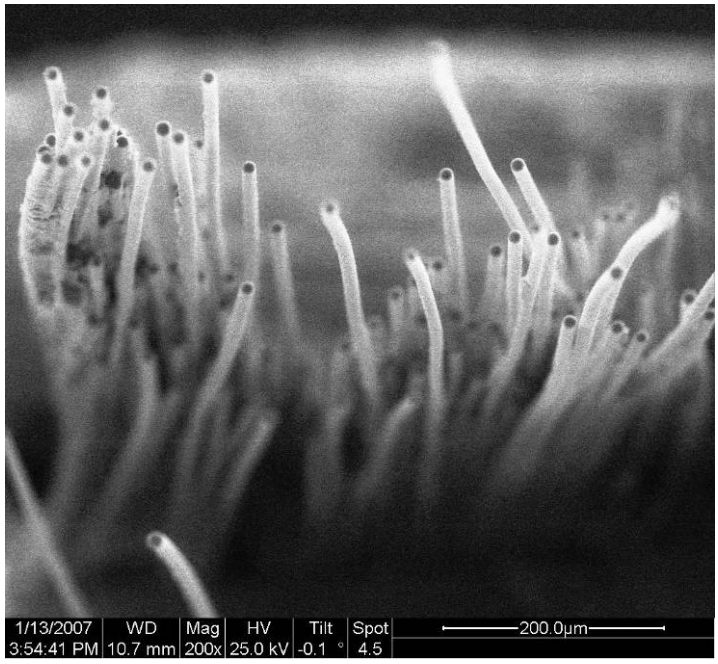

Figure 239. Fracture surface of N720/A specimen tested in creep at 100 MPa in steam at 1100 °C.

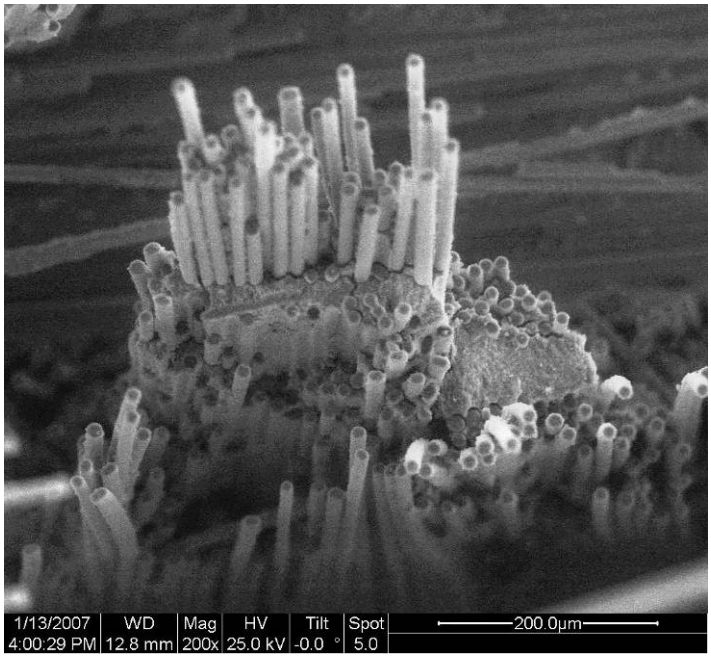

Figure 240. Fracture surface of N720/A specimen tested in creep at 100 MPa in steam at 1100 °C.

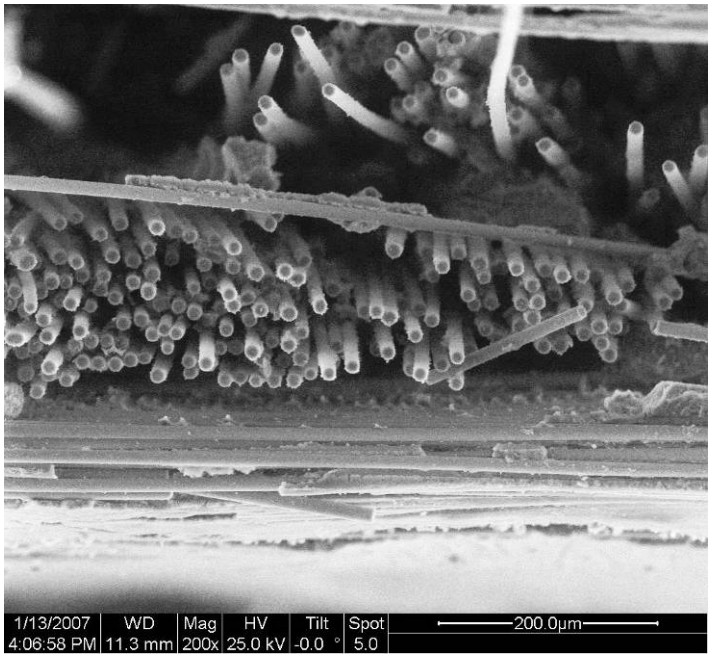

Figure 241. Fracture surface of N720/A specimen tested in creep at 100 MPa in steam at 1100 °C.

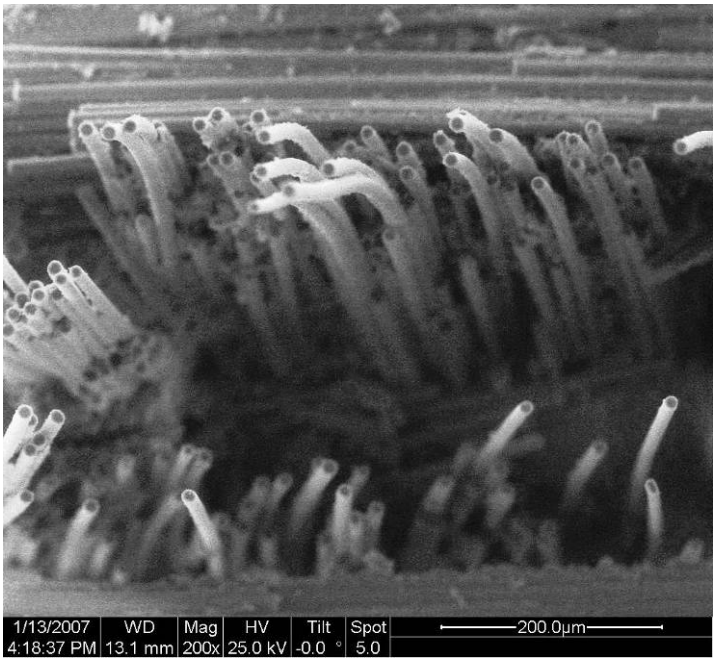

Figure 242. Fracture surface of N720/A specimen tested in creep at 100 MPa in steam at 1100 °C.

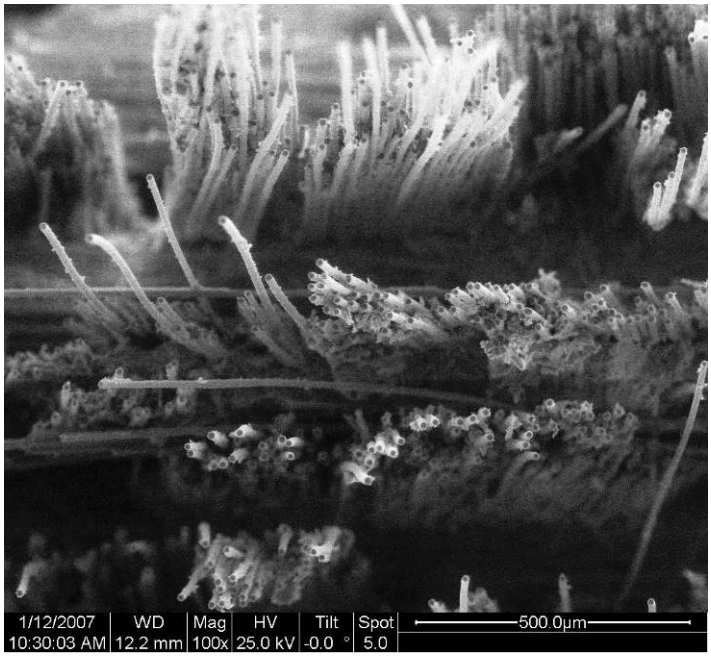

Figure 243. Fracture surface of N720/A specimen tested in creep at 100 MPa in steam at 1100 °C.

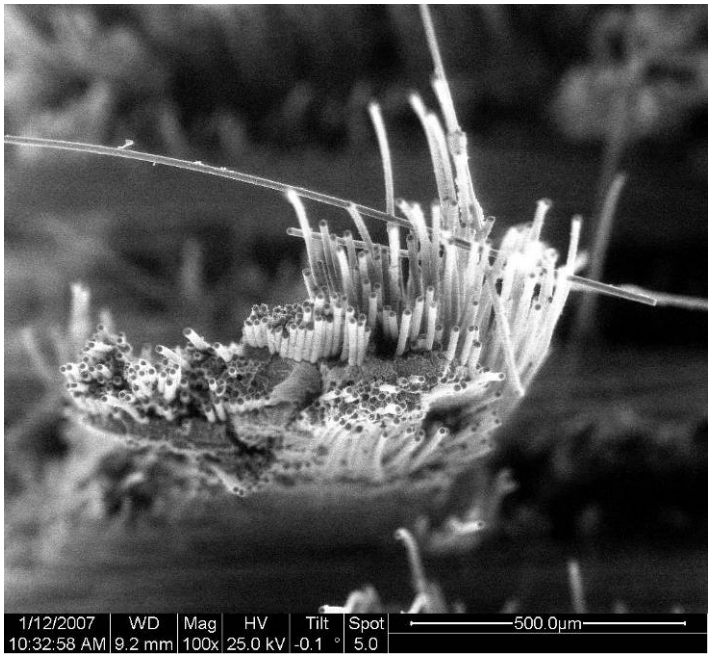

Figure 244. Fracture surface of N720/A specimen tested in creep at 100 MPa in steam at 1100 °C.

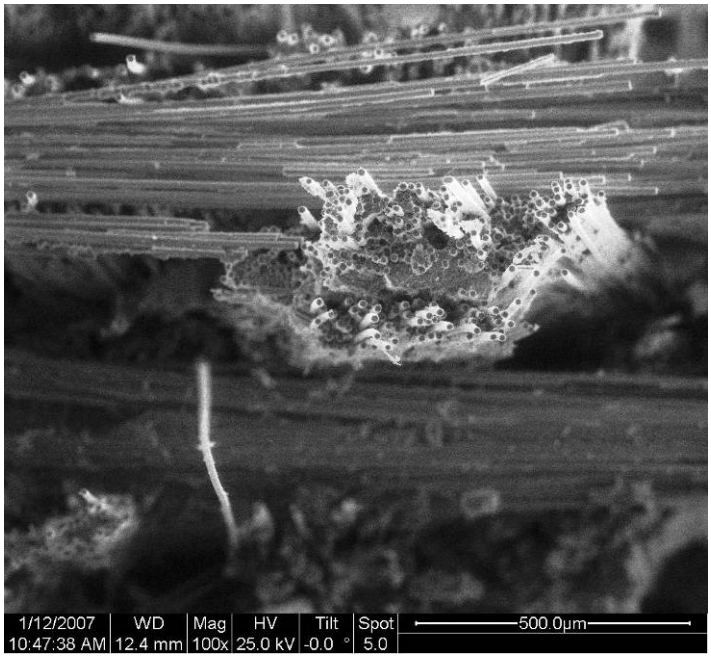

Figure 245. Fracture surface of N720/A specimen tested in creep at 100 MPa in steam at 1100 °C.

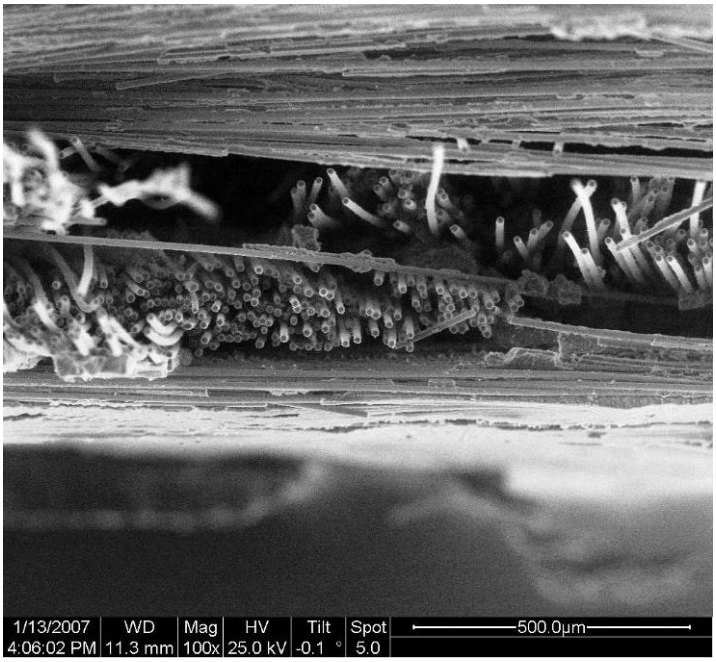

Figure 246. Fracture surface of N720/A specimen tested in creep at 100 MPa in steam at 1100 °C.

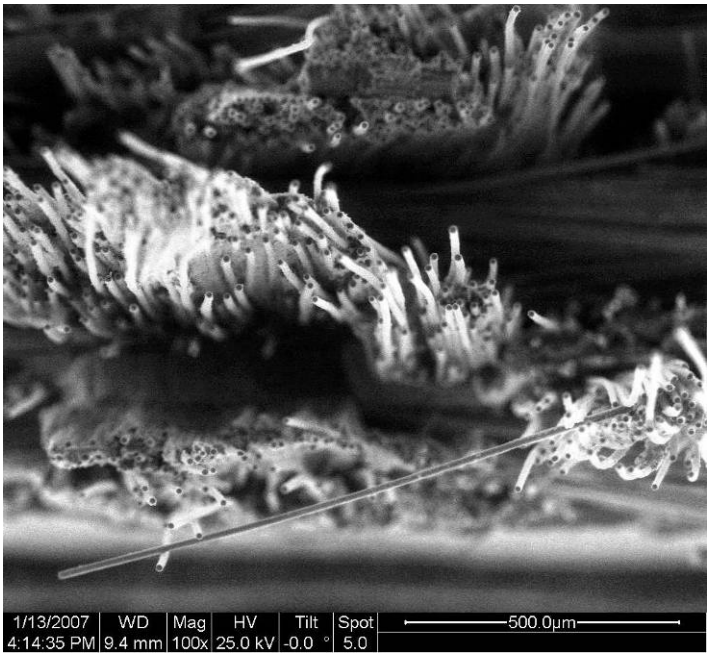

Figure 247. Fracture surface of N720/A specimen tested in creep at 100 MPa in steam at 1100 °C.

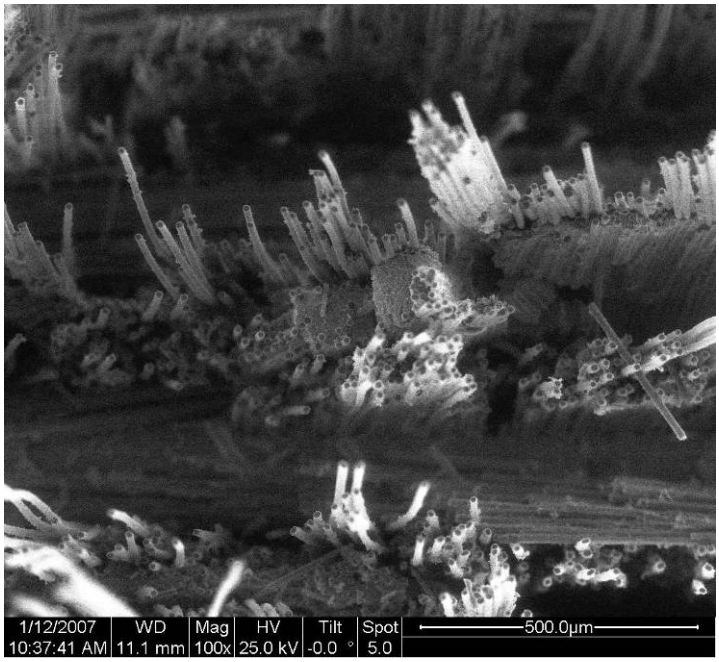

Figure 248. Fracture surface of N720/A specimen tested in creep at 100 MPa in steam at 1100 °C.

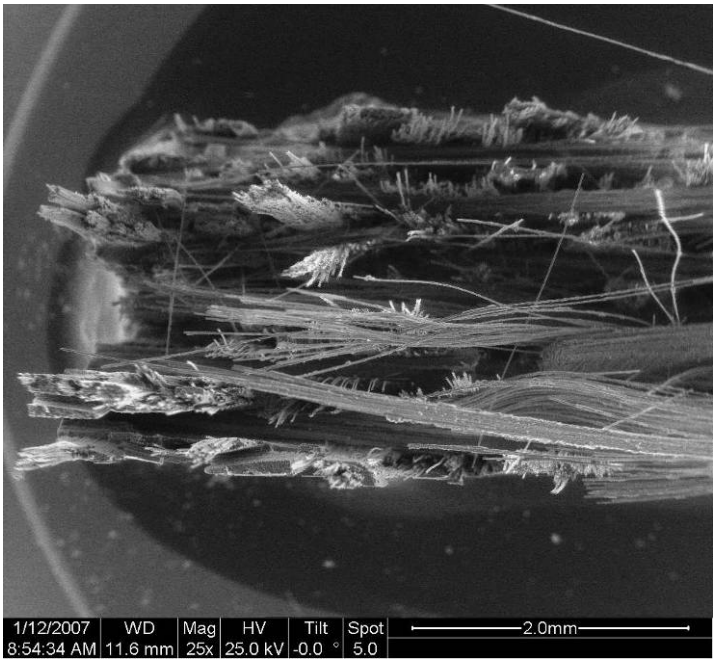

Figure 249. Fracture surface of N720/A specimen tested in creep at 125 MPa in steam at 1100 °C.

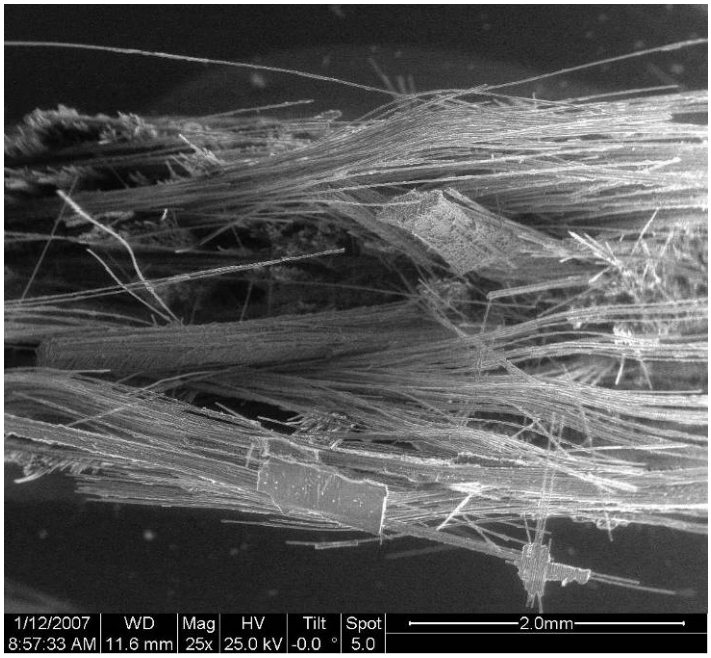

Figure 250. Fracture surface of N720/A specimen tested in creep at 125 MPa in steam at 1100 °C.

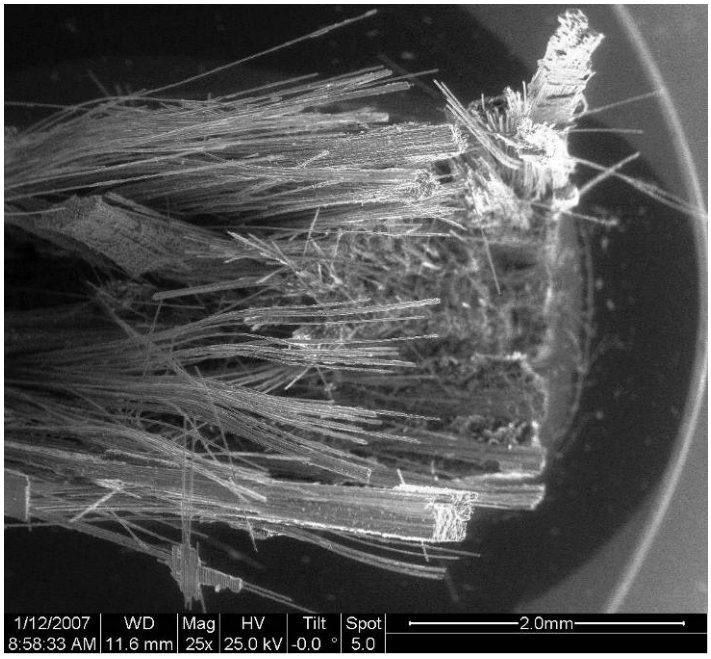

Figure 251. Fracture surface of N720/A specimen tested in creep at 125 MPa in steam at 1100 °C.

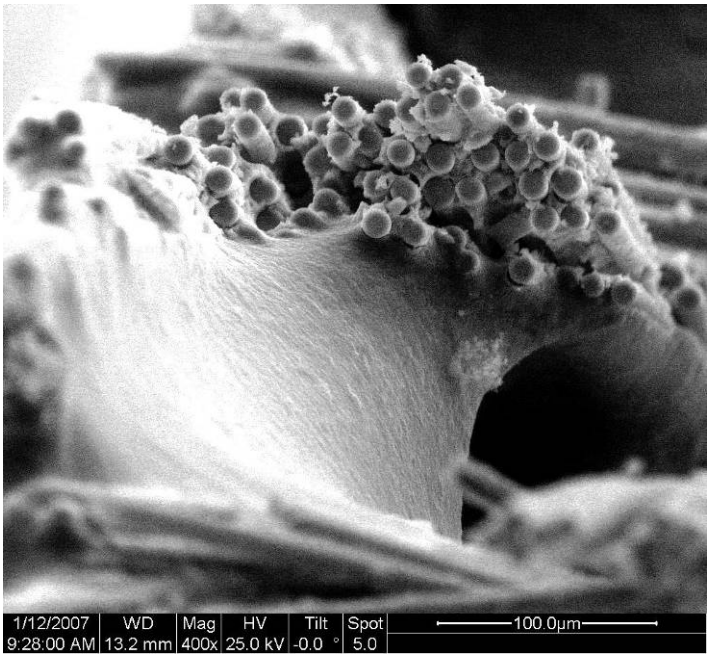

Figure 252. Fracture surface of N720/A specimen tested in creep at 125 MPa in steam at 1100 °C.

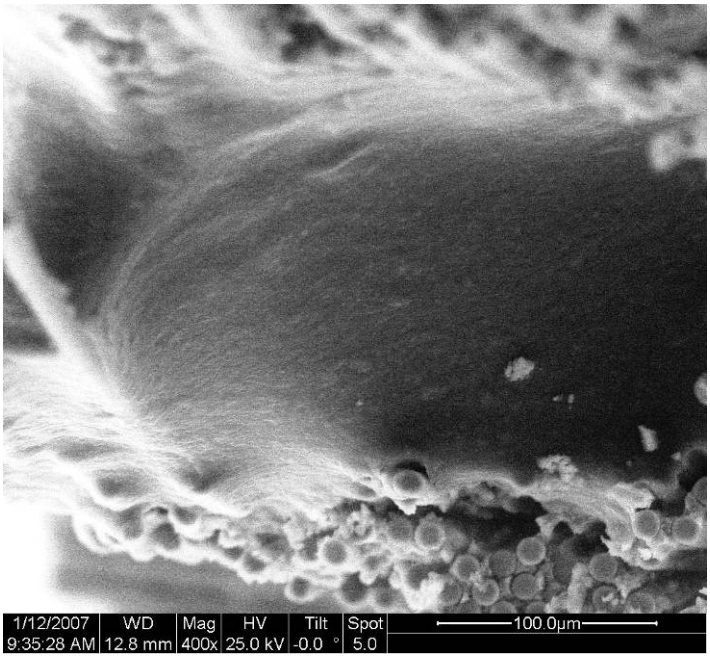

Figure 253. Fracture surface of N720/A specimen tested in creep at 125 MPa in steam at 1100 °C.

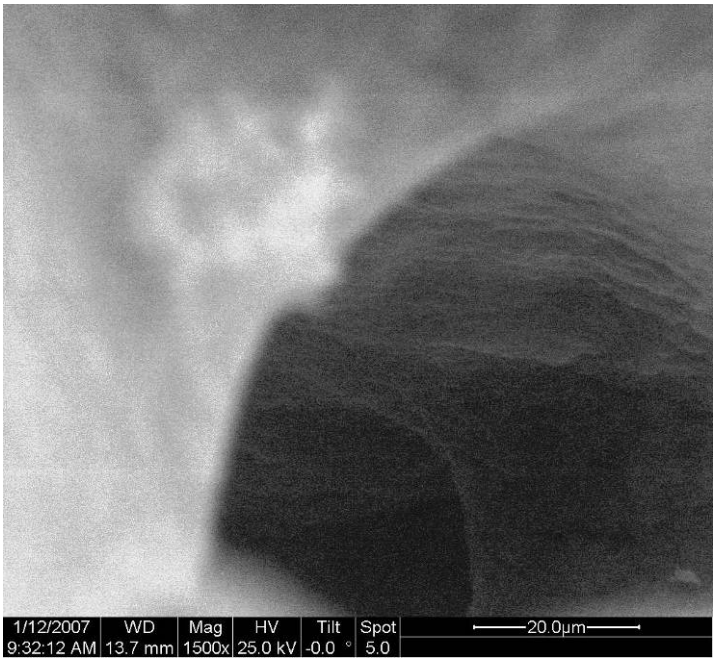

Figure 254. Fracture surface of N720/A specimen tested in creep at 125 MPa in steam at 1100 °C.

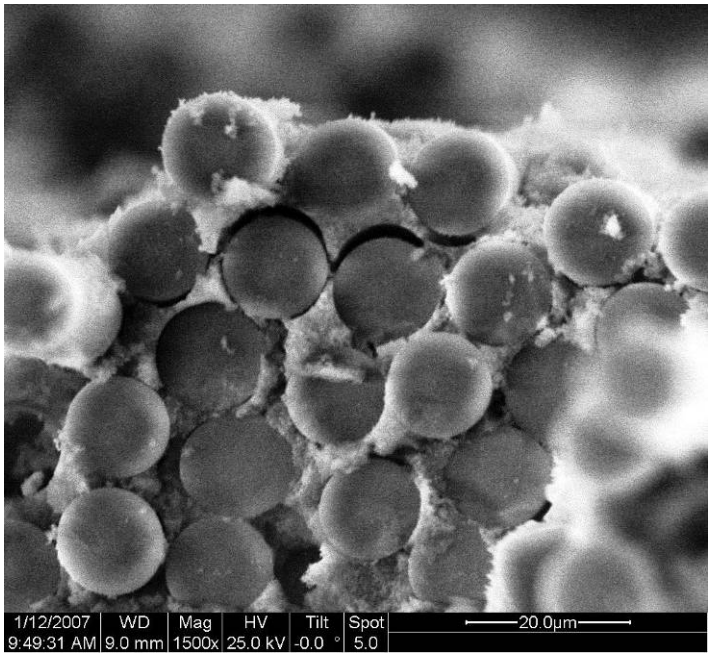

Figure 255. Fracture surface of N720/A specimen tested in creep at 125 MPa in steam at 1100 °C.

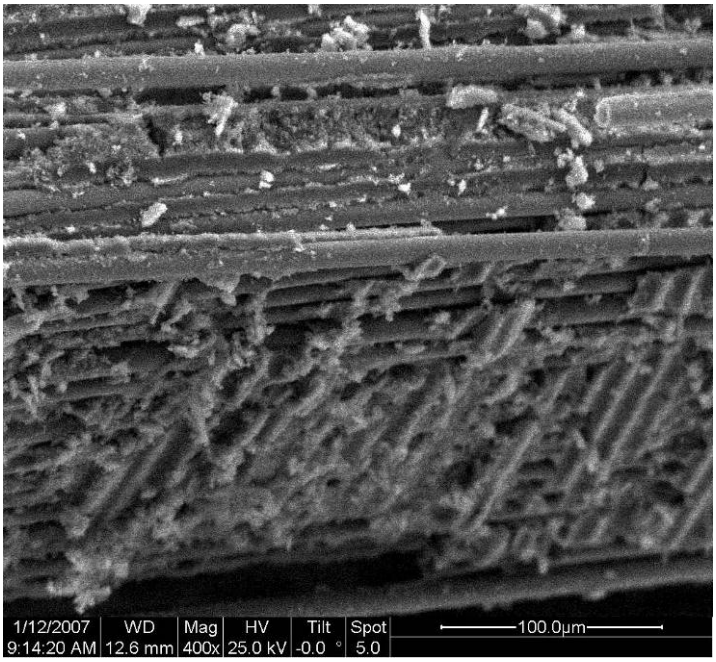

Figure 256. Fracture surface of N720/A specimen tested in creep at 125 MPa in steam at 1100 °C.

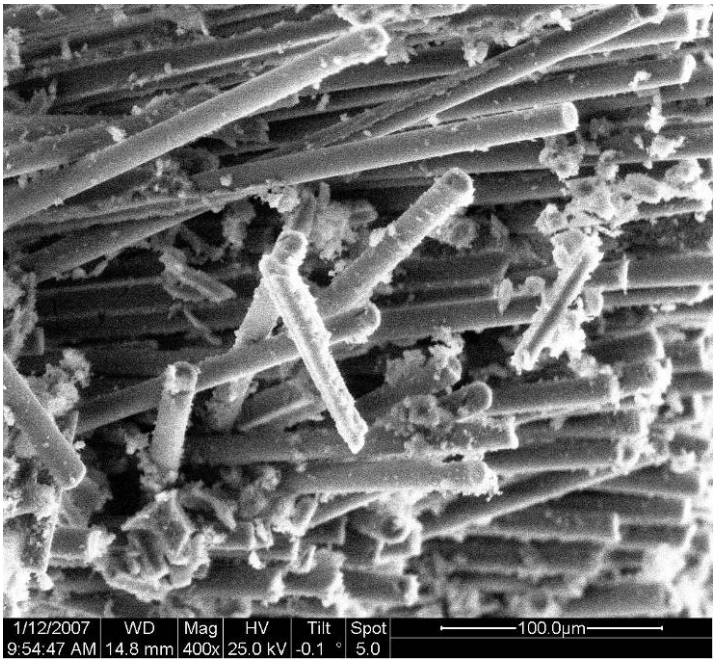

Figure 257. Fracture surface of N720/A specimen tested in creep at 125 MPa in steam at 1100 °C.

Figure 258. Fracture surface of N720/A specimen tested in creep at 125 MPa in steam at 1100 °C.

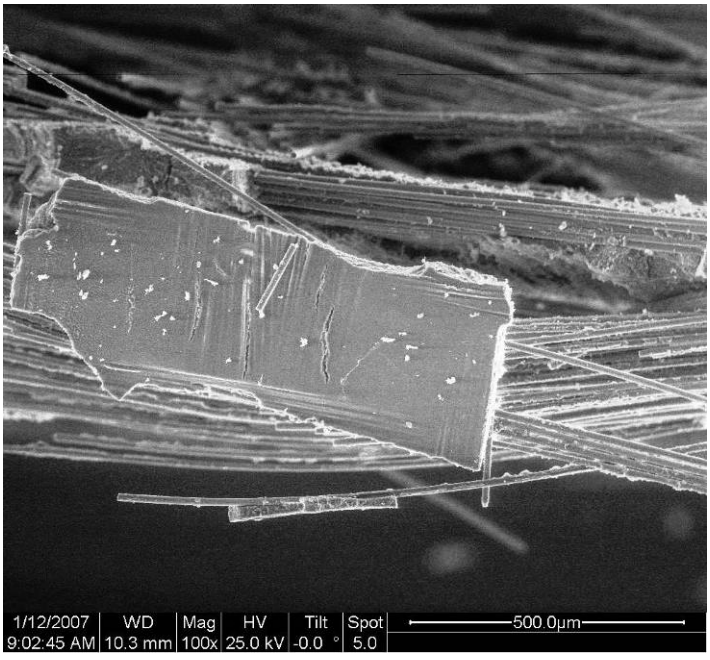

Figure 259. Fracture surface of N720/A specimen tested in creep at 125 MPa in steam at 1100 °C.

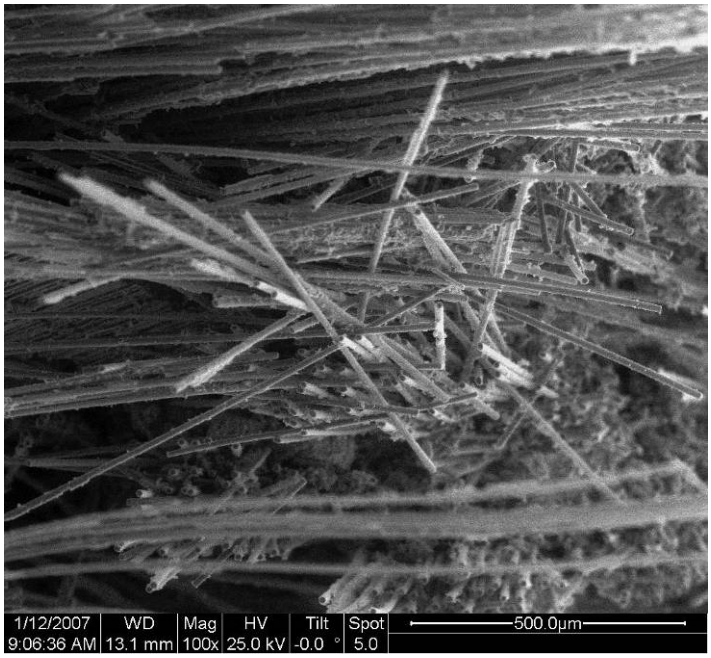

Figure 260. Fracture surface of N720/A specimen tested in creep at 125 MPa in steam at 1100 °C.

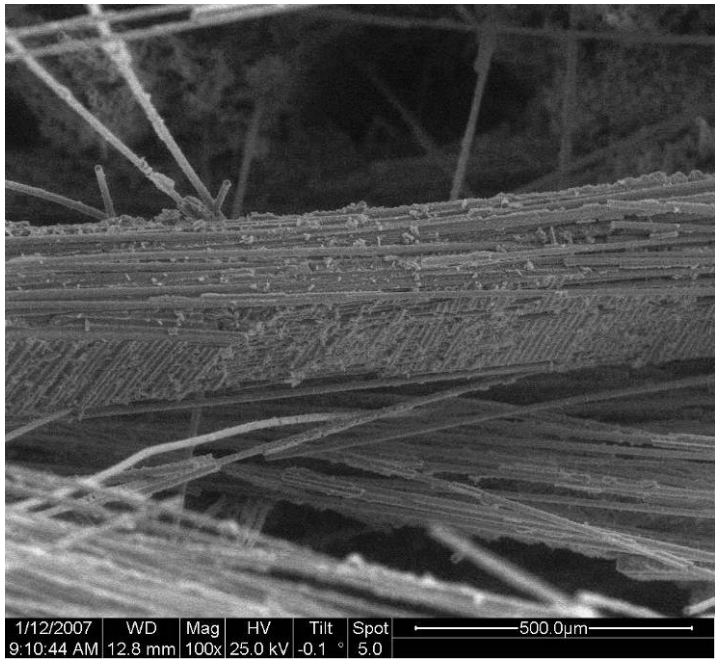

Figure 261. Fracture surface of N720/A specimen tested in creep at 125 MPa in steam at 1100 °C.

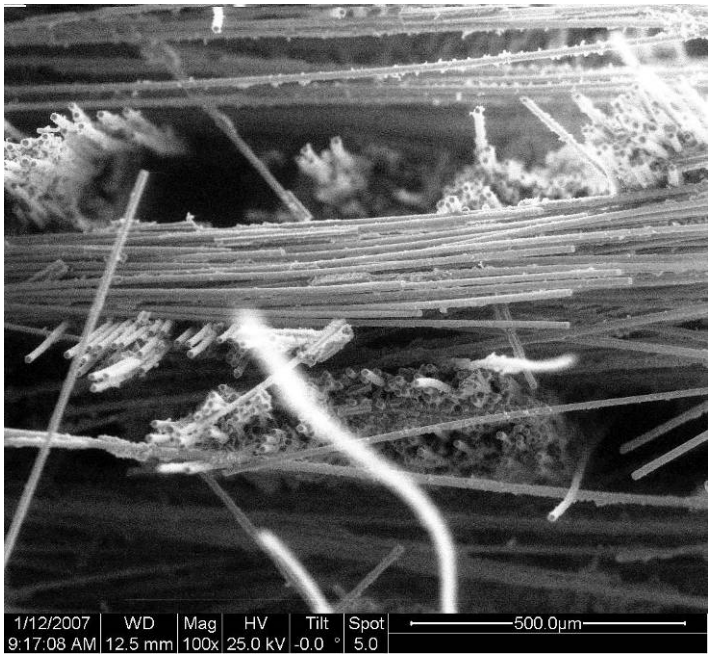

Figure 262. Fracture surface of N720/A specimen tested in creep at 125 MPa in steam at 1100 °C.

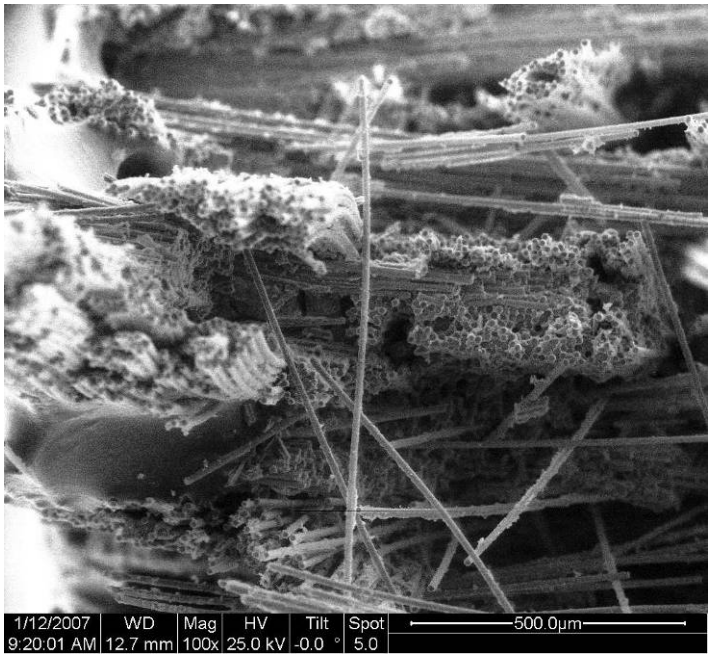

Figure 263. Fracture surface of N720/A specimen tested in creep at 125 MPa in steam at 1100 °C.

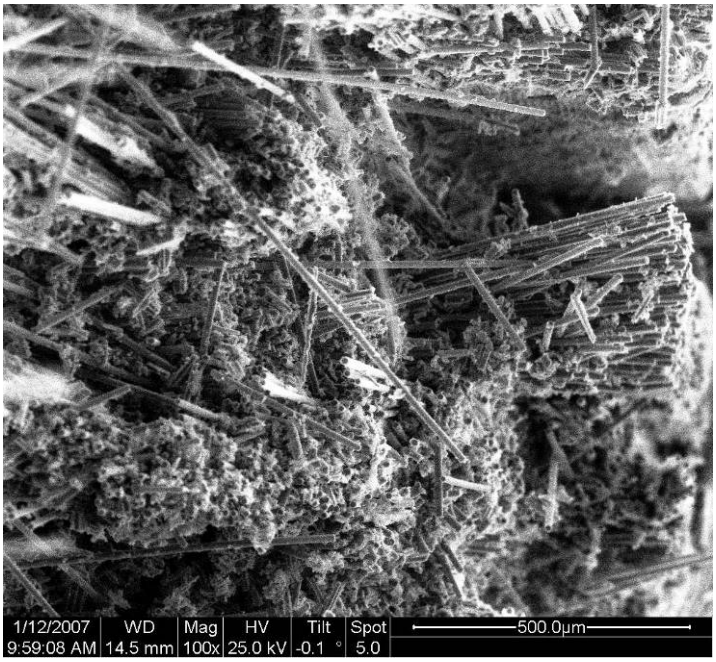

Figure 264. Fracture surface of N720/A specimen tested in creep at 125 MPa in steam at 1100 °C.

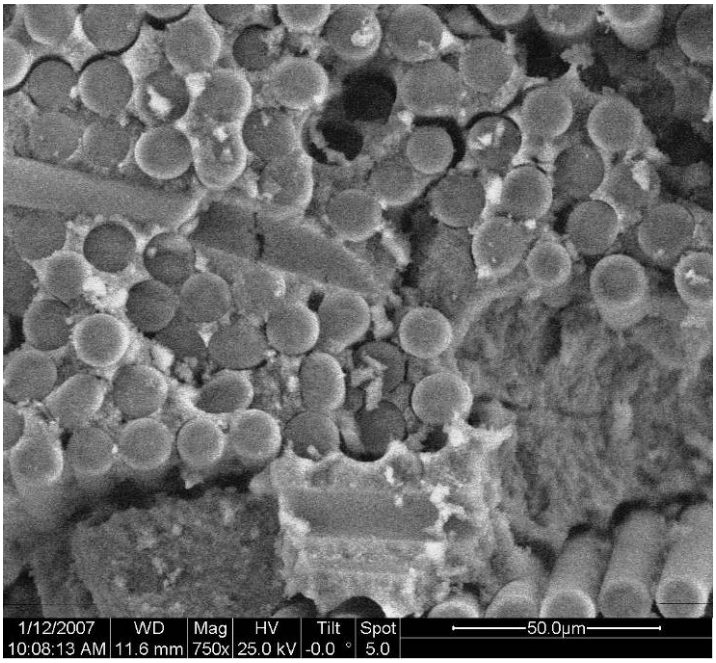

Figure 265. Fracture surface of N720/A specimen tested in creep at 125 MPa in steam at 1100 °C.

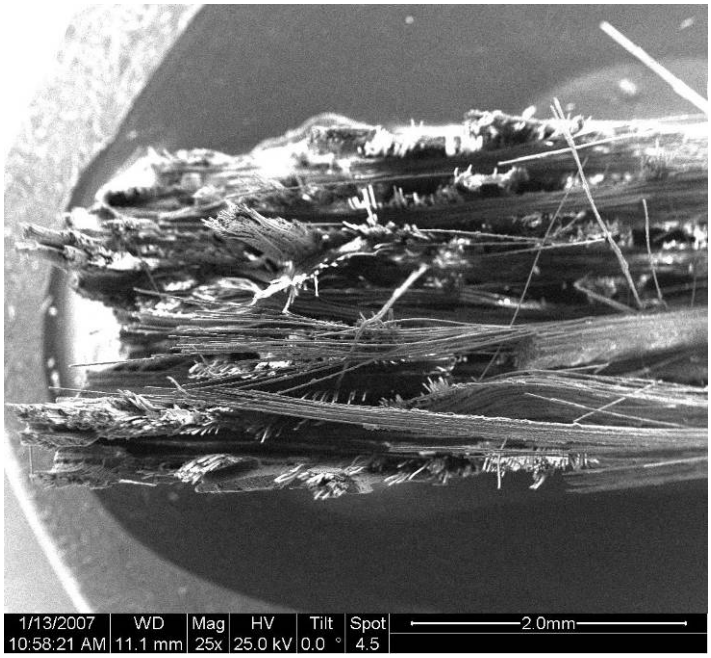

Figure 266. Fracture surface of N720/A specimen tested in creep at 125 MPa in steam at 1100 °C.

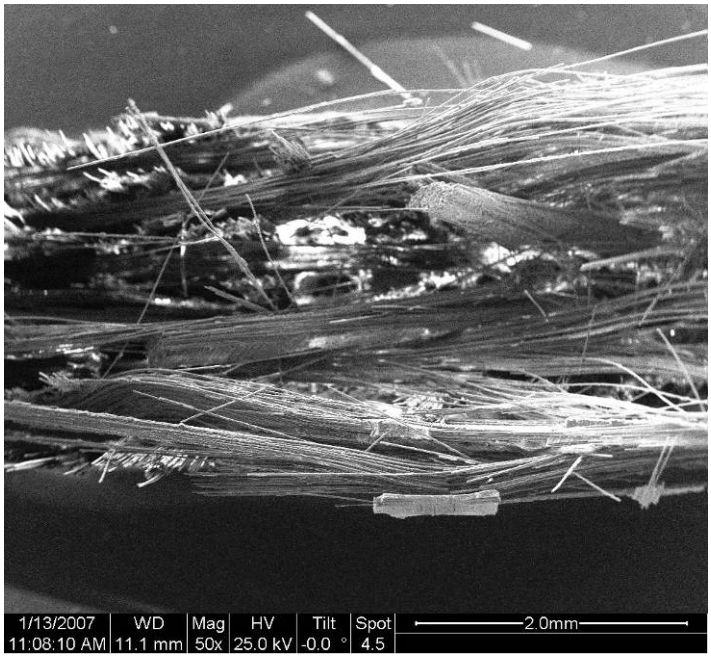

Figure 267. Fracture surface of N720/A specimen tested in creep at 125 MPa in steam at 1100 °C.

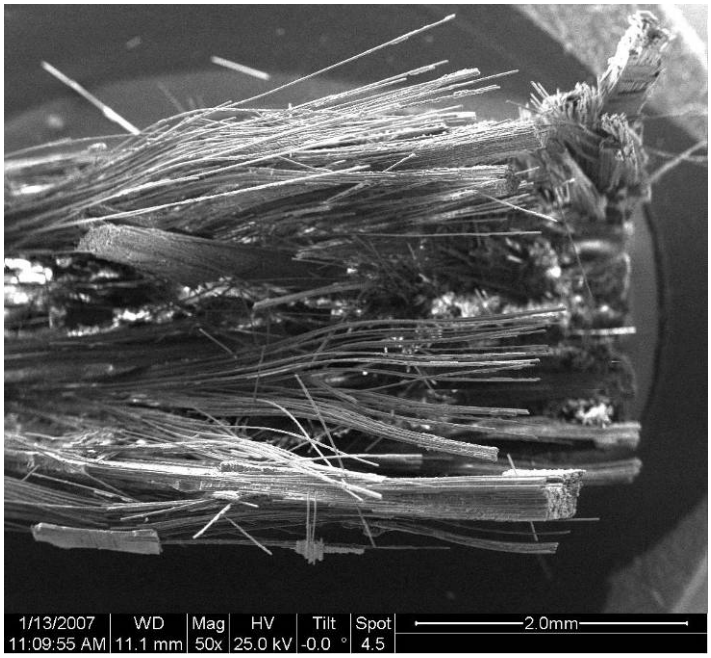

Figure 268. Fracture surface of N720/A specimen tested in creep at 125 MPa in steam at 1100 °C.

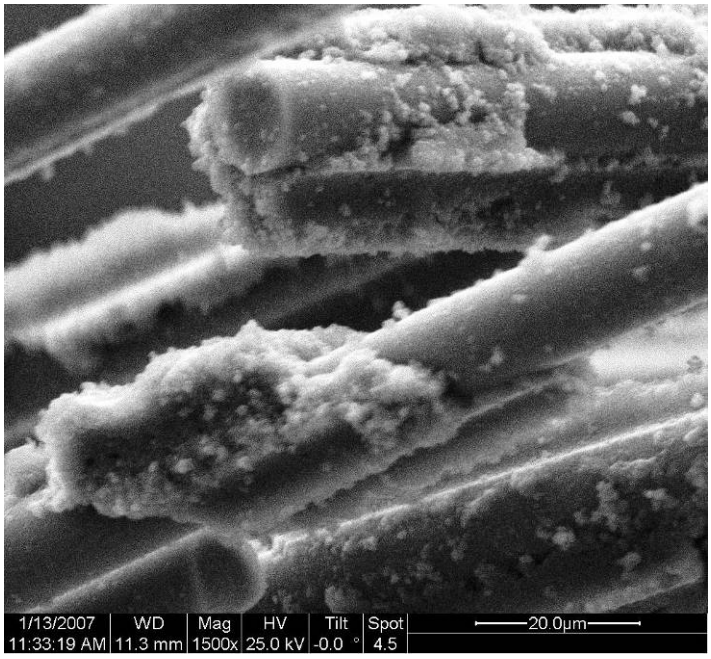

Figure 269. Fracture surface of N720/A specimen tested in creep at 125 MPa in steam at 1100 °C.

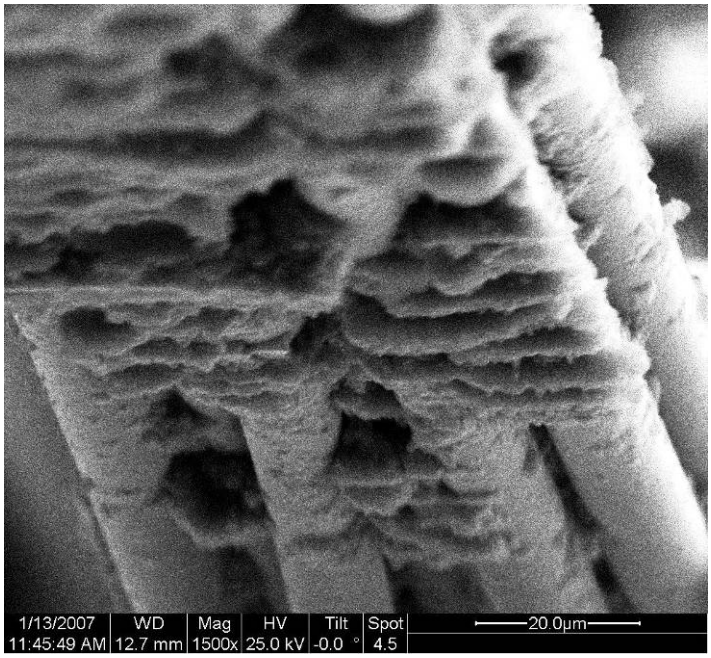

Figure 270. Fracture surface of N720/A specimen tested in creep at 125 MPa in steam at 1100 °C.

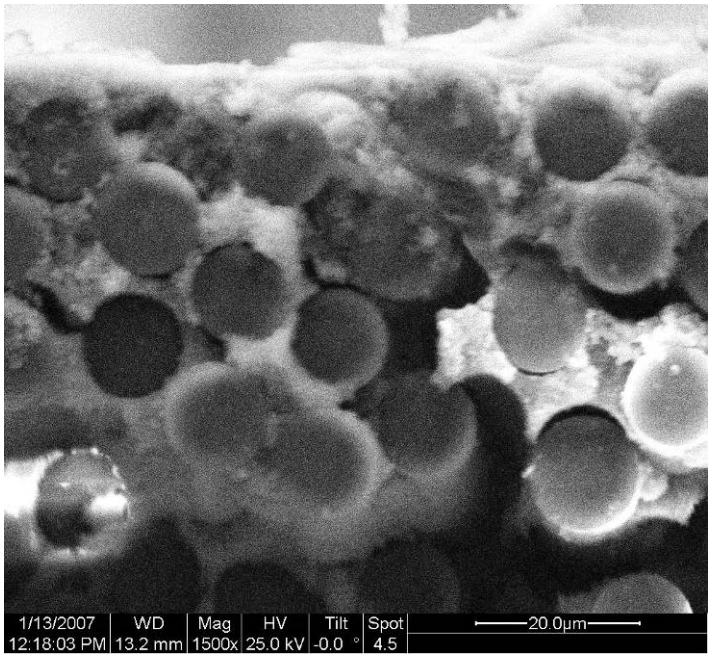

Figure 271. Fracture surface of N720/A specimen tested in creep at 125 MPa in steam at 1100 °C.

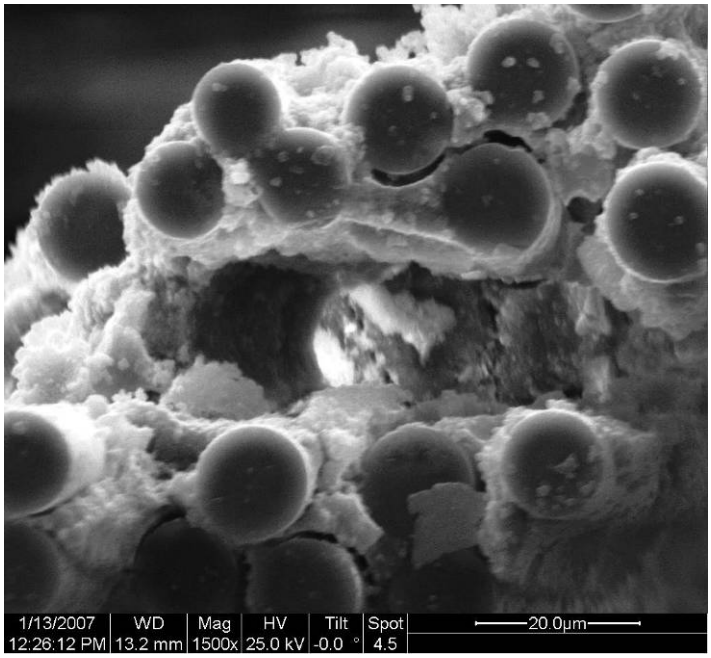

Figure 272. Fracture surface of N720/A specimen tested in creep at 125 MPa in steam at 1100 °C.

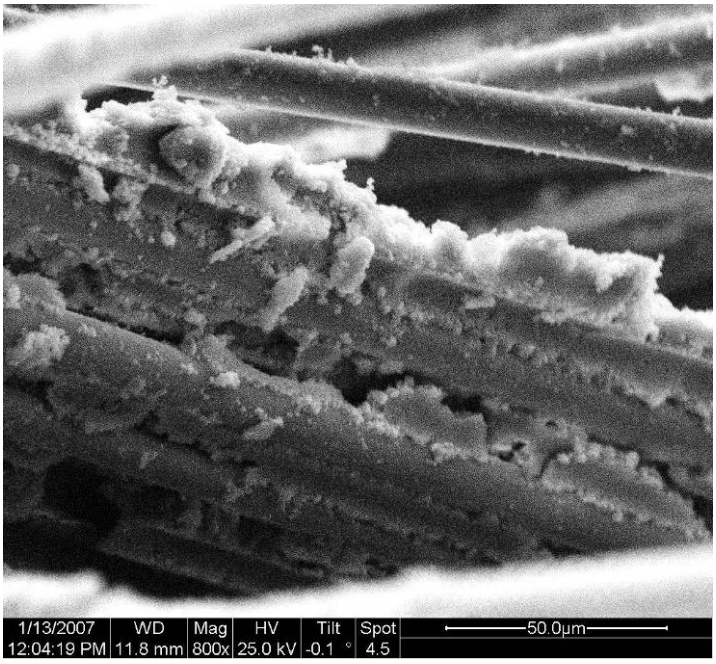

Figure 273. Fracture surface of N720/A specimen tested in creep at 125 MPa in steam at 1100 °C.

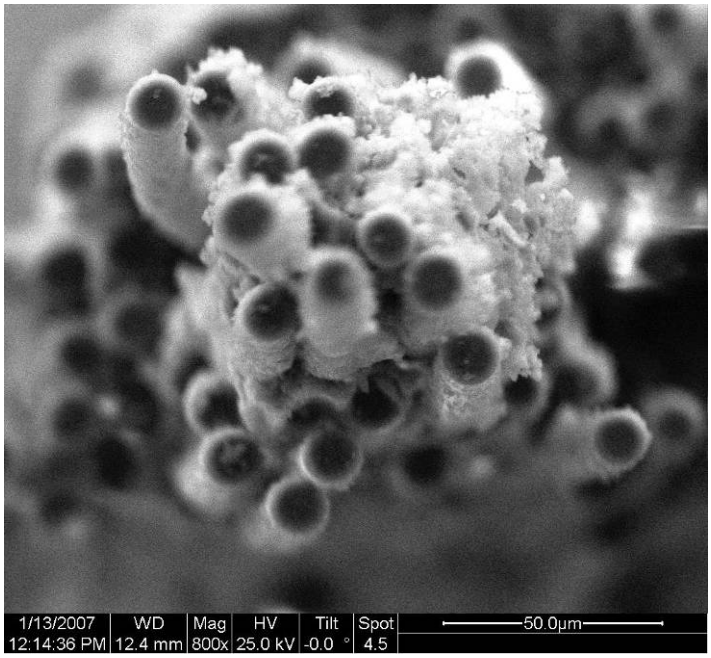

Figure 274. Fracture surface of N720/A specimen tested in creep at 125 MPa in steam at 1100 °C.

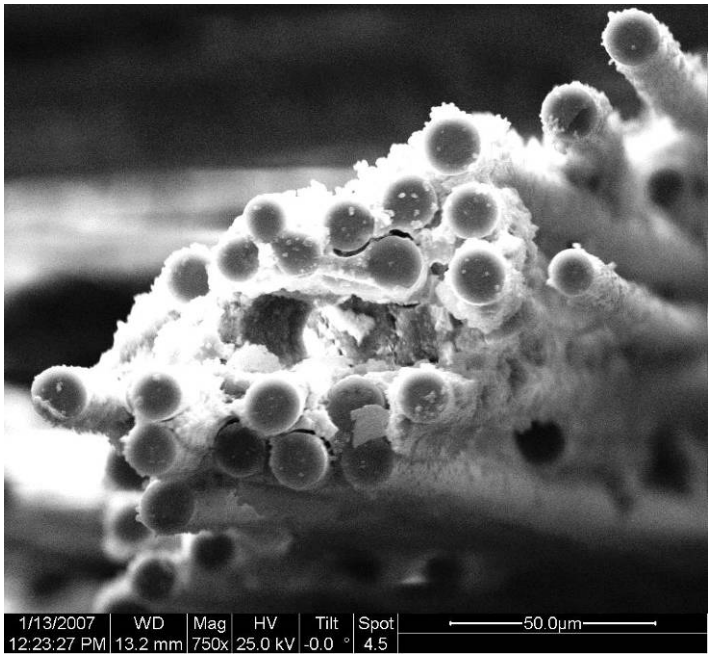

Figure 275. Fracture surface of N720/A specimen tested in creep at 125 MPa in steam at 1100 °C.

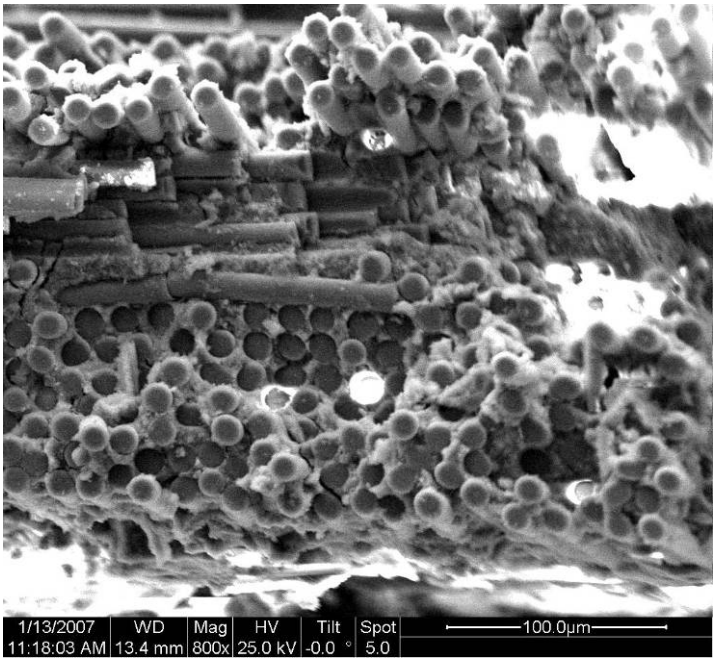

Figure 276. Fracture surface of N720/A specimen tested in creep at 125 MPa in steam at 1100 °C.

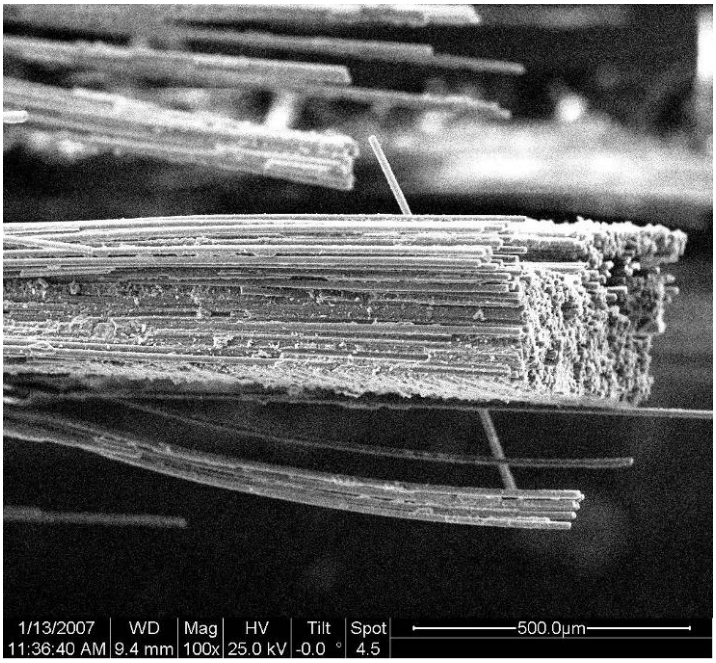

Figure 277. Fracture surface of N720/A specimen tested in creep at 125 MPa in steam at 1100 °C.

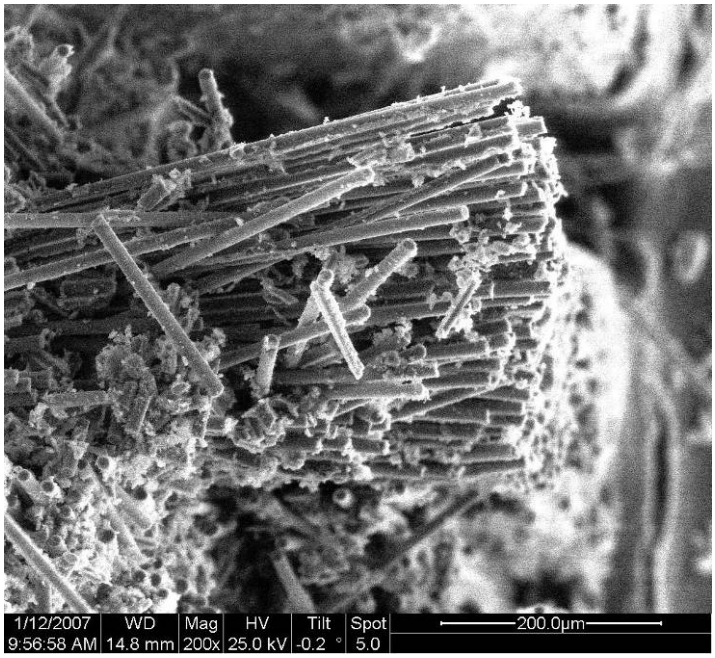

Figure 278. Fracture surface of N720/A specimen tested in creep at 125 MPa in steam at 1100 °C.

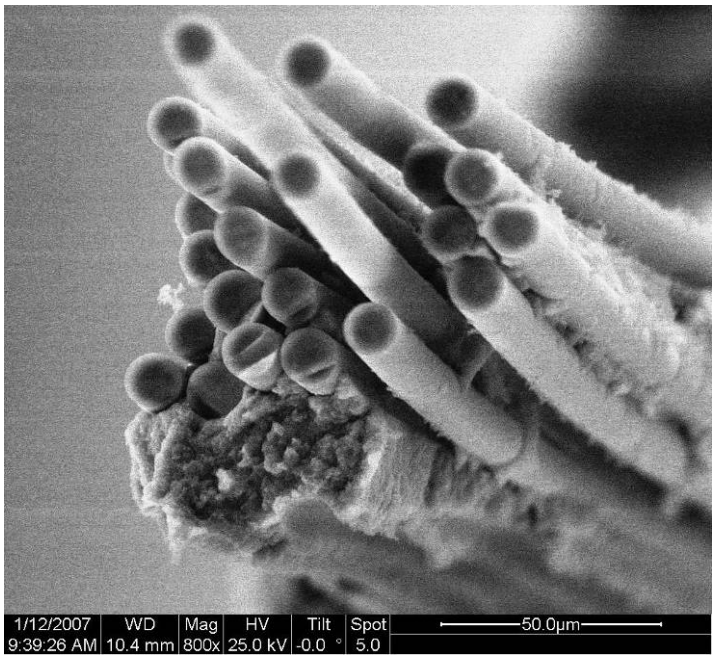

Figure 279. Fracture surface of N720/A specimen tested in creep at 125 MPa in steam at 1100 °C.

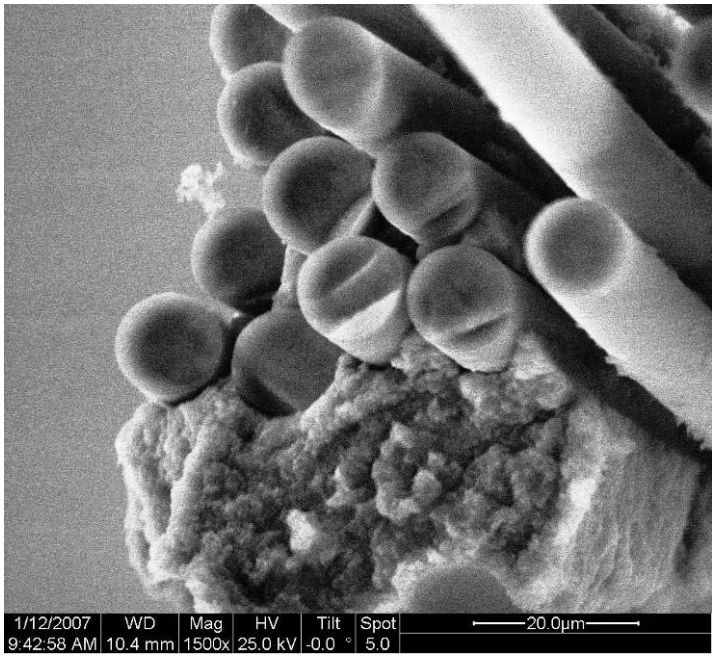

Figure 280. Fracture surface of N720/A specimen tested in creep at 125 MPa in steam at 1100 °C.

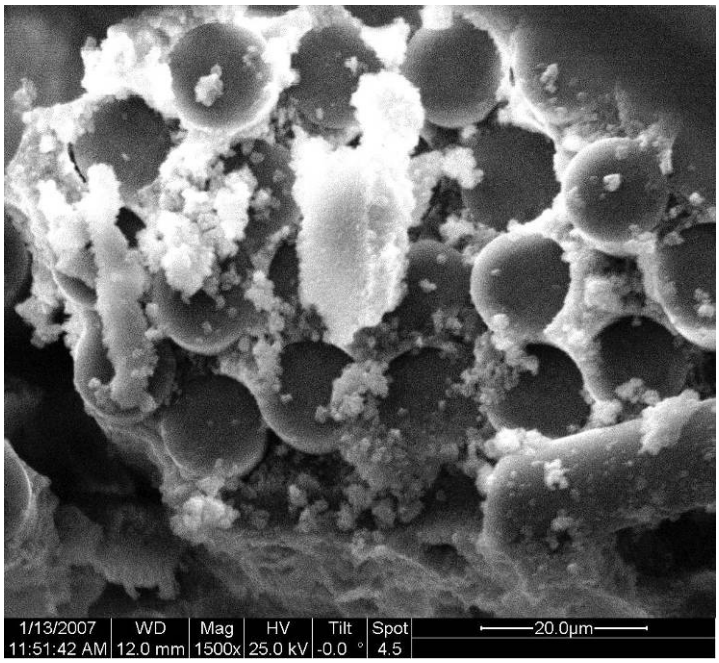

Figure 281. Fracture surface of N720/A specimen tested in creep at 125 MPa in steam at 1100 °C.

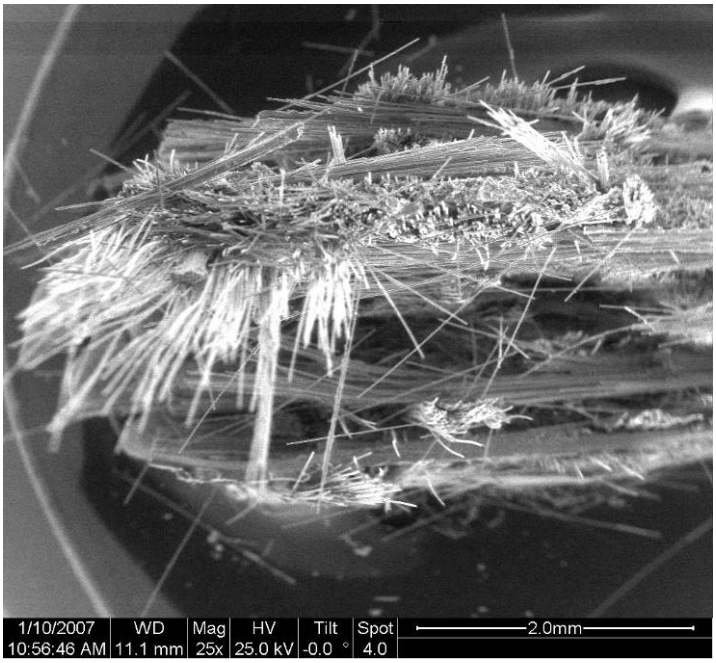

Figure 282. Fracture surface of N720/A specimen tested in creep at 150 MPa in steam at 1100 °C.

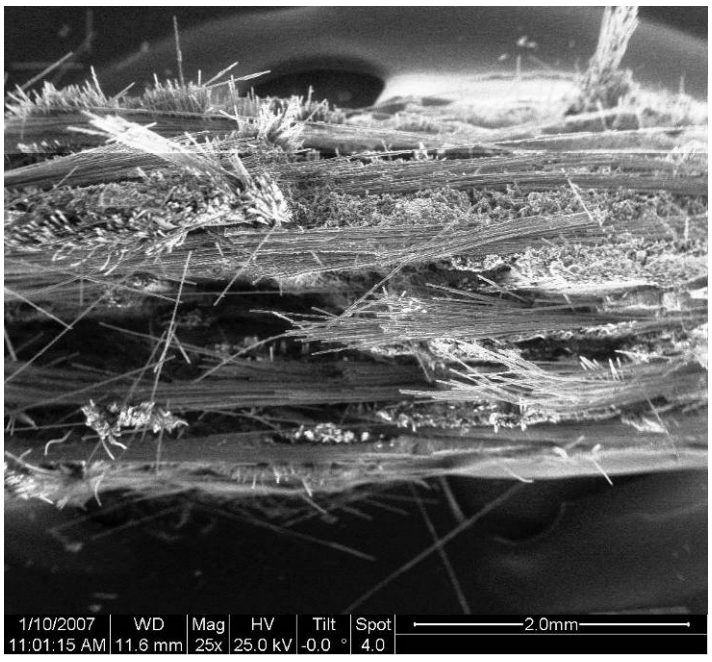

Figure 283. Fracture surface of N720/A specimen tested in creep at 150 MPa in steam at 1100 °C.

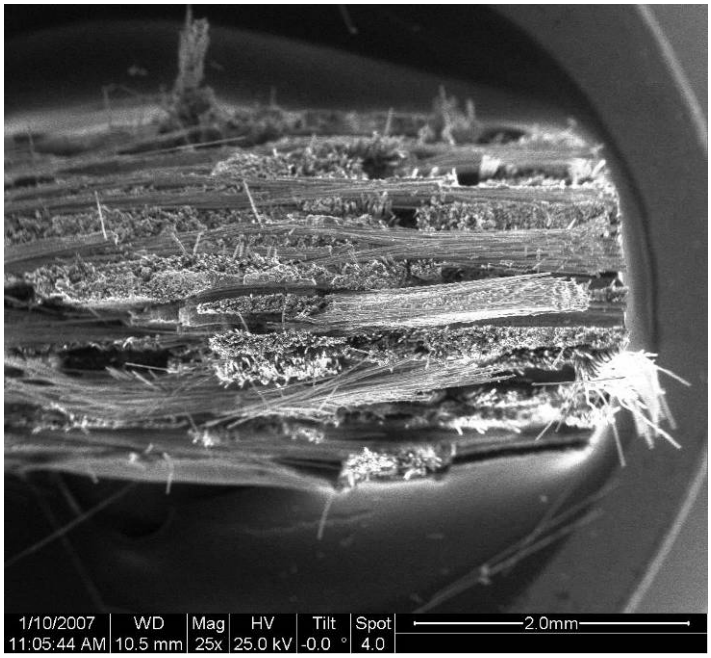

Figure 284. Fracture surface of N720/A specimen tested in creep at 150 MPa in steam at 1100 °C.

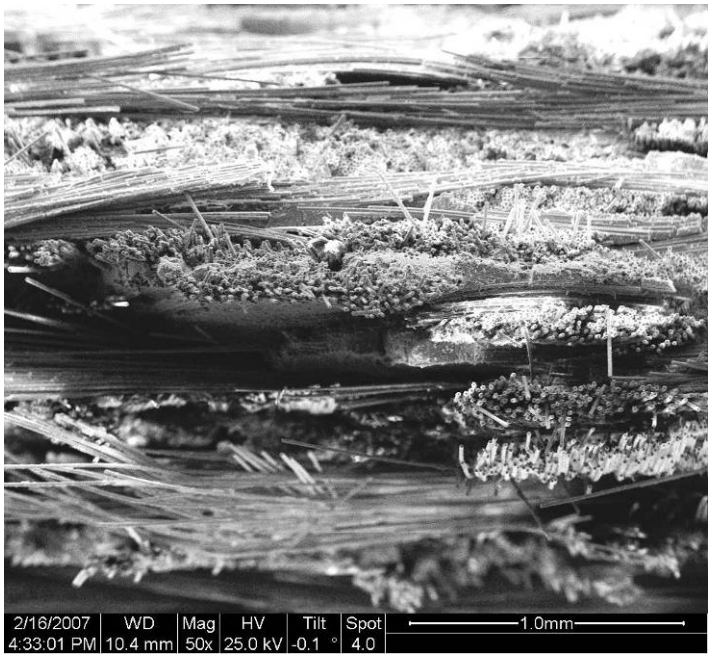

Figure 285. Fracture surface of N720/A specimen tested in creep at 150 MPa in steam at 1100 °C.

Figure 286. Fracture surface of N720/A specimen tested in creep at 150 MPa in steam at 1100 °C.

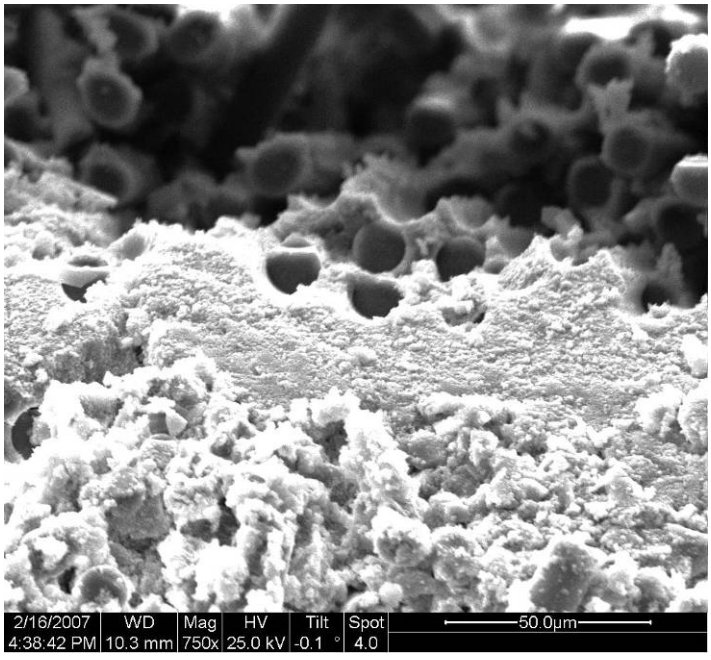

Figure 287. Fracture surface of N720/A specimen tested in creep at 150 MPa in steam at 1100 °C.

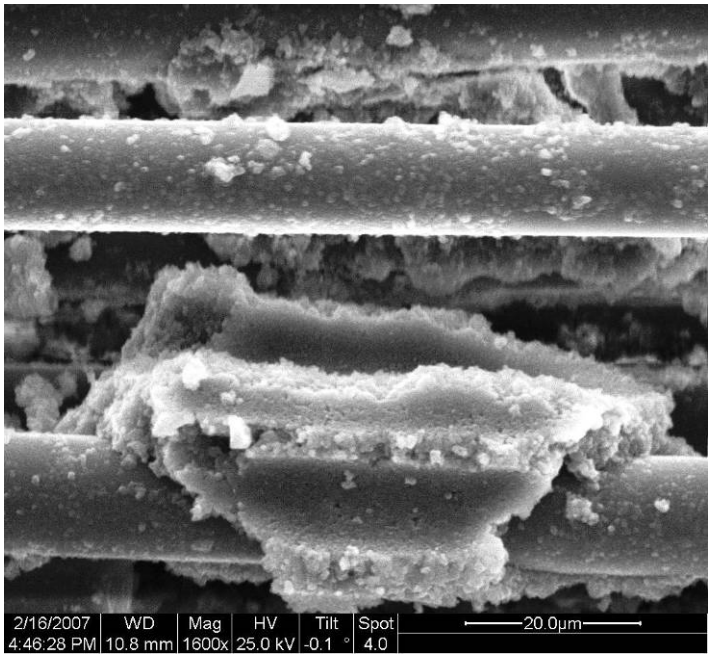

Figure 288. Fracture surface of N720/A specimen tested in creep at 150 MPa in steam at 1100 °C.

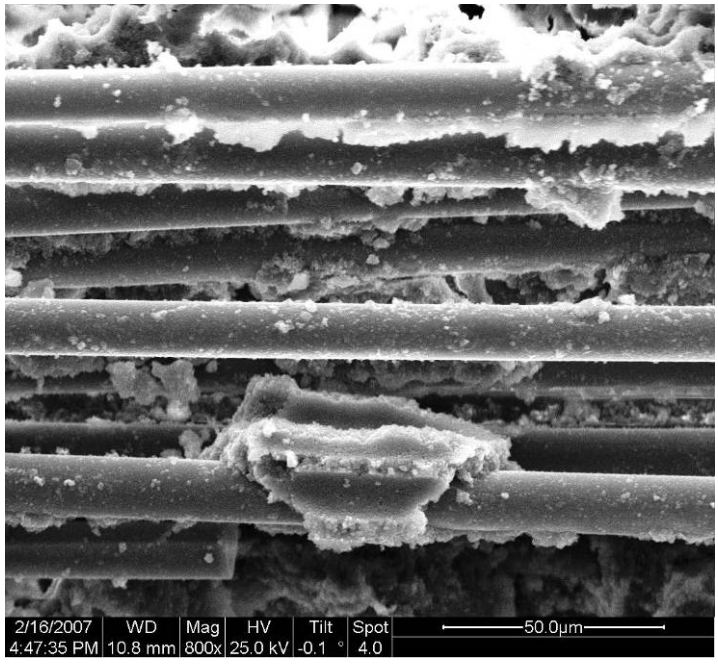

Figure 289. Fracture surface of N720/A specimen tested in creep at 150 MPa in steam at 1100 °C.

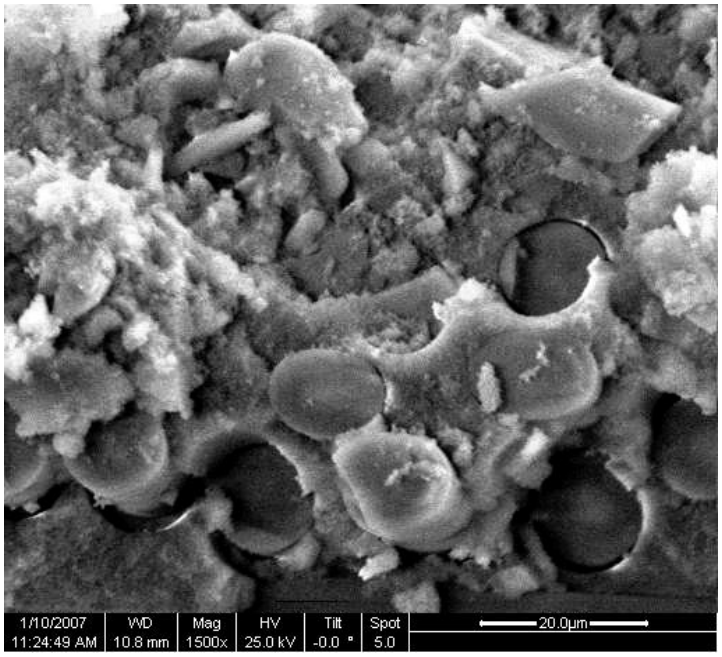

Figure 290. Fracture surface of N720/A specimen tested in creep at 150 MPa in steam at 1100 °C.

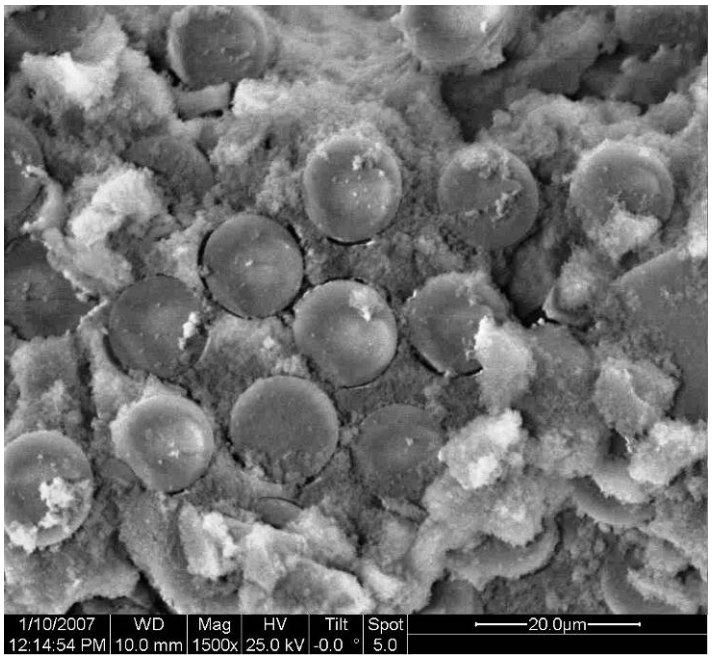

Figure 291. Fracture surface of N720/A specimen tested in creep at 150 MPa in steam at 1100 °C.

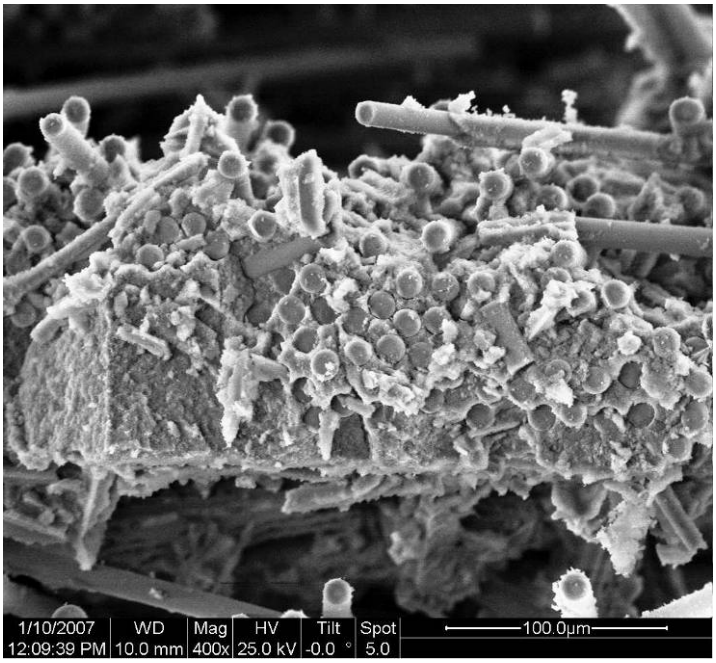

Figure 292. Fracture surface of N720/A specimen tested in creep at 150 MPa in steam at 1100 °C.

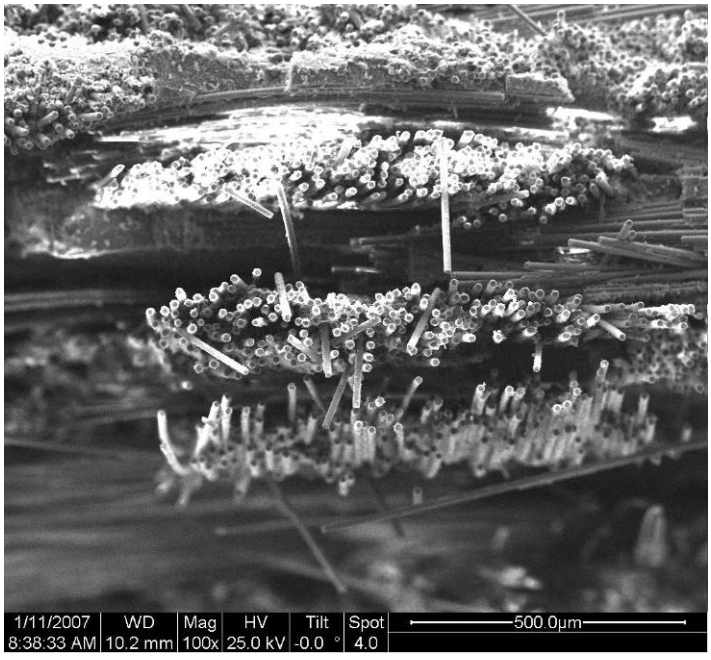

Figure 293. Fracture surface of N720/A specimen tested in creep at 150 MPa in steam at 1100 °C.

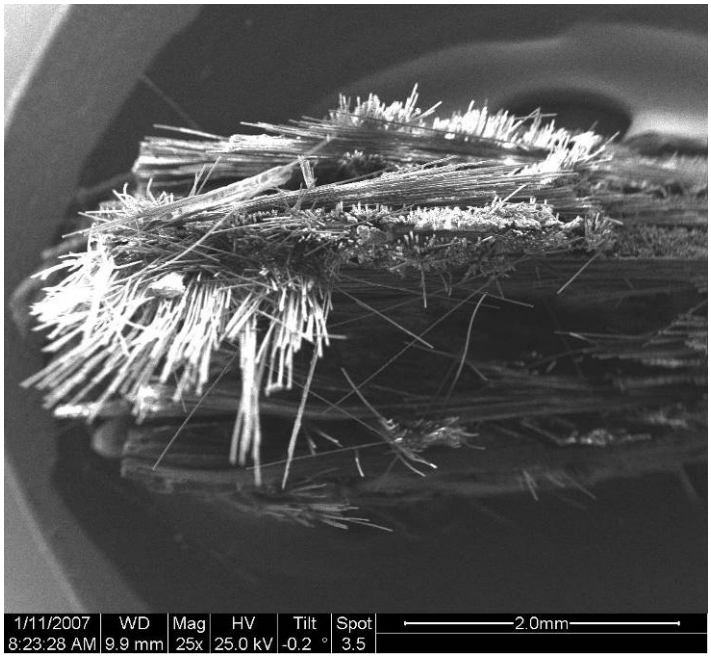

Figure 294. Fracture surface of N720/A specimen tested in creep at 150 MPa in steam at 1100 °C.

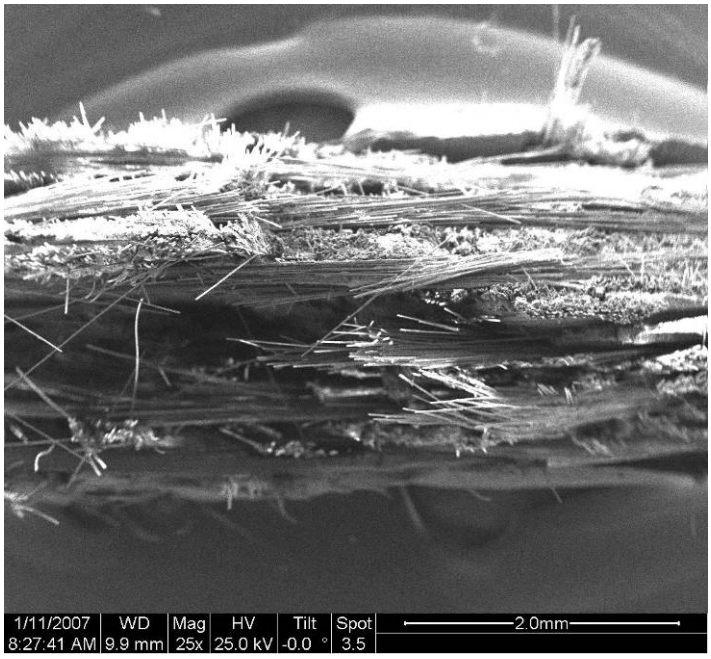

Figure 295. Fracture surface of N720/A specimen tested in creep at 150 MPa in steam at 1100 °C.

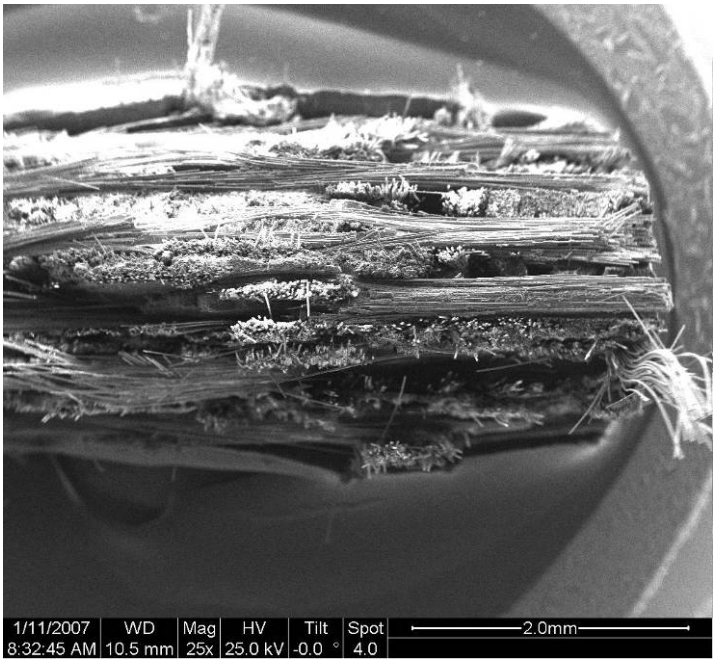

Figure 296. Fracture surface of N720/A specimen tested in creep at 150 MPa in steam at 1100 °C.

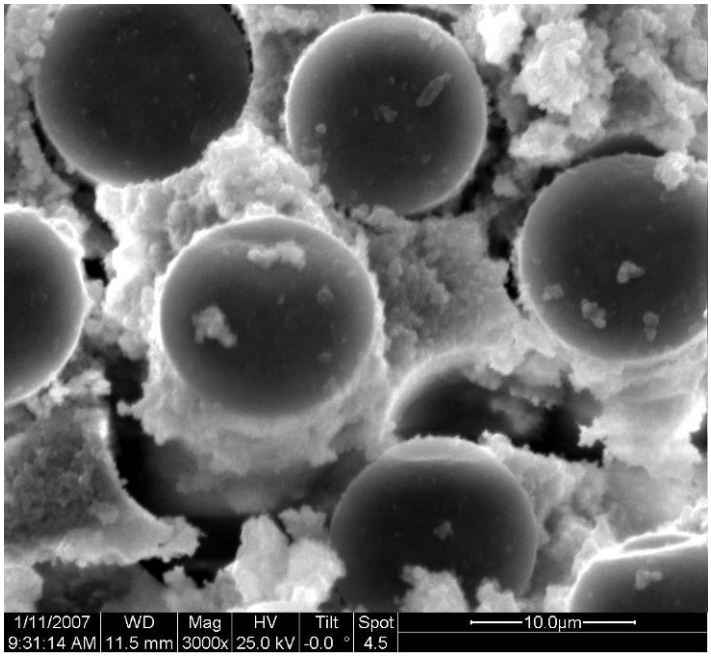

Figure 297. Fracture surface of N720/A specimen tested in creep at 150 MPa in steam at 1100 °C.

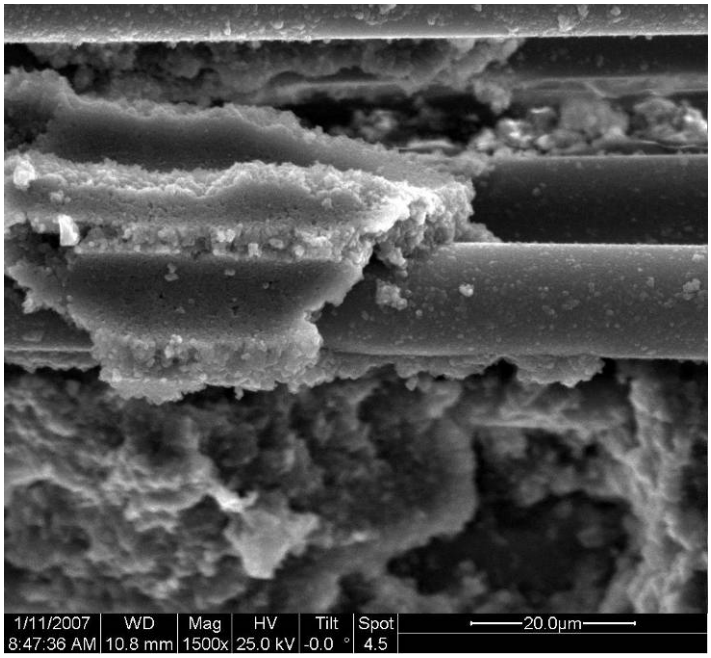

Figure 298. Fracture surface of N720/A specimen tested in creep at 150 MPa in steam at 1100 °C.

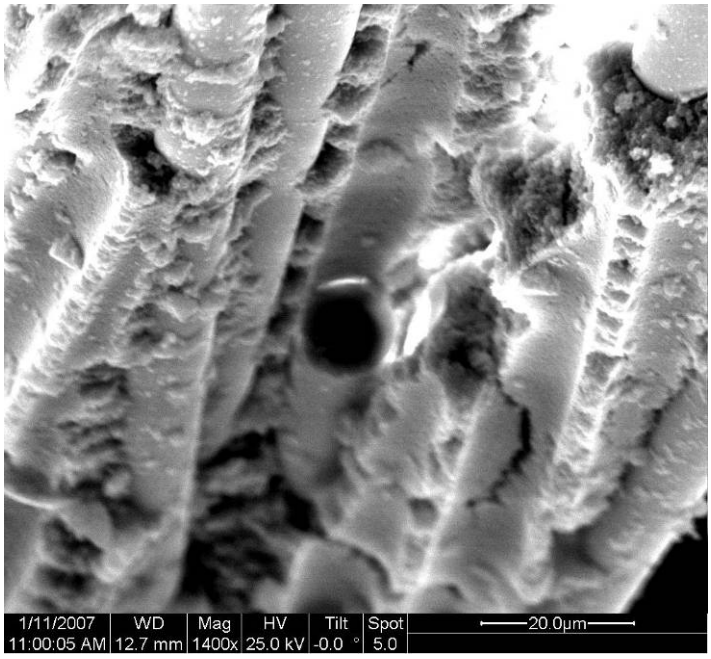

Figure 299. Fracture surface of N720/A specimen tested in creep at 150 MPa in steam at 1100 °C.

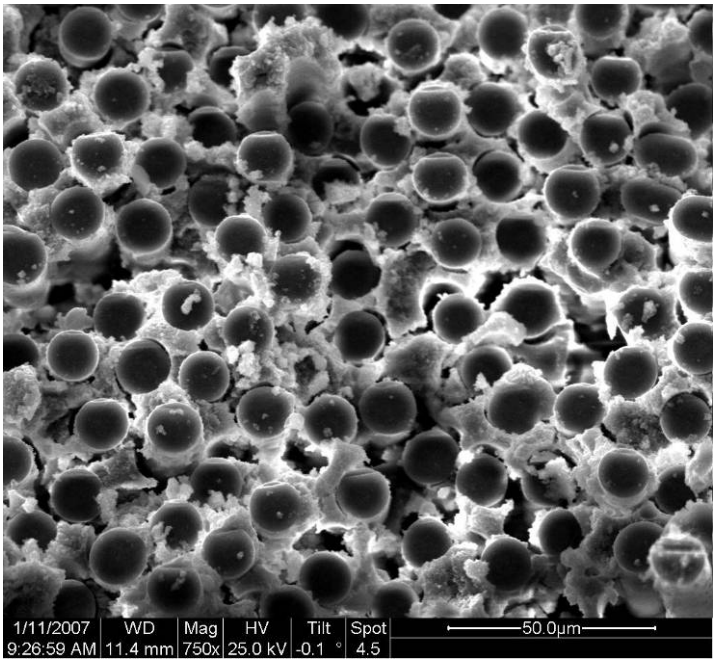

Figure 300. Fracture surface of N720/A specimen tested in creep at 150 MPa in steam at 1100 °C.

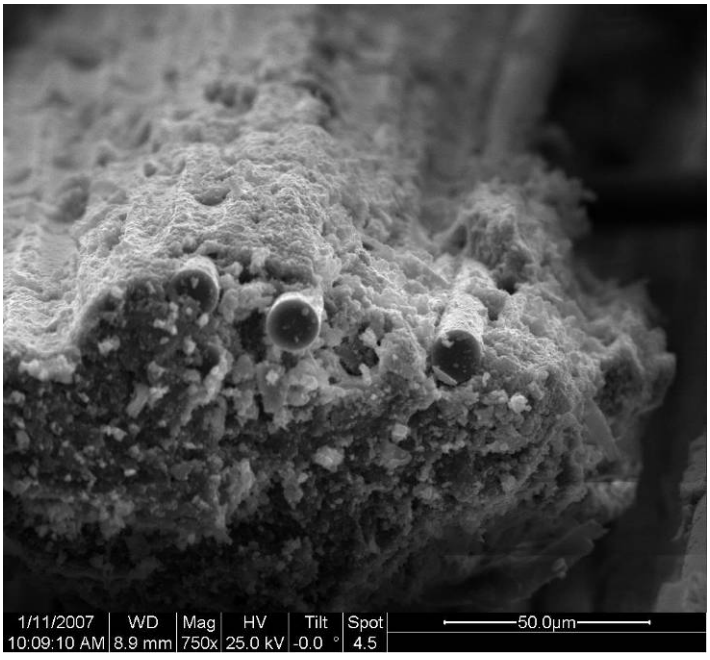

Figure 301. Fracture surface of N720/A specimen tested in creep at 150 MPa in steam at 1100 °C.

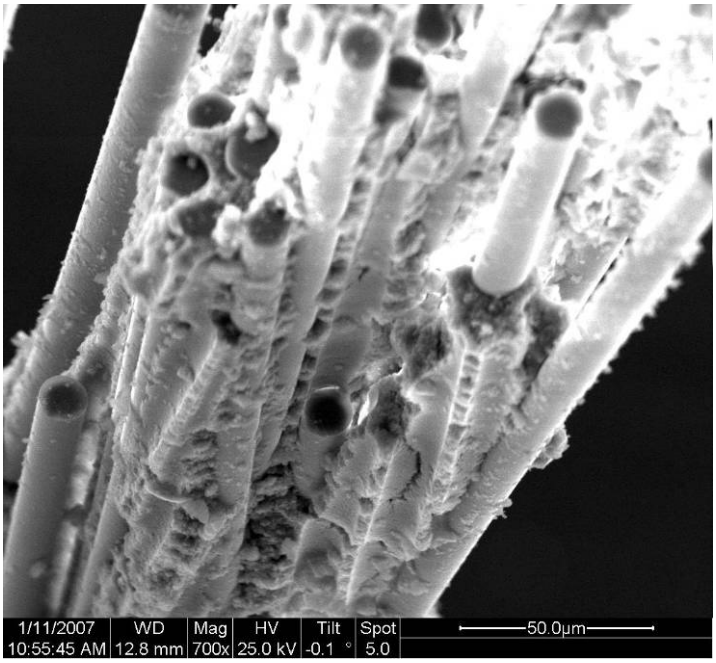

Figure 302. Fracture surface of N720/A specimen tested in creep at 150 MPa in steam at 1100 °C.

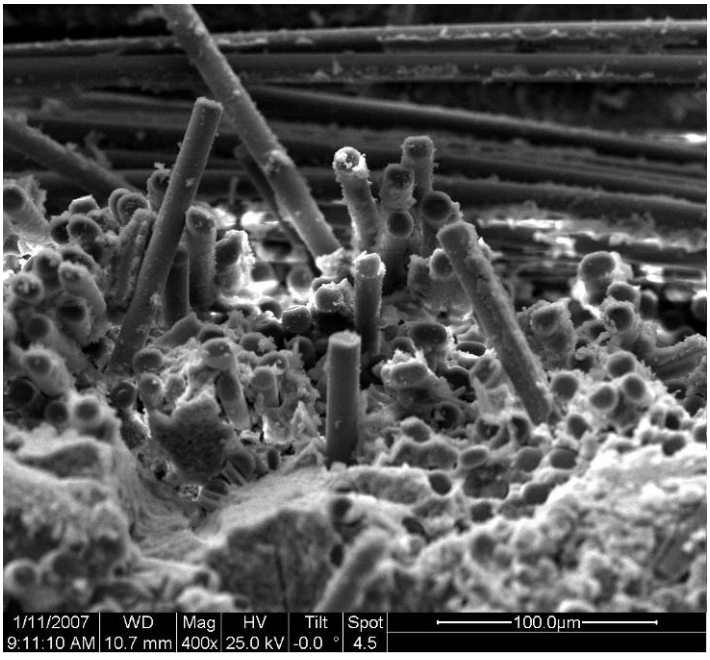

Figure 303. Fracture surface of N720/A specimen tested in creep at 150 MPa in steam at 1100 °C.

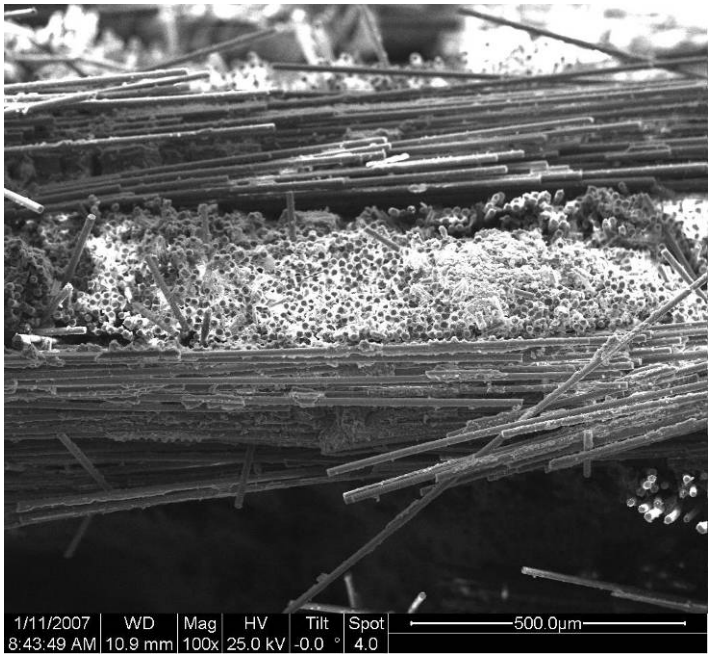

Figure 304. Fracture surface of N720/A specimen tested in creep at 150 MPa in steam at 1100 °C.

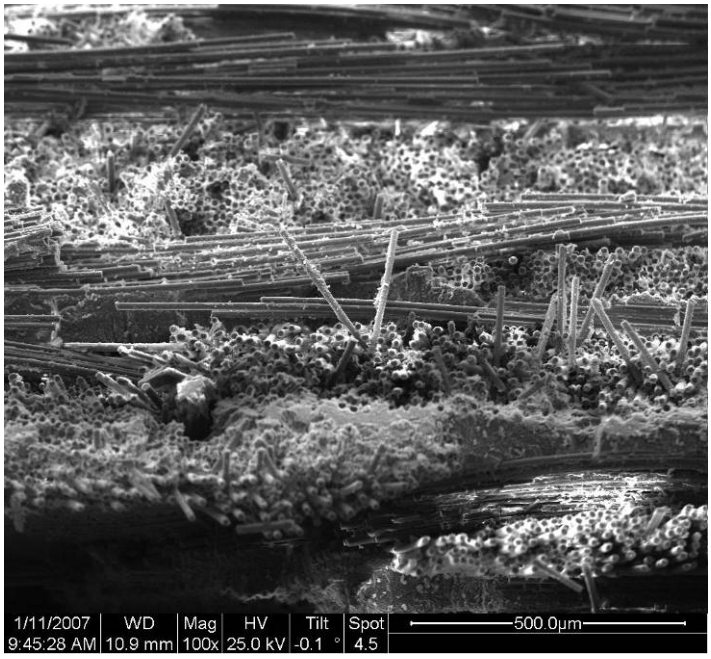

Figure 305. Fracture surface of N720/A specimen tested in creep at 150 MPa in steam at 1100 °C.

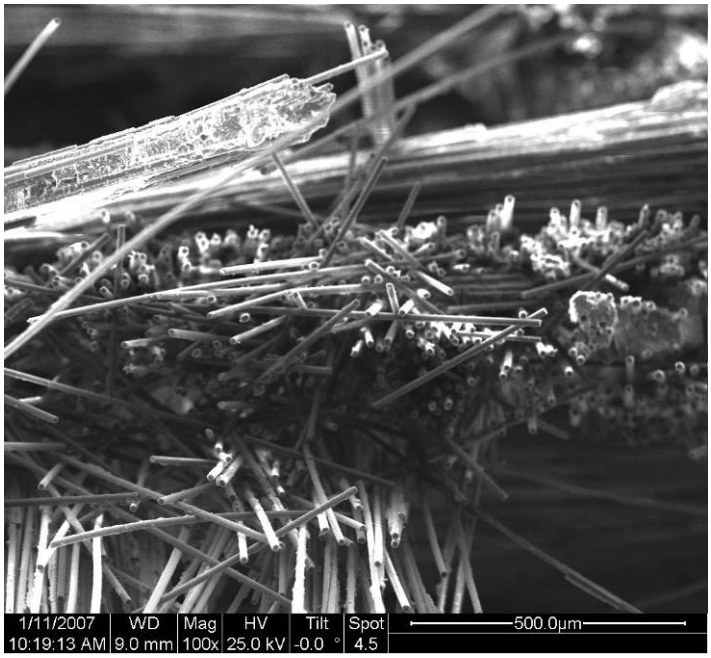

Figure 306. Fracture surface of N720/A specimen tested in creep at 150 MPa in steam at 1100 °C.

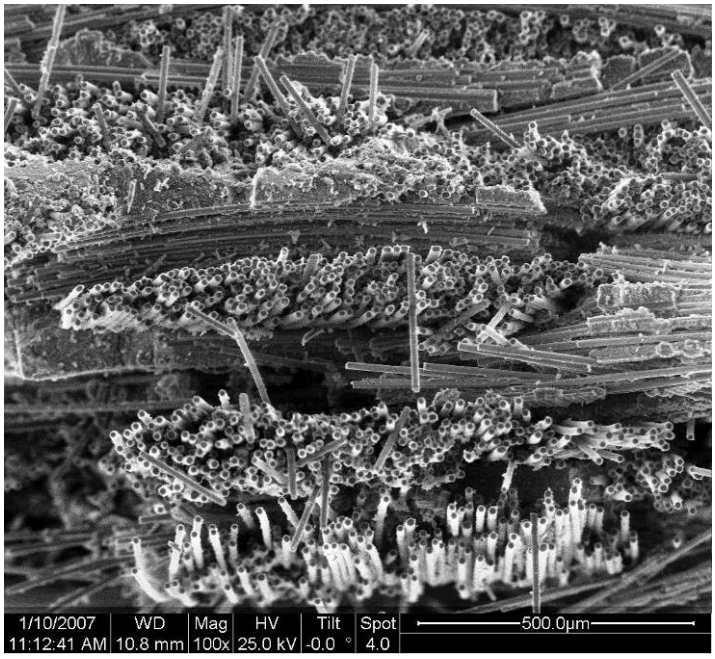

Figure 307. Fracture surface of N720/A specimen tested in creep at 150 MPa in steam at 1100 °C.

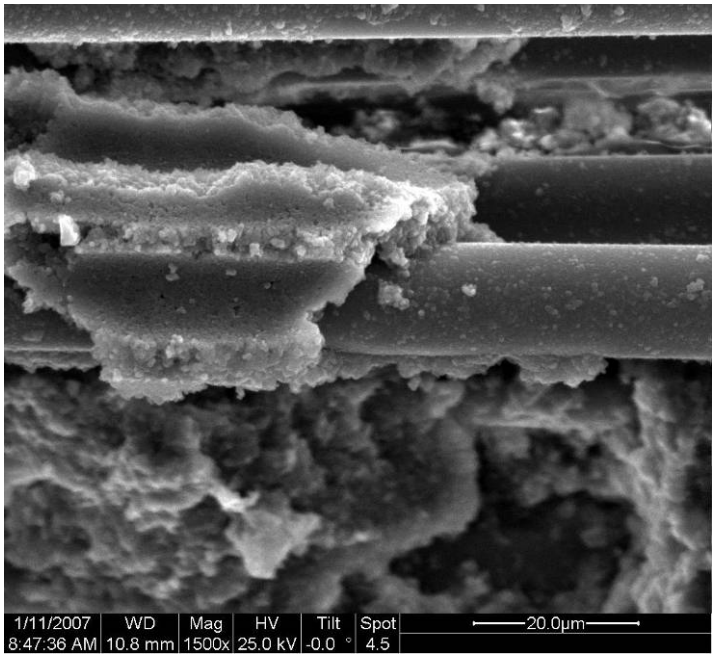

Figure 308. Fracture surface of N720/A specimen tested in creep at 150 MPa in steam at 1100 °C.

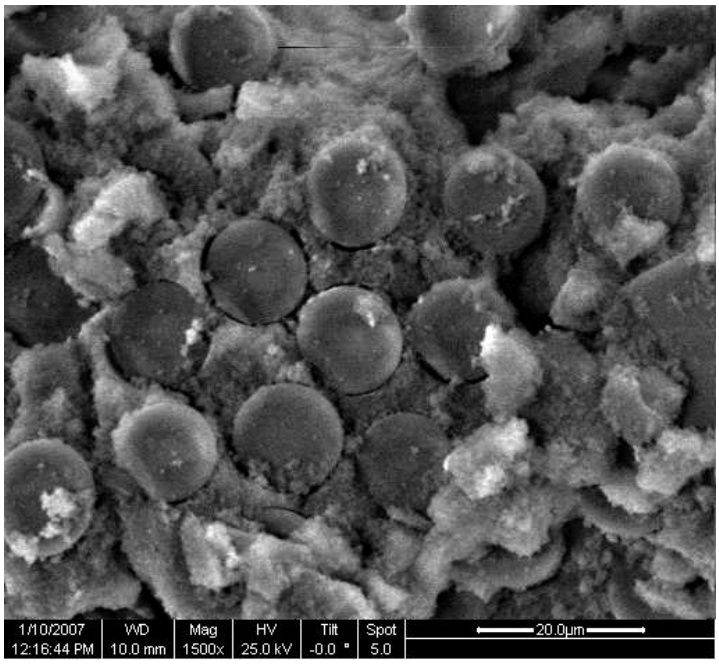

Figure 309. Fracture surface of N720/A specimen tested in creep at 150 MPa in steam at 1100 °C.

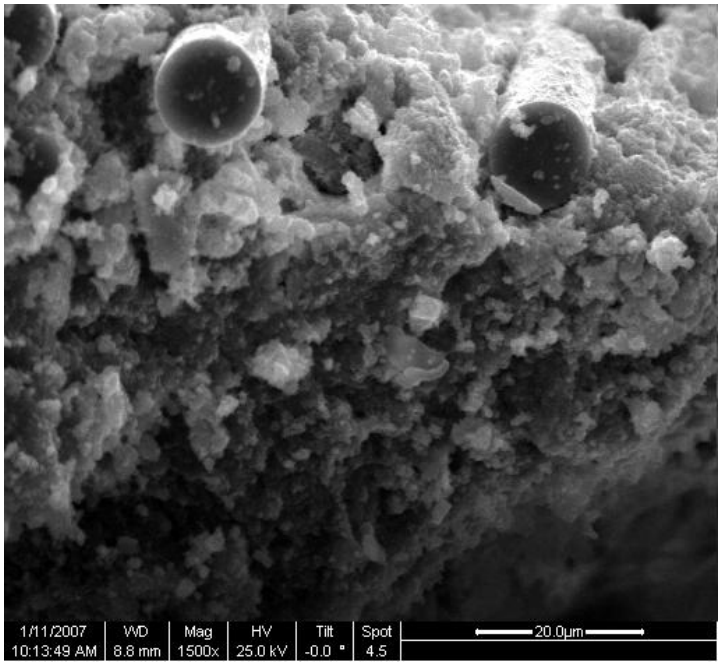

Figure 310. Fracture surface of N720/A specimen tested in creep at 150 MPa in steam at 1100 °C.

Appendix B. Additional Optical Micrographs

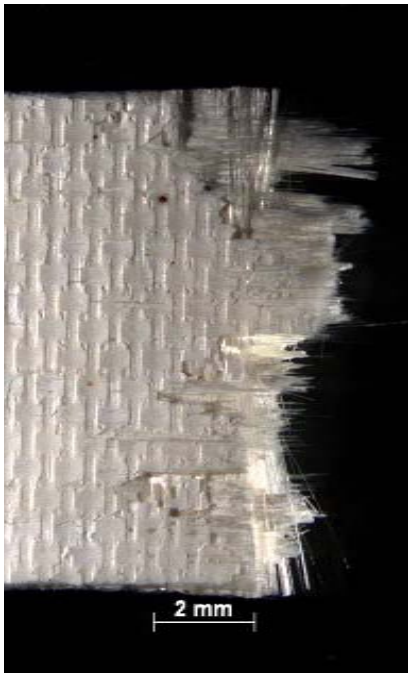

Figure 311. Fracture surface of N720/A specimen tested in tension at 800 °C in air.

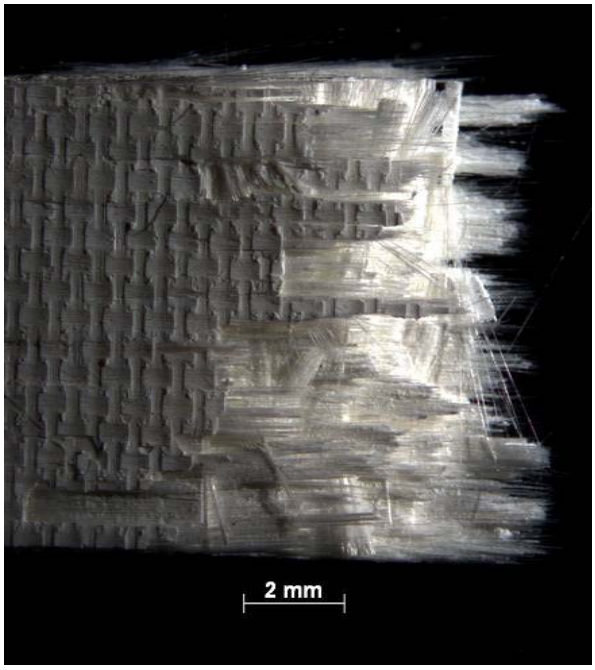

Figure 312. Fracture surface of N720/A specimen tested in tension at 900 °C in air.

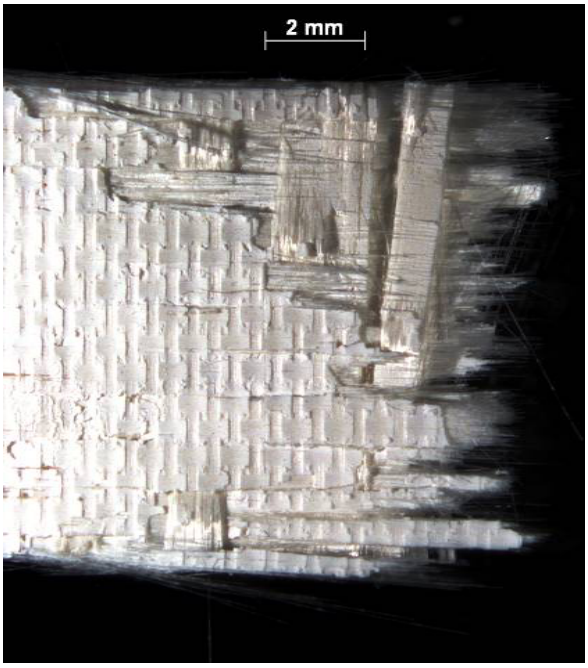

Figure 313. Fracture surface of N720/A specimen tested in tension at 900 °C in air.

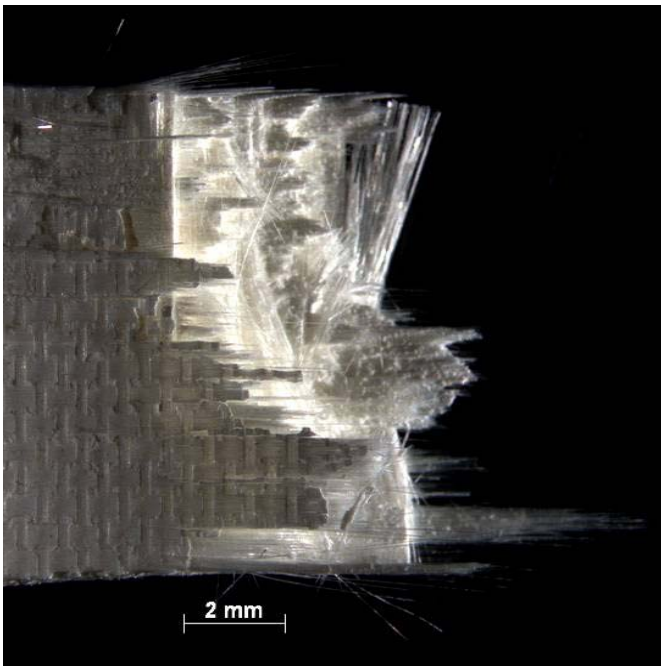

Figure 314. Fracture surface of N720/A specimen tested in tension at 900 °C in air.

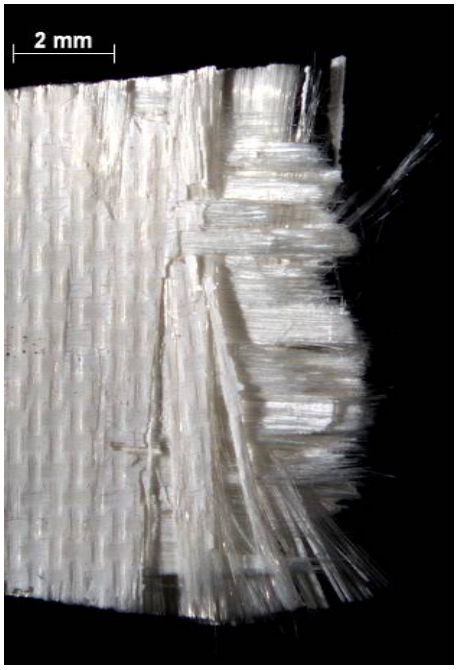

Figure 315. Fracture surface of N720/A specimen tested in tension at 1000 °C in air.

Figure 316. Fracture surface of N720/A specimen tested in tension at 1000 °C in air.

Figure 317. Fracture surface of N720/A specimen tested in tension at 1000 °C in air.

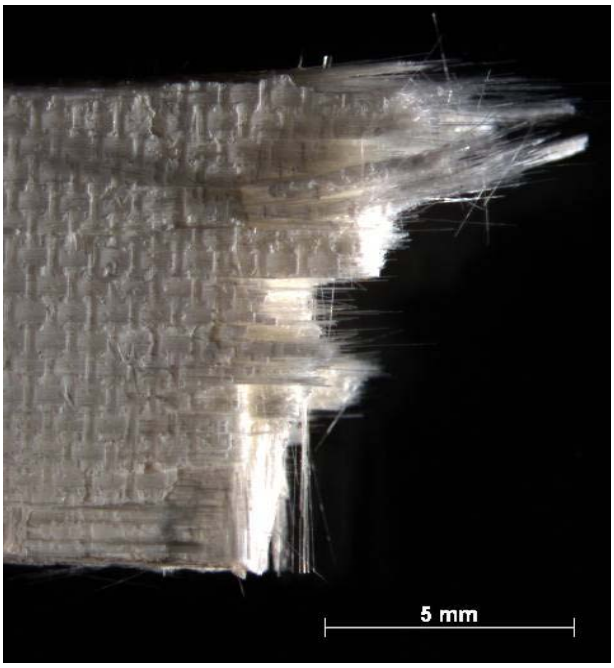

Figure 318. Fracture surface of N720/A specimen tested in tension at 1100 °C in air.

Figure 319. Fracture surface of N720/A specimen tested in tension at 1100 °C in air.

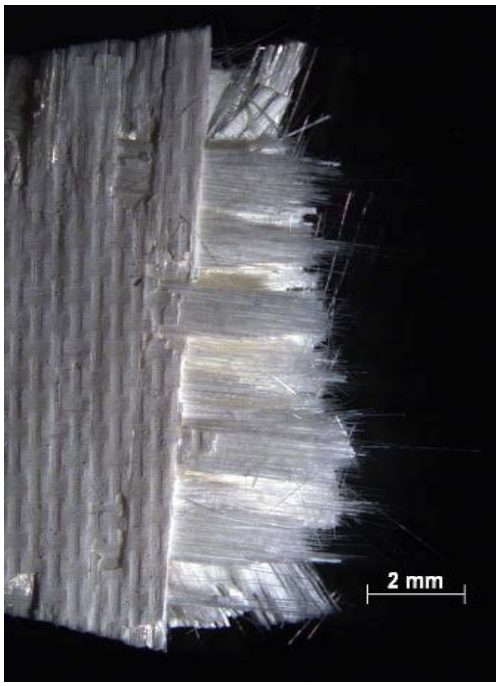

Figure 320. Fracture surface of N720/A specimen tested in tension at 1100 °C in air.

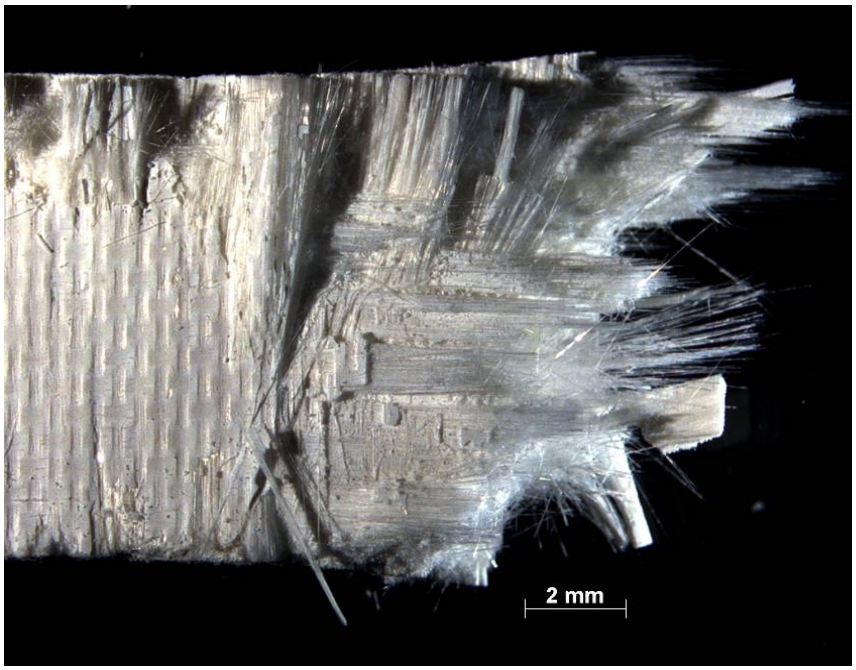

Figure 321. Fracture surface of N720/A specimen tested in creep at 1000 °C at 135 MPa in steam.

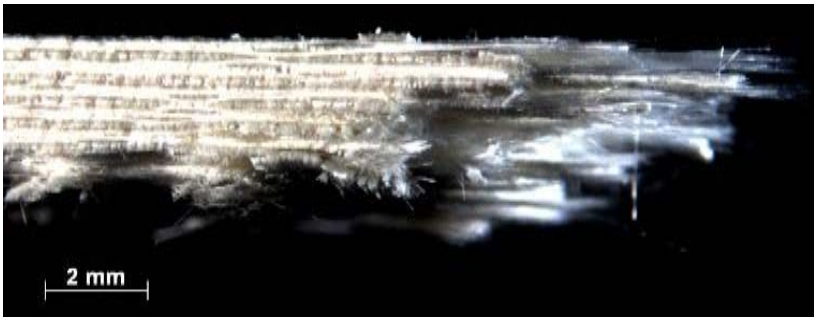

Figure 322. Fracture surface of N720/A specimen tested in creep at 1000 °C at 135 MPa in steam.

Figure 323. Fracture surface of N720/A specimen tested in creep at 1000 °C at 135 MPa in steam.

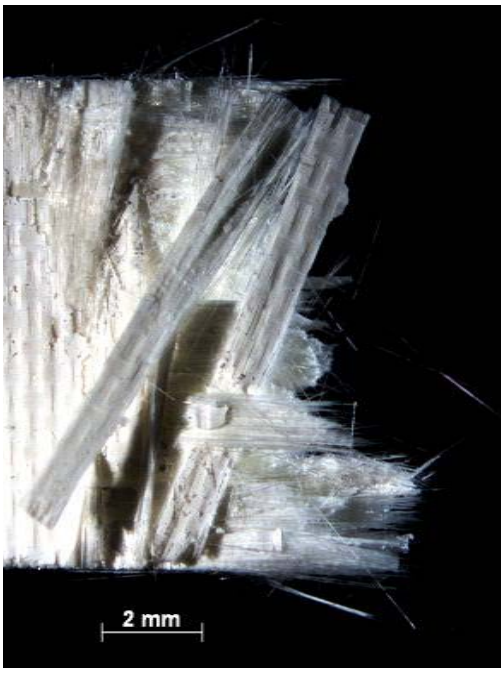

Figure 324. Fracture surface of N720/A specimen tested in creep at 1000 °C at 150 MPa in steam.

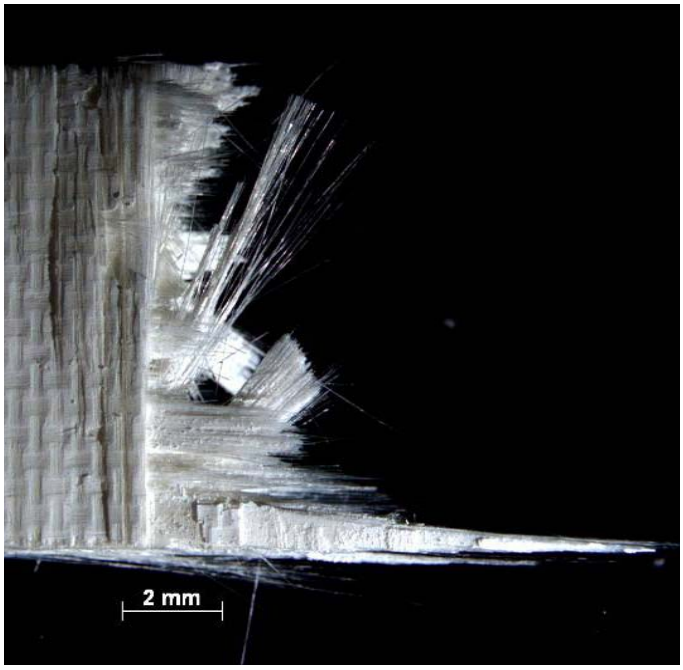

Figure 325. Fracture surface of N720/A specimen tested in creep at 1000 °C at 150 MPa in steam.

Figure 326. Fracture surface of N720/A specimen tested in creep at 1000 °C at 150 MPa in steam.

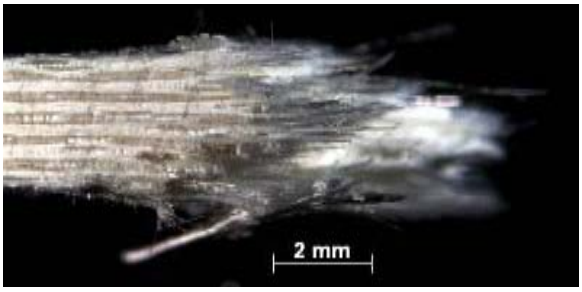

Figure 327. Fracture surface of N720/A specimen tested in creep at 1000 °C at 150 MPa in steam.

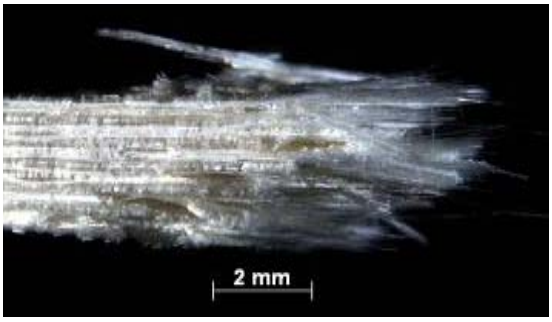

Figure 328. Fracture surface of N720/A specimen tested in creep at 1000 °C at 150 MPa in steam.

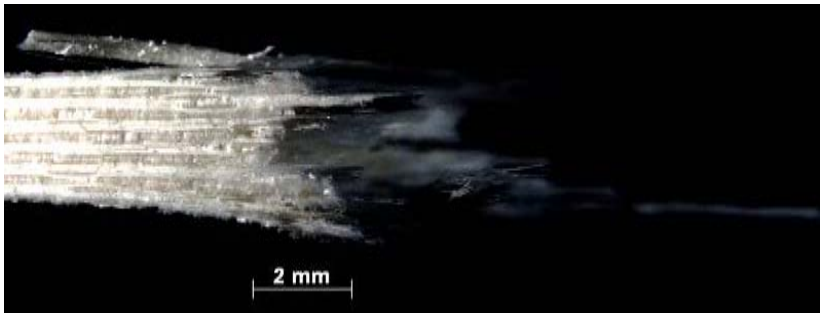

Figure 329. Fracture surface of N720/A specimen tested in creep at 1000 °C at 150 MPa in steam.

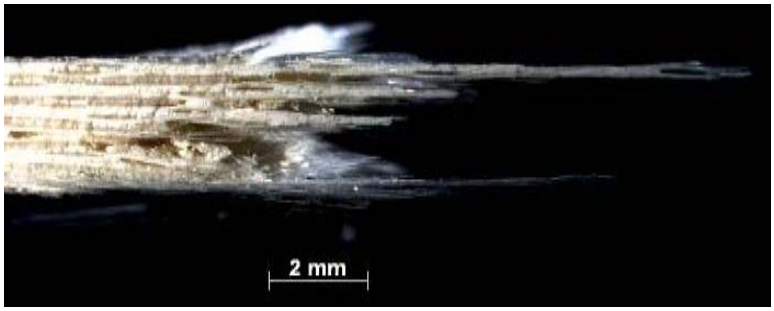

Figure 330. Fracture surface of N720/A specimen tested in creep at 1000 °C at 150 MPa in steam.

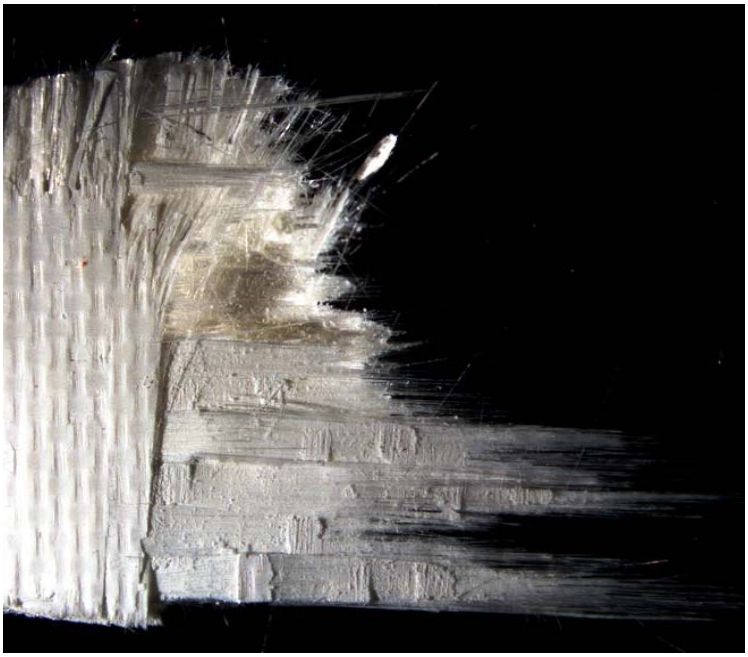

Figure 331. Fracture surface of N720/A specimen tested in creep at 1000 °C at 150 MPa in air.

Figure 332. Fracture surface of N720/A specimen tested in creep at 1000 °C at 150 MPa in air.

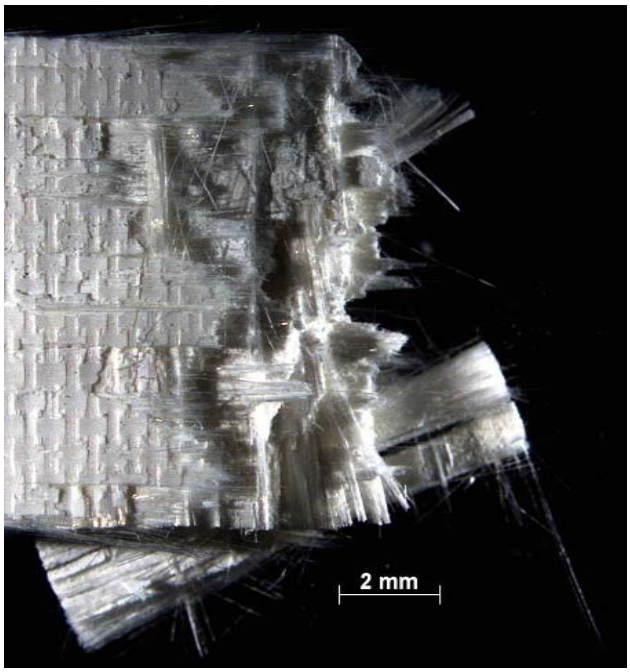

Figure 333. Fracture surface of N720/A specimen tested in creep at 1000 °C at 160 MPa in steam.

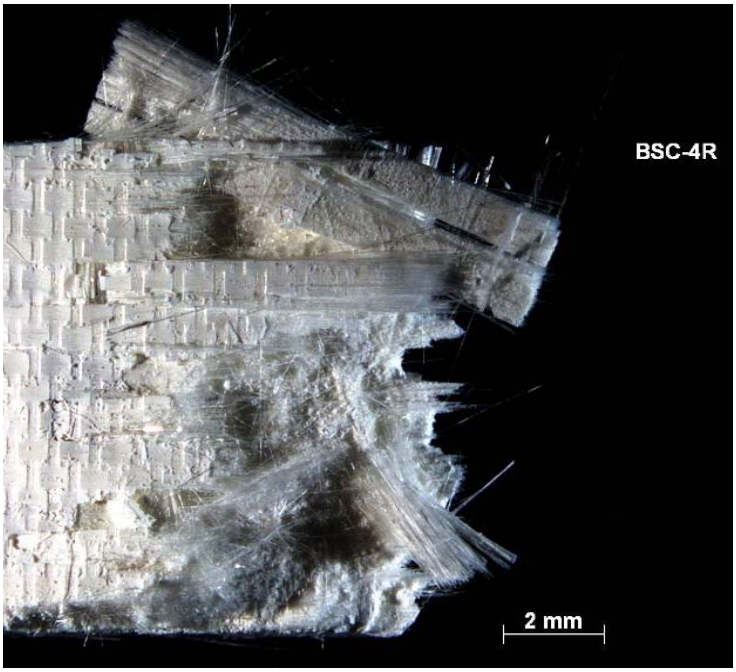

Figure 334. Fracture surface of N720/A specimen tested in creep at 1000 °C at 160 MPa in steam.

Figure 335. Fracture surface of N720/A specimen tested in creep at 1000 °C at 160 MPa in steam.

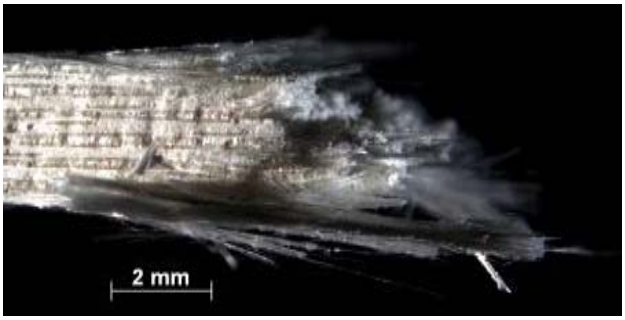

Figure 336. Fracture surface of N720/A specimen tested in creep at 1000 °C at 160 MPa in steam.

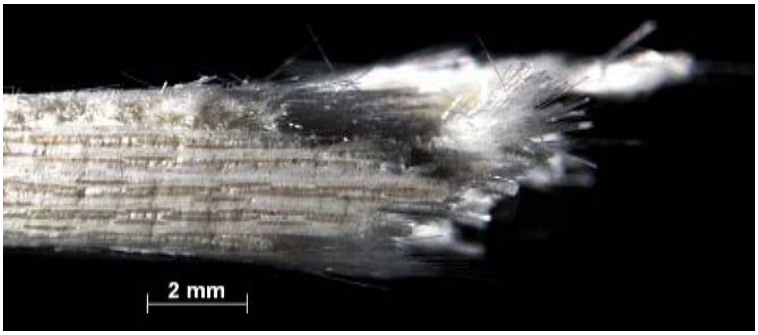

Figure 337. Fracture surface of N720/A specimen tested in creep at 1000 °C at 160 MPa in steam.

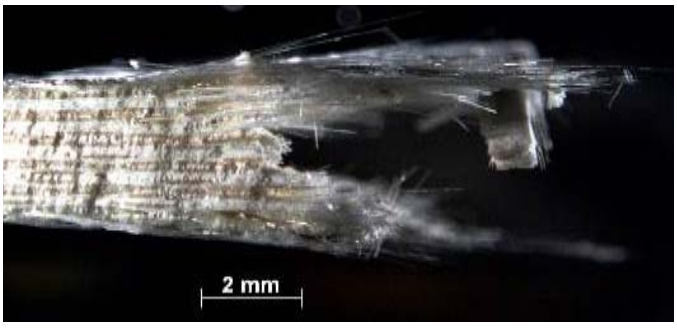

Figure 338. Fracture surface of N720/A specimen tested in creep at 1000 °C at 160 MPa in steam.

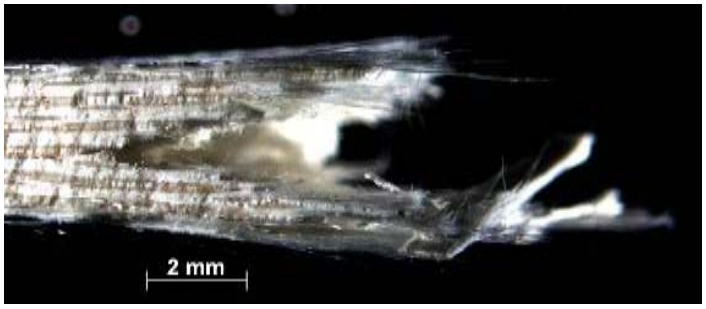

Figure 339. Fracture surface of N720/A specimen tested in creep at 1000 °C at 160 MPa in steam.

Figure 340. Fracture surface of N720/A specimen tested in creep at 1100 °C at 100 MPa in steam.

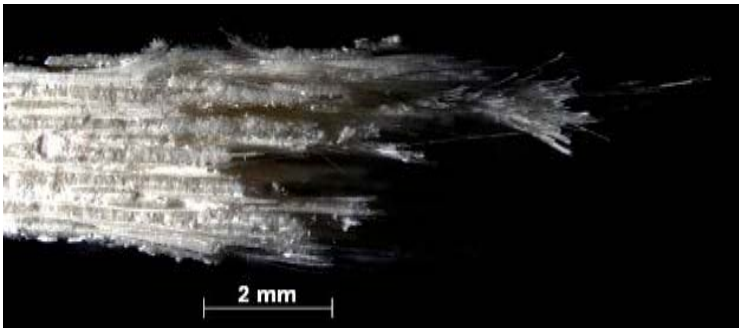

Figure 341. Fracture surface of N720/A specimen tested in creep at 1100 °C at 100 MPa in steam.

Figure 342. Fracture surface of N720/A specimen tested in creep at 1100 °C at 125 MPa in steam.

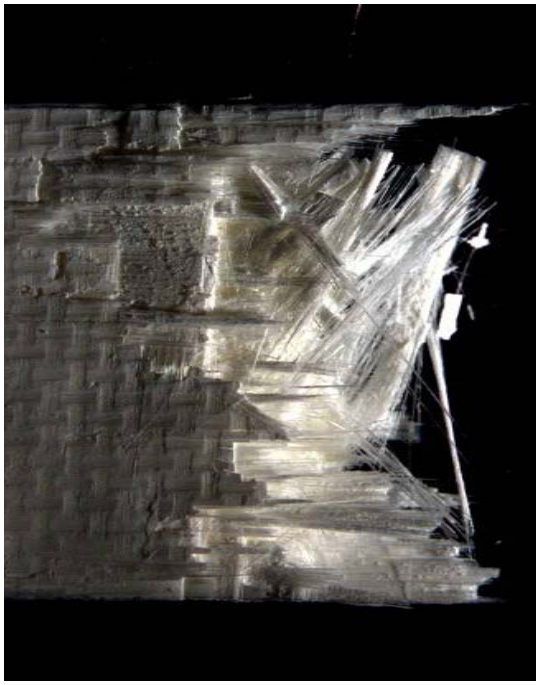

Figure 343. Fracture surface of N720/A specimen tested in creep at 1100 °C at 125 MPa in steam.

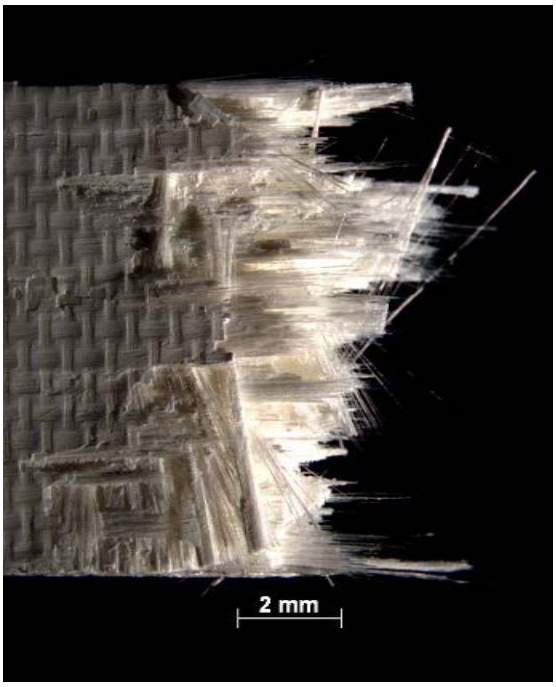

Figure 344. Fracture surface of N720/A specimen tested in creep at 1100 °C at 125 MPa in steam.

Figure 345. Fracture surface of N720/A specimen tested in creep at 1100 °C at 125 MPa in steam.

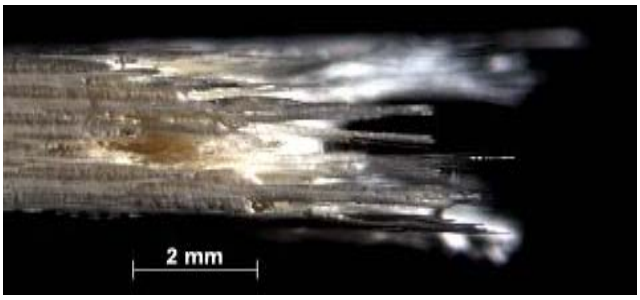

Figure 346. Fracture surface of N720/A specimen tested in creep at 1100 °C at 125 MPa in steam.

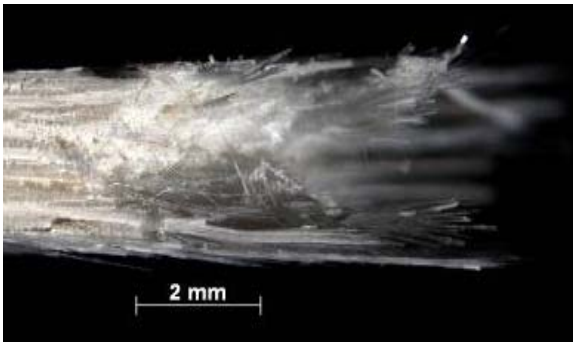

Figure 347. Fracture surface of N720/A specimen tested in creep at 1100 °C at 125 MPa in steam.

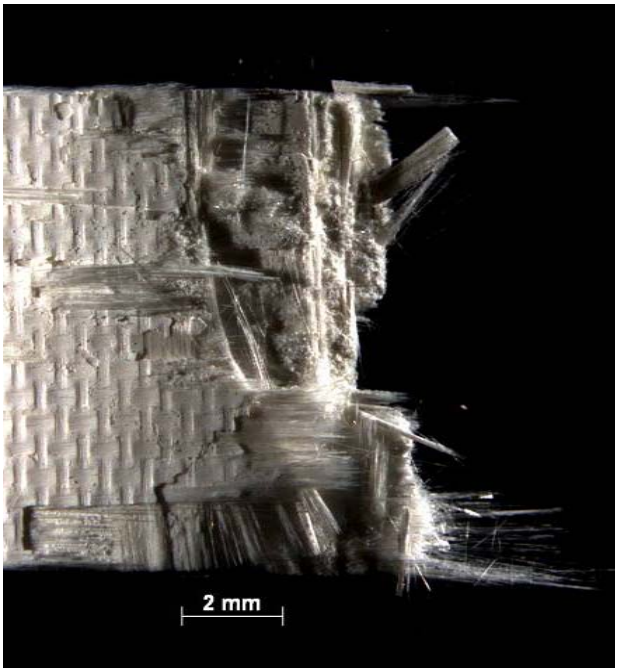

Figure 348. Fracture surface of N720/A specimen tested in creep at 1100 °C at 150 MPa in steam.

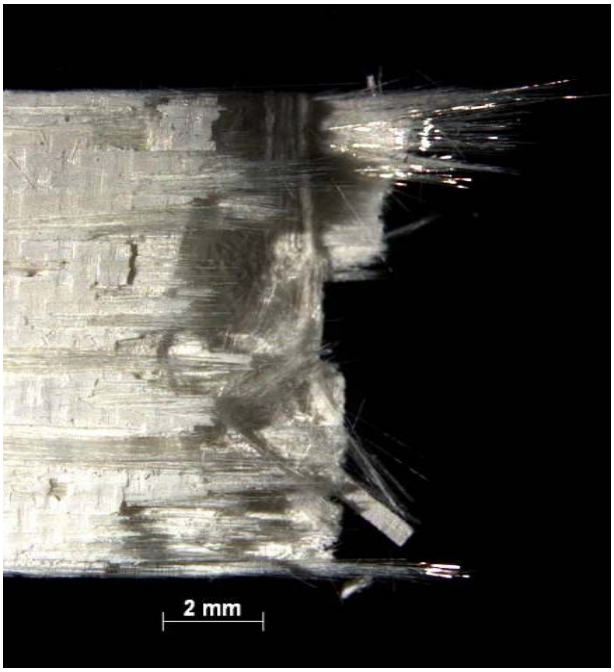

Figure 349. Fracture surface of N720/A specimen tested in creep at 1100 °C at 150 MPa in steam.

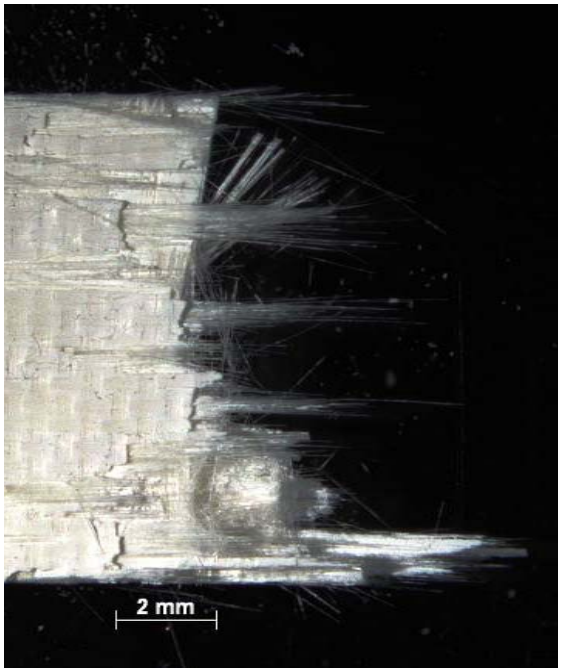

Figure 350. Fracture surface of N720/A specimen tested in creep at 1100 °C at 150 MPa in steam.

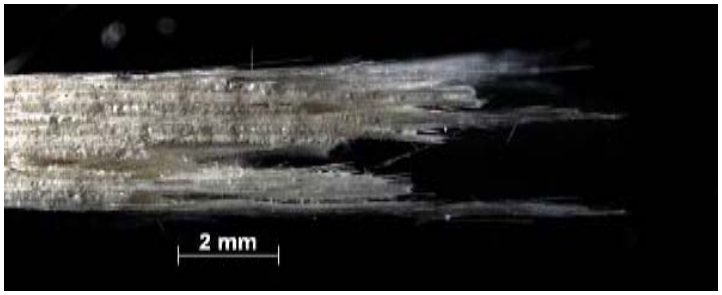

Figure 351. Fracture surface of N720/A specimen tested in creep at 1100 °C at 150 MPa in steam.

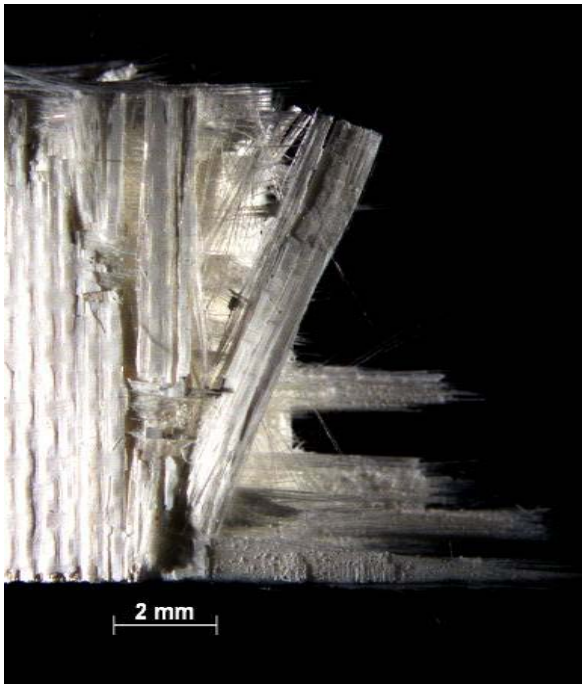

Figure 352. Fracture surface of N720/A specimen tested in creep at 1100 °C at 150 MPa in air.

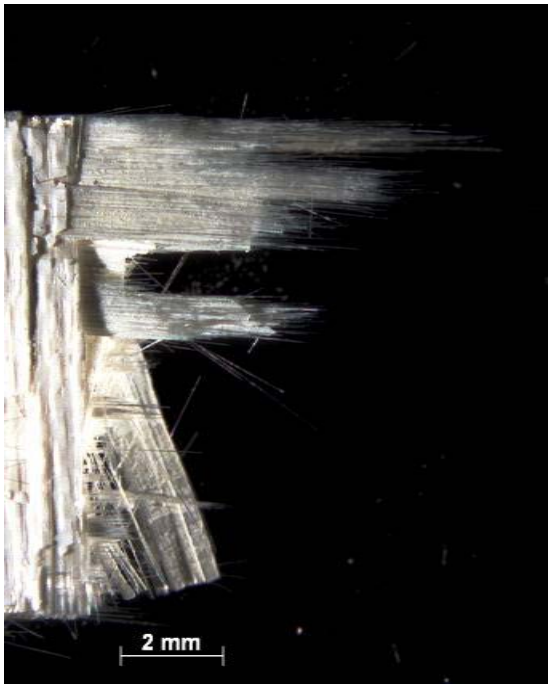

Figure 353. Fracture surface of N720/A specimen tested in creep at 1100 °C at 150 MPa in air.

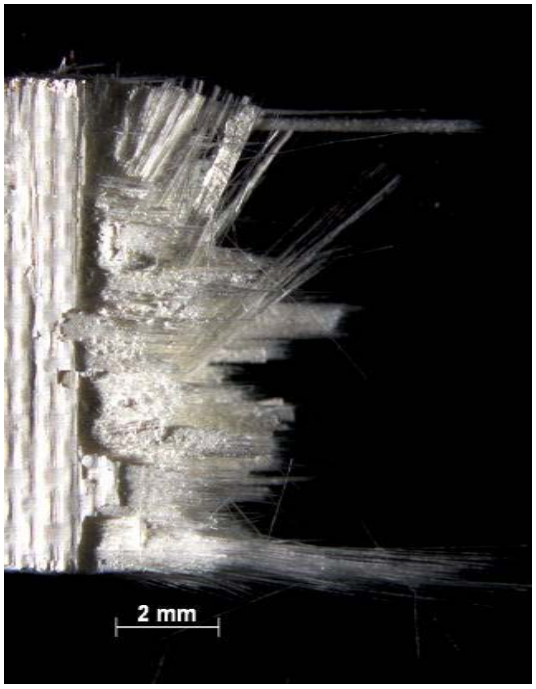

Figure 354. Fracture surface of N720/A specimen tested in creep at 1100 °C at 150 MPa in air.

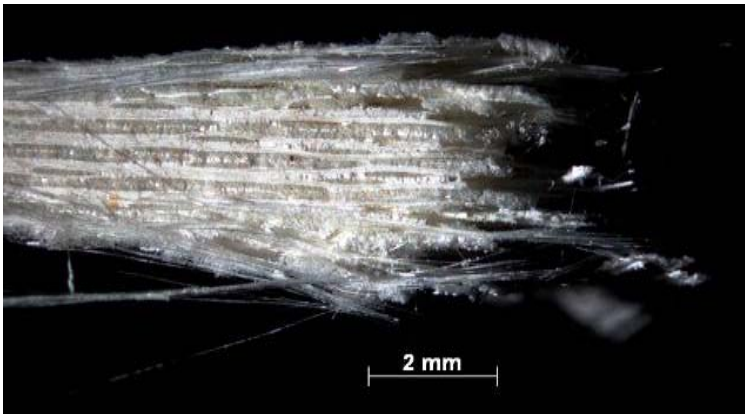

Figure 355. Fracture surface of N720/A specimen tested in creep at 1100 °C at 150 MPa in air.

Bibliography

1. *All You Wanted to Know About Electron Microscopy…but Didn't Dare to Ask.* Hillsboro, OR: FEI Company, no date. http//www.feicompany.com. 10 Feb 2006.

2. "F-22 Raptor Materials and Processes." Globalsecurity.Org. http://www.globalsecurity.org/military/systems/aircraft/f-22-mp.htm. 19 Dec. 2005.

3. "Report of the Committee on the Definition of the Term Ceramics," *Journal of the American Ceramic Society*, 3(7):526-542 (1920).

4. Antti, M-L, E. Lara-Curzio, and R. Warren. "Thermal Degradation of an Oxide Fibre (Nextel 720)/Aluminosilicate Composite," *Journal of the European Ceramic Society*, 24: 565-578 (2004).

5. Baker, A., Dutton, S., Kelly, D. *Composite Materials for Aircraft Structures* (Second Edition). Virginia: AIAA, 2004.

6. Buchanan, Dennis J., Reji John, and Larry P. Zawada. "Creep Rupture Behavior of ±45° Oxide/Oxide Nextel™720/AS Composite," in *25th Annual Conference on Composites Advanced Ceramics Materials, and Structures: A.* Ed. Waltruad M. Kriven and Hau-Tay Lin. Westerville, OH: The American Ceramic Society, 2003.

7. Campbell, C.X., Carelli, E.V., More, K.L., Varghese, P., Seal, S., and V. H. Desai, "Effect of High-Temperature Water Vapor Exposure on Nextel 720 in an Alumina-Matrix CMC," *Siemens Westinghouse Power Corporation Technical Document TP-02076*.

8. Carelli, E.A., Fujita, H., Yang, J.Y., and Zok, F.W. "Effects of Thermal Aging on the Mechanical Properties of a Porous-Matrix Ceramic Composite," *Journal of the American Ceramic Society,* 85[3]: 595-602 (2002).

9. Casas, L., and Martínez-Esnaola J.M. "Microstructural characterization of an alumina/mullite composite tested in creep," *Materials Science and Engineering*, A368: 139-144 (2004).

10. Charles RJ, Hillig WB. "The kinetics of glass failure by stress corrosion," in *Symposium on Mechanical Strength of Glass and Ways of Improving It, Florence, Italy, September 25–29 (1961).* Union Scientifique Continentale du Verre, Charleroi, Belgium, 1962. p. 511–527.

11. Charles R.J., and W.B. Hillig. "Surfaces, stress-dependent surface reactions, and strength," in: *High-strength materials.* Ed. V.F. Zackey. New York, NY: Wiley, 1965. p. 682–705.

12. Chawla, K. K. *Ceramic Matrix Composites* (Second Edition). Boston: Kluwer Academic Publishers, 2003.

13. COI Ceramics, Unpublished Data.

14. Daniel, Isaac M. and Ori Ishai. *Engineering Mechanics of Composite Materials*. New York, NY: Oxford University Press, 1994.

15. DiCarlo, James A. and Sunil Dutta. "Continuous Ceramic Fibers for Ceramic Matrix Composites," in *Handbook on Continuous Fiber-Reinforced Ceramic Matrix Composites.* Ed. Richard L. Lehman, Said K. El-Rahaiby, and John B. Wachtman, Jr.Westerville, OH: The American Ceramic Society, 1995.

16. Dowling, N.E. *Mechanical Behavior of Materials* (Second Edition). Upper Saddle River: Prentice-Hall, 1999.

17. Fujita, H., Levi, C. G., Zok, F. W., and G. Jefferson, "Controlling Mechanical Properties of Porous Mullite/Alumina Mixtures via Precursor-Derived Alumina," *Journal of the American Ceramic Society,* 88[2]: 367-375 (2005).

18. Fujita, H., Jefferson, G., McMeeking, R.M., and F.W. Zok, "Mullite/Alumina Mixtures for Use as Porous Matrices in Oxide Fiber Composites," *Journal of the American Ceramic Society*, 87[2]: 261-67 (2004).

19. Harada, Yoshihisa, Suzuki, Takayuki, and Hirano, Kazumi. "Influence of Moisture on Ultra-High-Temperature Tensile Creep Behavior of in Situ Single-Crystal Oxide Ceramic Alumina/Yttrium Aluminum Garnet Eutectic Composite," *Journal of the American Ceramic Society*, 86: 951-958 (2003).

20. Harlan, Lee B. *Creep-Rupture Behavior of an Oxide/Oxide Ceramic Matrix Composite at Elevated Temperatures in Air and Steam Environments.* MS thesis, AFIT/GA/ENY/05-M05. School of Engineering and Management, Air Force Institute of Technology (AU), Wright-Patterson AFB OH, March 2005.

21. Haslam, J.J., Berroth, K.E., and Lange, F.F. "Processing and Properties of an all oxide composite with a porous matrix," *Journal of the European Ceramic Society*, 20:607-618 (2000).

22. Haynes, J.A., Lance, M.J., Cooley, K.M., Ferber, M.K., Lowden, R.A., Stinton, D.P. "CVD Mullite Coating in High-Temperature, High-Pressure Air-H_2O," *Journal of the American Ceramic Society*, 83[3]:657-659 (2000).

23. Hetrick, Griffin. *Effects of Frequency and Environment on Fatigue Behavior of an Oxide-Oxide Ceramic Matrix Composite at 1200 °C.* MS thesis, AFIT/GA/ENY/06-

J05. School of Engineering and Management, Air Force Institute of Technology (AU), Wright-Patterson AFB OH, June 2006.

24. Holmquist, M.G. and Lange, F.F. "Processing and Properties of a Porous Oxide Matrix Composite Reinforced with Continuous Oxide Fibers," *Journal of the American Ceramic Society,* 86[10]:1799-40 (2003).

25. Jacobson, N.S. "Corrosion of Silicon-Based Ceramics in Combustion Environments," *Journal of the American Ceramic Society*, 76[1]:3-28 (1993).

26. Jacobson, N.S., Morscher, G.N., Bryant, D.R., Tressler, R.E. "High-Temperature Oxidation of Boron Nitride: II, Boron Nitride Layers in Composites," *Journal of the American Ceramic Society*, 82[6]:1473-1482 (1999).

27. Jurf, R.A. and Butner, S.C. "Advances in Oxide-Oxide CMC", *Journal of Engineering for Gas Turbines and Engine Power,* 122: 202-205 (April 2000).

28. Kaya, C., Butler, E.G., Selcuk, A., Boccaccini, A.R., and Lewis, M.H. "Mullite (Nextel™ 720) fibre-reinforced mullite matrix composites exhibiting favourable thermomechanical properties," *Journal of the European Ceramic Society,* 22: 2333-2342 (2002).

29. Kerans, R.J. and Parthasarathy, T.A. "Crack deflection in ceramic composites and fiber coating design criteria," *Composites: Part A,* 30:521-524 (1999).

30. Kooner, S., Westby, W.S., Watson, C.M.A., and Farries, P.M. "Processing of Nextel™720/mullite composition composite using electrophoretic deposition," *Journal of the European Ceramic Society,* 20:631-638 (2000).

31. LaRochelle, K.J. *Tensile Stress Rupture Behavior of a Woven Ceramic Matrix Composite in Humid Environments at Intermediate Temperatures.* Ph.D. dissertation, AFIT/DS/ENY/05-01. School of Engineering and Management, Air Force Institute of Technology (AU), Wright-Patterson AFB, OH March 2005.

32. Lange, F.F., Tu, W.C., Evans, A.G. "Processing of damage-tolerant, oxidation resistant ceramic matrix composites by a precursor infiltration and pyrolysis method," *Materials Science and Engineering*, A195:145-150 (1995).

33. Levi, Carlos G., James Y. Yang, Brian J. Dalgleish, Frank W. Zok, and Anthony G. Evans. "Processing and Performance of an All-Oxide Ceramic Composite," *Journal of the American Ceramic Society*, 81[8]: 2077-86 (1998).

34. Lewis III, David. "Continuous Fiber-Reinforced Ceramic Matrix Composites: A Historical Overview," in *Handbook on Continuous Fiber-Reinforced Ceramic Matrix Composites.* Ed. Richard L. Lehman, Said K. El-Rahaiby, and John B. Wachtman, Jr.Westerville, OH: The American Ceramic Society, 1995.

35. Mecham, Michael. "Composite Power." Aviation Week 17 Apr. 2006: 47-52.

36. Mehrman, J.M. *Effect of Hold Times on Fatigue Behavior of Nextel™ 720/Alumina Ceramic Matrix Composite at 1200 °C in Air and in Steam Environment.* MS thesis, AFIT/GA/ENY/06-M23. School of Engineering and Management, Air Force Institute of Technology (AU), Wright-Patterson AFB, OH March 2006.

37. Mehrman, J.M., Ruggles-Wrenn, M.B., and Baek, S.S. "Influence of Hold Times on the Elevated-Temperature Fatigue Behavior of an Oxide-Oxide Ceramic Composite in Air and in Steam Environment", *Composites Science and Technology,* in press (2006).

38. Michalske, T.A., and S.W. Frieman. "A molecular mechanism for stress corrosion in vitreous silica," *Journal of the American Ceramic Society,* 66[4]: 284-288 (1983).

39. Michalske, T.A. and B.C. Bunker. "A chemical kinetics model for glass fracture," *Journal of the American Ceramic Society,* 76[10]: 2613-2618 (1993).

40. -----. "Slow fracture model based on strained silicate structures," *Journal of Applied Physics,* 56[10]: 2686-2693 (1984).

41. *Minnesota Mining and Manufacturing Company (3M™).* "Nextel™ Ceramic Textiles Technical Notebook," Company produced technical notebook. No date

42. Morscher, G.N., Bryant, D.R., Tressler, R.E. "Environmental Durability of BN Based (For SiC/SiC Composites) in H_2O-Containing Atmospheres at Intermediate Temperatures," *Ceramic Engineering and Science Proceedings*, 18[3]: 525-533 (1997).

43. Musikant, S. *What Every Engineer Should Know About Ceramics.* New York: Marcel Dekker, 1991.

44. Musil, Sean S. *Characterization of Creep Behavior of Oxide/Oxide Composite with Monazite Coating at Elevated Temperature.* MS thesis, AFIT/GAE/ENY/05-M14. School of Engineering and Management, Air Force Institute of Technology (AU), Wright-Patterson AFB OH, March 2005.

45. Nutt, S.R., "Environmental Effects on High Temperature Mechanical Behavior of Ceramic Matrix Composites," *High Temperature Mechanical Behavior of Ceramic Composites.* Newton, MA: Butterworth-Heinemann, 1995.

46. Oates, G.C. *Aerothermodynamics of Gas Turbine and Rocket Propulsion, 3rd Ed.* Reston, VA: American Institute of Aeronautics and Astronautics, Inc 1997.

47. Ohnabe, H., Masaki, S., Onozuka, M., Miyahara, K., Sasa, T. "Potential

application of ceramic matrix composites to aero-engine components," *Composites: Part A, Applied Science and Manufacturing* 30: 489-496 (1999).

48. Ogbuji, L.U. "Degradation of SiC/BN/SiC Composite in the Burner Rig," *Ceramic Engineering and Science Proceedings*, 19[4]: 257-264 (1998).

49. Parthasarathy, T.A., Zawada, L.P., John, R., Cinibulk, M. K., Kerans, R. J., and Zelina, J. "Evaluation of Oxide-Oxide Composites in a Novel Combustor Wall Application," *International Journal of Applied Ceramic Technology,* 2 (2): 122-132 (2005).

50. Parlier, M. and Ritti, M.H. "State of the art and perspectives for oxide/oxide composites," *Aerospace Science and Technology*, 7: 211-221 (2003).

51. Radsick, T., Saruhan, B., and Schneider, H. "Damage tolerant oxide/oxide fiber laminate composites," *Journal of the European Ceramic Society*, 20: 545-550 (2000).

52. Radzicki, Andy T. *Rate-Dependence of Tensile Properties and Stress-Strain Behavior of an Oxide/Oxide Ceramic Matrix Composite at Elevated Temperature and the Effects of Low-Magnitude Sustained Loading on Composite Microstructure.* MS thesis, AFIT/GAE/ENY/06-S09. School of Engineering and Management, Air Force Institute of Technology (AU), Wright-Patterson AFB OH, September 2006.

53. Ramulu, M., Prasad, N.E., Malakondaiah, G. and Guo, Z. "Secondary Processing Effects and Damage Mechanisms in Continuous-Fiber Ceramic Composites," *Thermal and Mechanical Test Methods and Behavior of Continuous-Fiber Ceramic Composites, ASTM STP 1309*, Michael G. Jenkins, Stephan T. Gonczy, Edgar Lara-Curzio, Noel E. Ashbaugh, and Larry P. Zawada, Eds., American Society for Testing and Materials (1997).

54. Raymer, D.P. *Aircraft Design: A Conceptual Approach, 3rd Edition.* Reston, VA: American Institute of Aeronautics and Astronautics, Inc, 1999.

55. Ruggles-Wrenn, M.B., Mall, S., Eber, C.A., and Harlan, L.B. "Effects of Steam Environment on High-Temperature Mechanical Behavior of Nextel™720/Alumina (N720/A) Continuous Fiber Ceramic Composite**",** *Composites: Part A*, 37: 2029-2040 (2006).

56. Saruhan, B., Schmucker, M., Bartsch, M., Schneider, H., Nubian, K., and Wahl, G. "Effect of interphase characteristics on long-term durability of oxide-based fibre reinforced composites," *Composites: Part A*, 32:1095-1103 (2001).

57. Schmidt, S., Beyer, S., Knabe, H., Immich, H., Mestring, R., and Gessler, A. "Advanced ceramic matrix composite materials for current and future propulsion technology applications," *Acta Astronautica,* 55: 409-420 (2004).

58. Siegert, G. *Effect of Environment on Creep Behavior of an Oxide/Oxide CFCC with ±45° Fiber Orientation.* MS thesis, AFIT/GA/ENY/06-J15. School of Engineering and Management, Air Force Institute of Technology (AU), Wright-Patterson AFB, OH June 2006.

59. Steel, Steven G. *Monotonic and Fatigue Loading Behavior of an Oxide/Oxide Ceramic Matrix Composite.* MS thesis, AFIT/GMS/ENY/00M-02. School of Engineering and Management, Air Force Institute of Technology (AU), Wright-Patterson AFB OH, March 2000.

60. Tressler, R.E. "Recent developments in fibers and interphases for high temperature ceramic matrix composites," *Composites: Part A*, 30: 429-437 (1999).

61. Tu, W.C., Lange, F.F., Evans, A.G. "Concept for a Damage-Tolerant Ceramic Composite with Strong Interfaces," *Journal of the American Ceramic Society*, 79[2]: 417-424 (1996).

62. Wannaparhun S., Seal S., Desai V.H., Varghese P. Campbell, C.X. "A Combined Spectroscopic and Thermodynamic Investigation of Nextel-720/alumina Ceramic Matrix Composite in Air and Water Vapor at 1100 °C," *Journal of the American Ceramic Society,* 86[9]: 1628-1630 (2003).

63. Wiederhorn, S.M.. "Influence of water vapor on crack propagation in soda-lime glass," *Journal of the American Ceramic Society,* 50[8]: 407–14 (1967).

64. Wiederhorn S.M., and L.H. Bolz. "Stress corrosion and static fatigue of glass," *Journal of the American Ceramic Society,* 53[10]: 543–8 (1970).

65. Wiederhorn S.M. "A chemical interpretation of static fatigue," *Journal of the American Ceramic Society,* 55[2]: 81–85 (1972).

66. Wiederhorn, S. M. , Freiman S. W., Fuller, E. R. , and C. J. Simmons, "Effects of Water and Other Dielectrics on Crack Growth," *Journal of Material Science*, 17: 3460-3478 (1982).

67. Wilson, D.M. and Visser, L.R. "High Performance Oxide Fibers for Metal and Ceramic Composites," *Composites: Part A*, 32[8]: 1143-1153 (2001).

68. Wilson, D.M., Lieder, S.L., and D.C. Luenegurg, "Microstructure and high temperature properties of Nextel 720 fibers," *Ceramic Engineering and Science Proceedings,* 16[5]: 1005–1014 (1995).

69. Zawada, L.P. "Longitudinal and transthickness tensile behavior of several oxide/oxide composites," *Ceramic Science and Engineering Proceedings,* 19[3]: 327-340 (1998).

70. Zawada, L.P. and Staehler, J., Steel, S.G. "Consequence of Intermittent Exposure to Moisture and Salt Fog on the High-Temperature Fatigue Durability of Several Ceramic-Matrix Composites," *Journal of the American Ceramic Society*, 86 [8]: 1282-1291 (2003).

71. Zok, W. and Carlos G. Levi. "Mechanical Properties of Porous-Matrix Ceramic Composites," *Advanced Engineering Materials*, 3[1-2]: 15-23 (2001)

Vita

Captain Jason C. Braun graduated from Spring Lake High School in Spring Lake, Michigan in 1998. He entered undergraduate studies at the University of Notre Dame in South Bend, Indiana where he graduated with a Bachelor of Science degree in Mechanical Engineering. He was commissioned through the AFROTC Detachment 225 at the University of Notre Dame in May, 2002.

His first assignment was at Hill AFB, Utah in the Ogden Air Logistics Center's Landing Gear Sustainment Division. During his three years there he served as Landing Gear Engineer for the B-52 and F-16 airframes. He also spent a year as the Air Force Tire Engineer. In August 2005 he began graduate school work at the Air Force Institute of Technology's School of Engineering and Management toward a master's degree in Aeronautical Engineering. Upon graduation in March 2007, he will report to the Air Force Research Laboratory's Directed Energy Directorate's Adaptive Optics Division at Kirtland AFB, New Mexico.

REPORT DOCUMENTATION PAGE

Form Approved
OMB No. 074-0188

1. REPORT DATE *(DD-MM-YYYY)*	2. REPORT TYPE	3. DATES COVERED *(From – To)*
22-03-2007	Master's Thesis	Aug 2005 – Mar 2007

4. TITLE AND SUBTITLE

Effects of Temperature and Environment on Creep Behavior of an Oxide-Oxide Ceramic Matrix Composite

5a. CONTRACT NUMBER

5b. GRANT NUMBER

5c. PROGRAM ELEMENT NUMBER

6. AUTHOR(S)

Braun, Jason C., Captain, USAF

5d. PROJECT NUMBER

5e. TASK NUMBER

5f. WORK UNIT NUMBER

7. PERFORMING ORGANIZATION NAMES(S) AND ADDRESS(S)
Air Force Institute of Technology
Graduate School of Engineering and Management (AFIT/EN)
2950 Hobson Way, Building 640
WPAFB OH 45433-8865

8. PERFORMING ORGANIZATION REPORT NUMBER

AFIT/GAE/ENY/07-M04

9. SPONSORING/MONITORING AGENCY NAME(S) AND ADDRESS(ES)

AFRL/PRTC
Attn: Dr. Joseph Zelina
1950 Fifth Street
WPAFB OH 45433-7251

AFRL/MLLN
Attn: Dr. Ronald Kerans
2977 P Street
WPAFB OH 45433-7734

10. SPONSOR/MONITOR'S ACRONYM(S)

11. SPONSOR/MONITOR'S REPORT NUMBER(S)

12. DISTRIBUTION/AVAILABILITY STATEMENT

APPROVED FOR PUBLIC RELEASE; DISTRIBUTION UNLIMITED.

13. SUPPLEMENTARY NOTES

14. ABSTRACT

This research investigated the creep behavior of an N720/Al_2O_3 composite. The composite consists of a porous alumina matrix reinforced with laminated, woven mullite/alumina fibers (Nextel™ 720). This ceramic matrix composite (CMC) has no fiber coating and relies on the porous matrix for flaw tolerance.

The tensile stress-strain behavior was investigated and the tensile properties measured in the 800-1100 °C temperature range. Tensile creep behavior was examined at 1000 and 1100 °C in laboratory air and in steam environment. In air creep stress was 150 MPa. In steam creep stresses ranged from 100 to 160 MPa.

Primary and secondary creep, but no tertiary creep, were observed in all tests. Minimum creep rate was reached in all tests. Creep rates accelerated with increasing temperature and creep stress. The presence of steam further increased creep rates. At 1000 °C creep run-out, defined as 100 hours at creep stress, was achieved in all tests. At 1100 °C run-out was achieved at 150 MPa in laboratory air, but only at 100 MPa in steam. The residual strength and modulus of all specimens that achieved run-out were characterized. At 1100 °C in the presence of steam, creep performance deteriorated rapidly with increasing creep stress. Composite microstructure, as well as damage and failure mechanisms, were explored.

15. SUBJECT TERMS

Ceramic Matrix Composites, Composite Materials, Ceramic Fibers, Ceramic Materials, Fiber Reinforced Composites, Alumina, Mullite, Creep, Oxides, Nextel 720™ Fiber

16. SECURITY CLASSIFICATION OF:			17. LIMITATION OF ABSTRACT	18. NUMBER OF PAGES	19a. NAME OF RESPONSIBLE PERSON
a. REPORT	b. ABSTRACT	c. THIS PAGE			Dr. Marina B. Ruggles-Wrenn (ENY)
U	U	U	UU	267	19b. TELEPHONE NUMBER *(Include area code)* (937) 255-3636, ext 4641; email: marina.ruggles-wrenn@afit.edu